The influence of structure on seismic parameter estimation in anisotropic media

by

Thomas Kühnel

Diploma in Geophysics 1994
University of Karlsruhe (Germany)

Thesis submitted for the degree of Doctor of Philosophy
Department of Geology and Geophysics
University of Edinburgh
August 1998

We can imagine that this complicated array of moving things which constitutes "the world" is something like a great chess game being played by the gods, and we are observers of the game. We do not know what the rules of the game are; all we are allowed to do is to watch the playing. Of course, if we watch long enough, we may eventually catch on to a few of the rules.

Richard P. Feynman

Abstract

The presence of structural variation in seismically anisotropic media complicates the offset- and azimuth-dependent wave behaviour and leads to difficulties in interpretation and estimation. Studies of anisotropy are therefore often conducted in areas where the strata are known to be horizontal. The primary concern of this thesis is to investigate the effects of these non-horizontal reflecting interfaces on the parameter estimation. I achieve this by deriving approximate analytical equations for shot gathers, which allow me an insight into the physics governing the problems.

I consider three different, but important, types of anisotropic material: First, for transverse isotropic media with a vertical axis of symmetry (TIV), I investigate the effects of dip on the travel time for imaging purposes. Secondly, transverse isotropic media with a horizontal axis of symmetry (TIH) are used as a model for a vertically fractured materials; I extend existing techniques for fracture strike estimation to dipping layers. Finally, for a combination TIV and TIH media, which represents orthorhombic symmetry, analysis of the AVO behaviour in the symmetry plane leads to an inversion procedure for crack density.

For a dipping TIV layer I show that the shot gather formulation of the travel time can be decomposed into structure- and anisotropy-independent parts. A thorough investigation using synthetic seismograms reveals that this separation is valid for up to 15% P-wave anisotropy and dip angles of up to 20 degrees. I propose an additional processing step to enhance seismic data if anisotropy and dip both are present.

I extend an estimation method for the fracture strike in a TIH medium to dipping layers. An analytical analysis shows that the application of a non-linear global optimization scheme is required to invert the strike direction satisfactorily. This new method is applied to a real data set, and the general trend of the regional strike direction is confirmed.

The third type of anisotropy (orthorhombic), is investigated by its dynamic response. A derivation of all pure and mode-converted reflection coefficients in the symmetry plane is followed by a separation approach to extract the crack-dependent contribution. I demonstrate that a special acquisition geometry can lead to the inversion of the parameter crack density.

Acknowledgements

When I started the "adventure" Scotland three years ago, it was a trip into the unknown. Thankfully my girlfriend Petra and our daughter Katja were adventurous too and supported me morally throughout the time. I apologise for the many evenings and weekends which I spent on the thesis rather than with them. Living for the first time abroad means leaving old habits and old friends behind. Email is a great invention and I wish to express my gratitude to my friends who kept me informed about "back home" and were always good discussion partners especially Viola Zepp, Lars Zühlsdorff and Uwe Kästner. The habits changed quickly and the game of golf reimbursed me for some of the losses.

Even though new in the country, the friendliness and openness of the people impressed me. I'd like to mention Susan Francis and Mark Higgins at the department who were always a good laugh as well as serious discussion partners. Steve Horne with his vast literature knowledge has always been a good friend and I enjoyed those discussions during the long walks in the Pentlands with him. I met Tim Pointer, who critically reviewed some chapters of this thesis and with whom I fought many battles on the chess board. Thanks to you all.

From the beginning my supervisor Xiang-Yang Li was a permanent source of ideas and encouragement. He always had time for my problems and I admire his patience during all those numerous discussion we had. His expertise in presenting results in written form helped me enormously during the preparation of this thesis and I am extremely grateful for his excellent guidance.

My second supervisor Bob Pearce kept my involvement into the university's bureaucracy to an absolute minimum for which I'm grateful. His comments on all parts of my work were always very helpful and I enjoyed his linguistic abilities. It's a long way for me to go in that area.

I would cordially like to thank Ivan Pšenčík who allowed me to use the ray tracing package ANRAY. At all times he was very helpful concerning the usage of the programs and the proper set up of the models.

Beside the obvious, there are many other people who contributed to the successful completion of this thesis. Like Ruth Addinall from NCS who had to cope with ever-growing demands for new programs and better computer performances or Tom Bain and Fergus McTaggart from photographic services whose expertise helped me greatly to improve the quality of my presentations. Thanks for all your time.

I appreciate Frank Ohlsen's clear reviews which stripped the thesis of some unnecessary ballast. His unparalleled C-programming skills opened a whole new world for me. Reidar Bærheim commented on some chapters and his lectures on tensor algebra were very interesting. Colin MacBeth had always time for discussions and encouraged me throughout my time in Edinburgh. He also reviewed part of the manuscript and as a project director allowed me the opportunity to gain experience at conferences in Britain and abroad. Thanks a lot.

Finally, without the financial support from all the sponsors of the Edinburgh Anisotropy Project, this thesis would have never been started. I especially like to thank ELF and Saga Petroleum for the permission to work with their data.

P.S. I thank my examiners Dr. Paul Williamson and Prof. Anton Ziolkowski for their detailed analyses of this thesis. I appreciate their comments and suggestions to correct, clarify and improve my work.

Contents

Notations and conventions

In this section all the mathematical variables and other abbreviations that are use throughout the thesis are explained. They are arranged by chapters in the order of their appearance.

General

Symbol	Meaning
TI	transverse isotropic
TIV	transverse isotropic with a vertical axis of symmetry
TIH	transverse isotropic with a horizontal axis of symmetry
$TI_{\perp}$	transverse isotropic with an orientation of the symmetry axis perpendicular to the reflector
NMO	normal moveout
DMO	dip moveout
AVO	amplitude versus offset
GA	genetic algorithm

Chapter 2

Symbol	Meaning	Unit
t	time	s
Δ t	time increment	s
θ	phase angle	
ψ	group angle	
$\vec{x}$	point in space	m
$\delta\vec{x}$	point in the vicinity of $\vec{x}$	m
$\vec{U}(\vec{x})$	displacement of $\vec{x}$	m
$\frac{\partial \vec{U}_i}{\partial \vec{x}_j} = U_{i,j}$	derivative of the i-th component of the displacement with respect to the j-th spatial component	
e_{ij}	components of the strain tensor	
$\nu_i\nu_j$	components of the unit vector $\vec{\mathrm{x}}$	m
$\Delta V = \mathrm{dV}$	volume element	m^3
$\Delta S = \mathrm{dS}$	surface element	m^2
$\vec{T}$	traction	$\mathrm{N/m}^2$
$\vec{n}$	normal vector to the surface upon which $\vec{T}$ acts	
ρ	density	$\mathrm{kg/m}^3$
$\vec{F}$	force on the surface ΔS	N
f	forces acting on the volume ΔV	N
x_i, i=1,3	Cartesian axes	m
$\hat{\mathrm{x}}_i$	unit vectors in the directions of the Cartesian axes x_i	m
σ_{ij}	stress tensor	$\mathrm{N/m}^2$

Symbol	Meaning	Unit
$\ddot{\mathrm{U}}_i$	second derivative of U with respect to time	$\mathrm{m/s^2}$
c_{ijkl}	elastic tensor	$\mathrm{N/m^2}$
h_{ij}	volume source density of strain rate	$\mathrm{s^{-1}}$
W	energy	$\mathrm{kg\ m^2/s^2}$
λ	Lamé parameter	$\mathrm{N/m^2}$
μ	shear modulus	$\mathrm{N/m^2}$
c_{ij}	Voigt notation of the elastic tensor	$\mathrm{N/m^2}$
V_{qP}, V_{qSV}, V_{SH}	phase velocities for P, Sv and Sh waves	m/s
V_{qP0}, V_{qS0}	vertical phase velocities	m/s
Thomsen parameters: $\epsilon = \frac{C_{11}-C_{33}}{2C_{33}}$ $\delta = \frac{(C_{13}+C_{44})^2-(C_{33}-C_{44})^2}{2C_{33}(C_{33}-C_{44})}$ $\gamma = \frac{C_{66}-C_{44}}{2C_{44}}$		
V_G	group velocity	m/s
$A_i^{(n)}$	vectorial amplitude	
$\tau(x_j)$	eikonal	t
ω	frequency	Hz
$\vec{p}$	slowness	s/m
Γ_{ik}	Kelvin-Christoffel matrix	
G_m	eigenvalues of Γ_{ik}	$\mathrm{N/m^2}$
g_k^m	eigenvectors of Γ_{ik}	
$\mathrm{Q}_{ij}^{(x)} = \frac{\partial x_i}{\partial \gamma_j}$	transformation matrix from ray coordinates (γ_j) to Cartesian coordinates (x_i)	

Symbol	Meaning	Unit
$P_{ij}^{(x)} = \frac{\partial p_i}{\partial \gamma_j}$	matrix used to describe the dynamic ray tracing system	

Chapter 3

Symbol	Meaning	Unit
A_{ij}	density normalised elastic constants	m^2/s^2
t_0	zero-offset time	t
x	source-receiver offset	m
v	group velocity	m/s
S	indicator of the source position	
R	indicator of the receiver position	
ϕ	dip angle of the reflector	
D	distance to the reflector at the CMP point	m
v_{app}	apparent moveout velocity for a dipping reflector	m/s
x_1, x_2	offsets of the reflection from the top and the bottom of the target	m
θ	ray angle relative to the vertical	
ϕ_1, ϕ_2	azimuths 1 and 2	
v_{p1}, v_{p2}	phase velocity above and in the target layer	m/s
t_i	interval travel time	s
t_{ai}	azimuthal interval travel time	s
t_{top}, t_{bottom}	travel time for the the top and the bottom of the target	s

Symbol	Meaning	Unit
$s_1, s_2, s_1^{'}, \Delta s$	distances	m
$z_1, z, \Delta z$	depth of the top, the bottom and the interval of the target	m
p_x, p_z	horizontal and vertical slowness	s/m
$T(x)$	travel time for the walkaway VSP	t
a, b, x_0	parameters of the best fitting ellipse	s/m

Chapter 4

Symbol	Meaning	Unit
$\vec{R}(R_x, R_y, R_z)$	reflection point	m
$\vec{Rec}$		m
(Rec_x, Rec_y, Rec_z)	receiver	m
θ	phase angle	
ψ	group angle	
D_z	depth of the reflector at the source point	m
$\vec{I}(I_x, I_y, I_z)$	image point	m
d_1, d_2	the length of the two segments of the ray	m
L	length of the ray path	m
l	part of the length of the ray path related to horizontal layers	m
Δl	part of the length of the ray path related to the dip	m

Symbol	Meaning	Unit
ζ	anisotropic but dip-independent part	
Υ	anisotropic but dip-independent part	
x_{min}, x_0	offset where the minimum travel time is observed for anisotropic and isotropic layers	m

Chapter 5

Symbol	Meaning	Unit
v_h	horizontal velocity	m/s
v_{nmo}	NMO velocity	m/s
x_1, x_2, x_3, x_4	offsets of the different segments of the ray for a dipping target	m
$Z_{L_1}, Z_{L_2}, Z_{L_3}$	depths of the different segments	m
Z_A	depth of point A	m
L_1, L_2, L_3, L_4	lengths of the 4 segments	m
α, β	incidence and transmission angle	
$d_1, \Delta d$	depth and thickness of the target	m
ϕ	take off angle of the ray at the source	
θ	dip of the reflector	
x_0, y_0, a, b	parameters of the ellipse for the GA inversion	m

Chapter 6

Symbol	Meaning	Unit
r_{qP}, r_{qS}	reflected qP- and qS-coefficients	
t_{qP}, t_{qS}	transmitted qP- and qS-coefficients	
i_1, j_1	qP- and qS incidence angles	
i_2, j_2	qP- and qS transmission angle	
i^*, j^*	qP- and qS polarisation angles	
ρ_1, α_1, β_1	density, qP-velocity at angle i_1 and qS-velocity at angle j_1 of the upper medium	kg/m^3, m/s, m/s
ρ_2, α_2, β_2	density, qP-velocity at angle i_2 and qS-velocity at angle j_2 of the lower medium	kg/m^3, m/s, m/s
$\Delta i, \Delta j$	the Δ variations represent	
$\Delta\alpha, \Delta\beta$	change across the interface	m/s
$\Delta\rho$		kg/m^3
$\mathbf{R}$	reflectivity matrix	
$\mathbf{X}, \mathbf{Y}$	impedance matrices	
x_{1j}, y_{2j}	components of $\mathbf{X}$ and $\mathbf{Y}$	
x_{2j}, y_{1j}	components of $\mathbf{X}$ and $\mathbf{Y}$	kg/(m^{2}s)
$(e_{P_1}\ e_{P_3})^T$	qP polarisation vector	
$(e_{S_1}\ e_{S_3})^T$	qS-wave polarisation vector	
$(s_1\ s_{3_P})^T$	qP slowness vector	s/m
$(s_1\ s_{3_S})^T$	qS-wave slowness vector	s/m
ρ'	generalised density	kg/m^3
ζ_P, ζ_S	deviations between the polarisation direction (i^* and j^*) and the propagation direction (i and j) of qP-wave and the qS-wave	

Symbol	Meaning	Unit
ρ, α_b, β_b	isotropic background density and P and S velocity	kg/m^3, m/s, m/s
Z_P, Z_S	Isotropic P- and S impedances	$kg/(m^2s)$
$\Delta Z_P, \Delta Z_S$	Difference in Z wetween upper and lower medium	$kg/(m^2s)$
ϵ_d	fracture density	
ϵ_{ar}	the aspect ratio of the fractures	
α_f	P-wave velocity of the fluids within the fractures	m/s
α_0, β_0	vertical velocities	m/s
ζ_c	crack contribution to the deviation of the polarisation	
y_p, y_s	TIV dependent velocity parts	
y_c, ξ_c	crack-related velocity parts	

CHAPTER 1

Thesis objectives

1.1 Introduction

Investigations in the Earth's subsurface are designed to improve the knowledge about the interior of our planet and in a more commercial sense to assess the economical value of mineral or hydrocarbon resources. Among the objectives of experiments are the recovery of structural changes in the subsurface and physical parameters describing the rock and their variation with depth and location. Apart from information gathered in boreholes, most experiments are indirect, meaning that methods which intend to determine the relevant parameters are used without direct contact to the material of interest. Seismic reflection data fall into this category.

Estimations from seismic measurements are designed to recover the velocity structure with depth, the spatial distribution of seismically significant interfaces or other internal rock parameters such as porosity or permeability (Clærbout, 1994). A simplification of the mathematical framework and a reduction in the calculation time for the models is desirable. Traditionally this is achieved by assuming isotropic materials, even though the phenomena of anisotropy, an angular dependence of physical parameters, are known through theoretical contribution for over a century.

The models are based on the recordings from single azimuth P-wave data where anisotropy is extremely difficult to detect. However, with the improvement of acquisition technology, which allows multi-component and multi-azimuth recordings, the significance of anisotropy for exploration purposes is recognised gradually. The effects can be detected in both compressional- (Helbig, 1994) and shear-wave (Crampin, 1981) data. This thesis focuses on P-waves.

Evaluations of P-wave anisotropy can be traced back to Backus (1965), who determined approximate equations for the variation of the P-wave velocity as a combination of elastic constants. Levin (1978) analyses the accuracy of travel time equations based on these derivations and Helbig (1983) discusses the velocity variation in media with elliptical anisotropy. To be more applicable, Banik (1984) derives a set of effective parameters, a concept, which is applied very successfully to media with TIV symmetry and weak anisotropy by Thomsen (1986). Following his derivations, Sena (1991) extends the methodology to azimuthally anisotropic layers. Further work related to velocity and travel time analyses can be found in Li and Crampin (1993a) or Tsvankin and Thomsen (1994). All these studies contain analytical approximations describing the problems which are required because the complexity of the model has to be limited. Furthermore, first or second order linearizations in the parameters of interest are common and it is convenient to limit the model to horizontal layers.

But this may be an oversimplification if the strata are non-horizontal. Some techniques such as the reflectivity method (Fuchs and Müller, 1971) will fail because their foundations demand horizontal layers, and some such as the NMO correction, may lead to erroneous results. The investigation into the influence of dip on anisotropic parameters is vital. Either the structure dependency has to be corrected (Levin, 1990) or estimation methods have to be developed to calculate parameters including the dip (Tsvankin, 1995b).

The influence of dip and its significance has been widely recognised. During the course of my research, publications such as Tsvankin (1995b) or Alkhalifah (1995) showed the possibilities of the new developments. I investigate in this thesis how the anisotropic parameter estimation is influenced by the presence of dip. I analyse the effects of dip on estimation methods and quantify the influence using analytical approximations. These equations lead to extensions of existing or new estimation methods which take the dip into account. It is necessary to distinguish between different types of anisotropy as each is described by a different set of parameters.

1.2 Outline of the thesis

In Chapter 2 I introduce the theoretical concepts such as wave propagation, anisotropy and ray tracing, which build the basis for all the derivations presented during this thesis. I explain how the wave equation is derived and show the principles of ray tracing. This is important as most of the synthetic seismograms and travel time data in this thesis are calculated using a ray tracing package.

Chapter 3 shows the influence of dipping and anisotropic layers on a 3D survey. Travel time diagrams and principal investigation techniques are presented. For the detection of the fracture strike the basic investigation tool is explained and the difficulties arising from dipping targets are introduced. The concept of the influence of dip is extendible to transmission measurements and I show an application to a real data example from a walkaway VSP experiment.

The theoretical derivations for the travel time in a dipping anisotropic layer are laid down in Chapter 4. Different orientations of the symmetry axis of the elastic tensor are discussed and a separation approach of anisotropy and structure is derived from the synthetic investigations. The theory is applicable to 3D data as

well, and relevant formulas are given in Appendix A.

Chapter 5 shows the application and development of methods to estimate anisotropic parameters in the presence of dip. For a TIV material they are based on the derivations presented in Chapter 4. The results from the synthetic investigations are encouraging. For the fracture strike estimation a completely new method is developed. Theoretical investigations show that a non-linear global inversion scheme is required to overcome the difficulties. The mode of action of this genetic algorithm is explained and applied to a synthetic example.

Chapters 3, 4 and 5 focus on the investigation of the kinematic properties. In Chapter 6 I develop analytical equations for the reflection coefficient for the interface of two orthorhombic media. For thin cracks, the formulation for the P-P reflection coefficient can be separated in crack parameter dependent and independent parts and with a special acquisition geometry an inversion for the crack density may be possible.

Finally, in Chapter 7 I apply some of the methods to a marine data set. After a normal processing sequence to get a stacked section for each of the four marine lines, I use the NMO ellipse and the interval travel time for the non-linear inversion scheme to estimate the fracture strike. Analyses of the AVO gradient for the different directions confirm the results from the kinematic investigations.

CHAPTER 2

A review of anisotropy, seismic body waves and ray tracing

2.1 Introduction

In this chapter I review some of the basic theoretical concepts on which the mathematical derivations and methods applied in this thesis are based. It is designed to introduce the principal ideas and characteristics of anisotropy, wave propagation in an anisotropic medium and the synthesis of these waves using the concept of ray tracing.

I explain the basic principles of wave propagation which involves the formulation of the stress-strain relationship including the elastic tensor. It is designed to lay the foundation for all the methodology used throughout this thesis which does not explicitly involve wave propagation but contains it as an underlying concept. I demonstrate how the basic kinematic ray tracing system can be derived from the equations of motion and explain the method of dynamic ray tracing. It can be used to calculate amplitudes along the ray and is the concept on which the ray tracing package ANRAY (Gajewski and Pšenčík, 1987) is based. ANRAY is used extensively in later chapters to calculate synthetic seismograms and travel time curves in models with non-horizontal interfaces.

2.2 Seismic anisotropy

Seismic anisotropy is basically the angular dependency of elastic parameters which describe the rock. Every material is described completely by the elements of the elastic tensor and the density. If any material shows a directional dependency of the wave propagation it must therefore be expressed in the elements of the elastic tensor. Anisotropy causes a difference between the vertical and horizontal P and S-wave velocity as well as azimuthal changes (Helbig, 1994). One significant difference from an isotropic solid is the existence of a third distinct body wave instead of only two which exist in isotropic media (Červený, 1987). The second shear wave is polarised perpendicular to the first one and both are polarised in a plane perpendicular to the P-wave polarisation direction. During the passage through an anisotropic material, these two shear waves, usually referred as fast and slow, travel with different velocities, which allows the observation of a phenomenon called shear wave birefringence. But as the main area of investigation for this thesis are marine reflection data, shear waves play only a minor role.

Another complication worth mentioning is the difference between the phase and the group velocity in an anisotropic solid. The schematic illustration of Figure 2.1 describes this difference. If a point source excites one arbitrary mode, the wavefronts for an isotropic material is spherical and centred about the point source. A later wavefront at a time $t + \Delta t$ can be constructed using Huygens' principle or the superposition of plane waves (Helbig, 1994). In this case, the group velocity which is associated with the propagation of energy and the phase velocity which is associated with the advance of plane wavefronts, are the same. This is not true for wave propagation in an anisotropic medium, where the wavefronts are not spherical and the directions associated with the energy transport and the plane waves no longer coincide.

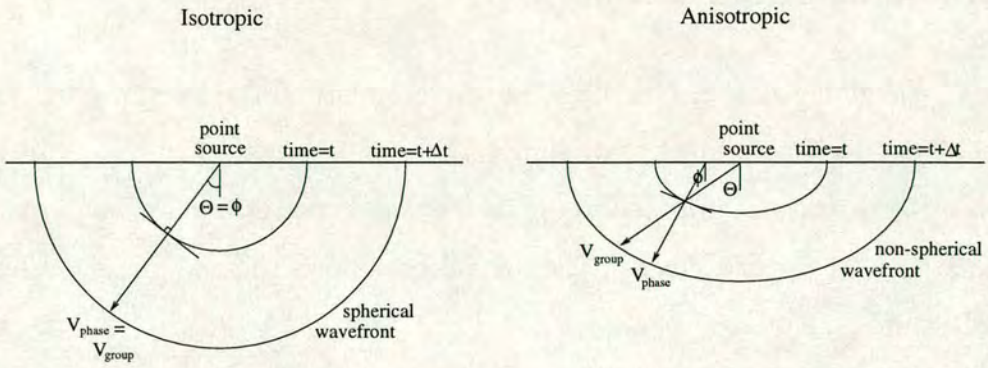

Figure 2.1: A graphical example for the difference between the phase and the group velocity for wave propagation in an isotropic and anisotropic media. The group velocity corresponding to the angle Θ is associated with the propagation of energy. The phase velocity corresponds to the angle ϕ and is associated with the plane wave locally perpendicular to the wavefront (after Thomsen, 1986)

All these phenomenon can mathematically be described for an elastic solid by the equations of motion and the generalised Hooke's Law. These two concepts are developed in greater detail in the following sections.

2.3 The principles of body wave propagation

If seismic motions are studied in the earth, an analytical framework is necessary to describe the equations for the energy that propagates. To formulate the equations of motion in a generally homogeneous elastic anisotropic medium it is important to define and formulate the relevant quantities such as displacement, strain and stress. They are derived from the analysis of particle motion inside a solid body if this body is exposed to forces. These derivations are laid down in great detail in many books on seismology, for example, Aki and Richards (1980) or Červený (1987) or in books on solid state physics (Feynman et al., 1963).

2.3.1 The strain tensor

The Lagrangian notation describes the displacement of a particular particle and the change in displacement with time. The symmetric strain tensor which describes the distortion of a medium is introduced here and I show how it can be derived from the displacement. The derivation follows the one presented by Aki and Richards (1980).

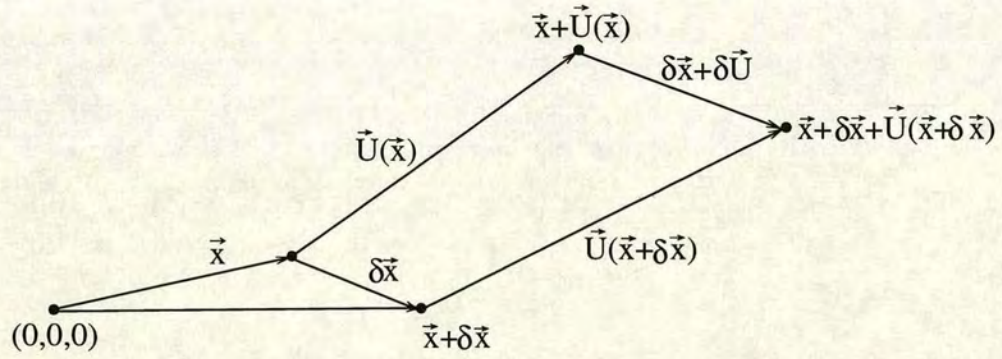

Figure 2.2: How the change in the displacement can be expressed

Consider a point $\delta\vec{x}$ and a point nearby $\vec{x}+\delta\vec{x}$. The idea is to derive an expression for the distance between the two points if $\delta\vec{x}$ has been displaced by $\delta\vec{U}$. From Figure 2.2 it follows that

$$\delta\vec{x} + \delta\vec{U} = \vec{x} + \delta\vec{x} + \vec{U}(\vec{x} + \delta\vec{x}) - \vec{x} - \vec{U}(\vec{x}), \tag{2.1}$$

$$\delta\vec{U} = \vec{U}(\vec{x} + \delta\vec{x}) - \vec{U}(\vec{x}), \tag{2.2}$$

where $\delta\vec{U}$ is the quantity which expresses the difference in the displacement. If the displacement $\delta\vec{x}$ is small, then the term $\vec{U}(\vec{x}+\delta\vec{x})$ can be expanded into a Taylor series. It has to be taken into account that it is a three-dimensional process. The strain tensor is derived by comparison of the lengths $\delta\vec{x}$ and $\delta\vec{x}+\delta\vec{U}$ where the assumption is made that $\frac{\partial\vec{U}_i}{\partial\vec{x}_j}$ can be expanded into a Taylor series and that the terms $\frac{\partial\vec{U}_i}{\partial\vec{x}_j}\frac{\partial\vec{U}_i}{\partial\vec{x}_j}$ are so small that they can be neglected. It follows that for small

linear deformations the correction between the two length can be expressed by the symmetric strain tensor

$$e_{ij} \equiv \frac{1}{2}(U_{i,j} + U_{j,i}). \tag{2.3}$$

The geometrical effect of the strain tensor is made apparent by relating the strained and unstrained displacement magnitudes

$$\underbrace{|\,\delta\vec{x} + \delta\vec{U}\,|}_{new\ length} = \underbrace{|\,\delta\vec{x}\,|}_{old\ length}\ (1 + \underbrace{e_{ij}}_{strain\ tensor}\ \nu_i\nu_j), \tag{2.4}$$

where $\nu_i\nu_j$ are the components of the unit vector $\vec{x}$.

2.3.2 The traction

To describe the forces which are acting between particles within a continuum the concepts of traction and stress tensor are introduced. Traction is defined as a vector of a contact force with which particles on one side of the surface act upon those on the other side. As can be seen from Figure 2.3, the traction is defined as the limit of the force applied over an infinitesimally small surface element.

2.3.3 The stress tensor

The deformation of a body is described by the inspection of an infinitesimally small volume element ΔV bounded by the surface ΔS. Both surface and volume forces act on ΔV. The alteration of the position of a point within ΔV is quantified by the sum of all these forces. This can be expressed mathematically as

$$\frac{\partial}{\partial t}\iiint_V \rho\frac{\partial\vec{U}}{\partial t}dV = \iiint_V \vec{f}dV + \iint_S \vec{T}(\vec{n})dS. \tag{2.5}$$

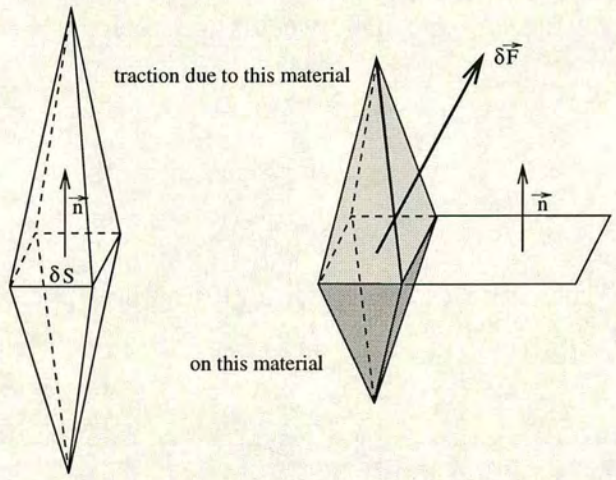

Figure 2.3: Traction $\vec{T} \equiv \lim_{\delta S \to 0} \frac{\delta \vec{F}}{\delta S}$

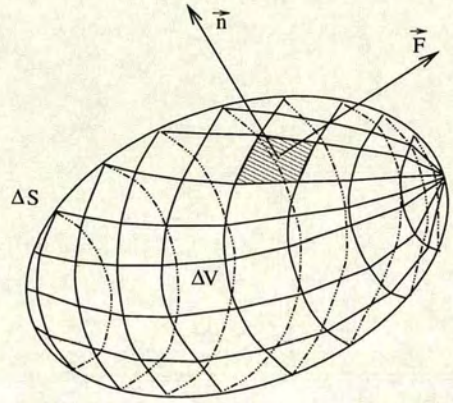

Figure 2.4: Body of the volume ΔV bound by the surface ΔS with force $\vec{F}$ and normal vector $\vec{n}$.

As the volume element becomes infinitesimally small it follows that $\iint_S dS$ vanishes slower with $\iint_S dS = O(\Delta V^{\frac{2}{3}}) \to 0$. Dividing equation 2.5 by $\iint_S dS$ yields

$$\frac{\iint_S \vec{T}\vec{n}dS}{\iint_S dS} = O(\Delta V^{\frac{2}{3}}) \to 0. \tag{2.6}$$

Suppose the volume becomes a thin disk as shown in Figure 2.5 then equation 2.6 implies that

$$\vec{T}(\vec{n}) = -\vec{T}(-\vec{n}). \tag{2.7}$$

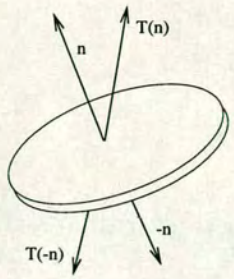

Figure 2.5: Position of the stress vectors if ΔV is represented by a thin disk.

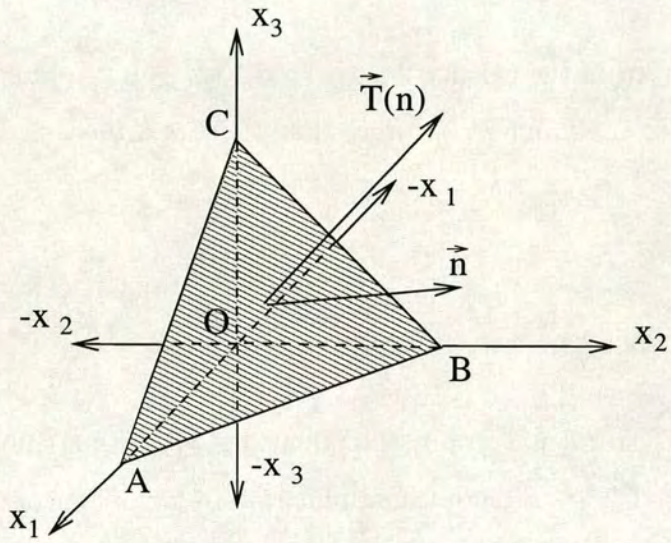

Figure 2.6: Tetrahedral shaped volume ΔV.

To derive the stress tensor the volume element ΔV is given a tetrahedral shape in the origin of the coordinate system as shown in Figure 2.6. $\hat{x}_i$ are the unit vectors in the directions of the Cartesian axes x_i. Equation 2.6 takes the following form for Figure 2.6:

$$\frac{1}{\Delta S}(\vec{T}(-\hat{x}_1)OCB + \vec{T}(-\hat{x}_2)OCA + \vec{T}(-\hat{x}_3)OAB + \vec{T}(\vec{n})ABC) \rightarrow 0. \qquad (2.8)$$

The components of the normal vector to the plane ABC can be written as

$$\vec{n} = (\frac{OCB}{ABC}, \frac{OCA}{ABC}, \frac{OAB}{ABC}), \qquad (2.9)$$

and a new description of the traction depending on its components parallel to

the coordinate axis can be stated as

$$\vec{\mathrm{T}}(\vec{\mathrm{n}}) = \vec{\mathrm{T}}(\hat{\mathrm{x}}_i)\mathrm{n}_i, \tag{2.10}$$

which leads to the definition of the stress tensor σ_{ij} through

$$\mathrm{T}_j = \sigma_{ij}\mathrm{n}_i. \tag{2.11}$$

It can be shown from the calculation of the rate of change of angular momentum in comparison to the moment of forces that the stress tensor is symmetric

$$\sigma_{ij} = \sigma_{ji}. \tag{2.12}$$

2.3.3.1 Equations of motion

Having defined stress and strain, the equations of motion can be derived from equations 2.5 and 2.11 through the application of Gauss' theorem to $\iint_S \mathrm{T}_i(\vec{\mathrm{n}}\mathrm{dS})$:

$$\iint_S \mathrm{T}_i(\vec{\mathrm{n}}\mathrm{dS}) = \iint_S \sigma_{ij}\mathrm{n}_j\mathrm{dS} = \iiint_V \sigma_{ij,j}\,\mathrm{dV}. \tag{2.13}$$

This allows the substitution of the surface integral by a volume integral and leaves only volume integrals in equation 2.5. In the following formulation of the equations of motion the double dots represent the second derivative with respect to time, the index describes the different components and the prime indicates the spatial derivative.

$$\iiint_V (\rho\ddot{\mathrm{U}}_i - \mathrm{f}_i - \sigma_{ij,j}) = 0 \tag{2.14}$$

$$\mathrm{f}_i + \sigma_{ij,j} = \rho\ddot{\mathrm{U}}_i. \tag{2.15}$$

These are the equations of motion where the acceleration times the mass ($\rho\ddot{\mathrm{U}}$) is equal to the sum of the forces $\mathrm{f}_i + \sigma_{ij,j}$.

2.3.4 Deformation-stress relation

To link material properties to the equations of motion the concept of elasticity has to be introduced. It connects the material properties to the stress and strain tensor. A medium is called elastic if it possesses a natural state ($\sigma_{ij} = \epsilon_{ij} = 0$) to which it returns in case all applied forces vanish. Hooke's Law for a linear elastic medium is an experimental determination for this and can be written in the following form

$$\sigma_{ij} = \mathrm{c}_{ijkl}\epsilon_{kl} \tag{2.16}$$

The relation between stress and displacement can then be expressed as

$$\sigma_{ij} = \mathrm{c}_{ijkl}\frac{1}{2}(\mathrm{U}_{i,j} + \mathrm{U}_{j,i}). \tag{2.17}$$

In case that action of external sources causes the deformation of the body the given time-rate of deformation can be written as (Savić, 1995)

$$\partial_t\sigma_{ij} = \mathrm{c}_{ijkl}[\frac{1}{2}(\dot{\mathrm{U}}_{i,j} + \dot{\mathrm{U}}_{j,i} - h_{ij})]. \tag{2.18}$$

where the symmetric tensor $h_{ij}$is known as the volume source density of strain rate.

Since σ_{ij} and ϵ_{ij} are symmetric, the so called elastic tensor c_{ijkl} contains certain symmetries itself.

$$\mathrm{c}_{ijkl} = \mathrm{c}_{jikl} \tag{2.19}$$

$$\mathrm{c}_{ijkl} = \mathrm{c}_{ijlk}. \tag{2.20}$$

A third symmetry relation can be found under the assumption that it is possible to use the adiabatic assumption in seismics. The high frequency used in seismic implies that the thermodynamic system is not able to adjust fast enough. Using the adiabatic approximation means that the energy of the deformation is equal

to the internal energy. Therefore, the deformation energy can be expressed in a similar form to the energy of a coiled spring as

$$W = \frac{1}{2} c_{ijkl} \epsilon_{ij} \epsilon_{kl}. \tag{2.21}$$

But the energy is independent of the exchange of ϵ_{ij} and ϵ_{kl} (Feynman et al., 1963). Therefore the final symmetry relation is given by

$$c_{ijkl} = c_{klij}, \tag{2.22}$$

which arises from the existence of a strain energy function.

A fourth rank tensor like c_{ijkl} where each index may take values between 1 and 3 contains 81 elements, but if the symmetry relations are considered the number of independent elements can be dramatically reduced. The first two symmetries (Equation 2.19 and 2.20) leave 6x6 elements which reduce to 21 if equation 2.22 is used. This means that these 21 constants completely describe any anisotropic elastic medium. The forth rank elastic tensor may be conveniently condensed by replacing the 4 suffixes, *ijkl*, with two suffixes, *mn*, defined such that

$$ij(ji) \text{ or } kl(lk) = 11 \rightarrow 1, 22 \rightarrow 2, 33 \rightarrow 3, 23 \rightarrow 4, 13 \rightarrow 5, 12 \rightarrow 6. \tag{2.23}$$

This notation, often refered as the Voigt notation, allows the elastic tensor to be written as a symmetric 6 by 6 matrix:

ij	$kl \rightarrow$	11	22	33	23	13	12
$\downarrow$							
11		c_{11}	c_{12}	c_{13}	c_{14}	c_{15}	c_{16}
22		·	c_{22}	c_{23}	c_{24}	c_{25}	c_{26}
33		·	·	c_{33}	c_{34}	c_{35}	c_{36}
23		·	·	·	c_{44}	c_{45}	c_{46}
13		·	·	·	·	c_{55}	c_{56}
12		·	·	·	·	·	c_{66}

2.3.5 Elastic tensors for special media

For most of this thesis a medium that requires 21 elastic constants is far too general. I will now introduce the elastic tensors for the media relevant to this thesis. Those are materials with isotropic, hexagonal and orthorhombic symmetries. Isotropic materials show no directional dependence of physical parameters while hexagonal materials consist of a single rotational symmetry axis so that in any direction perpendicular to this the material properties appear directionally invariant. These materials are commonly described as "Transversely Isotropic" (TI). The distinction between a vertical and a horizontal axis is important.

2.3.5.1 Isotropy

Isotropic materials are of the highest possible symmetry and show no directional dependency of any physical parameter. Therefore the stress tensor must be related to the strain tensor in a form which is independent of the choice of the coordinate direction. To describe the elastic tensor in the isotropic case two variables, the so-called Lamé parameters λ and μ are sufficient

$$\begin{pmatrix} \lambda+2\mu & \lambda & \lambda & 0 & 0 & 0 \\ & \lambda+2\mu & \lambda & 0 & 0 & 0 \\ & & \lambda+2\mu & 0 & 0 & 0 \\ & & & \mu & 0 & 0 \\ & & & & \mu & 0 \\ & & & & & \mu \end{pmatrix}. \tag{2.24}$$

Examples of such materials are water or glass.

2.3.5.2 Transverse isotropy with vertical axis of symmetry

In the case of transverse isotropy, 5 elastic constants are sufficient to describe the material as c_{66} can be expressed as $c_{66} = \frac{c_{11}-c_{12}}{2}$. This type of anisotropy is associated with fine layering where individual particles are preferentially aligned. The symmetry axis is usually orientated in the direction perpendicular to the layering (Figure 2.7) and the elements of the elastic tensor are distributed as shown in equation 2.25. The equivalent media theory states that this stack of layers can be replaced by an equivalent homogeneous anisotropic material which possesses an equivalent response. Any non-fractured horizontal sedimentary sequence could have transverse isotropy. Examples are sandstones or clay.

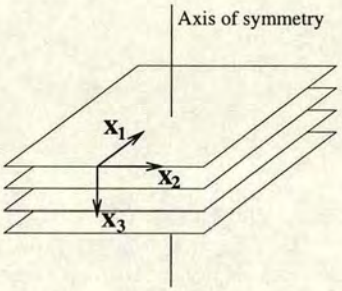

Figure 2.7: Model of a TIV material

$$\begin{pmatrix} c_{11} & c_{12} & c_{13} & 0 & 0 & 0 \\ & c_{11} & c_{13} & 0 & 0 & 0 \\ & & c_{33} & 0 & 0 & 0 \\ & & & c_{44} & 0 & 0 \\ & & & & c_{44} & 0 \\ & & & & & c_{66} \end{pmatrix} \tag{2.25}$$

2.3.5.3 Transverse isotropy with horizontal axis of symmetry

The number of independent elastic constants is exactly the same as in the TIV case. This type of anisotropy can be caused by differences in the horizontal components of the stress tensor. TIH anisotropy can be caused by a non-uniform horizontal stress regime. One possible model for a rock exposed to non-uniform horizontal stress is based upon cracks and fracture systems. A set of aligned circular cracks can be described by an equivalent

medium of a transverse isotropic material with a horizontal axis of symmetry where the direction of the symmetry axis is perpendicular to the crack face (Figure 2.8). Note that now the tensor elements 1,2 and 1,3 have the same value (equation 2.26) while for TIV materials 1,3 and 2,3 are the same.

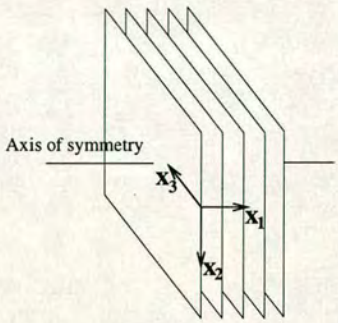

Figure 2.8: Model of a TIH material

$$\begin{pmatrix} c_{33} & c_{13} & c_{13} & 0 & 0 & 0 \\ & c_{11} & c_{12} & 0 & 0 & 0 \\ & & c_{11} & 0 & 0 & 0 \\ & & & c_{66} & 0 & 0 \\ & & & & c_{44} & 0 \\ & & & & & c_{44} \end{pmatrix} \tag{2.26}$$

2.3.5.4 Orthorhombic

A material with orthorhombic symmetry can be constructed as a combination of horizontally layered sedimentary sequence (TIV) which contains vertically aligned cracks (TIH) as shown in Figure 2.9. The number of elastic constants that are required to describe such a material has risen to nine (equation 2.27).

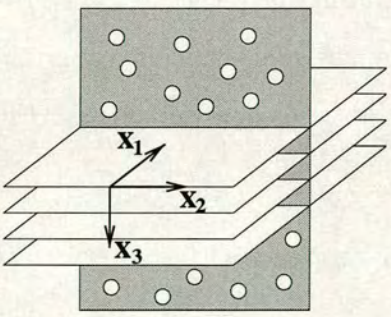

Figure 2.9: Model of an orthorhombic material

$$\begin{pmatrix} c_{11} & c_{12} & c_{13} & 0 & 0 & 0 \\ & c_{22} & c_{23} & 0 & 0 & 0 \\ & & c_{33} & 0 & 0 & 0 \\ & & & c_{44} & 0 & 0 \\ & & & & c_{55} & 0 \\ & & & & & c_{66} \end{pmatrix} \tag{2.27}$$

2.4 Theory of weak anisotropy

For weak TI, the phase velocities of V_{qP}, V_{qSV} and V_{SH} at the phase angle θ measured from the vertical axis can be expressed in terms of linear combinations of the Thomsen parameters ϵ, δ and γ (Thomsen, 1986)

$$V_{qP}(\theta) = V_{qP0}(1 + \delta \sin^2\theta \cos^2\theta + \epsilon \sin^4\theta), \tag{2.28}$$

$$V_{qSV}(\theta) = V_{qS0}[1 + \frac{V_{P0}^2}{V_{qS0}^2}(\epsilon - \delta) \sin^2\theta \cos^2\theta], \tag{2.29}$$

$$V_{SH}(\theta) = V_{qS0}(1 + \gamma \sin^2\theta), \tag{2.30}$$

where V_{qP0} and V_{qS0} are the vertical qP and qS-wave phase velocities. Thomsen's parameters are defined as combinations of elastic constants for a TI medium.

$$\epsilon = \frac{C_{11} - C_{33}}{2C_{33}}, \tag{2.31}$$

$$\gamma = \frac{C_{66} - C_{44}}{2C_{44}}, \tag{2.32}$$

$$\delta = \frac{(C_{13} + C_{44})^2 - (C_{33} - C_{44})^2}{2C_{33}(C_{33} - C_{44})}, \tag{2.33}$$

where ϵ and γ represent the P- and S-wave anisotropies. Elliptical anisotropy is present only if $\epsilon - \delta = 0$. Therefore $\epsilon - \delta \neq 0$ defines the deviation from elliptical anisotropy or the an-ellipticity of the medium. In the case of isotropy all Thomsen parameters reduce to zero.

For simplicity, I denote $V_{qP}(\theta)$ as $V_P(\theta)$ with P standing for phase. Travel time calculation requires the group velocity $V_G(\psi)$ at the ray angle ψ corresponding to the phase angle θ (Figure 2.10). To find the correct group velocity at the incidence angle ψ

$$V_G(\psi(\theta)) = \sqrt{V_P^2(\theta) + \left(\frac{dV_P(\theta)}{d\theta}\right)^2}. \tag{2.34}$$

The connection between ψ and θ is given (Berryman, 1979) by

$$\psi(\theta) = \theta + \Delta\theta, \tag{2.35}$$

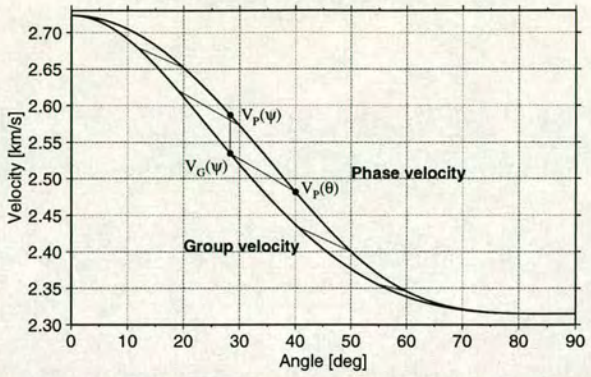

Figure 2.10: The phase and group velocity for a model with $\epsilon = 0.15$.

with

$$\tan(\Delta\theta) = \frac{1}{V_P(\theta)} \frac{dV_P(\theta)}{d\theta}. \tag{2.36}$$

$\Delta\theta$ is the angle between the phase and the group ray. Note that equation (2.28) is only valid for weak anisotropy while equations (2.34), (2.35) and (2.36) are valid for arbitrary TI anisotropy for wave propagation in symmetry planes. Inserting equation (2.28) into equation (2.34) and taking only the linear terms in ϵ and δ yields the weak anisotropy expression for the group velocity

$$V_G(\psi) = V_{P0}(1 + \delta \sin^2(\psi)\cos^2(\psi) + \epsilon \sin^4(\psi)), \tag{2.37}$$

A relationship between the phase velocity, the corresponding group velocity and the phase velocity at the ray angle can be derived as

$$V_P(\psi) > V_G(\psi) > V_P(\theta). \tag{2.38}$$

If equation 2.34 is expanded into a Taylor series it gives

$$V_G(\psi(\theta)) = V_P(\theta)\left(1 + \frac{1}{2V_P^2(\theta)}\left(\frac{dV_P(\theta)}{d\theta}\right)^2\right), \tag{2.39}$$

but here equation 2.36 can be inserted and expanded for small angles $\Delta\theta$ which

leads to

$$V_G(\psi(\theta)) = V_P(\theta) + \frac{1}{2}\frac{dV_P(\theta)}{d\theta}\Delta\theta, \tag{2.40}$$

which is greater than $V_P(\theta)$. To prove the second relationship, I insert equation 2.35 into $V_P(\psi(\theta))$ and expand it for small angles $\Delta\theta$. This gives

$$V_P(\psi(\theta)) = V_P(\theta) + \frac{dV_P(\theta)}{d\theta}\Delta\theta. \tag{2.41}$$

This is greater than $V_G(\psi(\theta))$ and proves the inequality.

2.5 Introduction to ray tracing

To allow the numerical solution of the equation of motion for a model composed of several materials as described above, the concept of ray tracing is introduced. The calculation package ANRAY (Gajewski and Pšenčík, 1987), which is used in later chapters to calculate synthetic seismograms for models with non-horizontal interfaces, is based on this theory. It was chosen for its flexibility as far as the model and the distribution of receivers is concerned and for the accuracy with which travel times and amplitudes can be calculated. An introduction to the theory is appropriate at this stage as it shows what is meant by "high-frequency approximation", why there is only one shear wave in isotropic media or why complex models can be handled. Many of the leading theoretical contributions to this area come from Červený (1987), Červený et al. (1977), Pšenčík (1979) or Hubral (1980). The following derivations of the eikonal equation and the ray tracing system are based on the work by Červený (1987).

The propagation of waves in a two-dimensional or even three-dimensional space is a highly complicated process. There are no analytical solutions of the elastodynamic equations of motion for this general problem. One of the numerical methods uses a high frequency (HF) approximation for the solution of the elas-

todynamic equations and is called ray tracing. To be applicable, the dimensions of the inhomogeneities have to be larger than the seismic wavelength. In 3D the two point ray tracing, where a source and receivers at arbitrary positions are connected, may be computationally very time consuming.

2.5.1 The elastodynamic equation

The elastodynamic equations can be derived if Hooke's Law [equation 2.16] is inserted into the equation of motion [equation 2.15]. This leads to the following form

$$\rho U_{i,tt} = \sigma_{ij,j} + f_i, \tag{2.42}$$

$$\rho U_{i,tt} = (\mathrm{C}_{ijkl} U_{k,l})_{,j} + f_i. \tag{2.43}$$

A possible solution to this equation is the so called ray series solution.

2.5.2 HF solution of the elastodynamic equations

The displacement U_i is expressed as a high frequency (HF) ray series where the vectorial amplitude $A_i^{(n)}$ depends on the frequency omega (w). It can be written in the following form

$$U_i = \Re(e^{-i\omega(t-\tau(x_j))} \sum_{n=0}^{n=\infty} A_i^{(n)} (-i\omega)^{-n}), \tag{2.44}$$

where $\tau(x_j)$ is the real-valued phase function or eikonal. The expression $\tau(x_j) - t$ = constant describes a moving wave front and the slowness vector $\vec{p} = \nabla\tau(x_j)$ is perpendicular to this wave front.

The solution to the problem is found if equation 2.44 is inserted into the elastodynamic equation [equation 2.43], assuming that there are no body forces ($f_i = 0$)

and only the zeroth order in the ray series is taken into account. This leads to an eigenvalue problem of the following form

$$(\Gamma_{ik} - \delta_{ik})A_k^{(0)} = 0, \tag{2.45}$$

where $\Gamma_{ik} = \frac{1}{\rho}C_{ijkl}\sigma_{,j}\sigma_{,l}$. This equation, the so called Kelvin-Christoffel equation, has three eigenvalues which correspond to the three high frequency seismic body waves which may generally propagate in an inhomogeneous anisotropic elastic medium. If equation 2.45 is compared to the general definition of the eigenvectors of a matrix Γ

$$(\Gamma_{ik} - G_m\delta_{ik})g_k^m = 0, \tag{2.46}$$

where G_m are the eigenvalues and g_k^m the eigenvectors, it is clear that

- the eigenvectors of equation 2.45 are given by $A_k^{(0)}$. They are usually called the polarisation vectors and are mutually perpendicular.
- equation 2.45 has a non-trivial solution if at least one of the eigenvalues equals unity.

The eigenvectors of 2.45 can only be determined if the three eigenvalues are non degenerant. This is not the case if the medium is isotropic, where the eigenvectors corresponding to the two identical eigenvalues are confined to a plane determined by any two of the independent eigenvectors.

2.5.3 The eikonal equations and the ray tracing system

From the fact that at least one of the eigenvalues of the Christoffel equation has to equal unity a set of first order non-linear partial differential equations can be derived, the so-called eikonal equations, whose characteristics or solutions

describe the ray tracing system. The eikonal equation takes the form

$$\tau_{,k}\tau_{,k} = \frac{1}{V^2(x_j)}, \tag{2.47}$$

and the ray tracing system is given by

$$\frac{\mathrm{d}x_i}{\mathrm{d}\tau} = V^2 p_i, \tag{2.48}$$

$$\frac{\mathrm{d}p_i}{\mathrm{d}\tau} = V\frac{\partial}{\partial x_i}(\frac{1}{V}). \tag{2.49}$$

To solve the system, a starting point and the initial conditions for the slowness at that point have to be known. The ray tracing system will lead to the ray and the travel time along it. This system is valid for isotropic materials where the distinction between the phase and the group velocity is not necessary because they are equal. However, in an anisotropic medium this is no longer true. The ray tracing system now written as

$$\begin{aligned} \frac{dx_i}{d\tau} &= \frac{1}{2}\frac{\partial G}{\partial p_i} \\ \frac{dp_i}{d\tau} &= -\frac{1}{2}\frac{\partial G}{\partial x_i} \end{aligned} \tag{2.50}$$

where $G(p_j, x_j)$ is the relevant eigenvalue of the elastodynamic ray theory matrix Γ and $p_i = \tau, i$.

This system requires the solution of the Eigenvalues G_m and therefore the phase velocity, but in addition the derivatives of the eigenvalues with respect to the slowness and spatial coordinates are also required. The derivative with respect to the slowness equals the group velocity and this is the velocity which determines the travel time along the ray (Červeným, 1987).

2.5.4 Dynamic ray tracing

To evaluate amplitudes along the ray a different set of differential equations has to be found which allows not only the calculation of kinematic properties but also

ray amplitudes. A useful concept is to evaluate the properties of the ray tube (see Figure 2.11), where a family of rays cut out a vectorial surface element (ABCD) for a given time τ.

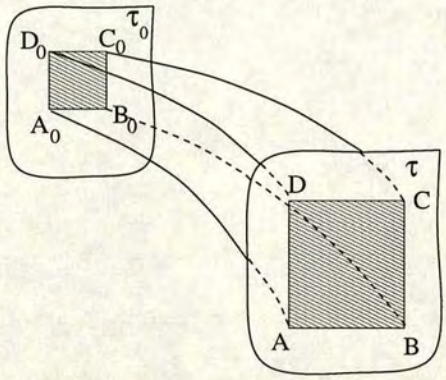

Figure 2.11: The concept of the ray tube

The density of the rays may change as the tube progresses from τ_0 to τ and therefore the size of the surface element changes. However, the size of the surface element is directly related to a quantity called the *ray Jacobian* which is inversely proportional to the ray amplitude. To implement the dynamic ray tracing a method to evaluate the ray Jacobian at any point of the ray has to be found. The ray Jacobian is defined as the determinant of the matrix $Q_{ij}^{(x)} = \frac{\partial x_i}{\partial \gamma_j}$ which describes the transformation from ray coordinates (γ_j) to Cartesian coordinates (x_i). Ray coordinates describe a coordinate system where two coordinates (γ_1, γ_2) specify the ray and the third parameter is varying along the ray. The matrix elements Q_{ij} (i=1,2,3; j=1,2) together with a matrix $P_{ij}^{(x)} = \frac{\partial p_i}{\partial \gamma_j}$ can be included in the ray tracing system [equation 2.48 and 2.49] and lead to a system of 12 differential equations. To calculate the complete transformation matrices P_{ij} and Q_{ij} the elements Q_{i3} and P_{i3} have to be determined. They evolve from kinematic ray tracing. To calculate the ray Jacobian, and with it the amplitude, therefore both the kinematic and the dynamic ray tracing system have to be solved.

CHAPTER 3

The effects of dip on travel time analysis

3.1 Introduction

The idea of a seismic experiment is to reveal as much information as possible about the subsurface. This chapter explains how the travel time can be used to accomplish this goal and how different influences such as dipping layers or different anisotropic materials complicate this task significantly. Nevertheless these effects may aggravate the estimations but will also lead to additional medium parameters apart from the isotropic velocity or the depth of the interface.

Seismic investigations can be divided into two major groups - the kinematic and dynamic aspects of wave propagation. The dynamics concentrate on the behaviour of the amplitude and the kinematics deal with the travel time as the main area of interest. Travel time is defined as the time a disturbance takes to travel from a source to a designated endpoint, when it expands according to the laws of elasticity throughout a model which may be of any complexity. It is the most simple and most reliable measurement in seismic, as it is independent of any mode changes and changes of the wavelet due to the model.

Travel time analyses have been carried out for a long time. With progress in

theoretical knowledge together with the need for the recovery of more parameters, the methods became progressively sophisticated. Levin (1990) showed that the moveout velocity for a transversely isotropic layer (TIV) with an orientation of the symmetry axis of the medium perpendicular either to the surface or the interface can be approximated by a cosine correction of the true velocity. Li and Crampin (1993b) gave a method to estimate anisotropic parameters as did Tsvankin (1994) or Sena (1991) among others. Recently, methods have evolved (Li, 1997) which allow even the estimation of the strike direction of a fractured reservoir just from surface seismic experiments.

Below I demonstrate how the travel time in three dimensions changes for models with varying reflector orientations and different types of anisotropic materials. The model which is used for the calculations is shown in Figure 3.1 and the parameters are given in Table 3.1.

Model	A_{11}	A_{12}	A_{13}	A_{33}	A_{44}	A_{66}	$\rho[g/cm^3]$	ϵ	δ	γ
Isotropic	5.41	-	-	5.41	2.05	-	2.0	0.0	0.0	0.0
TIV	6.68	1.56	1.31	5.41	2.05	2.56	2.0	0.11	0.0	0.12

Table 3.1: Material parameters (density normalised elastic constants, Thomsen parameters and density) for the travel time calculation. The TIH properties result from the TIV by a rotation of 90 degrees.

3.2 Isotropy

If a sequence of sediments is deposited horizontally and no further geological processes change the structure a suitable model representation is a stack of horizontal isotropic layers. The travel time from the first interface is given by

$$t^2 = t_0^2 + \frac{x^2}{v^2}, \tag{3.1}$$

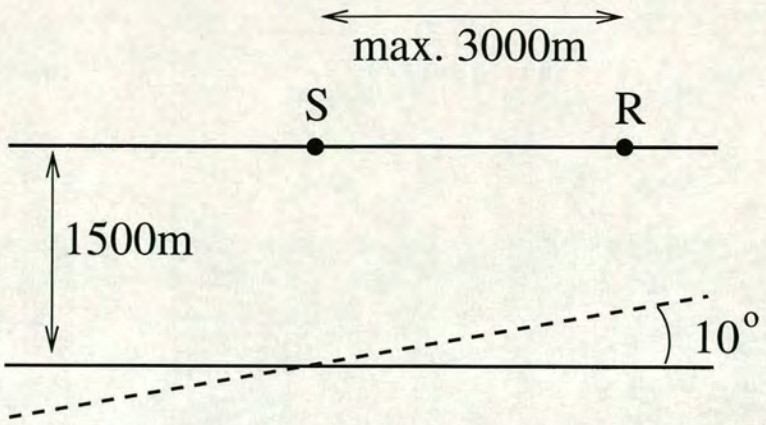

Figure 3.1: Section of the model along the x-axis for the travel time calculations. The dashed line indicates the position of the reflector in the dipping case.

which shows the well known hyperbolic moveout. Here x is the distance between the source and the surface receiver and t_0 is defined as the travel time for zero incidence. No azimuthal change is expected for the travel time and the medium velocity v can be recovered. Figure 3.2 shows the distribution of the travel time for such a model after a 3D survey.

The velocity v can be determined as the one which shifts the travel times for all offsets to the zero offset travel time. It is called the normal moveout velocity. The depth of the reflector can then be estimated from the zero offset travel time. Therefore a measurement along one line with arbitrary direction is enough to recover the parameters.

If the model is changed from a horizontal to a dipping interface an additional parameter is introduced. It is useful to write the travel time equation for this problem in two ways: first for a shot gather and then for a common-midpoint gather (CMP) as each of the formulations is designed to recover different parameters. The travel times for all diagrams are calculated for shot gathers because it is extremely computation time consuming to construct CMP gathers with ANRAY especially if the reflector is dipping (3.3).

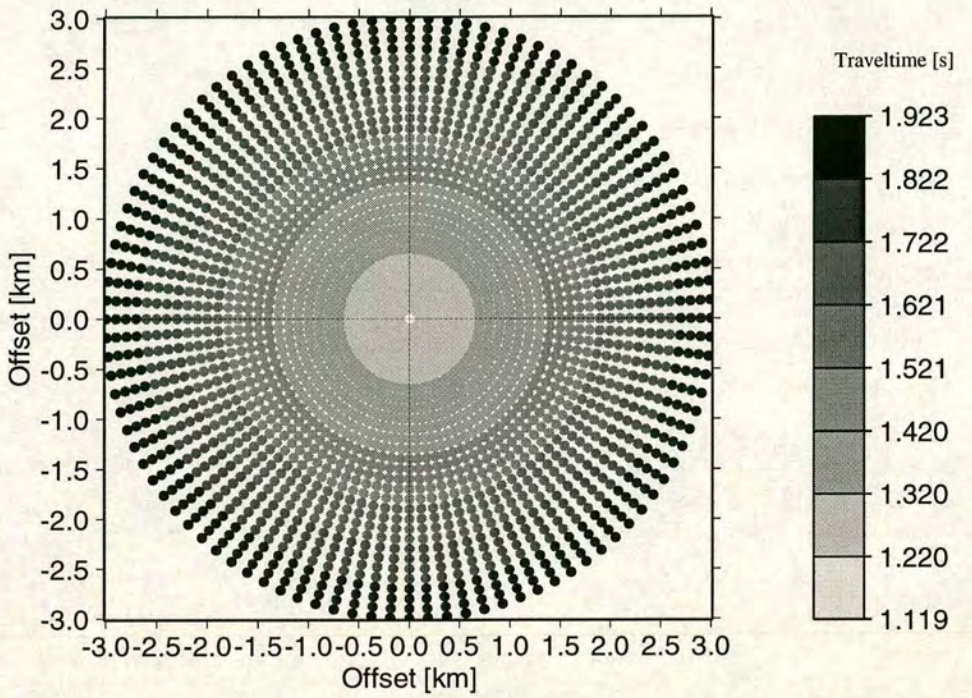

Figure 3.2: Travel time variation for a 3D survey and a horizontal reflector beneath an isotropic layer

The shot-gather formulation can be derived from equation 4.9

$$t^2 = t_0^2 - \frac{2t_0 x v \sin\phi - x^2}{v^2}, \tag{3.2}$$

where t_0 is the zero offset time, ϕ the dip angle, x the source to surface receiver offset and v the medium velocity. For a measurement in the dip direction the offset at which the minimal travel time is recorded, can be used to evaluate the dip of the reflector.

The CMP gather formulation leads to an apparent NMO velocity (Levin, 1990)

$$t^2 = \left(\frac{2D}{v}\right)^2 + \left(\frac{x}{v_{app}},\right)^2 \tag{3.3}$$

where D is the distance between the surface and the reflection point measured normal to the reflector at the midpoint, x is the source-surface receiver offset and v_{app} the apparent moveout velocity which is given by

$$v_{app} = \frac{v}{\cos\phi}. \tag{3.4}$$

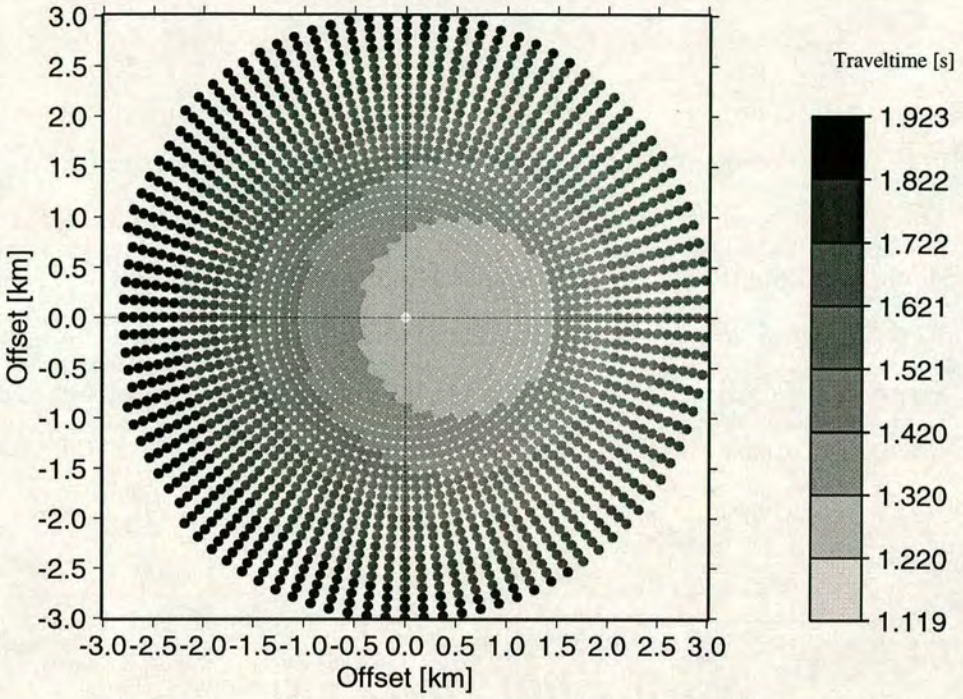

Figure 3.3: Travel time variation for a 3D survey and a 10 degrees dipping reflector beneath an isotropic layer.

From a single line it is only possible to estimate the dip properly if the survey is conducted in the dip direction. If on the other hand the aim of the experiment is to gain a good image of the reflector any line will give the same results because different apparent velocities will be used for different directions during the NMO correction.

3.3 Anisotropy

In the following sections the influence of a dipping interface is investigated for materials with hexagonal symmetry. For both cases, vertical and horizontal orientation of the symmetry axis are covered.

3.3.1 Transverse isotropy with vertical axis of symmetry (TIV)

As stated earlier, the vertical axis of symmetry indicates that no azimuthal change in the travel time is considered. However, in a vertical plane the angular dependent velocity is higher for horizontal propagation than for vertical. Therefore, the zero offset time does not differ from that shown in Figure 3.2 but all the non-zero offset arrivals are earlier. The percentage difference between the fast and the slow velocity is a measure of the anisotropy of the medium. This is indicated by Figure 3.4 where the same scale is used as in the previous figures.

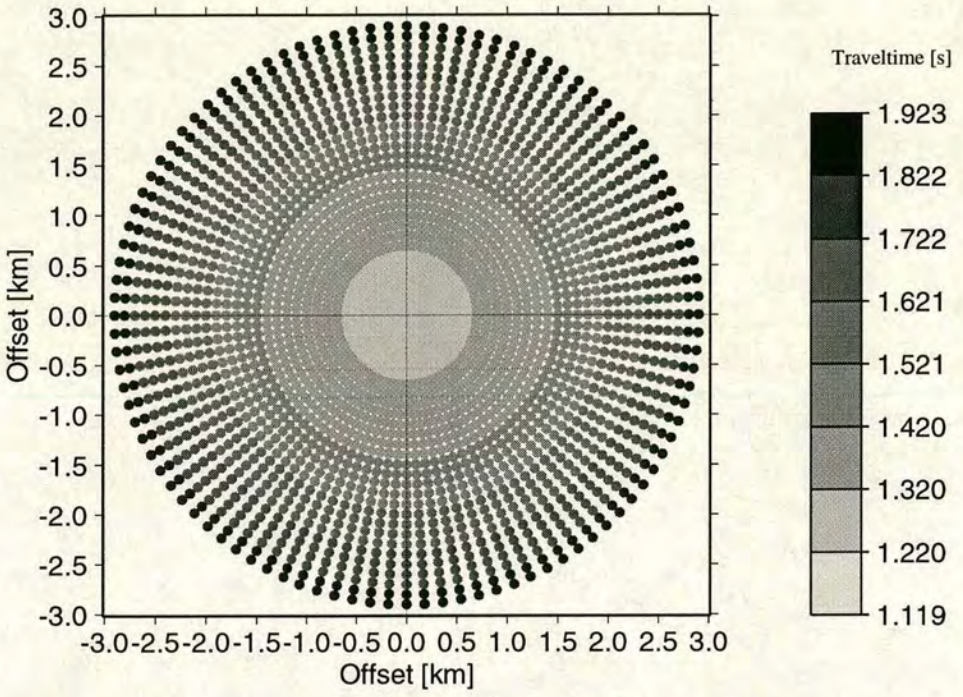

Figure 3.4: Travel time variation for a 3D survey and a horizontal reflector beneath a horizontal TIV layer.

The estimation process combines two different stages. If the motivation is to calculate anisotropic parameters, a technique should be applied which uses the residual moveout to estimate the horizontal velocity (Li and Crampin, 1993b).

This quantity is the moveout left in the data after isotropic processing. The strategy is somehow different if the objective is to find the best image of the reflector. In this case anisotropy has to be included in the NMO process as suggested by Tsvankin (1994) or Alkhalifah and Tsvankin (1995) to compensate for the non-hyperbolic moveout.

For a dipping reflector with the symmetry axis of the medium still perpendicular to the reflector ($TI_{\perp}$) the travel time distribution shows the same shift as the isotropic model (Figure 3.5). To use the estimation techniques described above the influence of the dip has to be removed (Kühnel and Li, 1997).

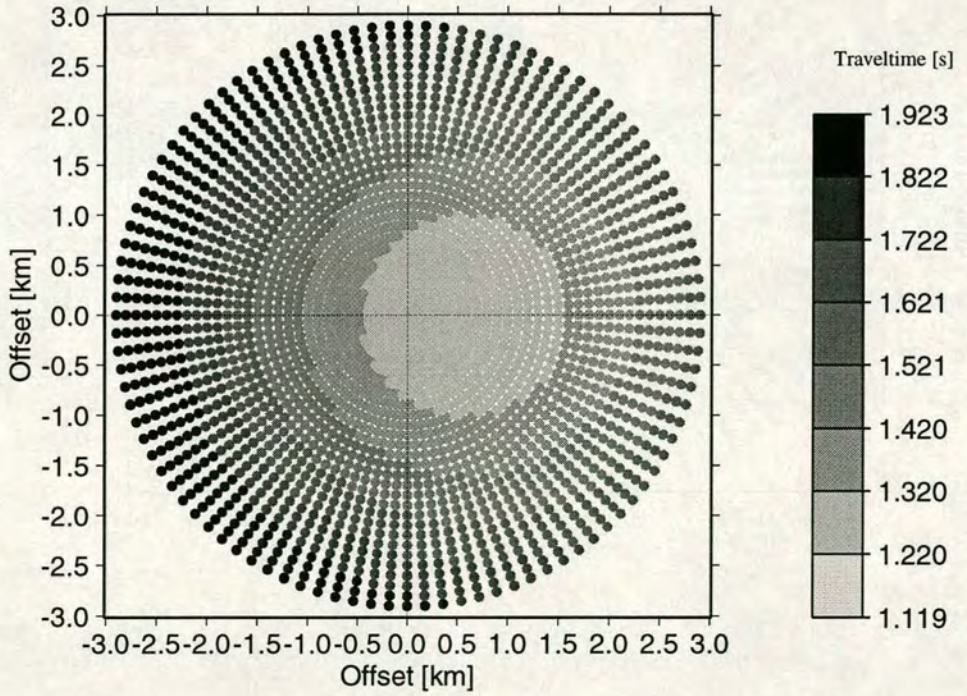

Figure 3.5: Travel time variation for a 3D survey and a 10 degrees dipping reflector beneath a 10 degrees dipping TI layer with the symmetry axis perpendicular to the reflector ($TI_{\perp}$).

3.3.2 Transverse isotropy with horizontal axis of symmetry (TIH)

Another type of material can be composed by a rotation through 90 degrees of the symmetry axis of the TIV medium. For a horizontal layer the axis is parallel to the surface. One consequence is that the velocity changes for different azimuths. A 3D travel time survey (Figure 3.6) should therefore clearly show an azimuthal variation in the travel time. Also the vertical velocity is now faster than the horizontal which is indicated by the earlier arrival of the zero-offset in Figure 3.6

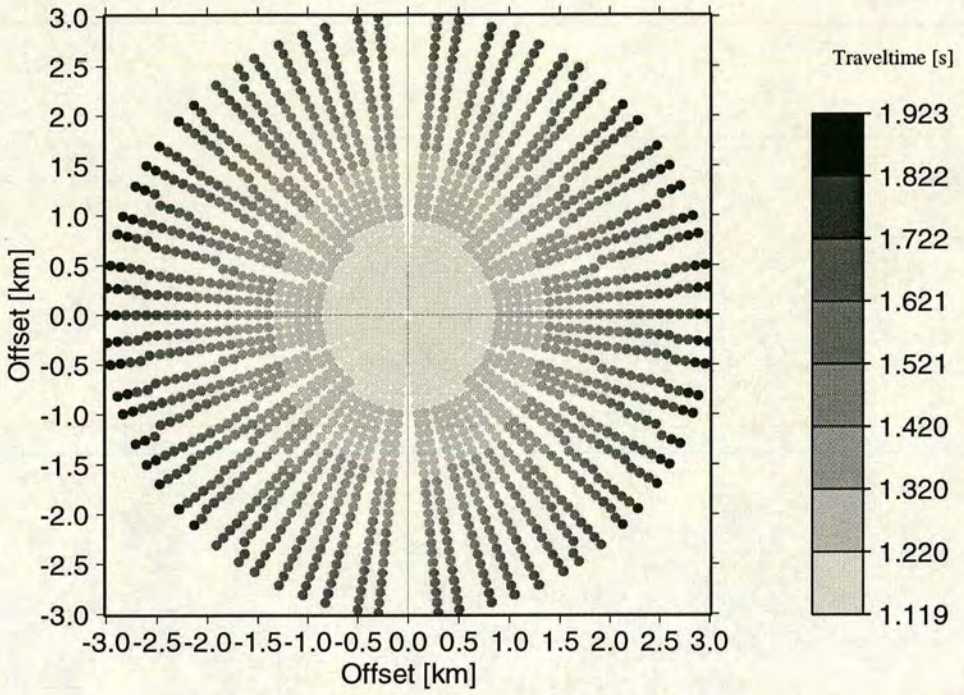

Figure 3.6: Travel time variation for a 3D survey and a horizontal reflector beneath a horizontal TIH layer.

To achieve a better image in any direction the anisotropic NMO correction will suffice. However, to estimate anisotropic parameters accurately, such as the difference between direction of the fast and slow velocity, a 3D survey is necessary even for a single layer.

For a dipping interface the ray paths are not confined to one vertical plane and the energy may travel along different segments of the ray at different speeds. The dip moves the minimum travel time in the up-dip direction and the non-circular form of the travel time distribution is still maintained as shown in Figure 3.7. An estimation method for this parameter combination is presented in chapter 5, based on the fracture strike estimation scheme which is explained in the next section.

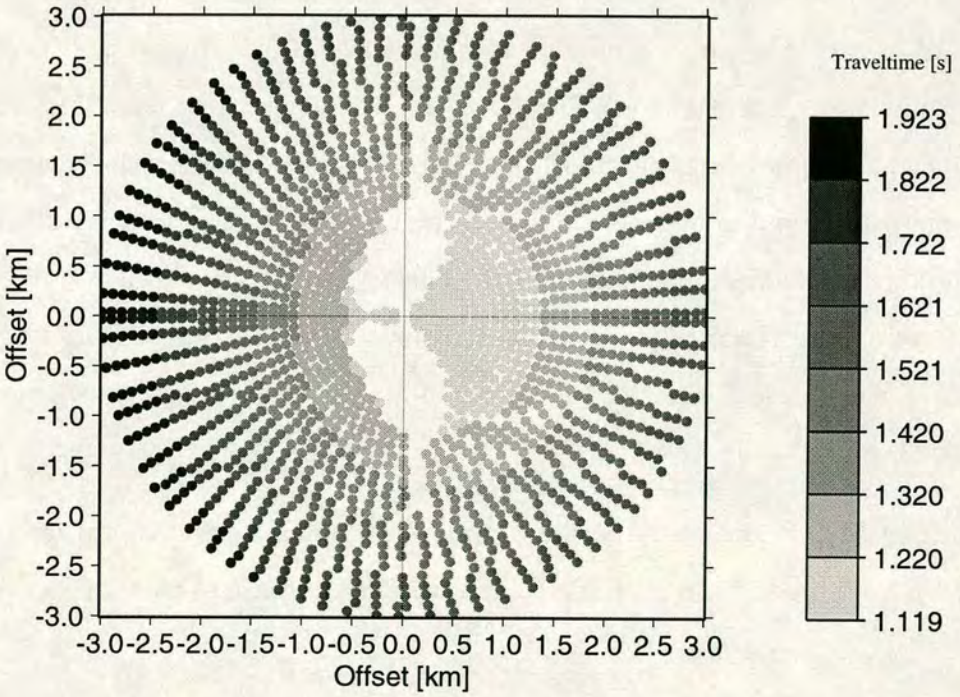

Figure 3.7: Travel time variation for a 3D survey and a 10 degrees dipping reflector beneath a 10 degrees dipping TIH layer. The lack of data points is a result of the ray tracing package ANRAY95, which requires the take-off angle of the rays at the source. Only a very fine grid would have had the chance to hit all receiver points but the computation time would have increased dramatically.

3.4 Interval moveout

One anisotropic parameter which can be detected from surface measurements is the strike direction of fractures described by a transverse isotropic medium with a horizontal axis of symmetry (TIH). Sena (1991) or Tsvankin (1995a) suggested the detection of the fracture strike from azimuthal variations in the P-wave NMO velocity. Li (1997) gives a scheme to evaluate the fracture strike relative to the survey direction for a four line configuration based on the interval travel time. All these techniques assume a horizontally layered model and the effects of dipping layers are not addressed.

For transverse isotropy with a vertical symmetry axis (TIV), Kühnel and Li (1996) discussed the anisotropic effects on P-wave travel time in the presence of dip and argued that the effects of the dip and anisotropy show an ordered relationship and may be separated from each other using an iteration scheme for weak anisotropy and gentle dips. For the fractured TIH medium, Sayers (1997) presented a method to compensate for the effects of dip using P-wave travel time to determine the fracture strike from walkaway VSPs. However, for fracture detection using surface seismics the effects of dip and how to compensate for the dips has not been fully investigated.

I will first review and examine the estimation method for horizontal layers followed by a synthetic data example to illustrate the required steps.

3.4.1 The horizontal target - a review

In the following section I give a brief review of the method formulated by Li (1997) for a horizontal fractured layer, and examine the effects of offset variation and extend the concept for 3D data analysis. The model is assumed to contain two horizontal layers: a TIV overburden and a fractured reservoir as shown in

Figure 3.8. S and R denote the source and receiver position.

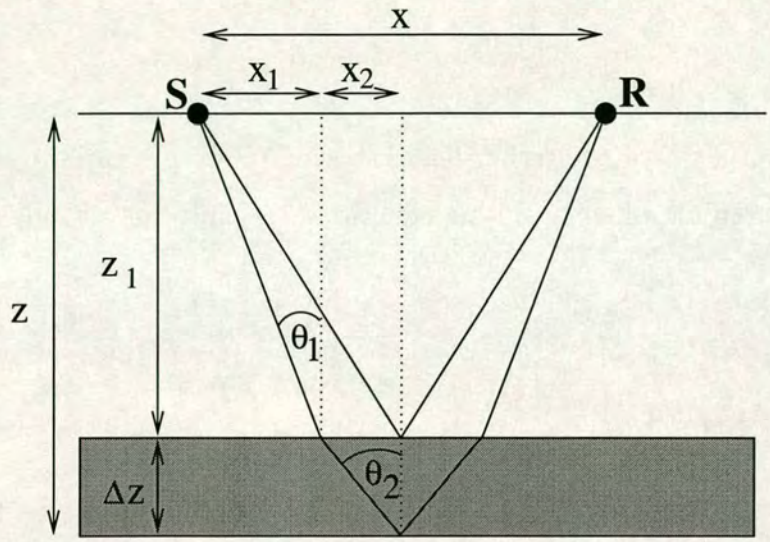

Figure 3.8: Ray path for the P-P reflection from the top and the bottom of the reservoir.

Consider a line-azimuth at ϕ to the strike direction of the symmetry axis of the TIH target layer. The interval moveout for this line azimuth is defined as the differential moveout between the reflection events from the top and the bottom of the target. Δt_i is a function of the azimuth and offset,

$$\Delta t_i(\phi, x) = t_{bottom} - t_{top} = \frac{2\sqrt{x_2^2 + \Delta z^2}}{v_{p2}(\theta_2, \phi)} + \frac{2\sqrt{x_1^2 + z_1^2}}{v_{p1}(\theta_1)} - t_{top}, \qquad (3.5)$$

where, as shown in Figure 3.8, x is the source-receiver offset, x_1 the offset of the transmission point at the top of the fractured target, $x_2 = x/2 - x_1$, θ_1 the incidence angle at the transmission point, and θ_2 the incidence angle at the bottom of the target. z_1 and Δz are the thickness of the overburden and the target and v_{p1} and v_{p2} are the compressional velocities of the overburden and the target.

Consider now two line-azimuths at ϕ_1 and ϕ_2 to the strike direction of the TIH target. The azimuthal interval moveout is defined as the differential interval

moveout between the two azimuths. Denoting the interval moveout for the two line-azimuths as Δt_{i1} and Δt_{i2}, Δt_{ai} can be written as

$$\Delta t_{ai} = \Delta t_{i2} - \Delta t_{i1}. \tag{3.6}$$

For a horizontally-layered overburden as shown in Figure 3.8 and to the first order of the Thomsen parameters, noting equation (3.5) and the ray velocity equation (Sena, 1991)

$$v_p(\theta, \phi) = v_{p0}[1 + (\delta - 2\epsilon)\sin^2\phi\sin^2\theta + (\epsilon - \delta)\sin^4\phi\sin^4\theta], \tag{3.7}$$

gives (see Appendix A.4),

$$\Delta t_{ai} = \frac{(x - 2x_1)}{v_{p02}}(\sin^2\phi_2 - \sin^2\phi_1)\sin\theta_2\left[2\epsilon - \delta - (\epsilon - \delta)(\sin^2\phi_2 + \sin^2\phi_1)\sin^2\theta_2\right] \tag{3.8}$$

where

$$\sin\theta_2 = \frac{x - 2x_1}{\sqrt{(x - 2x_1)^2 + 4\Delta z^2}}, \tag{3.9}$$

and v_{p02} is the interval vertical velocity of the fractured layer.

Equation (3.8) allows the calculation of the azimuthal interval moveout for any two azimuths. For two orthogonal azimuths (Figure 3.9), equation (3.8) can be greatly simplified. Letting $\phi_1 = \phi$ and $\phi_2 = \phi + \pi/2$ gives,

$$\Delta t(\phi, x) = \frac{x - 2x_1}{v_{p02}}\sin\theta_2[2\epsilon - \delta - (\epsilon - \delta)\sin^2\theta_2]\cos 2\phi = A(x, \epsilon, \delta)\cos 2\phi \tag{3.10}$$

which agrees with experimental results published by Garotta (1989).

If the second set of orthogonal lines (lines 3/4 Figure 3.9) is rotated by 45° relative to the first one (lines 1/2 Figure 3.9) it enables the calculation of the strike angle ϕ of the reservoir because the second set will have a $\sin 2\phi$ periodicity instead of the $\cos 2\phi$ variation of the original set. A cross-plot analysis of the two sets shows a linear trend. The fracture strike is then found as half the slope of the best fitting line to the cross plotted data.

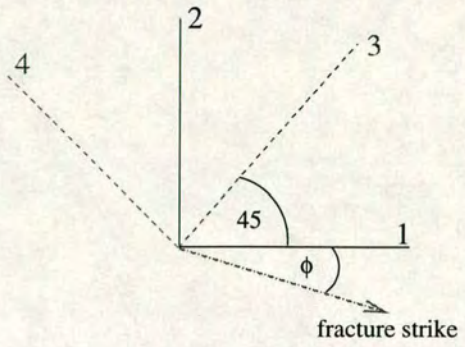

Figure 3.9: The four line configuration for the detection of the fracture strike ϕ. The lines 1/2 and 3/4 each built a set of orthogonal lines. The two sets are separated by 45 degrees. After Li (1997).

3.4.2 Variation with offset

As offset increases, the time separation of the reflection events from the top and bottom of the fracture layer decreases. Thus, the interval moveout for the layer decreases with increasing offset. This can be demonstrated analytically for a weak impedance contrast. For zero incidence the interval moveout is given by

$$\Delta t(0) = 2\frac{z - z_1}{v_2}, \tag{3.11}$$

and for any other angle by

$$\Delta t(\theta) = 2\left(\frac{s_2}{v_2} - \frac{\Delta s}{v_1}\right), \tag{3.12}$$

where the variables are shown in Figure 3.10.

Figure 3.10 shows the ray diagram and the variables which will be used. Δs is the distance between the points A and B. The difference in the travel time for a weak velocity contrast is simply the difference in length between s_2 and Δs, divided by the velocity of the layer. The next step is to find expressions for these quantities.

In this derivation I assume a small impedance contrast between the overburden and the target and therefore neglect Snell's law at the interface. The derivation

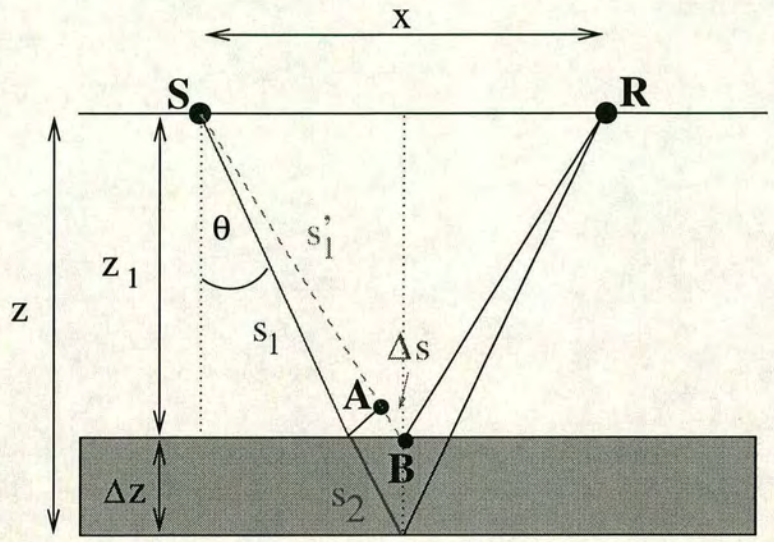

Figure 3.10: Ray paths and variable definitions for the following derivation of the interval moveout.

is designed to explain why the zero-offset interval travel time is larger than the far-offset. This is sufficiently achieved by the approximation. It follows from Figure 3.10 that

$$\tan\theta = \frac{x}{2z}, \tag{3.13}$$

$$\cos\theta = \frac{z_1}{s_1}, \tag{3.14}$$

and therefore

$$s_1 = \frac{z_1}{\cos[\arctan(\frac{x}{2z})]}, \tag{3.15}$$

$$s_1' = \frac{1}{2}\sqrt{x^2 + 4z_1^2}. \tag{3.16}$$

The difference is given by

$$\begin{aligned} \Delta s &= s_1' - s_1, \\ &= \frac{1}{2}\sqrt{x^2 + 4z_1^2} - \frac{z_1}{\cos[\arctan(\frac{x}{2z})]}. \end{aligned} \tag{3.17}$$

s_2 is given by the difference between the whole segment s and s_1

$$s = s_1 + s_2, \tag{3.18}$$

$$s_2 = \frac{1}{2}\sqrt{x^2 + 4z^2} - \frac{z_1}{\cos[\arctan(\frac{x}{2z})]}. \tag{3.19}$$

For the simplest of all cases, where the two velocities are equal, the interval moveout is directly proportional to the difference in length between s_2 and Δs. This difference can be expressed as

$$s_2 - \Delta s = \frac{1}{2}\sqrt{x^2 + 4z^2} - \frac{1}{2}\sqrt{x^2 + 4z_1^2}. \tag{3.20}$$

Developing the square roots of equation 3.20 into a Taylor series gives

$$\begin{aligned} s_2 - \Delta s &\approx \frac{x}{2}(1 + \frac{4z^2}{x^2}) - \frac{x}{2}(1 + \frac{4z_1^2}{x^2}) \\ &= \frac{2}{x}(z^2 - z_1^2) \end{aligned} \tag{3.21}$$

which clearly shows the decrease with offset. An example for $z_1 = 1500$m, $z = 1900$m is given in Figure 3.11.

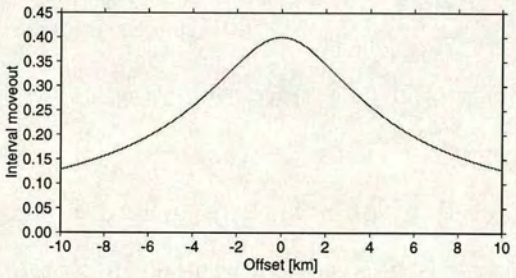

Figure 3.11: Difference in the ray path for $z = 1900$m, $z_1 = 1500$m and $v_1 = v_2$.

3.4.3 3D variations

An example of the variation of the interval moveout resulting from a 3D survey is presented in Figure 3.12.

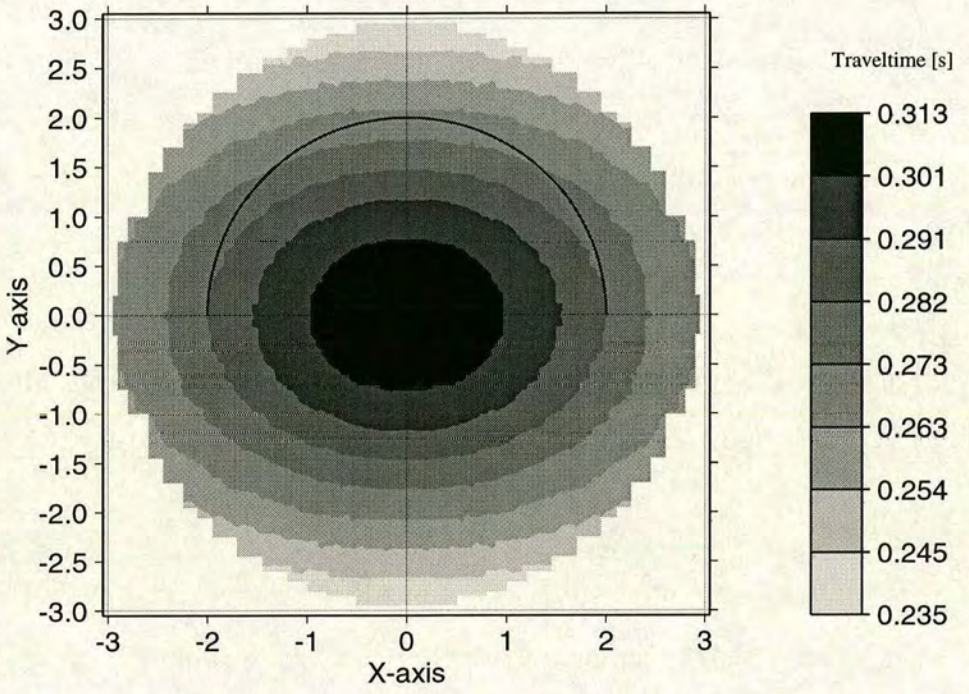

Figure 3.12: Variation of the interval travel time for a TIH target layer.

The parameters of the model are: Two reflectors at 1500m and 1900m. The material in the overburden is TIV ($\epsilon = 0.11, \delta = 0.0, \gamma = 0.12$). δ is zero because the material is constructed by thin layering where δ zero by definition. The material of the target layer is derived from the same isotropic parameters as the top but now showing TIH anisotropy with $\epsilon = 0.16, \delta = 0.0, \gamma = 0.17$.

The decrease in the internal moveout with increasing offset is clearly visible, as predicted. The maximum of the interval moveout coincides with the source location (zero-offset rays), where both the top and the bottom reflections have a minimum. This is the essential requirement for the method to work. The black semi circle indicates a survey with a fixed offset at 2km. The formula for the

interval moveout predicts a $\cos 2\phi$ behaviour. Figure 3.13 shows the difference between the interval travel time for two perpendicular lines with offsets along the semi circular path (solid line) together with the results calculated by Equation 3.10 using the known model parameters (dotted line). The two curves fit well and this is strong evidence that Equation 3.10 is correct.

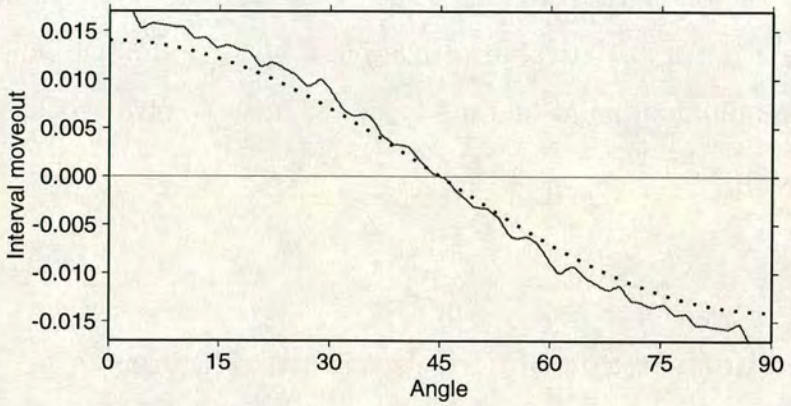

Figure 3.13: Azimuthal variation of the difference in the interval moveout between two perpendicular lines.

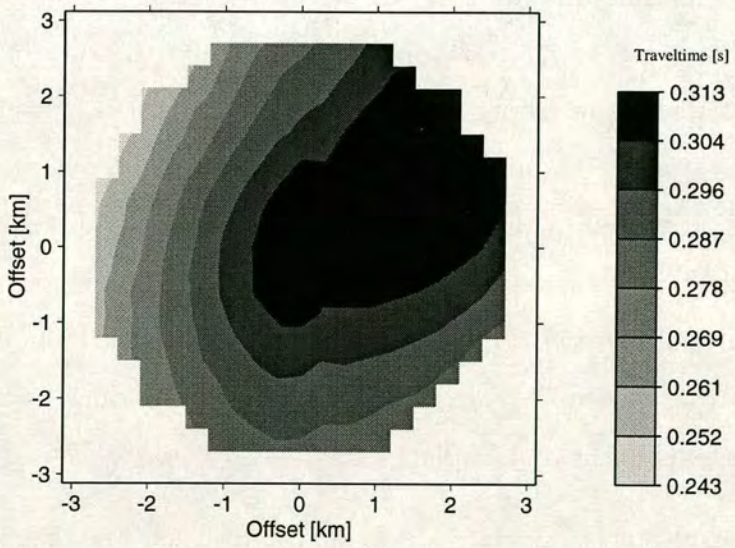

Figure 3.14: Interval travel time variation of the interval moveout for a 10 degrees dipping TIH target layer with the orientation of the fast axis rotated by 45 degrees. All the other parameters are the same as in the horizontal case (Figure 3.12).

I do not expect the method to be directly applicable if the target layer is dipping,

because of the asymmetry of the ray path. Figure 3.14 shows the results for the same parameters as the previous model, but with a 10 degree dipping target. The centre of the resulting geometrical feature (ellipse etc.) has shifted due to the change in the minimum of the travel time for both layers.

Although the directionality of the TIH material can be picked visually from the 3D data plot, the four line estimation scheme will not give any results without further processing. An analytical investigation of how the dip will influence the position of the minimum point and a scheme for how to solve this problem are presented in Chapter 5.

3.4.4 Synthetic example for horizontal layers

I now estimate the direction of the symmetry axis of a TIH medium for a synthetic model using the method described in the previous section. The model consists of two layers with the top of the reservoir at 1500m and a thickness of 300m. The overburden is a weak anisotropic material ($\epsilon = 0.03, \delta = 0.02, \gamma = 0.03$) but the reservoir has a strong TIH anisotropy of $\epsilon = 0.13, \delta = 0.08$ and $\gamma = 0.12$. The symmetry axis is rotated in the x/y plane so that its strike direction is now 15 degrees. The four lines have azimuths of 0, 45, 90 and 135 degrees respectively. Each line consists of 29 receiver positions equally spaced at a 100m interval. The seismograms are calculated by ANISEIS (Taylor, 1991) which is based on the reflectivity method (Fuchs and Müller, 1971).

The interval moveout is calculated individually for each line (Figure 3.16) and for the cross-plot analysis the difference between the azimuths 135 and 45 as one pair and 90 and 0 as the other is evaluated.

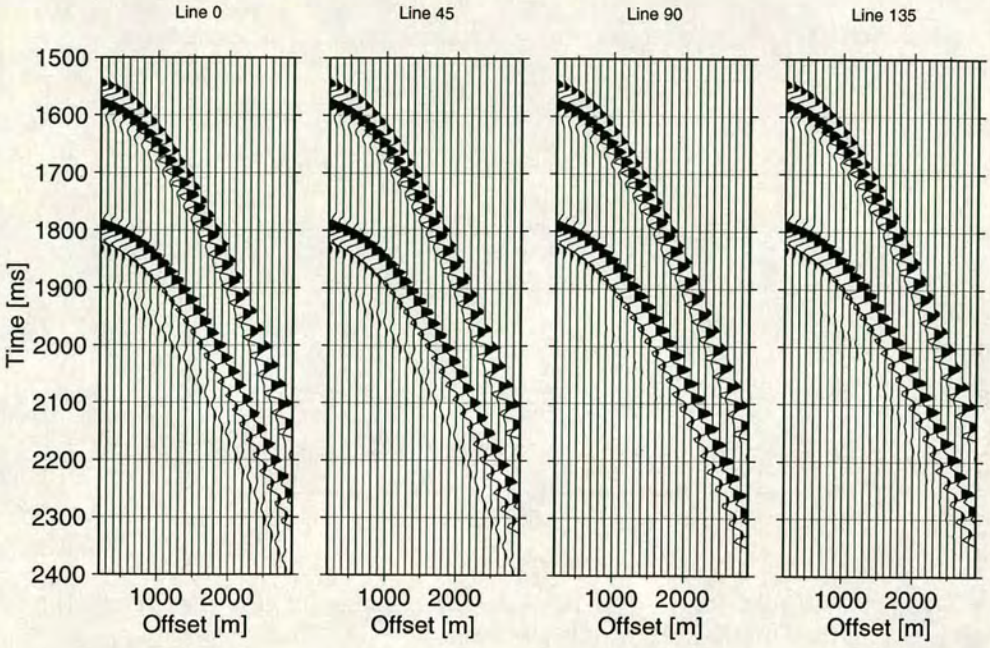

Figure 3.15: The shot gathers for the four lines.

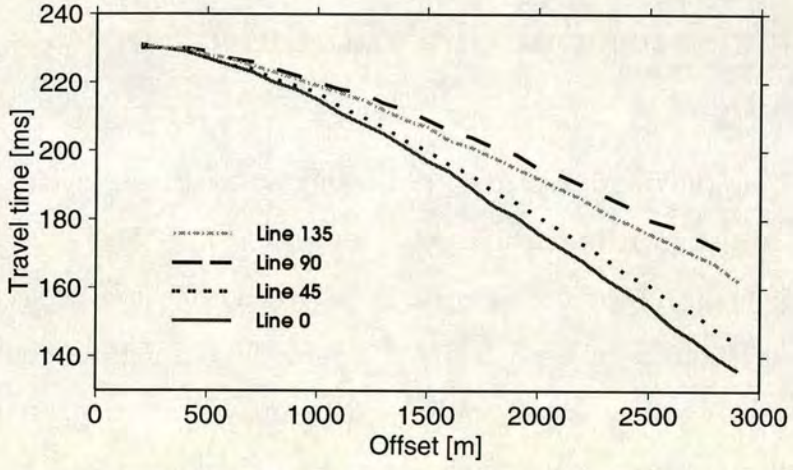

Figure 3.16: Time picks for the four lines. The solid graph: Line 0; The dashed graph: Line 90; The dotted graph: Line 45 and the dashed/dotted graph: Line 135.

These results are shown in Figure 3.17, together with best fitting linear trend. The function of the best fit can be written as $f(x) = -0.073 + 0.57669 \cdot x$. The strike angle estimated from this line is 14.98 degrees, which is very close to the 15 degrees of the model.

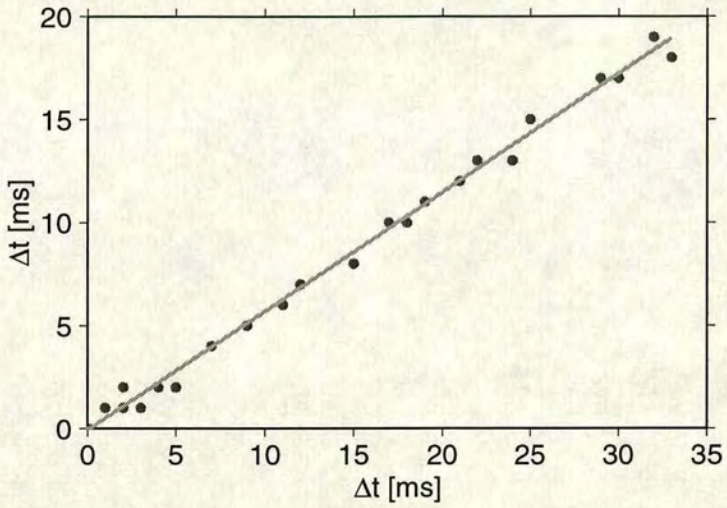

Figure 3.17: Cross-plot for the horizontal case. The solid line represents the best fitting line for the whole data set.

3.5 Transmission, dip and anisotropy

Many years of studying anisotropic processing and estimation techniques have demonstrated the great importance of considering these effects. It is necessary to account for anisotropy during seismic processing because neglecting the effect can lead to errors in the velocity analysis, the normal moveout correction (Tsvankin, 1994) and the AVO analysis. The analyses concentrate on the estimation of the anisotropic parameters ϵ, δ and γ (Thomsen, 1986), the horizontal and vertical velocity (Li and Crampin, 1993c), the normalised parameters of the elastic tensor (Miller and Spencer, 1994), polarisation direction or shear wave time delays (Crampin, 1981) as shown in the previous sections. These estimations of anisotropic parameters are influenced by the presence of dip as well as lithology (Sayers, 1997). These effects do not only occur in reflection but also in transmission data which are recorded in a borehole. This section introduces a procedure for the detection of any dipping layers above the receiver zone and demonstrates the application to real data.

3.5.1 The estimation idea

The effect of anisotropy manifests itself in the form of the deviation from the circular form of a horizontal (p_x) versus vertical (p_z) slowness diagram for a walk-away VSP (vertical seismic profile) experiment. The circle is the expected form for an isotropic medium. A walk-away VSP is a special form of VSP where a short receiver tool is lowered into the bore-hole and one or more lines with different azimuths are shot for offsets -x to +x (Figure 3.18). The furthest offset x has a significant aperture in comparison to a zero-offset VSP where the shot is located as close as technically possible to the borehole. The estimation process

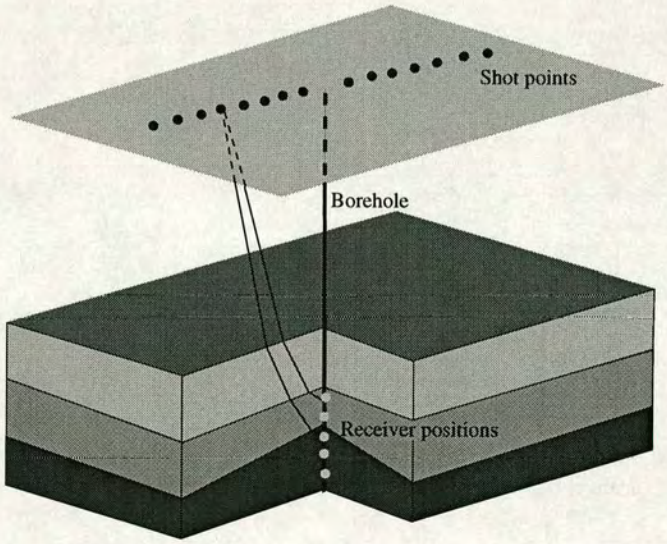

Figure 3.18: Source and receiver positions for a walk-away experiment.

of the p_z-p_x diagram (horizontal slowness versus vertical slowness) requires two steps. The horizontal components of the slowness vector in a horizontally-layered medium do not vary. To derive the horizontal slowness the data are sorted into a common receiver gather (Figure 3.19a) and then the formula

$$p_x = \frac{\partial T(x)}{\partial x}, \tag{3.22}$$

is applied at each shot point. Any dip in the layers above the receiver array results in a shift (Sayers, 1997) of the p_x-p_z diagram and therefore lead to errors in the estimation of the anisotropic parameters. To obtain the vertical slowness, p_z, the data are sorted into a common shot gather (Figure 3.19b) and

$$p_z = \frac{\partial T(z)}{\partial z}, \tag{3.23}$$

is evaluated at each receiver. Usually this is achieved by fitting a line to the first arrivals. If the depth difference Δz between the receivers is much smaller than the absolute depth of the first receiver, this means that as a first order approximation the travel time is linear in Δz. Because of the small number of receivers the calculation of p_z is very sensitive and small errors in the picking of the first arrival time can lead to errors in the estimation.

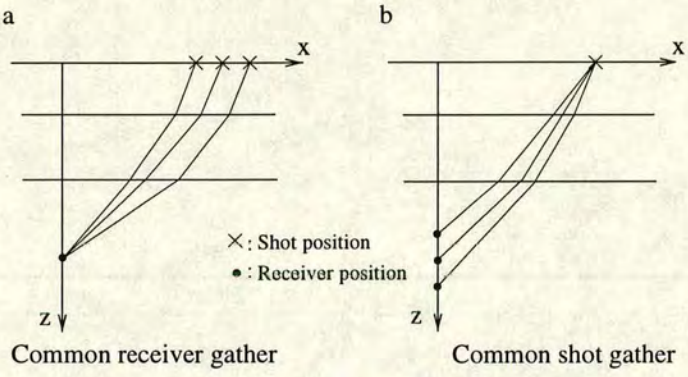

Figure 3.19: Source and receiver positions for the different gathers used to calculate the horizontal and vertical slowness.

The resulting p_x-p_z diagram is constructed by combining the values of p_x and p_z for each shot position. For a single isotropic layer the diagram shows a perfect circle because an isotropic medium shows no angular dependence of the velocity. Any deviation from the circular form may be interpreted as an influence of layering or anisotropy. From the p_x-p_z values an estimation of the normalised elastic constants (Miller and Spencer, 1994) is possible. Sayers (1997) shows that this

Layer	Depth [m]	ρ [g/cm^3]	V_p^2 [km^2/s^2]	V_s^2 [km^2/s^2]
1	122	1.00	2.25	0.00
2	2000	2.10	5.42	1.80
3	2600	2.23	7.00	3.11
4	3700	2.50	9.90	4.76

Table 3.2: Material parameters for the isotropic ray tracing.

estimation is influenced by any dip in the layers above the geophones. A dipping layer results in a shift of the p_x-p_z diagram towards smaller values of p_x for the down-dip direction.

3.5.2 The model data

In this section I demonstrate this shift by using ray tracing through a layered isotropic model (Table 3.2) with interfaces that are horizontal or dipping by 5 degrees.

The depth of the geophones is 3045m to 3105m in 15m intervals. This particular geometry is chosen because it is the same as the acquisition geometry which is used for the real data which is presented in the following section. Figure 3.20 shows the horizontal slowness calculated for a receiver at z = 3075m. The graph is smooth as it is expected for synthetic data.

The corresponding diagram for the vertical slowness is shown in Figure 3.21. This graph is not as smooth as the one for the horizontal slowness. The reason is that only five levels can be used to calculate the derivative. Even for synthetic ray tracing small errors (±1-2ms) in the arrival time can occur.

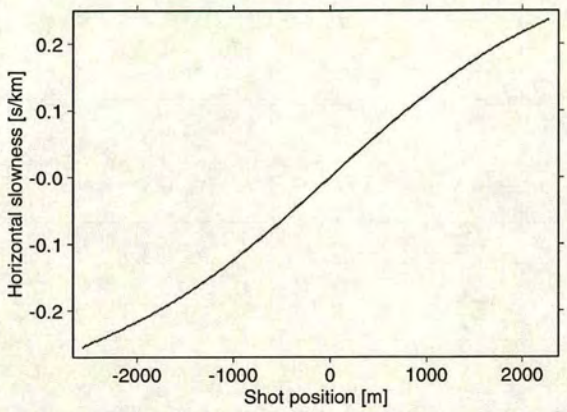

Figure 3.20: Horizontal slowness for the common receiver gather.

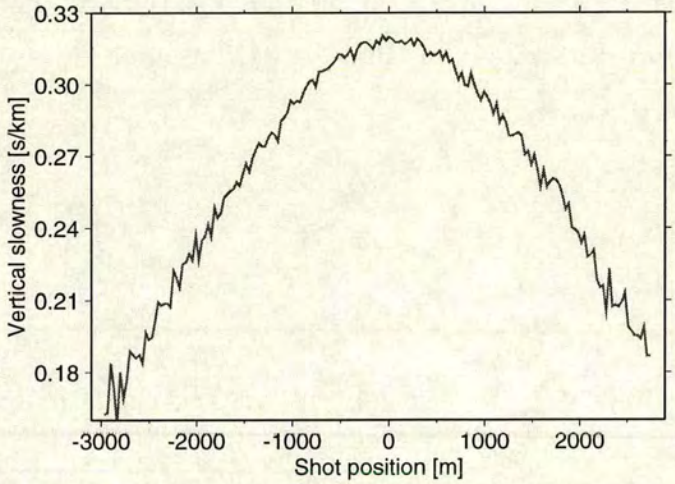

Figure 3.21: Vertical slowness for the common shot gather for the geophone at z=3075m.

The derived horizontal and vertical slowness, together with the best fitting ellipse are shown in Figure 3.22. The parameters for the ellipse are the length of the half axes a and b and the position of the centre x_0. The results for the horizontally layered model are a = 0.31764, b = 0.31820 and $x_0 = 3 \cdot 10^{-3}$. The idea to fit an ellipse originates from the fact that an ellipse is the next closest curve to a circle. Any deviation from a circle which indicates layering or anisotropy therefore shows in the parameters of the best fitting ellipse. For this model the deviation from the circle is less than 0.2%.

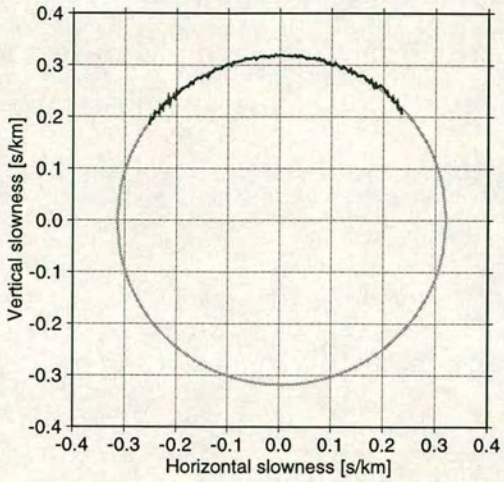

Figure 3.22: Slowness diagram for the horizontally layered isotropic model.

For the next calculations the synthetic model is changed. All interfaces apart from the sea-floor dip at 5° in the direction of the seismic line. As predicted by Sayers (1997) the whole graph is shifted in the positive p_x direction while maintaining the form of an isotropic circle. This fact is expressed by the parameters of the best fitting ellipse: a = 0.31554, b = 0.31729, $x_0 = 1.4 \cdot 10^{-2}$ as seen in Figure 3.23.

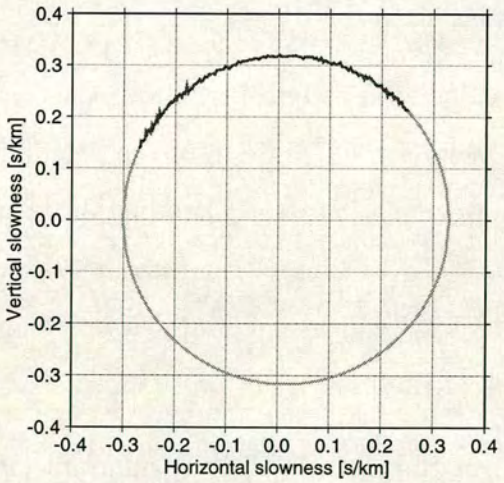

Figure 3.23: Slowness diagram for the isotropic model with 5 degrees dipping interfaces.

I can conclude that thick isotropic layers will not change the shape of the slowness diagram and therefore any deviation from the circular form for such a model is purely due to anisotropic influence. Secondly the shift of the whole model for dipping layers can be observed as predicted which may lead to miscalculations of the elastic parameters.

3.5.3 The real data example

In the following section one line of a walk-away VSP dataset provided by ELF is used to demonstrate the effect of anisotropy on the slowness diagram and show the influence of dipping layers above the receiver array. For reasons of confidentiality no geographical position can be given. The slowness curve derived from the real data shows a clear shift (Figure 3.26) which indicates, as outlined above, dipping layers. The idea is to derive a model from the provided log data and change the anisotropy and dip of the layers until the resulting slowness diagram matches the real data. This is by no means a unique inversion but gives one possible model that satisfies the slowness diagram.

The p_x, p_z diagram is calculated as outlined above after applying the standard processing steps. They include the definition of the geometry, the connection of the geometry information to the data the introduction of new header words to allow an easier sorting and the picking of the first break times. The data are of very high quality (Figure 3.24) which makes any data enhancing steps (filtering, trace killing) for the pick of the first break times unnecessary.

The non-circular form of the resulting p_x, p_z diagram (Figure 3.26) suggests that either anisotropy or thin layering is present. To rule out thin layering I look at the log data (density and velocity) for a region between 1400m and 3700m as

shown in Figure 3.25.

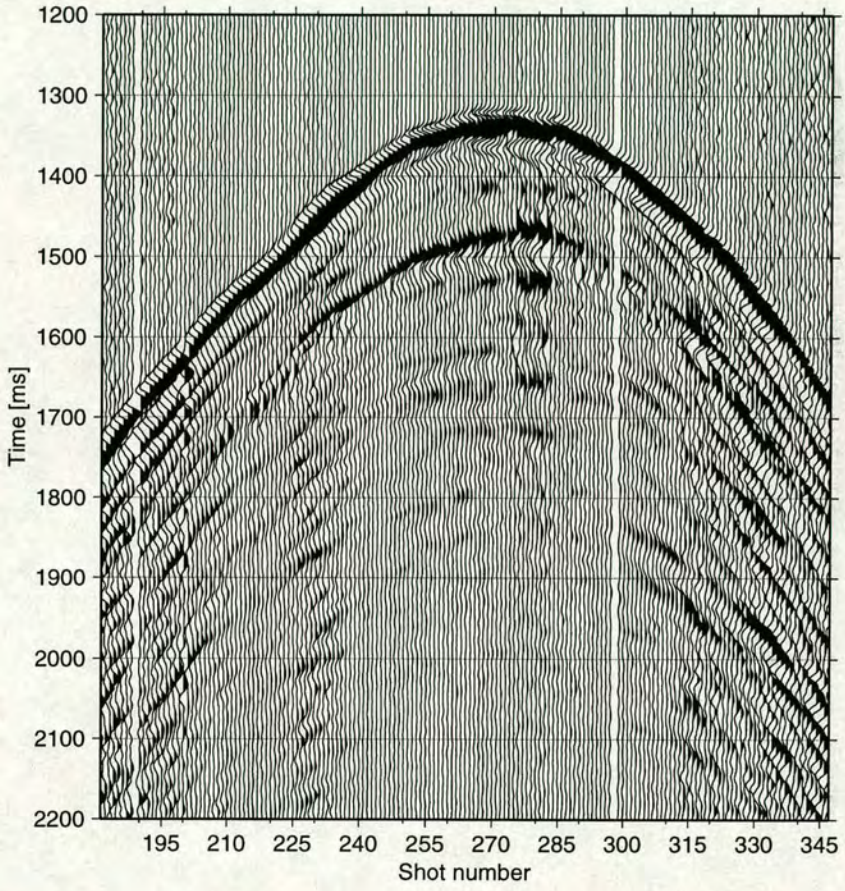

Figure 3.24: Common receiver gather for z=3075m.

Although the log data varies a lot, big blocks are still visible. These isotropic blocks form the basis for the ray tracing model which is also shown in Figure 3.25. The slowness diagram demonstrates clearly, that the best fitting curve is not a circle. The parameters of the ellipse are a = 0.30449, b = 0.3300, $x_0 = 0.98 \cdot 10^{-2}$ with a ratio 0.922 for the shot against the long axis.

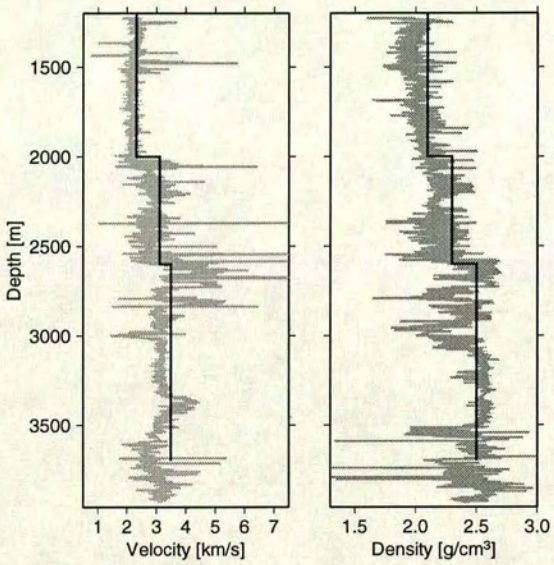

Figure 3.25: Density and velocity log for the walk-away VSP. The thick line on top of the log data shows the parameters used for the isotropic model.

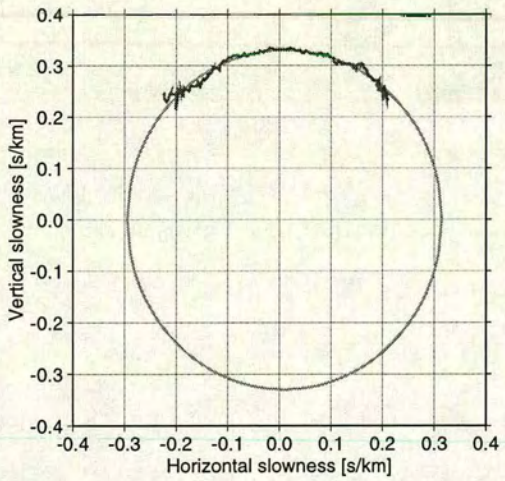

Figure 3.26: Horizontal versus vertical slowness for the real data.

3.5.3.1 Modelling of the slowness for the real data

In contrast to the real data result, slowness for the initial isotropic model which is based on the log data, shows no sign of deviation from the circular form. The next step is to change the isotropic parameters of the model to achieve the curvature which is expressed by the parameters of the best fitting ellipse, of the slowness diagram of the real data. I use a zero-offset VSP experiment to model the vertical slowness at $p_x = 0$ and then change the isotropic medium parameters for the layers 2 and 4 until the difference between the parameters of the best fitting ellipse is marginal. The anisotropic elastic tensor is constructed using PTL (periodic thin layering) (Bush and Crampin, 1991) which results in an elastic tensor with a vertical axis of symmetry (TIV).

The best results are achieved for Thomsen parameter values of $\epsilon = 0.11, \delta = 0.01$ and $\gamma = 0.13$ in layer 2 and $\epsilon = 0.14, \delta = 0.03$ and $\gamma = 0.20$ in layer 4 with the layers dipping by 5 degrees. The parameters of the resulting best fitting ellipse are $a = 0.30559$, $b = 0.33203$, $x_0 = 1.45 \cdot 10^{-2}$ where the ratio between the short and long axis is 0.92. The most interesting point is the difference in x_0 between the model and the real data. This indicates that although other processing stages of the data set assume horizontal layering a small dip may be detected above the receiver level.

The model with a 5 degrees dip maintains almost the same aspect ratio of the ellipse as the real data. The orientation of the symmetry axis is chosen perpendicular to the surface but for small dips the influence of a different orientation (perpendicular to the interface) can be neglected in the p_x, p_z diagram (Sayers, 1997). The interesting point is a shift in p_x of $x_0 = 0.0145$. This is too high but allows me to conclude that the dip of the interfaces is smaller than 5 degrees, but not zero.

3.6 Conclusions

I have shown in this chapter that any dip of a reflection interface changes the 3D distribution of the travel time. Even though CMP gathers are more common practice I used shot gathers because the calculation of CMP gathers using ray tracing for dipping interfaces is extremely computation time consuming. This is also the reason why the theoretical investigations in the next chapter are based on shot gathers.

Different anisotropic materials have different effects. While a dipping TIV layer shifts the offset where the minimum travel time is measured in the up-dip direction, the contours of equal travel time still maintain the circular shape observed for an isotropic layer. In contrast, a TIH layer shows a similar shift but also a change in the shape of the contours towards an elliptical shape. This behaviour is observed for a single as well as a multi-layer model. The interpretation of the observation is not complicated by these facts if a complete 3D survey is available. But if only a few 2D lines are measured, the parameter estimation is influenced by the dip. This influence is observed in reflection as well as transmission data. Traditional estimation methods such as the one for the fracture strike detection are not able to predict correct results in that case. It is therefore necessary to investigate the influence of the dip from a theoretical point of view and try to derive advanced estimation methods from the synthetic data results. This is done in the following chapters.

CHAPTER 4

Anisotropy versus structure: a separation approach for TIV

4.1 Introduction

In this chapter I introduce the theory of the travel time equation. I will demonstrate that the travel time equation can be separated into these four terms for 15-20% anisotropy (Thomsen parameter $\epsilon = 0.15$ to 0.2) and 20 degrees dip and incidence angles up to 30 degrees. The accuracy of the equation and the contribution of each term can then be evaluated and corrected. The four terms can be ranked in order of magnitude as: isotropic dip term (zeroth-order), isotropic dip-residual term (first order), dip-independent anisotropic residual term (second order), and the dip-dependent and anisotropy-dependent residual term (third order). I then construct a separation algorithm based on this ordered relationship to estimate the dip and anisotropic residual terms from the travel time.

4.2 A review of previous work

The presence of structural variation in anisotropic media complicates the offset-dependent and azimuth-dependent wave behaviour and leads to difficulties in

interpretation and estimation. To minimize the structural influence, those studying seismic anisotropy often choose areas where the geology is known to be simple and the strata are horizontal or nearly horizontal (e.g. Mueller, 1991; Lewis et al., 1991, Shuck et al., 1993). Processing methods for estimating and interpreting anisotropy are also derived for a horizontally-layered model (Alford, 1986; Thomsen, 1988; Sena, 1991; Li and Crampin, 1993a). This model has, to some extent, limited the application of seismic anisotropy, thus it is important to examine and understand the coupling effects of anisotropy and structure, and to develop processing methods for estimating and correcting for these effects.

The coupling effects of anisotropy and structure were first discussed by Hood and Schoenberg (1989) and are important in image processing, which requires proper compensation for anisotropy effects. To improve DMO (dip moveout) processing, Levin (1990) numerically examined the effects of anisotropy and dip on moveout variations, Tsvankin and Thomsen (1994) and Tsvankin (1995b) presented analytical equations for calculating travel time and moveout velocity in the presence of anisotropy and dip. Uren et al. (1990a) presented an anisotropic migration algorithm and demonstrated, using laboratory seismic data, that anisotropy must be taken into account for better imaging of structure. This result was confirmed by Alkhalifah (1995) using real data and an improved anisotropic DMO and migration algorithm. However, the use of seismic anisotropy for reservoir studies raises a separate issue. Here the macro structure is well defined and constrained, but compensation for structural effects is required in order to obtain a better and reliable estimation of the anisotropy.

4.3 The approach

I consider a simple model with a single dipping interface (Figures 4.1 and 4.2). I assume that the media above and below the interface are TI (transversely

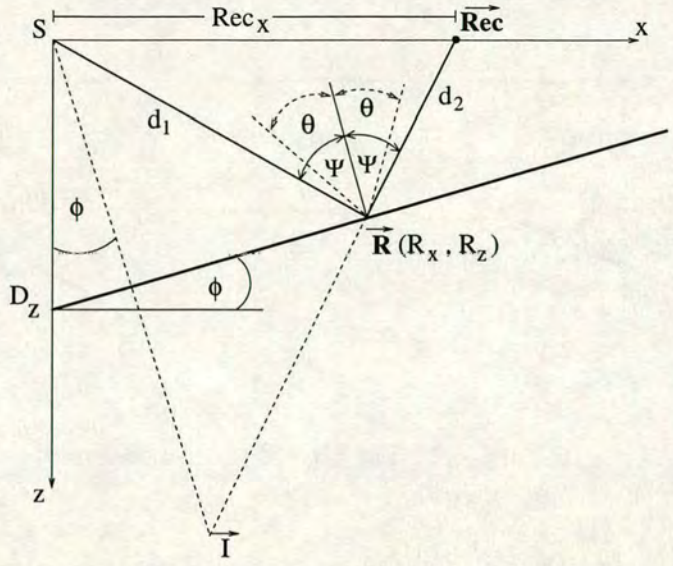

Figure 4.1: The ray path and the image point construction for a single dipping reflector where ψ is the ray angle and θ the phase angle.

isotropic) with the symmetry axis either perpendicular to the interface due to geological processes that tilted the original horizontal beds, or perpendicular to the surface due to deposition against a tilted background (Levin, 1990). For such a model, the dip-dependent moveout and lateral movement of the reflection point are the two major effects caused by the presence of dip: non-hyperbolic moveout and ray deviation are the corresponding kinematic effects caused by anisotropy. These effects superimpose and cause difficulties in both structural imaging and anisotropic estimation. One of the diagnostic features of these effects is the travel time variation. Here I extend the developments of Levin (1990) and Tsvankin and Thomsen (1994) , and reformulate the approximate travel time equation for the single layer model in terms of dip-dependent and anisotropy-dependent and dip-independent and anisotropy independent terms, so that the anisotropic term (dip-independent) can be separated from the structural term (isotropic dip-dependent) as shown in Figure 4.2.

As in other travel time studies (e.g. Sena, 1991; Li and Crampin, 1993a; Tsvankin and Thomsen, 1994), this study is based on weak anisotropy (Thomsen, 1986). The assumption of weak anisotropy is required for both the construction

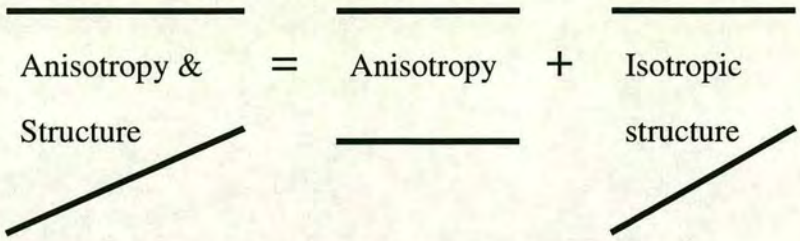

Figure 4.2: The idea of the separation.

of the ray path geometry and for the determination of group velocity variations for analytical analysis. Further assumptions are required regarding the angular difference between the direction of the group velocity and the phase velocity. All these assumptions inevitably require addressing the basic question of how weak is 'weak' in terms of the accuracy and limitations of the travel time equations. Using different amounts of anisotropy (different values of the Thomsen parameter ϵ) and dip angles, I compare the travel time calculated from the approximate equation for different assumptions with the travel time from anisotropic ray tracing (Gajewski and Pšenčík, 1995). Once the accuracy of the travel time equation is established, I evaluate the contribution of each term within the equation and investigate to what extent it is possible to separate the effects of anisotropy and dip. I show how to compensate for each term individually or both together. All these results are obtained assuming a 2-D structure and a symmetry axis of the elastic tensor perpendicular to the interface. 3-D analysis and a symmetry axis perpendicular to the surface, are also discussed briefly and the extension of the results for these cases and some essential results are included in Appendix A.

4.4 The travel time equation

To begin with, I examine the travel time equation in a TI (transversely isotropic) medium with the symmetry axis perpendicular to the interface (Figure 4.1). The source S is assumed to be located at the origin of the coordinate system. This is the set up for shot gathers. I use this description because the calculation of the alternative CMP gathers for dipping layers using ANRAY is computational very time consuming. In this case the ray can be constructed using the image point method (Dellinger and Muir, 1988). The length of the ray path L is given by (Figure 4.1)

$$L = \sqrt{R_x^2 + R_z^2} + \sqrt{(Rec_x - R_x)^2 + R_z^2}, \tag{4.1}$$

where R_x and R_z are the coordinates of the reflection point $\vec{R}$ and Rec_x the x-coordinate of the receiver. Because the receiver is placed on the surface, the z-coordinate is zero. The reflection point $\vec{R} = (R_x, R_z)$ is found as the intersection point of the reflector and the line connecting the image point $(\vec{I})$ with the receiver $(\vec{Rec})$. The coordinates can be written as

$$R_x = Rec_x - \frac{-Rec_x \sin\phi + D_z \cos\phi}{2D_z \cos\phi - \sin\phi Rec_x}(Rec_x - I_x), \tag{4.2}$$

$$R_z = \frac{-Rec_x \sin\phi + D_z \cos\phi}{2D_z \cos\phi - \sin\phi Rec_x} I_z, \tag{4.3}$$

where ϕ is the geological dip, D_z is the depth of the reflector at the source point and I_x and I_z are the coordinates of the image point,

$$I_x = 2D_z \sin\phi \cos\phi, \tag{4.4}$$

$$I_z = 2D_z \cos^2\phi. \tag{4.5}$$

Let ψ be the ray angle, corresponding to the phase angle θ (Figure 4.1) and $V_G(\psi)$ the ray velocity in the direction ψ relative to the symmetry axis for the two path

segments when the symmetry axis of the elastic tensor is perpendicular to the interface. Once the ray path is known I can derive the travel time equation.

In the case of no dip, the travel time equation is given by

$$tV_G(\psi) = 2\sqrt{(\frac{Rec_x}{2})^2 + D_z^2}, \tag{4.6}$$

or

$$t^2V_G^2(\psi) = \underbrace{Rec_x^2 + 4D_z^2}_{l^2_{(\phi=0)}}. \tag{4.7}$$

If I introduce dip, the equation changes to

$$t^2V_G(\psi)^2 = (Rec_x - I_x)^2 + I_z^2, \tag{4.8}$$

because the length of the ray path from the source to receiver is equal to the distance between the image point and the receiver. Substituting equation (4.4) and equation (4.5) into equation (4.8) leads to

$$t^2V_G^2(\psi) = Rec_x^2 - 4Rec_xD_z\sin\phi\cos\phi + 4D_z^2\sin^2\phi\cos^2\phi + 4D_z^2\cos^4\phi. \tag{4.9}$$

To isolate the dip-independent term [equation (4.7)] I add and subtract $4D_z^2$,

$$\begin{aligned} t^2V_G^2(\psi) &= \underbrace{Rec_x^2 + 4D_z^2}_{l^2_{(\phi=0)}} - 4D_z^2 - 4Rec_xD_z\sin\phi\cos\phi \\ &+ 4D_z^2\sin^2\phi\cos^2\phi + 4D_z^2\cos^4\phi \\ &= l^2_{(\phi=0)} - \underbrace{4D_z(\frac{Rec_x}{2}\sin(2\phi) + D_z\sin^2\phi)}_{\Delta l^2(\phi)}. \end{aligned} \tag{4.10}$$

The above shows that it is possible to separate the equation into a dip independent $[l^2(\phi = 0)]$ and an dip dependent $[\Delta l^2(\phi)]$ term. To extend this separation to the influence of anisotropy I have to analyse the dependency on the velocity $V_G(\psi)$. Exact values of the velocity variation can be found numerically by solving the

Kelvin-Christoffel equation (Helbig, 1994). The required analytical equation for the velocity variation can be derived for the assumption of weak anisotropy. I examined weak anisotropy theory in Section 2.4 and apply it here to estimate the accuracy of the travel time equation for different assumptions related to the determination of $V_G(\psi)$.

Equation 2.37 suggests $V_G(\psi) = V_P(\psi)$, or the phase and the group velocities at a given angle are the same. I call this assumption 1. Similarly by ignoring the deviation $\Delta\theta$ I can assume $V_G(\psi) = V_P(\theta)$ the phase velocity to be equal to the corresponding group velocity (Thomsen, 1986). I call this assumption 2. Because, $V_P(\psi) > V_G(\psi) > V_P(\theta)$, as shown in Figure 2.10 and proved in Section 2.4, for assumption 1, any amount of anisotropy will be over-expressed; while for assumption 2 any amount of anisotropy will be under-expressed. This is demonstrated in Figure 2.10 which will be discussed in more detail in the section 4.5.

Assumption 1 originates from Brown et al. (1991) who demonstrate that the difference between the phase and the group angle propagates into a second order effect of the ray velocity and can therefore be neglected in first order approximations. Assumption 2 was introduced by Thomsen (1986). A comparison of the assumptions can be found in Rommel (1993).

Tsvankin and Thomsen (1994) derived travel time equations using $V_G(\psi) \approx V_P(\theta)$. After substituting ψ for θ, where they only used linear terms in the Thomsen parameters δ and ϵ, they end up with the assumption $V_G(\psi) \approx V_P(\psi)$. Their travel time equations involve the NMO velocity and are based on assumption 1.

4.5 Accuracy and limits: How weak is 'weak'?

To demonstrate the accuracy of the travel time equation (equation (4.10), for different assumptions of the group velocity $V_G(\psi)$, I calculate travel times for models with different amounts of anisotropy ($=\epsilon \times 100$ in percent), different an-ellipticities ($\epsilon - \delta$) as shown in Table 4.1 and different dip angles. These results are compared with those from anisotropic ray tracing (ANRAY: Gajewski and Pšenčík, 1995). For all the models the source is at the origin of the coordinate system. The reflector is defined by a given depth (11km) at the source position. The receiver line contains 50 receivers, equally spaced at 0.5 km starting at 1 km. To get a better impression of the connection between the geophone position, the incidence angle at the reflector for different reflectors, and the offset to depth ratio, Table 4.2 shows the values for selected geophones.

Density [g/cm^3]	Vertical P-velocity [km/s]	ϵ	Anisotropy [%]	An-ellipticity $\epsilon - \delta$
2.0	2.73	0.1	10	0.117
2.0	2.72	0.15	15	0.192
2.0	2.69	0.25	25	0.388
2.0	2.67	0.3	30	0.520

Table 4.1: Parameters for anisotropic modelling.

Figure 4.3 shows the travel times for a 10 degrees dipping interface where the symmetry axis of the medium is perpendicular to the interface. In all four diagrams the graph with the star symbol (correct group velocity) perfectly corresponds to the one using the lightly shaded symbol (ANRAY), which means that the ray path as well as the velocity is correct. The shift of the minimum point of the travel time to be nearly equal in all four diagrams: The influence of the material properties on the minimum position is smaller than the structural effect.

	Geophone number	1	9	19	29	39	49
	Distance [km]	1	5	10	15	20	25
	Distance to depth ratio	0.091	0.455	0.91	1.364	1.818	2.273
	Squared distance[km^2]	1	25	100	225	400	625
Dip	Incidence angle at the reflector						
0		2.60	12.89	24.44	34.29	42.27	48.65
10		2.62	13.32	26.30	37.78	47.27	54.87
20		2.65	13.92	28.58	42.20	53.65	62.70
30		2.67	14.66	31.64	48.35		

Table 4.2: Incidence angles for selected geophone positions.

If this influence were greater, different minimum positions for different amounts of anisotropy would be noticeable. To quantify the accuracy of the measurement I use the difference between the ray tracing and the other results relative to a quarter of the period of the dominant wavelength which is 10ms for a 25Hz signal. For $\epsilon = 0.1$ for all graphs up to a squared distance of 144km^2 (offset of 12km or offset to depth ratio of 1.091) the time difference is smaller than 10ms (Figure 4.4a).

For larger offsets one can see the predicted under-expression of anisotropy using assumption 2, because the graph of the triangles is closer to the straight line (isotropic case) than the correct curve. In contrast, the results using assumption 1 (diamond symbol) deviate further from the isotropic line than the correct curve (overestimation). For $\epsilon = 0.15$ (Figure 4.4b) both assumptions are valid up to an offset of 9.5km (offset to depth ratio of 0.864). For $\epsilon = 0.25$ (Figure 4.4c) the under/overestimation becomes very clear. Up an offset of 7km (offset to depth ratio of 0.636) a coincidence (difference smaller than 10ms) of the curves can be

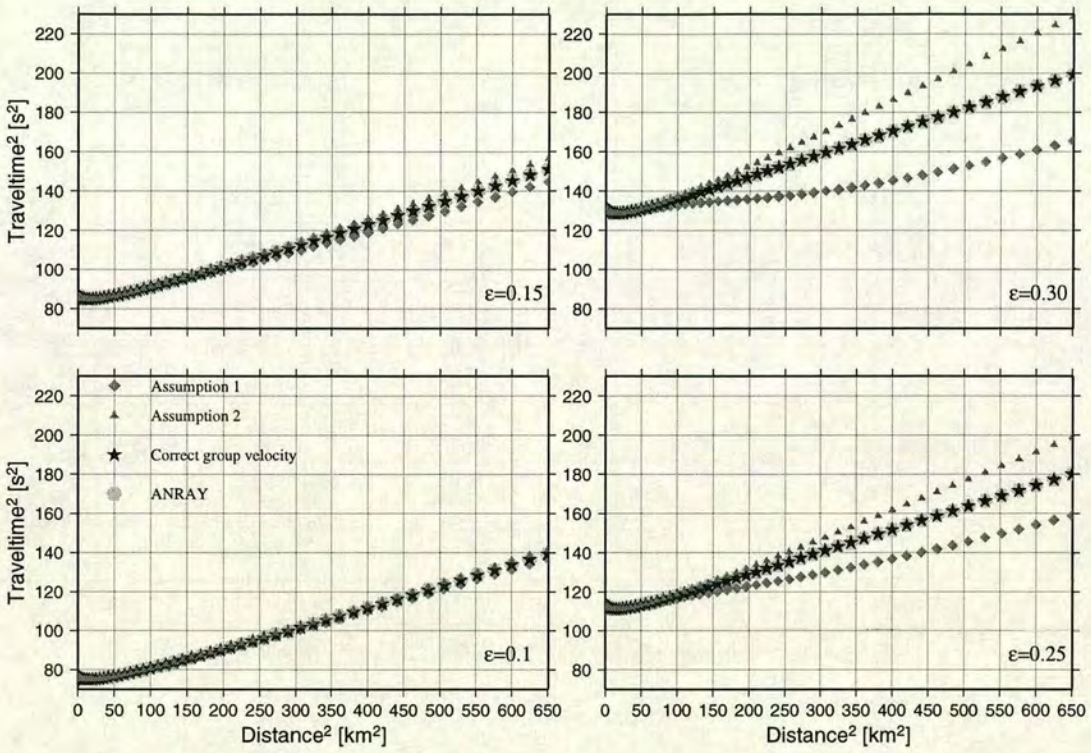

Figure 4.3: The squared travel time curves (t^2 against x^2) calculated for 10 degrees of dip for symmetry axis perpendicular to the interface. There are four different diagrams for different values of ϵ: 0.1, 0.15, 0.25, 0.3. Each diagram has four different curves for different calculation methods: Assumption 1 (the diamonds) where the group velocity is equal to the phase velocity at the ray angle ($V_G(\psi) = V_P(\psi)$), Assumption 2 (the triangle) where the group velocity is equal to the corresponding phase velocity ($V_G(\psi) = V_P(\theta)$), correct group velocity (stars) and the ray tracing results from ANRAY (slightly shaded hexagons).

found. The same is valid for $\epsilon = 0.3$ perhaps with the breakdown point at a slightly smaller angle.

Figure 4.5 shows the influence of different dip angles on the quality of the modelling results. The medium has in all three diagrams $\epsilon = 0.15$ but the dip angle changes. Figure 4.5a are the results for an horizontal reflector. Here both assumptions are valid for an offset of about 11km (offset to depth ratio of 1). This changes to 9.5km (offset to depth ratio of 0.864) for a dip angle of 10 degrees (Figure 4.5b) and stays almost the same for a dip of 20 degrees (Figure 4.5c).

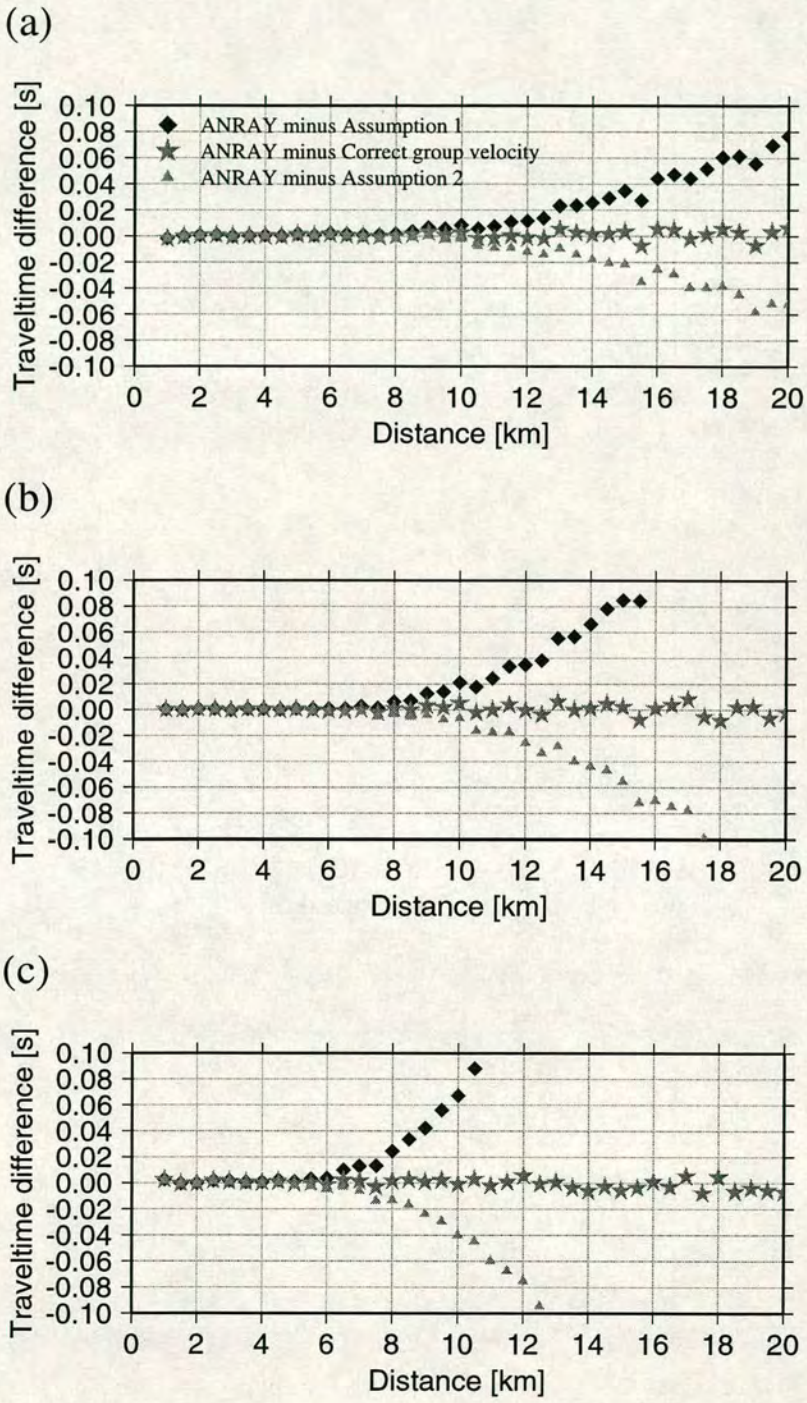

Figure 4.4: Difference in the travel time between the accurate ray tracing and the approximate travel times for a 10 degrees dipping reflector with the symmetry axis of the elastic tensor perpendicular to the interface for the three different velocities for $\epsilon = 0.1$ (a), $\epsilon = 0.15$ (b), $\epsilon = 0.25$ (c).

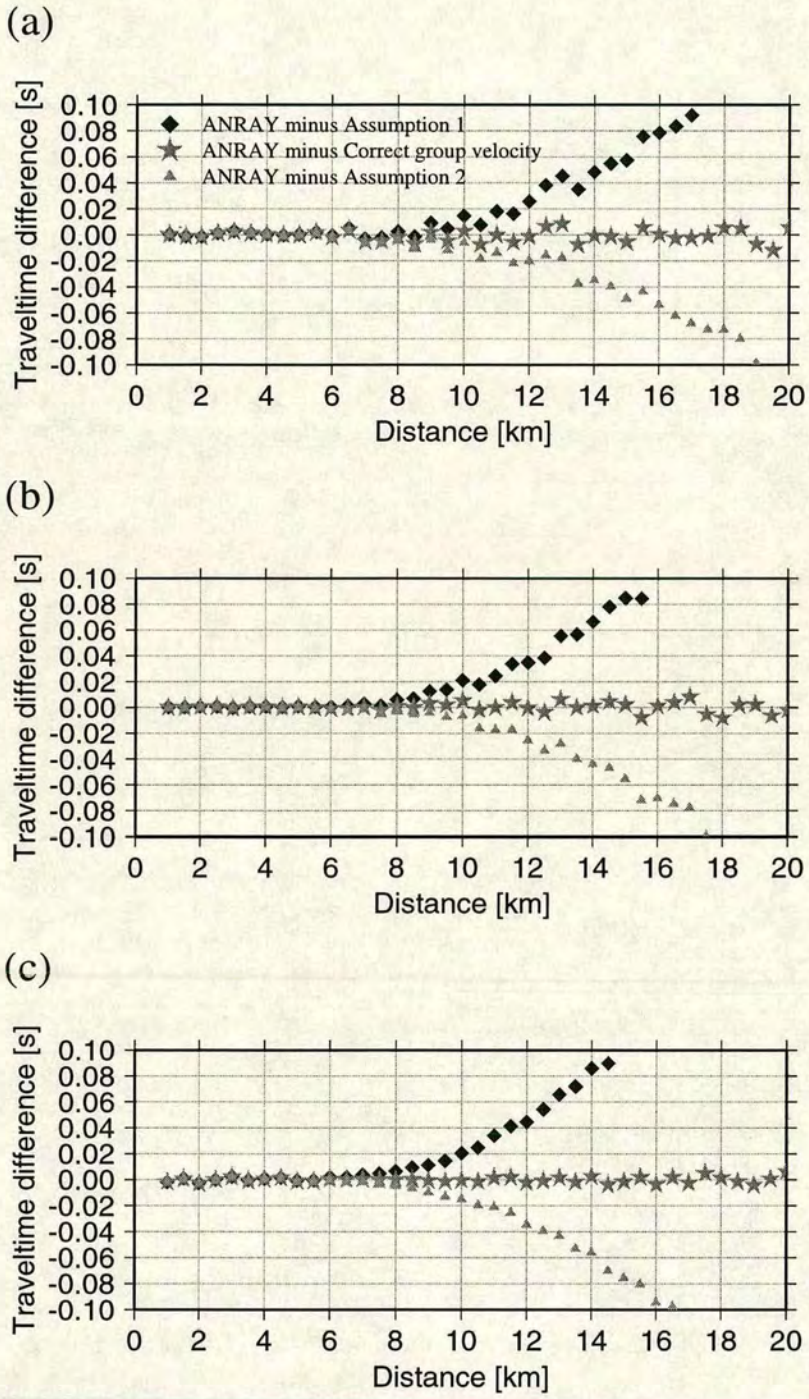

Figure 4.5: Difference in the travel time between the accurate ray tracing and the approximate travel times for a medium with $\epsilon = 0.15$ with the symmetry axis of the elastic tensor perpendicular to the interface for three different dip angles. (a) zero, (b) 10 degrees, (c) 20 degrees.

Figure 4.3 shows clearly a predicted over/underestimation of anisotropy. The curve with the underestimated values of the velocity lies above (less influence of the anisotropy) the correct values and the overestimated one appears below the correct values. This suggests that the accuracy of the travel time equation and the anisotropy estimation is sensitive to different assumptions of the group velocity, a fact which has been generally ignored in previous studies (e.g. Tsvankin and Thomsen, 1994).

Although this approach is based on the assumption of weak anisotropy as well as the approximation of the group by the phase velocity, a comparison of the analytical results from the approximate equation with the results from anisotropic ray tracing shows that for up to $\epsilon = 0.2$, an an-ellipticity range of 0 to $\pm$ 0.3 and a dip of 20-30 degrees with incidence angles up to 30 degrees these approximations are still valid.

4.6 Separation procedure and results

To search for a procedure to separate anisotropy and structure, I reformulate the travel time equation in terms of isotropic dip-independent, isotropic dip-dependent, anisotropic dip-independent and anisotropic dip-dependent terms. An ordered relationship among the four terms is established and its implication is used to construct an iterative separation procedure for anisotropy and structure.

4.6.1 Decomposition of the travel time equation

If I take equation (4.10) and use only linear terms in δ and ϵ for the inverse of the squared velocity $V_G^{-2}(\psi)$ I get

$$t^2 = \frac{l^2_{(\phi=0)} - \Delta l^2(\phi)}{v^2_{P0}}(1 - 2\delta \sin^2(\psi)\cos^2(\psi) - 2\epsilon \sin^4(\psi)). \qquad (4.11)$$

I can now write the linearization as

$$t^2 = \frac{l^2_{(\phi=0)}}{v^2_{P0}} - \frac{l^2_{(\phi=0)}}{v^2_{P0}}(2\delta\sin^2(\psi)\cos^2(\psi) + 2\epsilon\sin^4(\psi)) - \frac{\Delta l^2(\phi)}{v^2_{P0}} + \frac{\Delta l^2(\phi)}{v^2_{P0}}(2\delta\sin^2(\psi)\cos^2(\psi) + 2\epsilon\sin^4(\psi)), \quad (4.12)$$

or

$$t^2 = \underbrace{\frac{l^2_{(\phi=0)}}{v^2_{P0}}}_{zero-dip,isotropic} - \underbrace{\frac{\Delta l^2(\phi)}{v^2_{P0}}}_{dip,isotropic} - \underbrace{\frac{l^2_{(\phi=0)} - \Delta l^2(\phi)}{v^2_{P0}}(2\delta\sin^2(\psi)\cos^2(\psi) + 2\epsilon\sin^4(\psi))}_{residual,anisotropic}. \quad (4.13)$$

I express the ray angle ψ (see Appendix A) for small offsets using the known parameters ϕ, D_z, Rec_x, and separate the anisotropic influence in dip-dependent (Υ) and dip-independent (ζ) parts. This procedure is also valid for the qSV and the SH wave (results are given in Appendix A).

$$t^2 = \underbrace{\frac{l^2_{(\phi=0)}}{v^2_{P0}}}_{(a)} - \underbrace{\frac{\Delta l^2(\phi)}{v^2_{P0}}}_{(b)} - \underbrace{\frac{l^2_{(\phi=0)}}{v^2_{P0}}\zeta}_{(c)} + \underbrace{\frac{\Delta l^2(\phi)}{v^2_{P0}}\zeta - \frac{l^2_{(\phi=0)} - \Delta l^2(\phi)}{v^2_{P0}}\Upsilon}_{(d)}, \quad (4.14)$$

where

$$\zeta = \delta\frac{Rec_x^2}{2D_z^2} + (\epsilon - 2\delta)\frac{Rec_x^4}{8D_z^4}, \quad (4.15)$$

$$\Upsilon = \delta\frac{\sin(\phi)Rec_x^3}{2\cos(\phi)D_z^3} + \delta\frac{3Rec_x^4}{8D_z^4}\tan(\phi)^2, \quad (4.16)$$

and (a) denotes the zero-dip isotropic, (b) the dip isotropic, (c) the zero-dip anisotropic and (d) the dip anisotropic term.

4.6.2 Significance and implication of equation (4.14)

Equation (4.14) shows that the travel time of a wave in an anisotropic medium above a dipping interface can be decomposed into dip-dependent and dip-

independent terms and anisotropy-dependent and anisotropy-independent terms. This makes it possible to separate the effects of anisotropy and dip and correct for these effects whenever necessary. I now evaluate the contribution of each term to the total travel time of a given wave. Testing for a range of different anisotropic models and different dip angles shows that each component of the travel time is at least an order of magnitude larger than the following one and that the travel time is divided into dip/horizontal, isotropic/anisotropic parts which makes it possible to compensate for each one individually. As an example, Figure 4.6 shows the individual contribution of each term for a 20 degrees dip, ($\epsilon = 0.15$, an-ellipticity=0.19), revealing clearly this ordered relationship. Note that the scale on the vertical axis is logarithmic.

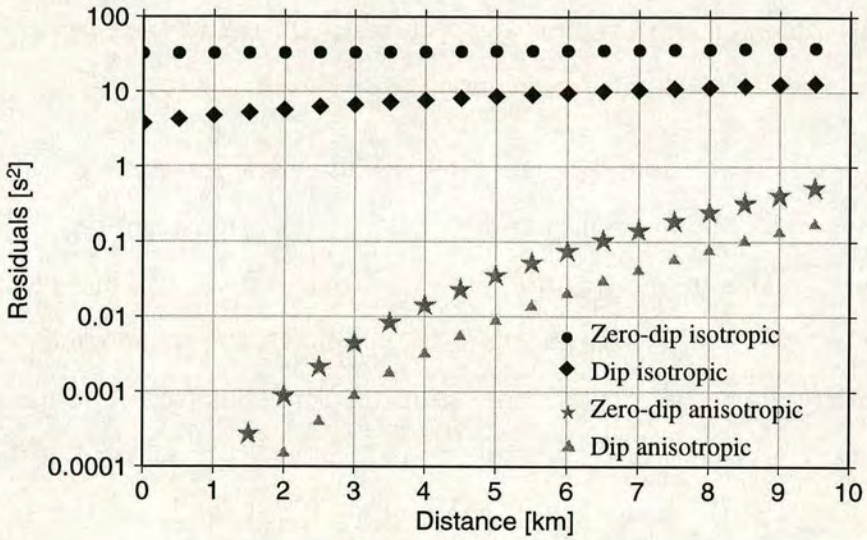

Figure 4.6: Ordering of the four different terms of the travel time equation as given in equation (4.14) for a medium with $\epsilon = 0.15$ and a dip angle of 20 degrees.

For processing purposes, the fourth term (dip, anisotropic residual) in equation (4.14) (Figure 4.6) may be neglected because it is three orders of magnitude smaller than the leading term. The total travel time has only three parts related to, respectively, the horizontally-layered isotropic background, the dip (or the structure), and the anisotropy. Thus, to compensate for the anisotropy effects

and obtain a better structural image it is necessary to estimate and correct for the third term in equation (4.14); to remove the effects of structure and obtain a reliable estimate of anisotropy it is necessary to estimate and correct for the second term in equation (4.14).

4.6.3 Separation procedure

From above, the anisotropy influence is at least an order of magnitude smaller than the dip influence, and one can compensate for the structural effect without considering the anisotropy in the initial step. After the influence of the dip is removed, the anisotropy estimation method for horizontal layers (Li and Crampin, 1993a, Rommel, 1993, Tsvankin and Thomsen, 1994) can then be applied. This sequence may be repeated if necessary.

Note that I do not intend to carry out a full elastic inversion of the Thomsen parameters, but to determine the dip angle, so that the structural influence can be removed. This is only possible due to the decomposition of equation (4.14) and the ordered relationship shown in Figure 4.6. If the travel time is given, the approximate dip angle can be found from the x position of the minimum of the travel time curve. The minimum position of the travel time curve is the same as the x-position of the image point [equation (4.4)]. If the x position is measured from the data, I find the angle as

$$\phi = \frac{1}{2}\arcsin(\frac{x}{D_z}). \tag{4.17}$$

This is only true for isotropic layers, where the phase and the group velocity are the same. But I will now show that for moderate dips equation 4.17 can still be used because the error in the estimation of the minimum of the travel time are small. The squared travel time is given by equation 4.10. The x position of the

minimum can be found as the solution of

$$\frac{\partial(t^2)}{\partial x} = 0 \tag{4.18}$$

This leads to a form where the difference in the position of the minimum travel time between the anisotropic and the isotropic case ($x_{min} - x_0$) is expressed by a term which depends on the deviation of the group from the phase velocity

$$x_{min} - x_0 = \frac{l^2}{V_G} \frac{\partial V_G}{\partial x}. \tag{4.19}$$

Figure 4.7 shows the difference of the x position of the minimum point (left) as well as the error in the angle estimation which is introduced by the x-shift.

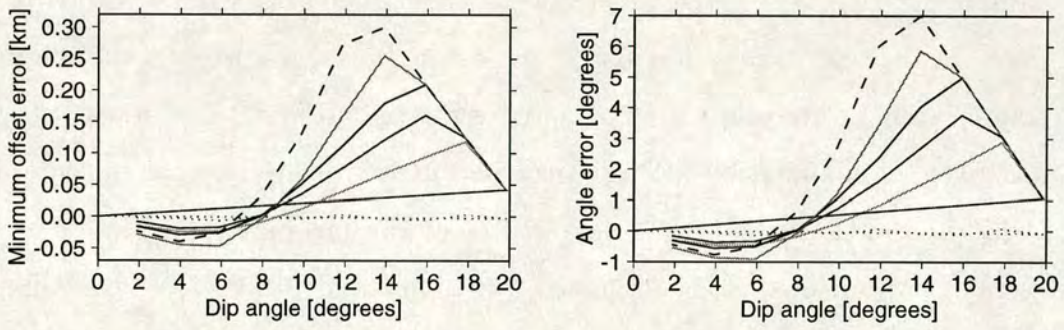

Figure 4.7: Difference between the x position of the minimum point for an isotropic (dotted) and anisotropic (dashed, $\epsilon = 15\%$) medium for different dip angles (left). The solid curves represent different values of ϵ, ranging from 3 to 10. The right diagram shows the error in the angle estimation which results from the shift.

To evaluate how the error in the angle estimation affects the separation process I calculate the error in the travel time that is introduced by the error in the angle. Figure 4.8 shows the percentage error in the travel time for a 5 degrees error in the angle estimation if the dip of the interface is 15 degrees.

Therefore equation 4.17 can be used even in the anisotropic case for a first estimate of the dip angle. It has to be noted that the knowledge D_z is required which might be sometimes difficult to assess.

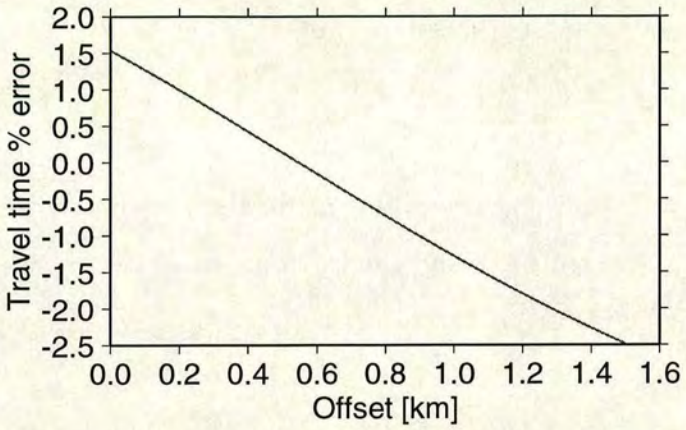

Figure 4.8: Percentage error in the travel time for different offsets for a 5 degree error in the angle estimation resulting from an approximation of the anisotropic medium by the isotropic minimum point.

From equation (4.17), the value of the residual is calculated and added to the data. In the second iteration step, I can estimate the anisotropy assuming horizontal layers. The results are compared with the initial data. If waveform data are given, the influence of the dip can be removed using isotropic dip-moveout (DMO) correction (Hale, 1984) followed by an anisotropic residual moveout correction. Details of this are discussed by Kühnel and Li (1997) and in Chapter 6.

4.7 Separation results

Here I present, for given travel time data, the results of the separation procedure above for different anisotropic models. If the effects of anisotropy and structure on the wave propagation were totally decoupled, all graphs should be identical. This is not the case. Therefore I expect the method to be valid for approximately the same region as the forward modelling. As discussed previously, I have to estimate and correct for the second term in equation (4.14) in order to remove the influence of the structure. To demonstrate the accuracy of the separation

procedure, the corrected travel time (the sum of the remaining horizontal isotropic and anisotropic terms) is compared with the travel time calculation from ANRAY for the same model but with an horizontal interface at the same depth beneath the source as for the dipping model (Figure 4.1). Figures 4.9 and 4.10 show the results for models with $\epsilon = 0.15$ and $\epsilon = 0.25$.

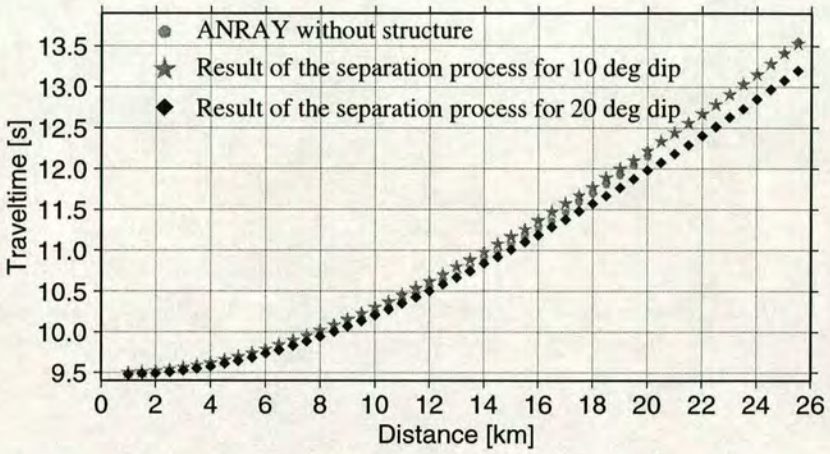

Figure 4.9: The results of the separation process for anisotropy and structure for $\epsilon = 0.15$ and symmetry axis perpendicular to the interface. The three curves in the figure represent the results for a horizontal reflector obtained by ray tracing (dot), the processing results from models with 10 degrees of dip (star) and 20 degrees of dip (diamond).

The three curves in Figures 4.9 and 4.10 are, the ANRAY results (dot), the separation results from a model with 10 degrees dip (star) and 20 degrees dip (diamond). The ANRAY result acts as a reference curve, which represents the correct measurements. All curves in Figure 4.9 show a very high similarity even for far offsets. In this case the separation method provides sufficient accuracy because for the estimation of the anisotropy (Li and Crampin, 1993a) only the difference between the zero-offset and the other offsets is interesting. It re-confirms the ordering of the wavefield as expressed in equation (4.14). If the anisotropic influence were larger or if any assumptions during the derivation of the travel time equation were not valid, a significant difference between the curves would be noticeable. If the anisotropy (Figure 4.10) is increased, it becomes clear that

only incidence angles of 25-30 degrees can be treated with the method.

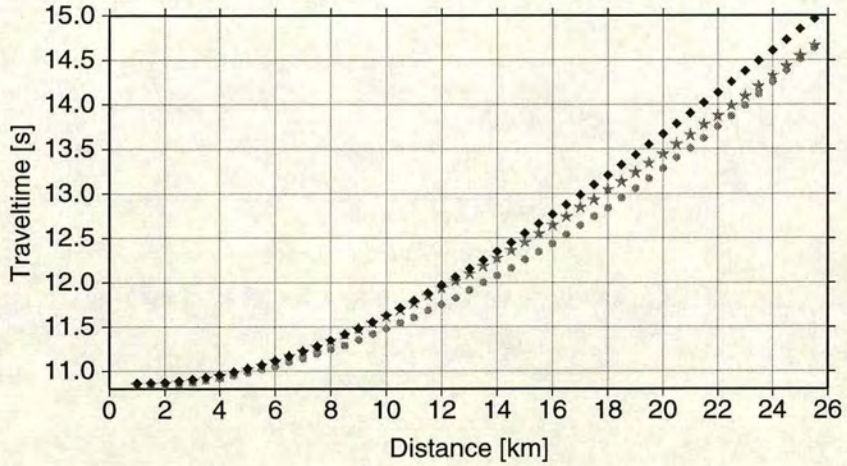

Figure 4.10: The same as Figure 4.9 but for $\epsilon = 0.25$. The different zero-offset times are caused by a model where the anisotropy has effected the vertical velocity.

The time differences between the ray tracing results and the results of the separation process are given for $\epsilon = 0.15$ in Figure 4.11a and for $\epsilon = 0.25$ in Figure 4.11b. For an offset of 5km (offset to depth ratio of 0.455) the difference is smaller than 10ms (a quarter of the wave period). The limiting factor is the high amount of anisotropy. The image point construction is valid as long as the symmetry axis of the elastic tensor is perpendicular to the interface regardless of the degree of TI anisotropy. But the weak anisotropy assumption for the group velocity has reached its limits. The ordered travel time equation is based on the weak anisotropy assumption for the velocity and therefore breaks down both for high anisotropic materials and for large offsets.

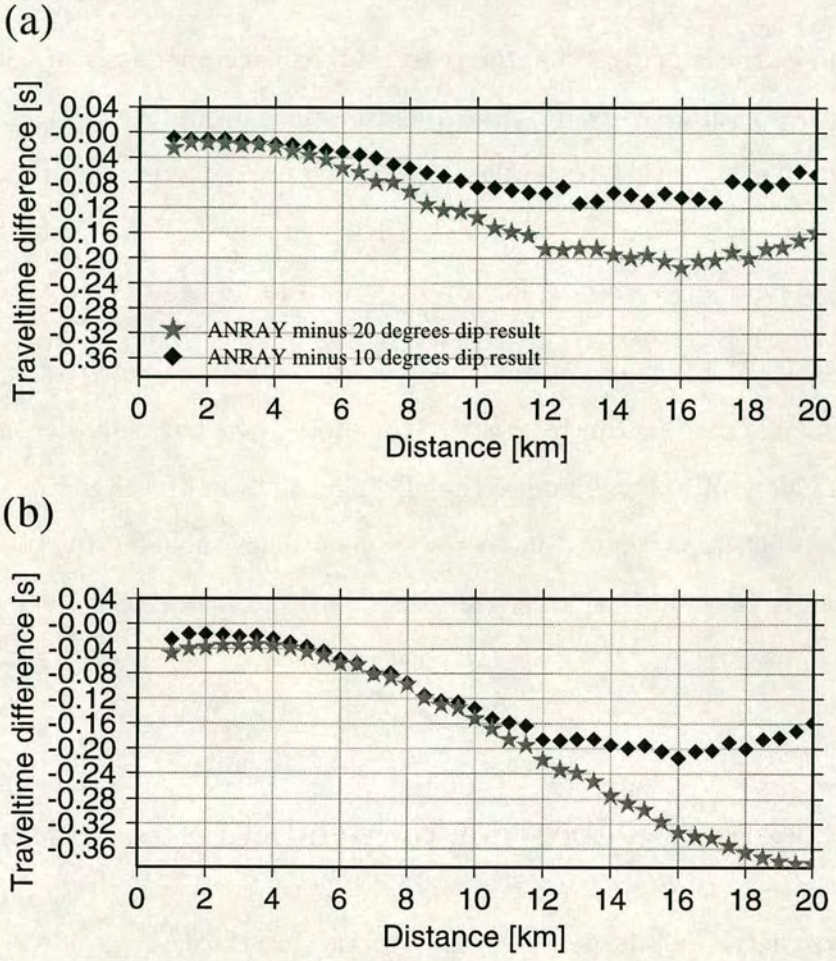

Figure 4.11: Difference in the travel time between the accurate ray tracing result for the horizontal reflector and the results of the separation process for the symmetry axis perpendicular to the interface with $\epsilon = 0.15$ (a) and $\epsilon = 0.25$ (b). The two graphs in each diagram show the two different dip angles of 10 and 20 degrees.

4.8 Discussion

The main purpose of this chapter is to establish whether it is possible to separate anisotropy and structure, and to determine the limits and accuracy of this approach. An algorithm is developed for a symmetry axis perpendicular to the interface for a single layer 2-D model. I have shown that the separation is valid for values of ϵ of 0.15 to 0.25, for dip angles up to 20 degrees.

The image point construction is not valid if the axis has any other orientation than perpendicular to the interface. Therefore the analytical decomposition is not possible. I will now examine the effect on the quality of the results if I still apply the separation algorithm. An error analysis is included in Appendix A. A brief discussion of the 3-D case is also included and some relevant equations are given in Appendix A.

4.8.1 Symmetry axis not perpendicular to the interface

If the symmetry axis is perpendicular to the interface (Figure 4.1), the image point construction is correct. Therefore the corresponding group velocities are equal for both segments of the ray. When the symmetry axis is perpendicular to the surface, resulting from, for example, deposition on a rotated substratum (Levin, 1990) the image point construction is no longer valid. The incident and reflected rays have different angles relative to the symmetry axis of the elastic tensor and, hence have different velocities. However, for weak anisotropy or a small dip one could expect that the deviation of the reflected ray from the ray predicted by the image point construction will be small (see Appendix A). Thus, if I use the corresponding velocities for the incident and reflected rays, it can be expected that the accuracy of the travel time and the separation procedure will be sufficient up to certain values of anisotropy and dip. I test this approach for

different anisotropic models to find out the exact range of applicability.

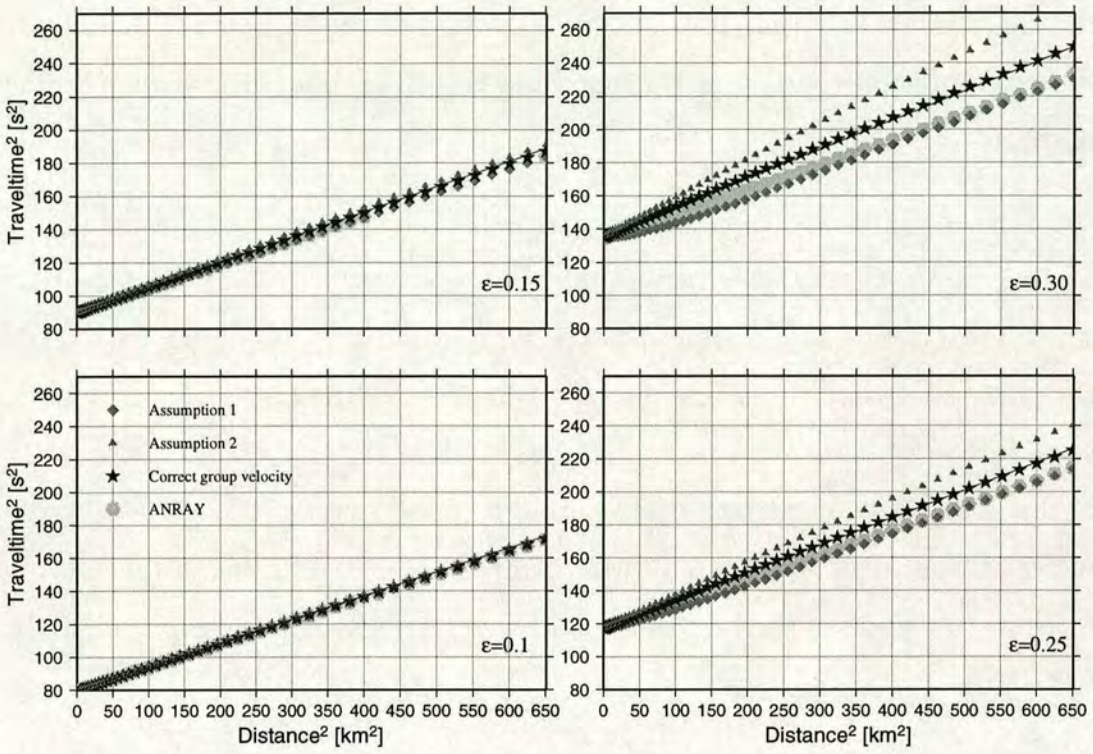

Figure 4.12: The squared travel time curves (t^2 against x^2) calculated for 0 degrees of dip and a symmetry axis of the elastic tensor rotated by 20 degrees from the vertical. There are four different diagrams corresponding to different values of ϵ: 0.1, 0.15, 0.25, 0.3. Each diagram contains five different curves for different calculation methods: Assumption 1 (the diamonds) where the group velocity is equal to the phase velocity at the ray angle ($V_G(\psi) = V_P(\psi)$), assumption 2 (the triangle) where the group velocity is equal to the corresponding phase velocity ($V_G(\psi) = V_P(\theta)$), correct group velocity (stars), the ray tracing results from ANRAY (slightly shaded hexagons) and the straight line as the solution for the isotropic case.

Figure 4.12 shows the travel time calculated for zero dip. The symmetry axis is rotated 20 degrees from the vertical towards the x-axis; One can see that the travel time obtained using the correct group velocities for the two segments of the ray (the star symbol) is sufficiently accurate up to $\epsilon = 0.15$ and 25 degrees of incidence angle. For higher ϵ, the star symbol deviates slightly from the shaded symbol, which is expected. The correct group velocity is measured at the same

angle as if the image point construction was valid but is different for the two segments of the ray. Therefore a deviation from zero of the difference between the ray tracing and the results for the correct group velocity express the inaccuracy of the image point construction if the symmetry axis is not perpendicular to the interface.

An interesting phenomenon can be observed if the symmetry axis of the elastic tensor is rotated from the vertical towards the x-axis (Figure 4.12). It seems that the anisotropy has disappeared. There is no possibility to detect any anisotropy from the travel time curves calculated for materials with $\epsilon = 0.1$ and $\epsilon = 0.15$. Even in the two higher cases ($\epsilon = 0.25$ and $\epsilon = 0.3$) the star symbol lies directly on the isotropic line and the ANRAY results are also very close to the isotropic line. This happened both for a rotation of 20 degrees towards the positive x-axis, or 20 degrees towards the negative x-axis, though only the former case is shown here.

Figure 4.13 shows the influence of the orientation of the symmetry axis of the elastic tensor on the quality of the modelling results. The medium has in all three cases an ϵ value of 0.15. The amount of anisotropy and the dip angles are exactly the same as in Figure 4.5 and the two Figures can therefore be used to describe the effect of a change in the axis orientation on the modelling results. Figure 4.13a is calculated for an horizontal reflector but with a symmetry axis rotated by 20 degrees from the vertical as described in the last paragraph and in Figure 4.12. Only for short offsets up to 3.5km (offset to depth ratio of 0.318) the results are below the 10ms margin. The same result can be found in Figure 4.13c where the axis is perpendicular to the surface but the reflector is dipping with 20 degrees. This means only the axis orientation relative to the interface is important, not the absolute value of the dip. For gentle dips (10 degrees), as shown in Figure 4.13b, the calculation is valid for an offset of 7km (offset to depth ratio of 0.636). This is the same result as in Figure 4.5c where the symmetry axis is perpendicular to

the interface but the reflector dips with 20 degrees. Therefore a change in the orientation of the symmetry axis away from the direction perpendicular to the interface shifts the accuracy of the results towards smaller dip angles.

(a)

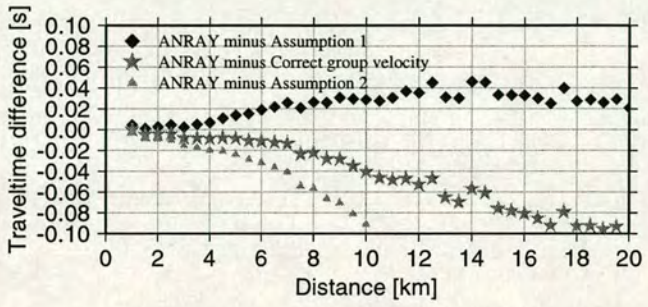

(b)

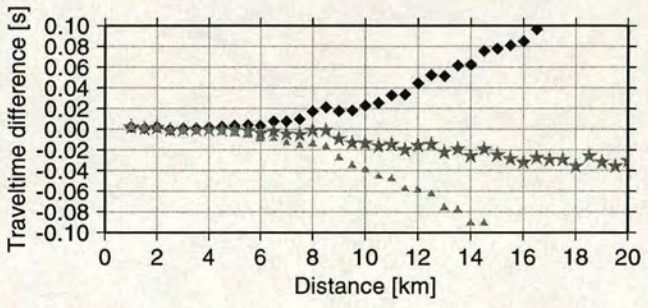

(c)

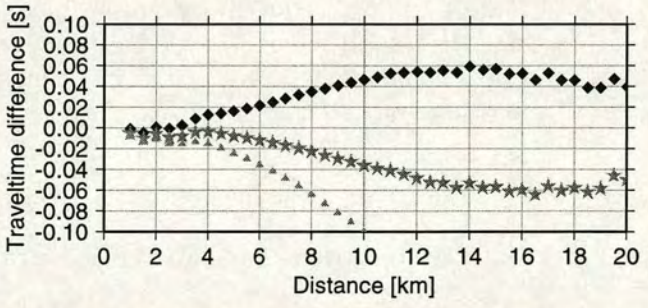

Figure 4.13: Difference in the travel time between the accurate ray tracing and the approximate travel times for a medium with $\epsilon = 0.15$ with the symmetry axis of the elastic tensor rotated by 20 degrees from the vertical for a horizontal reflector: (a) perpendicular to the surface for the two different dip angles; (b) 10 degrees dip, (c) 20 degrees dip.

In the following, the accuracy of the separation procedure is examined. Because this is an additional approximation in ray construction, I expect the accuracy range in terms of anisotropy and dip to decrease. By analogy with Figure 4.9, Figure 4.14 shows the separation results for the rotated symmetry axis. Figure 4.14 shows that only for a dip of 10 degrees and a smaller offset range the separation results (the star curves) are close to the ANRAY results. For 20 degrees of dip, the separation results (the diamond curve) show no similarities to the ANRAY values especially the shape and curvature of the graph is very different.

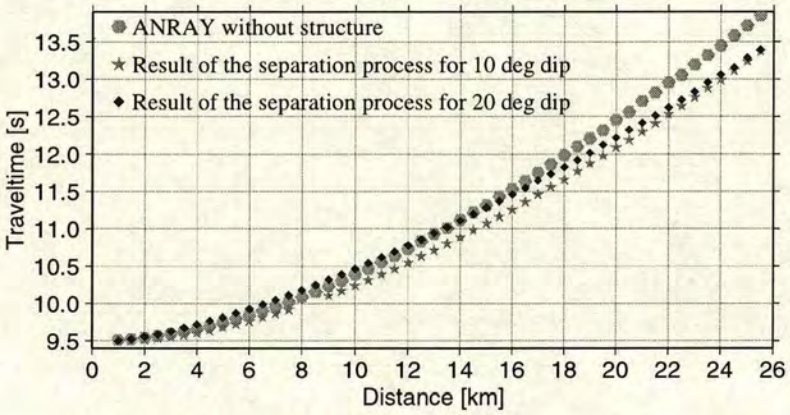

Figure 4.14: The results of the separation process for anisotropy and structure for models where the symmetry axis of the elastic tensor is perpendicular to the surface and $\epsilon = 0.15$. The three curves in the figure represent the results for a horizontal reflector obtained by ray tracing (dot), the processing results from models with 10 degrees of dip (star) and 20 degrees of dip (diamond).

In summary, by using the image point construction with two different velocities for the incident and reflected rays, the travel time and the separation method are valid for values of ϵ up to 0.15 and for at least 10 degrees of dip. This suggests that the deviation of the reflected ray from the one predicted by the image point construction may be neglected for gentle dips and weak anisotropy. I demonstrate this analytically in Appendix A. The difference between the incidence and the reflection angle $\Delta\theta$ is less than 1 degree for $\epsilon = 0.15$, 10 degrees dip and an incidence angle of 30 degrees. The velocity variation for 1 degree difference (see Figure 2.10) is less than 2%.

4.8.2 3-D travel time equation

The formulation of the travel time equation using the image point construction can easily be transferred into 3-D as long as the symmetry axis is perpendicular to the plane interface. Some relevant equations are included in Appendix A which shows the solution for the 3-D P-wave travel time equation.

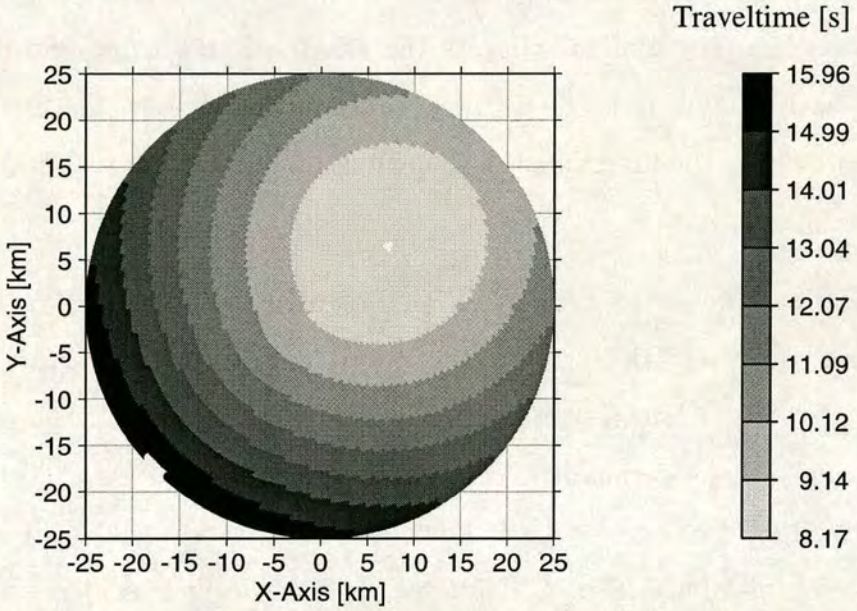

Figure 4.15: 3D travel time measurements for 135 degrees striking and 20 degrees dipping reflector. The medium has $\epsilon = 0.15$. The source is located at the origin, each line contains 100 receivers equally spaced at 0.5km and the depth of the receiver at the source is 11km. 1000 lines are calculated with an angular difference of 0.36°

.

Again, the wavefield is ordered and I can apply the same separation approach as in the 2-D case. The additional variable (strike angle) can be evaluated from the additional information of the y position of the minimum of the travel time curve, or from horizontal time slices (Figure 4.15). The relation between the x, y position of the minimum of the travel time curve and the dip and strike angle is given also in Appendix A. An example of a 3D travel time measurement is given in Figure 4.15, where the dip direction (the structure terms) can be estimated more easily using the extra azimuthal information.

4.9 Conclusions

A travel time equation for a 2-D anisotropic medium with a single dipping layer has been derived and it was shown that the equation can be decomposed into four terms: an isotropic horizontal, an isotropic dip residual, an anisotropic horizontal residual and an anisotropic dip residual. I have demonstrated each consecutive term is at least one order of magnitude lower than the previous one. This means there exists the potential to separate the effects of anisotropy and dip, based on the travel time using an hierarchical procedure. However, the inherent non-uniqueness within the inversion and the extension of the work to 3-D is a subject for further developments.

An anisotropic ray tracing code (ANRAY) is used to find the limitations of the travel time equation with respect to the P-wave anisotropy (ϵ) , ellipticity ($\epsilon - \delta$), dip and orientation of the symmetry axis of the elastic tensor. The travel time equation for an axis perpendicular to the interface is valid for at least $\epsilon = 0.2$ ($\epsilon - \delta \approx 0.19$) and 20 degrees dip (32 degrees of incidence angle). The separation procedure is valid for dips up to 20 degrees (25-30 degrees incidence angle) and $\epsilon = 0.15$ to $\epsilon = 0.2$.

In the case of the symmetry axis perpendicular to the surface, for $\epsilon = 0.15$ and a dip of 10 degrees (30 degrees incidence angle), the deviation of the reflected ray from the incidence angle is less than one degree. Hence the deviation of the exact reflected ray from the ray predicted by image point construction may be neglected. In this case, with different velocities applied for the incident and reflected rays, the travel time equation and the separation procedure are still valid. Cases can occur where the anisotropic effects are compensated by a special orientation of the symmetry axis as shown in Figure 4.12. In such cases the anisotropy may no longer be detected and the separation process is thus not applicable.

CHAPTER 5

Estimation of anisotropic parameters in the presence of dip

5.1 Introduction

In this chapter I examine how anisotropic parameters such as the fracture strike can be calculated and how the image of a stacked section can be improved even though the reflectors are not horizontal. The chapter is divided into two parts. The first one examines a single layer and shows how the image of the stacked section can be improved if the anisotropy is TIV. The second part concentrates on a dipping, vertically fractured target layer underneath a TIV overburden. The basis for the single layer approach is the formula for the travel time for a dipping anisotropic layer which is derived in Chapter 4 and the estimation process involves a derivation of the residual travel time given by Li and Crampin (1993a). In the dipping target section I demonstrate some of the difficulties of the fracture strike estimation method for such a model if the seismic survey consists only a limited number of lines. I show that traditional inversion schemes such as least-squares algorithms are not able to solve the problem satisfactorily. Only the application of a non-linear global optimisation scheme, a genetic algorithm, proved sufficient to recover the desired parameters. The same method is applied in Chapter 7 to a real data set.

5.2 TIV layer

The presence of anisotropy causes residual moveout (RMO) of the reflection events in a common mid-point gather, and, if uncorrected, degrades the quality of the stacked results. Further complications arise when coupled with the presence of dipping reflectors. To compensate for these effects, various anisotropic dip-moveout (DMO) algorithms have been developed (Uren et al., 1990b, Anderson and Tsvankin, 1994). Here, I use a separation approach, which adds anisotropic RMO correction to the traditional processing sequence of normal moveout (NMO) correction followed by isotropic DMO (Hale, 1984). It is important to notice that the proposed scheme is wavetype independent and can therefore be used for both P- and S-waves. During this anisotropic RMO the horizontal velocity is estimated and therefore the amount of anisotropy can be calculated.

5.2.1 Anisotropic residual moveout

As shown in Chapter 4, the P-wave travel time for a single dipping layer in a transversely anisotropic medium and the corrections for each contribution ((a): Isotropic NMO, (b): Isotropic DMO, (c): Anisotropic RMO) can be written as

$$t^2 = \underbrace{\frac{l^2_{(\phi=0)}}{v^2_{P0}}}_{(a)} - \underbrace{\frac{\Delta l^2(\phi)}{v^2_{P0}}}_{(b)} - \underbrace{\frac{l^2_{(\phi=0)}}{v^2_{P0}}\zeta_P}_{(c)} + 4th\ Order, \tag{5.1}$$

where l is the length of the ray path, ϕ the dip angle, v^2_{P0} the vertical isotropic P-wave velocity and ζ_P a combination of anisotropic parameters. This form of the travel time equation is also valid for the S-wave. The velocity changes to the vertical S-wave velocity and the parameter ζ_{Sv} is defined by a different combination of Thomsen parameters.

$$\zeta_P = \delta\frac{Rec_x^2}{2D_z^2} + (\epsilon - 2\delta)\frac{Rec_x^4}{8D_z^4}, \tag{5.2}$$

$$\zeta_{Sv} = (\delta - \epsilon)\frac{V_{P0}^2}{2V_{SV0}^2}\frac{Rec_x^2}{D_z^2}(\frac{13}{8}\frac{Rec_x^2}{D_z^2} - 1), \tag{5.3}$$

where D_z is the depth of the reflector at the source location and Rec_x is the x-position of the receiver.

The first way to estimate the anisotropy is to extract the residual moveouts (Δt) of the offset traces by cross-correlation with the pilot zero-offset trace after the isotropic DMO. Following Li and Crampin (1993a), in a transversely isotropic medium with horizontal layers, Δt can be expressed as

$$\Delta t_i^2 = x_i^2 \left(\frac{1}{v_h^2} - \frac{1}{v_{nmo}^2}\right) \sin^2\theta, \tag{5.4}$$

where x_i is the offset, θ the phase angle at the reflection point, v_h the horizontal velocity, and v_{nmo} the NMO velocity. To estimate the amount of anisotropy I calculate the least-squares solution for v_h using the given offset x_i and its residual travel-time Δt_i. The incidence angle θ is found by ray tracing through an initial velocity model built from v_{nmo} assuming a small magnitude of the Thomsen parameter δ (Thomsen, 1986).

A second method is to use Equation 5.2 and find the least squares solution for ϵ and δ using the residual travel time for all offsets.

5.2.2 Separation method

As demonstrated in Chapter 4, the P-wave travel time (Equation 5.1) can be decomposed into four different terms, each about an order of magnitude smaller than the previous one for dip angles less than about 25 degrees. Because of this ordering I can compensate for each contribution individually during processing. For the first two terms, this is done by the conventional NMO correction followed by an isotropic DMO correction. The data now contain mainly anisotropy related

contributions which can be corrected by the anisotropic RMO correction (Figure 5.1).

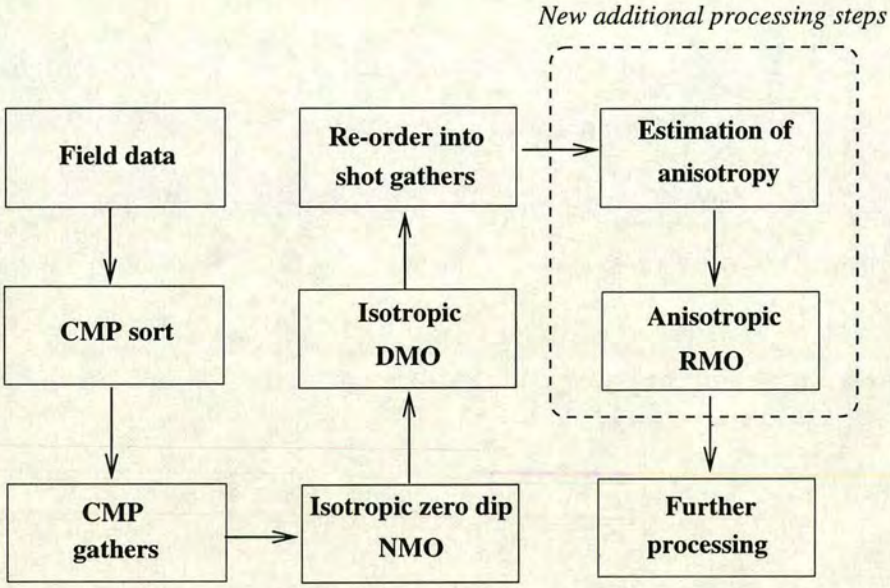

Figure 5.1: The new processing flow to compensate the influence of the anisotropy on the stacking and to estimate its strength.

5.2.3 Results

The synthetic model consists of two reflectors, one horizontal and one with a dip angle of 30 degrees. Both media are anisotropic, with Thomsen parameters for the top layer $\epsilon = 0.12, \delta = 0.0, \gamma = 0.1$ and for the bottom $\epsilon = 0.19, \delta = 0.0, \gamma = 0.2$. Figure 5.2 shows the difference between the results of the processing scheme as described in Figure 5.1. For the NMO correction the horizontal velocities from the input model are used to show clearly the effect of the dip and the anisotropy. Another velocity pick from a semblance analysis might have flattened the dipping event better but would have also disguised the dip or the anisotropy. The conventional isotropic processing would stop after the DMO correction. The better horizontal alignment of the events for both reflectors after the additional anisotropic RMO processing demonstrates the ability of the method to improve stacking results.

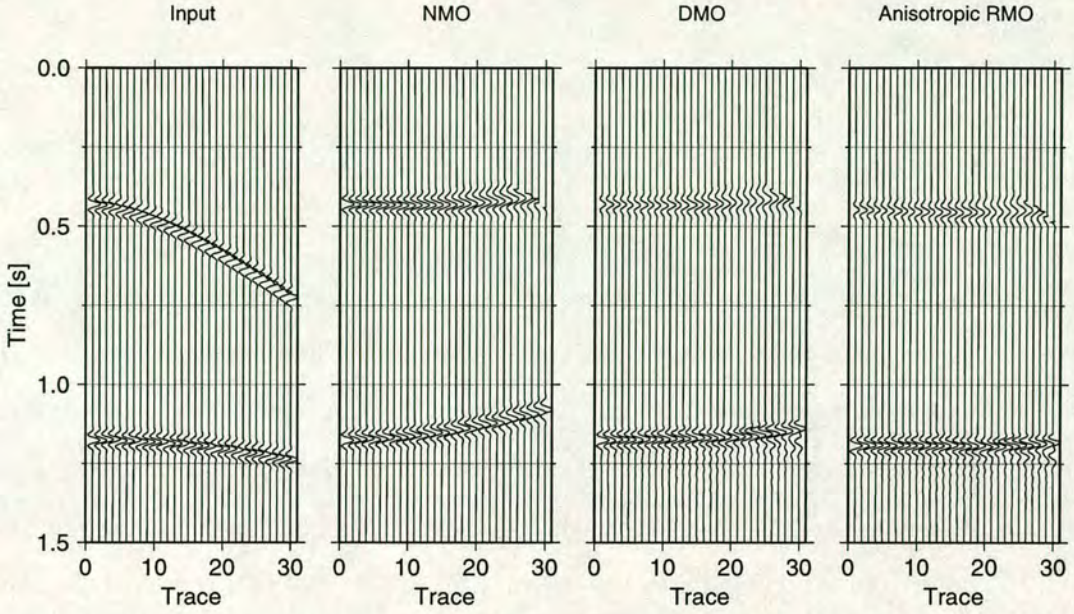

Figure 5.2: Synthetic data set with a horizontal first and a dipping second reflector after different processing stages. First the input data itself, then the data after the isotropic NMO correction, then after the isotropic DMO correction and finally after the anisotropic residual moveout correction.

During the estimation process a least-squares fit for the horizontal velocity using an initial model derived from the NMO velocities to estimate the incidence angle at the reflector required by the inversion process leads to a difference between the horizontal and the NMO velocity of 17%. Because δ is zero as an effect of the material building which uses thin layering, the NMO velocity equals the vertical velocity and therefore the 17% is an expression of ϵ. The difference to the input model arises from the ray tracing which has to be based on the NMO velocities and therefore ignores anisotropy. Errors in the incidence angle at the reflection point leads to errors in the estimation. Using the second estimation method, a multi-parameter search for the best fit leads to the estimation of the anisotropic parameters $\epsilon = 0.21$ and $\delta = 0.02$ which again is in good agreement with the model parameters. Errors are due to the required knowledge of the length of the ray path which can also only be derived by ray tracing from the model based on the NMO velocities.

5.3 TIH target

As shown in Chapter 3, it is possible to estimate the strike direction of the symmetry axis of a TIH target layer with an TIV overburden using a four line cross-plot scheme. The underlying assumptions are that the symmetry axis of the elastic tensor of the overburden is vertical and that the interfaces are all horizontal. As a consequence of these assumptions the minimum travel times of both layers coincide with the shot point of the four lines. Only if these assumptions are fulfilled will the resulting azimuthal variation of the travel time show the $\cos(2\phi)$ behaviour which leads to the estimation of the strike direction. I demonstrate below that any dip of the target layer severely violates the assumptions and therefore invalidates the whole procedure.

5.3.1 Shift of the minimum point

In the following I derive a formula for the position of the offset at which the minimum travel time is recorded. I show that the take-off angle at the source for this minimum ray is exactly the same as for a single layer. All the variables are described in Figure 5.3.

The known parameters are $d_1, \Delta d, v_1, v_2$ and θ. The idea is to express the travel time as a function of the take-off angle at the source (ϕ) in terms of the known parameters, find the angle for the minimum time, and insert this angle in an expression for the offset $x(\phi)$. This derivation is given in Appendix B.

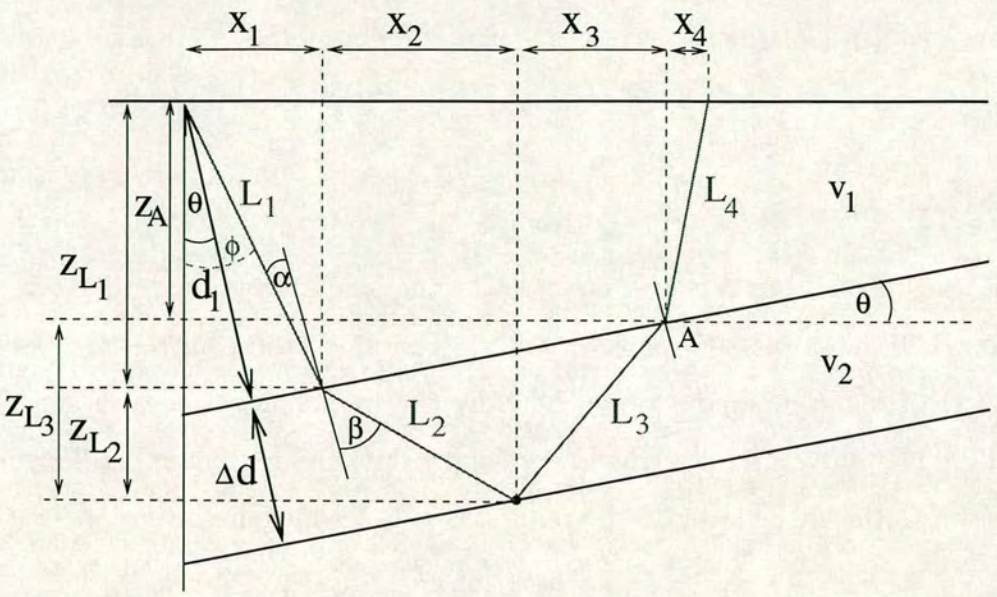

Figure 5.3: Ray path and variables for a dipping target layer.

The travel time dependence on the take-off angle ϕ is given by

$$t(\phi) = \frac{L_1}{v_1} + \frac{L_2 + L_3}{v_2} + \frac{L_4}{v_1} \tag{5.5}$$

$$= \frac{d_1}{\cos(\phi-\theta)v_1} + 2\frac{\Delta d}{v_2\sqrt{1-\frac{v_2^2}{v_1^2}\sin^2(\phi-\theta)}}$$

$$+ \frac{\frac{d_1}{\cos(\phi-\theta)}\cos\phi - \frac{2\Delta d}{\sqrt{1-\frac{v_2^2}{v_1^2}\sin^2(\phi-\theta)}}\frac{v_2}{v_1}\sin\theta\sin(\phi-\theta)}{\cos(\phi-2\theta)v_1}. \tag{5.6}$$

To find the minimum for $0 < \phi < 90$,

$$\frac{\partial t(\phi)}{\partial \phi} = 0, \tag{5.7}$$

has to be evaluated. Through the use of a symbolic calculation software (Maple) the following important solution is found

$$\phi_{min} = 2\theta. \tag{5.8}$$

This means that the take-off angle for the ray with the minimum travel time is exactly the same as for a single layer. It is not influenced by the thickness or the

impedance contrast of the second layer! The minimum offset changes, but not the take-off angle from the source. The offset is given by (see Appendix B)

$$o(\phi) = x_1 + x_2 + x_3 + x_4. \tag{5.9}$$

Because the take-off angle is the same as for the single layer, x_1 is the same. Equation B.29 shows that the expression for x_4 contains a term $\sin(\phi - 2\theta)$. This term is zero for the minimum ray. Therefore the minimum ray always arrives vertically. The only variables which are left to shift the minimum position in comparison to the single layer are therefore x_2 and x_3 which are given by

$$x_2 + x_3 = \frac{2\Delta d}{\sqrt{1 - \frac{v_2^2}{v_1^2}\sin^2(\theta)}} \frac{v_2}{v_1} \sin\theta\cos\theta, \tag{5.10}$$

where $\phi = \phi_{min} = 2\theta$ is inserted. This shows that the x position of the minimum is a linear function of the thickness of the layer and scaled by the velocity ratio. Figure 5.4 underlines the above. Notice that there is no change if the thickness is zero.

5.3.2 Residual travel time for dipping layers

In the previous section I demonstrated that any dip influences the position of the minimum point for the second layer in comparison to the first. I now examine what influence this behaviour has on the residual travel time, show models for isotropic and anisotropic target layers, and investigate to what amount of anisotropy the resulting residual travel time can be used to find the fracture strike. Figure 5.4 shows that the minimum of the second layer is only shifted by at most 200m, for a realistic target thicknesses of about 400m. Further, as shown in Chapter 3, the contours of the 3D distribution of the travel time for a isotropic layer are circular and that for a TIH layer are elliptical. In the following investigation I will therefore use synthetically calculated circles and ellipses. The

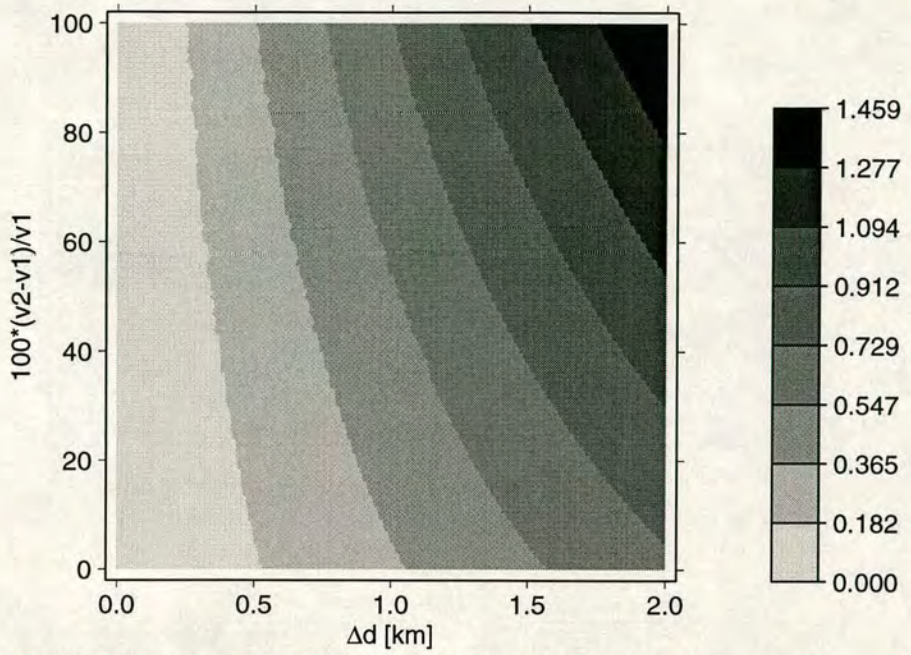

Figure 5.4: Variation of the offset where the minimum travel time is observed for the second layer relative to the minimum point for the first layer for varying thickness (Δd) and varying velocity of the second layer in percent of the first. The dip angle is 10 degrees and the velocity in the upper layer 2.3km/s. The unit for the colour bar is km.

top layer is represented by a circle (isotropic or TIV), with a steeper moveout than the ellipses for the bottom but a lower apex. Anisotropy is introduced as the ratio between the long and short half axis of the ellipses and varies between 0 and 20 percent.

For each of these anisotropic materials the residual moveout is calculated and the result is shown in Figure 5.5. For isotropy (Figure 5.5a) the resulting contour plot still shows circles but dip affected the position of the maximum. Therefore it is not be possible to apply the four line cross plot method. Similarly, for TIH anisotropy between 5 and 15% (Figures 5.5b-d) the contours still show ellipses, but again shifted ones. The azimuthal behaviour for a circle centred at the origin of the coordinate system does show the $\cos(2\phi)$ variation the fracture strike estimation method requires. In the next sections I therefore examine what kind of azimuthal variations the shifted contours produce and how these information can be used to find the fracture strike.

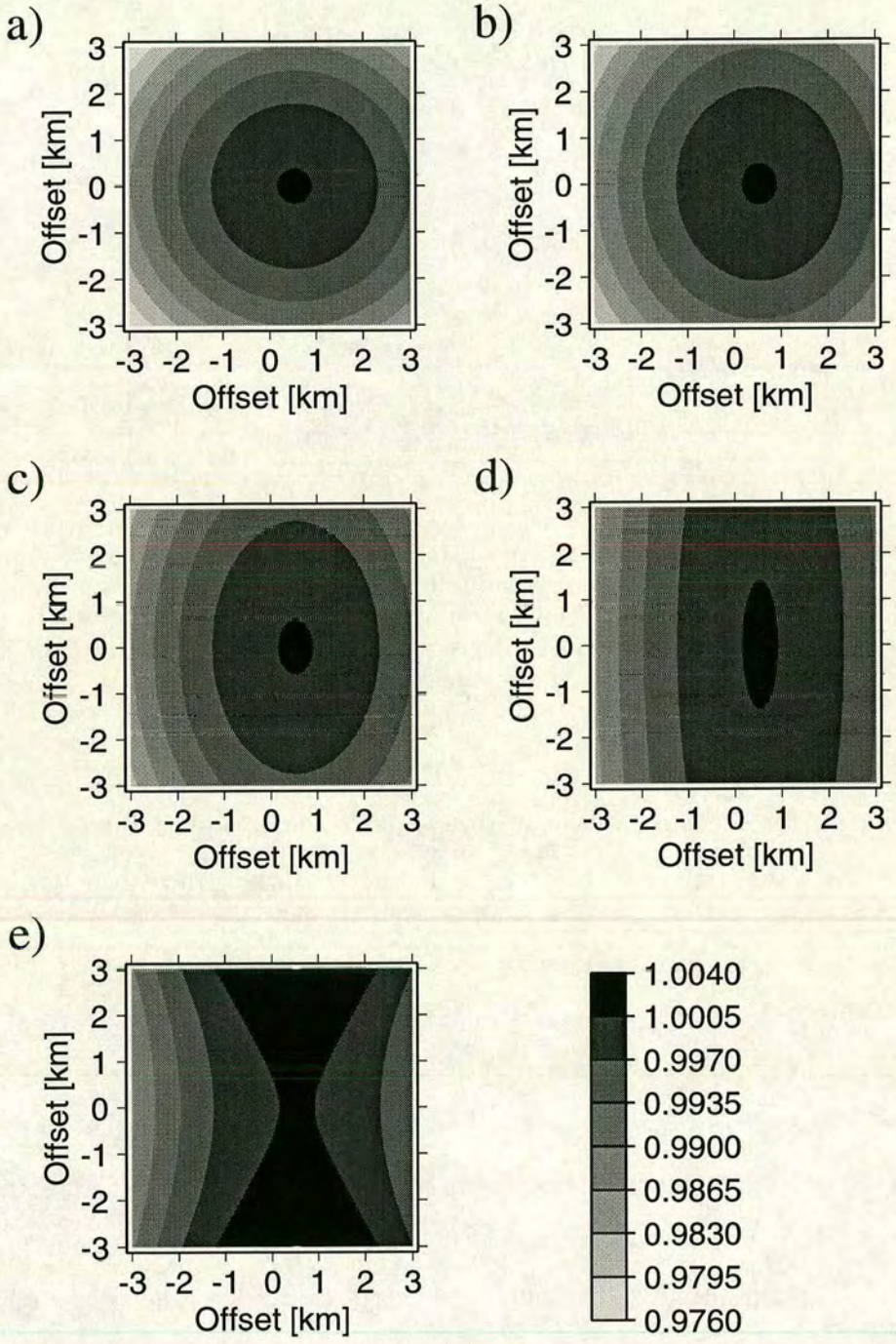

Figure 5.5: Variation of the residual moveout for an isotropic overburden and a 10 degrees dipping TIH target layer with varying strength of P-wave anisotropy. a): 0%, b): 5%, c): 10%, d): 15%, e): 20%.

5.3.3 Estimation of the strike direction

An analyses of least-squares procedures showed that it is not possible to estimate the position and orientation satisfactorily. The problem is still to find the ellipse that gives the best fit to a set of data points of equal travel time for which all positions on or around an ellipse are known. To calculate the centre of gravity for the resulting polygonal fails because of the unequally distributed values. There are far more points on the side closer to the centre of the survey lines than on the opposite side, which shifts the centre.

An analysis similar to the estimation of the first motion for P-waves, where an eigen-analysis of the covariance matrix is performed in order to find the axis of the best fitting ellipsoid, fails as well. The assumption that the centre of the ellipsoid is located at the presumed geophone position can not be maintained for the residual travel time.

In order to solve the problem for the shot gather domain, a more sophisticated inversion technique has to be applied. A non-linear optimisation technique should lead to good results. Due to the huge parameter range it seem unwise to use a simple linear search through the whole parameter space. Instead I use a genetic algorithm (GA) to perform the search for the best fitting ellipse. An explanation as to how a GA works is given in the next section. The advantage is that the resulting parameters not only describe the centre but also the length of the half axis and therefore the strike direction of the symmetry axis of the TIH target layer as well as the strength of the anisotropy.

5.3.3.1 Genetic algorithms

The problem is how to find the best values for a multi-parameter model. Traditional search algorithms often depend highly on a good *a priori* model or the

smoothness of the parameter space, in order not to get trapped in local minima. In each step only a single value is considered.

In contrast, a genetic algorithm uses many models simultaneously. In a similar way to biological evolution it improves the solution from generation to generation by the principles of "the survival of the fittest" and "mating". To achieve an improvement, a number of steps are repeated for every generation. Matching the biological equivalent to these steps requires the transfer into mathematics and then simulation by a computer program (see Goldberg (1989) for more details).

Initially, an ancestral population has to be available containing enough diversity to assure a broad genetic spectrum. In every generation each individual is exposed to the same fitness test ("the survival of the fittest"), which depends on the actual environmental conditions. The better an individual is adapted to these conditions, the higher are its chances to mate successfully, pass on its genetic information and therefore produce more off-spring. After many generations the best solution will dominate the population.

Adaption of a GA to the problem of fitting an ellipse The transformation from the DNA of the living world to a computer program is performed by coding the parameters in a sequence of binary bits (0 or 1). The number of bits necessary for each parameter depends on the required accuracy with which the problem is to be solved. The best fitting ellipse with its axes parallel to the coordinate axes is described by four parameters. The midpoint x_0, y_0 and the length of the half axis a and b. If $2^{10} = 1024$ different values for each variable are allowed, the bit code for each individual of the population will consist of a 40 bit sequence.

$$individual = \underbrace{1000110101}_{x_0}\underbrace{1110101011}_{y_0}\underbrace{0111010011}_{a}\underbrace{0001101011}_{b} \tag{5.11}$$

For the ancestral population 2000 of these individuals are created randomly.

The overall fitness of an individual is given by the sum of the values of a certain function for all the input data. This function is defined for the best fitting ellipse problem as the distance between a data point and the ellipse calculated for the actual parameters. The exact evaluation procedure is shown in Figure 5.6.

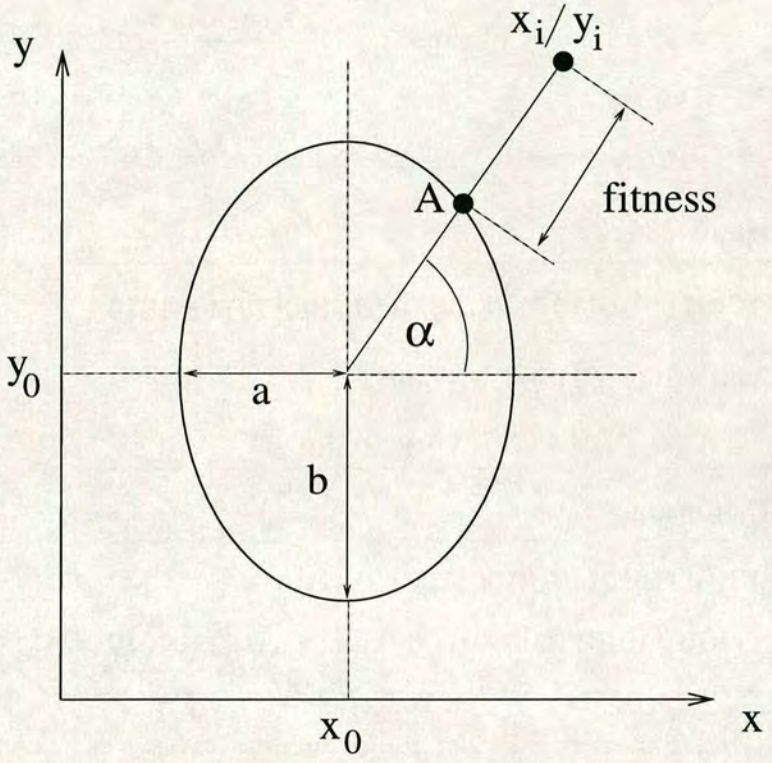

Figure 5.6: Definition of the fitness of the ellipse for a given set of parameters (x_0, y_0, a, b). First the angle α between the midpoint and the data point x_i, y_i is estimated, then the point on the ellipse for this angle (A) is calculated. The fitness function for an individual of the population is given by the sum of the fitnesses for all data points.

In principle a GA is designed to find the individual with the highest fitness value. In order to apply it to a minimisation problem such as here, a new function is defined as the difference between the maximum and the actual fitness value. After this transformation the best individual will have the highest number and the usual GA procedure can be followed.

While in biology the single step of reproduction includes mating and with it automatically the survival of the fittest, it is necessary to split it into two stages

for the computer algorithm. First a new generation is formed based on the fitness value. It is simulated by a biased roulette wheel, whose slots are allocated according to the percentage of the fitness of each individual on the sum of all the fitnesses. A roulette wheel that consists of 100000 slots

$$\text{number of slots} = 10^5 \frac{fitness_i}{\sum_i fitness_i}, \tag{5.12}$$

is chosen and spun 2000 times to find the individuals of the next generation.

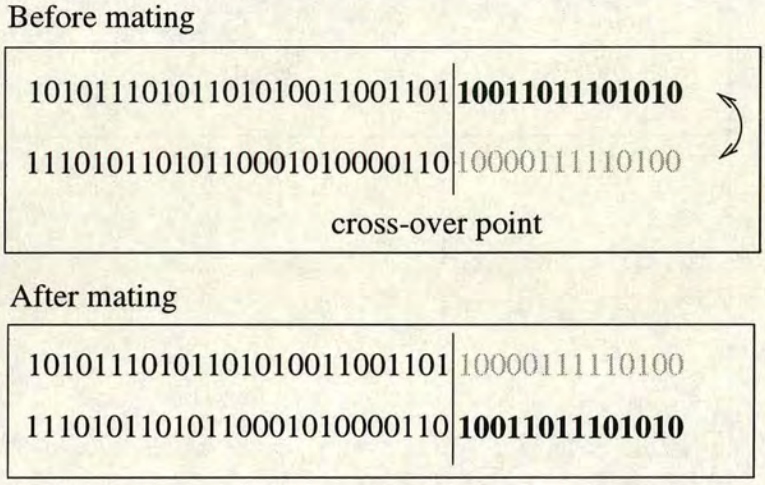

Figure 5.7: Mating procedure for two individuals of the new generation. The cross-over point is determined randomly for each pair and the bit sequence is exchanged.

Secondly the "mating" procedure, which requires the exchange of information between two individuals, is performed. The selection process of the individuals of the new generation is already random it is not necessary to search for mating partners. Always the two neighbouring individuals are used. For each pair the cross-over point beyond which the bits of the two individuals are exchanged (Figure 5.7) is determined randomly.

Other more sophisticated implementations include the biological equivalent of mutation where a factor can be introduced which allows the random change of single bits with a probability of f.g. 0.001. This is not considered in this algorithm.

It has to be mentioned that one disadvantage of the GA is the high number of individuals that are necessary to achieve a good result. If the fitness function is complicated then the computation time prevents a successful application.

5.3.3.2 Example

As a realistic example a four-line configuration for the model with a 10% TIH target layer is chosen. Instead of a contour plot of the residual travel time now only four lines are given (Figure 5.8).

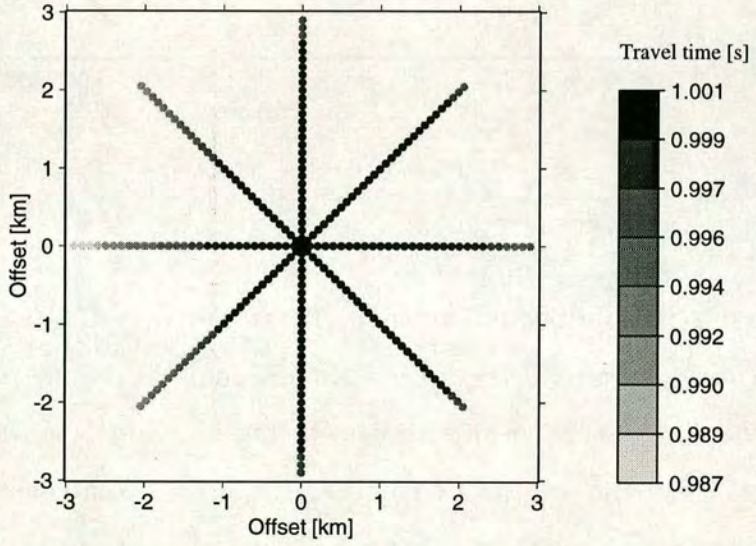

Figure 5.8: Azimuthal variation of the residual travel time for a 10 degrees dipping 10% TIH target layer for four survey lines.

For these lines the x,y position of a given residual travel time (here 0.998s) is estimated and used as an input for the GA. The range for the midpoint (x_0, y_0) and the length of the half axis (a, b) is subdivided into 1024 $(= 2^{10})$ steps which allows an accuracy of 5.8 metres. The calculation is performed with a starting population of randomly chosen 2000 individuals. Two hundred generations are calculated and for each generation the parameters (x_0, y_0, a, b) for the best fitting individual are written to a file.

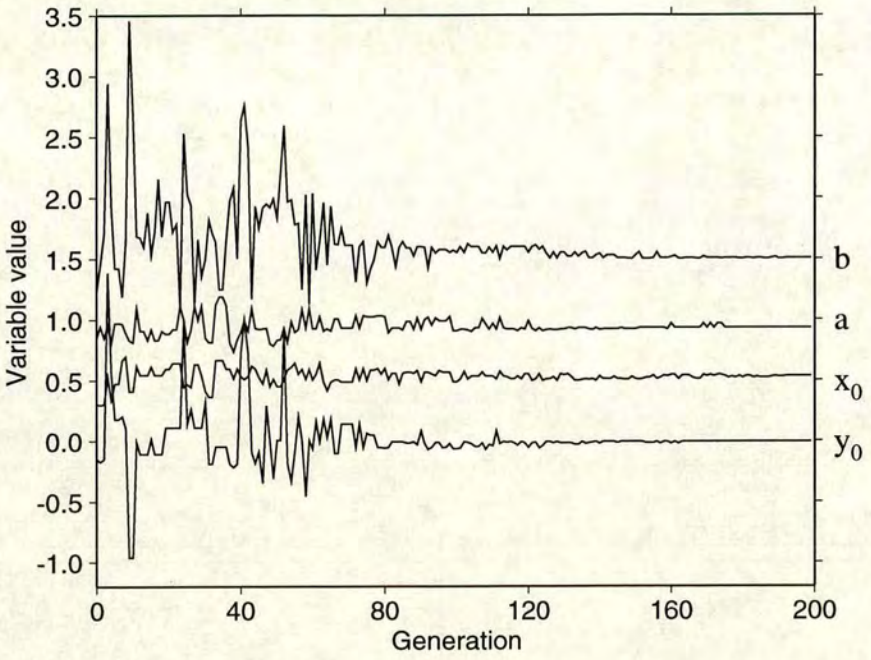

Figure 5.9: Development of the parameters (x_0, y_0, a, b) for the best fitting individual for 200 generations.

The result is shown in Figure 5.9. It is clearly visible that, after an initial random distribution where the best fitting individuals are very different from each generation to the next, the best fitting individuals start to dominate the population and the solution converges very rapidly to a constant level. This is because almost all members in the population represent the same parameter set.

Figure 5.10 shows the ellipse and the input data for the best result calculated by the GA. The direction of the longer half axis (here $b \equiv y - axis$) indicates the direction of the fracture strike in the target layer.

5.4 Conclusions

I have shown that it is possible to extract information about anisotropic parameters even if the reflectors are not horizontal. In the case of a single layer

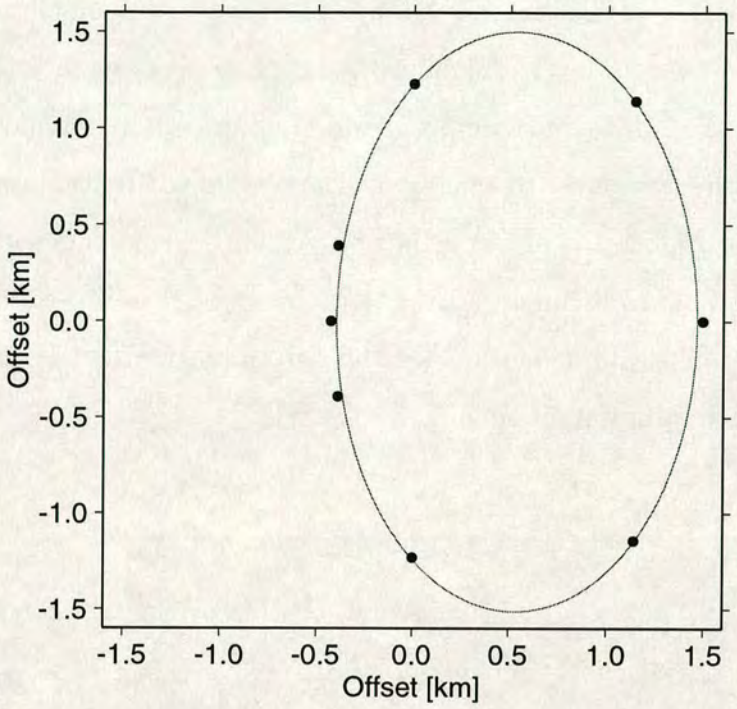

Figure 5.10: Best fitting ellipse and input data for the 10% TIH target layer. The parameters of the ellipse are: $x_0 = 0.5332, y_0 = -0.0058, a = 0.9316, b = 1.506$.

the application of an additional processing step, the residual moveout correction (RMO) was able to improve the quality of the stacked section. During this process an accurate estimate of the horizontal velocity leads to the determination of the anisotropy of the layer. In order to apply the technique the data have to be re-sorted into shot gathers.

For the two layer case it was necessary to introduce a sophisticated inversion scheme to resolve the problem of the symmetry direction for a TIH layer. One possible model is that of vertical parallel fractures. Therefore the fracture strike can be interpreted as one of the symmetry directions. The application of the method for the horizontal layer is not able to produce any reliable results, because the assumptions are violated as soon as the shot point and the point where the minimum travel time for the two layers is recorded do not coincide. The study of the behaviour of the residual travel time for a dipping target zone reveals that the

contour lines of the travel time can still be approximated by an ellipse if the TIH anisotropy of the target layer is smaller than 20%. This observation leads to the inversion idea. For any given number of survey lines equal residual travel times are assumed to lie on or close to an ellipse. The problem of determining this ellipse is solved by the application of a non-linear inversion scheme, a genetic algorithm. This scheme is able to estimate all the parameters of the ellipse simultaneously and therefore represents a method for the determination of the fracture strike direction for a dipping target zone.

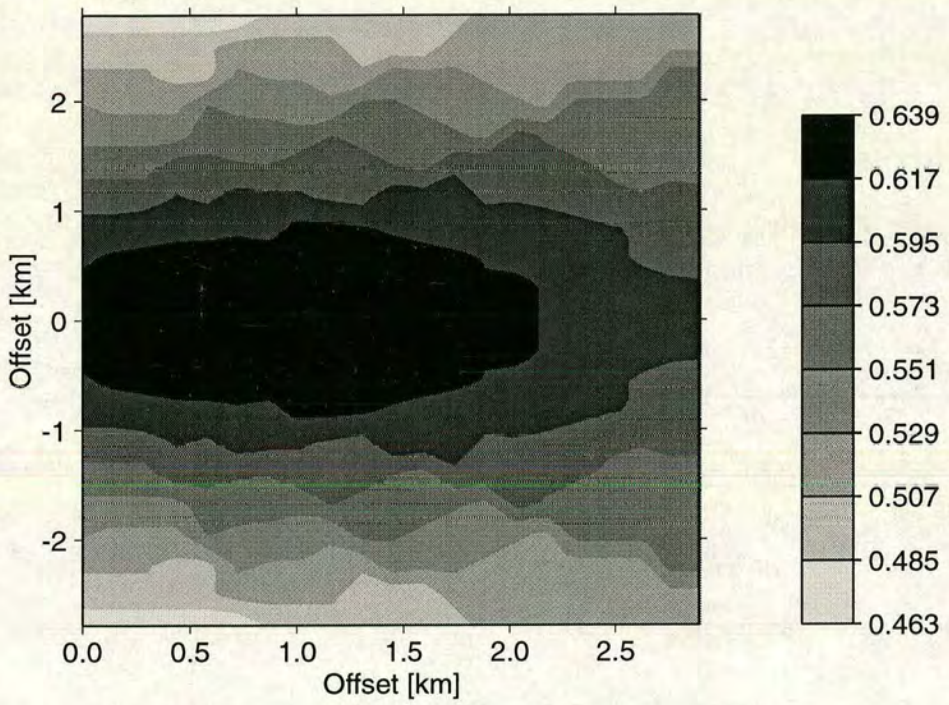

Figure 5.11: Variation of the interval travel time for non-parallel interfaces. The difference in dip is 5 degrees. All the other model parameters are the same as Figure 3.12. The scale of the colour bar is seconds.

Figure 5.11 shows the same model as Figure 3.12 but with a 5 degrees dip difference for the top and the bottom interface. Even in this case, where the interfaces are not parallel, it is possible to estimate the direction of the strike from the interval travel time. Investigations into oblique dip angles and other

phenomena are subject to future studies.

The restriction that in the example presented, the fracture are parallel to the coordinate axes is not essential. It is straightforward to introduce a rotation angle as an additional parameter in the GA and therefore the detection of any orientation of the fracture strike is possible.

The estimation of the major and minor axes of the ellipse and even the shift of the centre itself arises because I do the calculations and derivations of the relevant equation for shot gathers rather than CMP gathers because of the difficulty with ANRAY to produce CMP gathers. An investigation into how CMP gathers can be used to estimate the symmetry direction of a dipping TIH material, has to be refered to future studies.

CHAPTER 6

AVO analysis for orthorhombic media

6.1 Introduction

In this chapter I concentrate on a dynamic aspect of wave propagation, the reflection coefficient. After a review of the derivation for two isotropic media the reflection coefficient for the contact of two orthorhombic media is presented for all pure and mixed wave modes. It can further be shown that the result for the P-P coefficient can be separated under certain conditions into a TIV background and a TIH contribution.

The problem is to find the reflection response for a plane wave at the contact between two welded solids. The values for the boundary conditions which have to be fulfilled at the interface vary, depending on whether the half-spaces involved are a solid, a fluid or vacuum. The fluid/solid contact occurs at the sea bottom or the core mantle boundary, the contact to the air at the earth's surface. The kinematic boundary condition for the interface between two welded solids is that the components of the displacement are continuous across the interface. The dynamic boundary condition requires the traction to be continuous across the interface. Using the description of the potentials of plane P and S waves combined with the boundary conditions, a set of equations can be derived. Their result

describes the amplitudes of the reflected and converted wave as a fraction of the incident wave amplitude.

The results for all possible combinations of incidence and reflected waves and types of half-spaces are listed in Aki and Richards (1980). But these exact solutions are algebraically complicated and offer little insight to the physics involved. Further difficulties arise as these solutions depend on the density, the compressional and shear velocity of both media and therefore any numerical study involves the exploration of a six-parameter model space (Thomsen, 1993).

Fortunately, it is possible to introduce appropriate linearizations for these equations in many practical applications. The linearization is based on the assumption that the differences in the parameters between the two media are small. The resulting expression contains only three parameters and because of its simplicity allows the physics to be understood.

In a similar way Daley and Hron (1977) gave the exact equations for the reflection coefficient for TIV media but their solution was even more complex than the isotropic case. Thomsen (1993) and with an improvement Rüger (1995) gave the linearised equations based on a small contrast in the vertical elastic properties and the assumption of weak anisotropy. It was shown that anisotropy has a first order influence on the reflection coefficient even for small angles of incidence.

Li et al. (1996b) and Li et al. (1996a) gave the linearised solutions for the reflection coefficients for all mixed and converted modes in an orthorhombic medium. This approach is outlined in greater detail in section 6.3 later in this chapter.

6.2 Effects of dip

Studies of amplitude variation with offset often assume all the reflectors to be horizontal. A dipping interface poses problems in several areas: Errors will occur

in all the parameter estimations that depend on the reflection angle, the NMO corrections depend on the reflector dip and mis-positioned events could interfere (Resnick et al., 1987). In order to apply the estimation techniques developed in the next section the data have to be corrected for any influence of the dip of the interface. This correction has to preserve the amplitude information. Resnick et al. (1987) showed that in order to observe the AVO behaviour properly, the prestack migration algorithm needs to be amplitude preserving. These techniques show that it is possible to correct data for the influence of any dipping layer even in the dynamic respect.

The reflection coefficient for a dipping layer has the same meaning as in the horizontal case: it is an expression of the impedance contrast between the two materials. For a dipping interface between two isotropic materials it will therefore change the offset dependency of the reflection coefficient in comparison to horizontal layers because the incident angle at the reflection point changes. Additionally, for two anisotropic layers the impedance at the same incidence angle can change as well because the dip will change the direction of the symmetry axis. The following sections will focus on special estimation methods for in the symmetry plane of horizontal but orthorhombic media.

6.3 Orthorhombic AVO

To derive a linearised form of the reflection coefficient the symmetry plane of two orthorhombic media for all pure and mixed modes, the concept of impedance matrices introduced by Schoenberg and Protazio (1992) is used. The results of these linearised equations are then compared with numerical solutions to evaluate the accuracy of the approximations.

Orthorhombic anisotropy may be the most common form of anisotropy in sedi-

mentary basins, resulting from a combination of thin layers and aligned fractures. As shown in Chapter 2, the orthorhombic medium is described by nine elastic constants.

Wave propagation is considered in the vertical symmetry plane of $(x_1 - x_3)$ (Figure 6.1) where the mediums response is equivalent to TIV. The orthorhombic element is the difference between the behaviour in the two vertical symmetry planes. In this case, the qP - and qSV-waves are decoupled from the SH wave. Thus for simplicity, qS can be used to denote the quasi- SV wave, and the impedance matrices reduce to a 2x2 form,

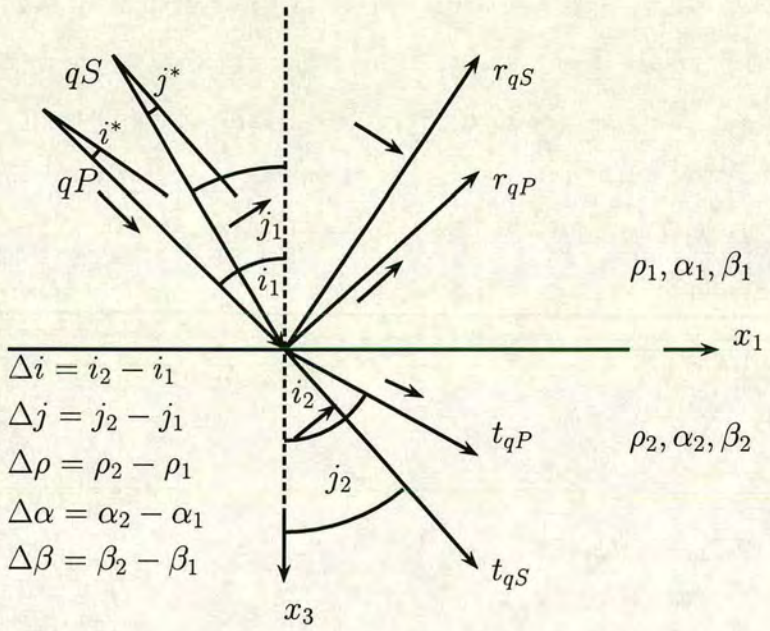

Figure 6.1: The reflection and transmission of qP- and qS-wave in a vertical symmetry plane at a single anisotropy/anisotropy interface. The following notation is used:
r_{qP} and r_{qS}: reflected qP- and qS-amplitudes; t_{qP} and t_{qS}: transmitted qP- and qS-amplitudes i_1 and j_1: qP- and qS incidence angles i_2 and j_2: qP- and qS transmission angle i^* and j^*: qP- and qS polarisation angles ρ_1, α_1 and β_1: density, qP-velocity at angle i_1 and qS-velocity at angle j_1 of the upper medium ρ_2, α_2 and β_2: density, qP-velocity at angle i_2 and qS-velocity at angle j_2 of the lower medium The Δ variations represent the change across the interface.

$$\mathbf{R} = \begin{pmatrix} r_{qPqP} & r_{qSqP} \\ r_{qPqS} & r_{qSqS} \end{pmatrix} = \frac{1}{2}(\mathbf{X}^{-1}\Delta\mathbf{X} - \mathbf{Y}^{-1}\Delta\mathbf{Y}). \tag{6.1}$$

The two matrices $\mathbf{X}$ and $\mathbf{Y}$ can be derived (Schoenberg and Protazio, 1992) if the velocity field in the incidence halfspace due to the incident and reflected P and S waves is considered. The second equation that is necessary to define $\mathbf{X}$ and $\mathbf{Y}$ is the stress-velocity law. These two formulations allow the reordering of the velocity and traction components in the incident medium in matrix form. In this formulation the matrices $\mathbf{X}$ and $\mathbf{Y}$ have the dimension of impedance.

First the expression for the impedance matrices $\mathbf{X}$ and $\mathbf{Y}$, and their corresponding changes $\Delta\mathbf{X}$ and $\Delta\mathbf{Y}$ for wave propagation in the $(x_1 - x_3)$ plane of an orthorhombic medium is presented. For a wave propagation in the vertical symmetry plane $(x_1 - x_3)$ of an anisotropic medium with orthorhombic symmetry these matrices are given by (Schoenberg and Protazio, 1992):

$$\begin{pmatrix} x_{11} & x_{12} \\ x_{21} & x_{22} \end{pmatrix} = \begin{pmatrix} e_{P_1} & e_{S_1} \\ -(C_{13}s_1e_{P_1} + C_{33}s_{3_P}e_{P_3}) & -(C_{13}s_1e_{S_1} + C_{33}s_{3_S}e_{S_3}) \end{pmatrix} \tag{6.2}$$

$$\begin{pmatrix} y_{11} & y_{12} \\ y_{21} & y_{22} \end{pmatrix} = \begin{pmatrix} -C_{55}(s_1e_{P_3} + s_{3_P}e_{P_1}) & -C_{55}(s_1e_{S_3} + s_{3_S}e_{S_1}) \\ e_{P_3} & e_{S_3} \end{pmatrix}, \tag{6.3}$$

where $(e_{P_1}\ e_{P_3})^T$ and $(e_{S_1}\ e_{S_3})^T$ are the qP- and qS-wave polarisation vectors, and $(s_1\ s_{3_P})^T$ and $(s_1\ s_{3_S})^T$ the qP- and qS-wave slowness vectors (horizontal and vertical slowness). It is shown in Appendix D that this formulation including the deviation of the polarisation direction leads to the reflection coefficient for all modes in the symmetry plane of the contact of two orthorhombic media.

The linearised reflection coefficients for orthorhombic media are given by

$$
\begin{aligned}
r_{qPqP} &= \frac{1}{2}\left(\frac{\Delta C_{33}}{C_{33}} - \frac{\Delta\alpha}{\alpha}\right) + \frac{1}{2}\left[\frac{\Delta\alpha}{\alpha} - \frac{2\rho'\beta^2}{C_{33}}\left(\frac{\Delta\rho'}{\rho'} + 2\frac{\Delta\beta}{\beta}\right) - \frac{2\beta^2}{\alpha^2}\frac{\Delta C_{55}}{C_{55}}\right]\sin^2 i \\
&+ \frac{1}{2}\frac{\Delta\alpha}{\alpha}\sin^2 i\tan^2 i + \frac{1}{2}\left(1 - \frac{\beta^2}{\alpha^2}\right)\tan^2 i\,\Delta\zeta_P, \qquad (6.4)
\end{aligned}
$$

$$
\begin{aligned}
r_{qPqS} &= \frac{\sin i}{\cos j}\left[-\frac{1}{2}\left(\frac{\Delta C_{33}}{C_{33}} - 2\frac{\Delta\alpha}{\alpha}\right) - \frac{\beta}{\alpha}\frac{\Delta C_{55}}{C_{55}}\cos i\cos j\right. \\
&+ \left.\frac{\rho'\beta^2}{C_{33}}\left(\frac{\Delta\rho'}{\rho'} + 2\frac{\Delta\beta}{\beta}\right)\sin^2 i + \frac{1}{2}\left(1 - \frac{\sin 2j}{\sin 2i}\right)\Delta\zeta_P\right], \qquad (6.5)
\end{aligned}
$$

$$
\begin{aligned}
r_{qSqP} &= \frac{\sin j}{\cos i}\left[-\frac{1}{2}\left(\frac{\Delta C_{55}}{C_{55}} - 2\frac{\Delta\beta}{\beta}\right) - \frac{\rho'\alpha\beta}{C_{33}}\left(\frac{\Delta\rho'}{\rho'} + 2\frac{\Delta\beta}{\beta}\right)\cos i\cos j\right. \\
&+ \left.\frac{\Delta C_{55}}{C_{55}}\sin^2 j + \frac{1}{2}\left(1 - \frac{\sin 2i}{\sin 2j}\right)\Delta\zeta_S\right], \qquad (6.6)
\end{aligned}
$$

$$
\begin{aligned}
r_{qSqS} &= -\frac{1}{2}\left(\frac{\Delta C_{55}}{C_{55}} - \frac{\Delta\beta}{\beta}\right) - \frac{1}{2}\left[\frac{\Delta\beta}{\beta} - \frac{2\rho'\alpha^2}{C_{33}}\left(\frac{\Delta\rho'}{\rho'} + 2\frac{\Delta\beta}{\beta}\right) - 2\frac{\Delta C_{55}}{C_{55}}\right]\sin^2 j \\
&- \frac{1}{2}\frac{\Delta\beta}{\beta}\sin^2 j\tan^2 j + \frac{1}{2}\left(\frac{\alpha^2}{\beta^2} - 1\right)\tan^2 j\,\Delta\zeta_S. \qquad (6.7)
\end{aligned}
$$

In the above equations, the Δ variables represent a change of the elastic properties across the interface, following the convention of Aki and Richards (1980). Variable ρ' reduces to the density ρ for isotropic media, as defined in equation (D.11). ζ_{Pk} and ζ_{Sk} $(k = 1, 2)$ can be calculated using the same expression for ζ_P and ζ_S, equation (D.29), by simply replacing the average elastic properties in (D.29) with the elastic properties in the corresponding medium. The equations contain hidden angular dependencies. They are resolved in the following section where reduced formulations for TI media are introduced. Finally the accuracy of these results is compared with numerical solutions and in case of the P-P reflection coefficient with that of other publications.

6.4 Weakly fractured medium

A medium containing aligned vertical fractures can give rise to an effectively TIH medium. There are different models to describe such a medium in the literature. Hudson (1981) used physical parameters such as crack density, aspect ratio and fracture contents. Schoenberg and Douma (1988) introduced fracture compliances for a more general representation. On the other hand, Thomsen (1986) proposed a set of parameters which are linked to practical seismic measurements. Here a link between the Hudson fracture model and the Thomsen parameters will be introduced. Then the reduced equations are presented in terms of Thomsen parameters and their significance for determining fracture parameters is discussed.

6.4.1 Hudson fracture parameters

Consider the TIH medium with aligned vertical fractures striking at the x_2 direction. Assume this TIH medium is obtained by fracturing an isotropic background medium with density ρ, P-velocity α_b and S-velocity β_b, and use ϵ_d as the fracture density, ϵ_{ar} as the aspect ratio of the fractures, and α_f as the P-wave velocity of the fluids within the fractures if any. To the first order of ϵ_d and ϵ_{ar}, the elastic constants C_{kl} can be written as (Hudson, 1981),

$$\begin{aligned}
C_{11} &= \rho\alpha_b^2\left(1-\frac{\alpha_b^2}{\beta_b^2}\epsilon_d U_{33}\right)\\
C_{13} &= \rho(\alpha_b^2-2\beta_b^2)\left(1-\frac{\alpha_b^2}{\beta_b^2}\epsilon_d U_{33}\right)\\
C_{33} &= \rho\alpha_b^2\left[1-\left(\frac{\alpha_b}{\beta_b}-2\frac{\beta_b}{\alpha_b}\right)^2\epsilon_d U_{33}\right]\\
C_{44} &= \rho\beta_b^2\\
C_{66} &= \rho\beta_b^2\left(1-\epsilon_d U_{11}\right),
\end{aligned} \tag{6.8}$$

where

$$
\begin{aligned}
U_{11} &= \frac{16}{3}\frac{\alpha_b^2}{3\alpha_b^2 - 2\beta_b^2} \\
U_{33} &= \begin{cases} \frac{4}{3}\frac{\alpha_b^2}{\alpha_b^2 - \beta_b^2} & \text{for dry fractures,} \\ \frac{4}{3}\frac{\beta_b^2}{\alpha_f^2}\pi\epsilon_{ar} & \text{for fluid-satuated fractures.} \end{cases}
\end{aligned} \tag{6.9}
$$

Although there are quite some recent theories about the fracture model, such as Schoenberg and Douma (1988), Thomsen (1995), and Liu et al. (1996), these recent theories all reduce to the above equations of Hudson to the first order of fracture density.

6.4.2 Thomsen parameters

The Thomsen parameters for the TIH medium can be written as:

$$
\epsilon = \frac{C_{33} - C_{11}}{2C_{11}}; \quad \delta = \frac{2C_{66} + C_{13} - C_{11}}{C_{11}}; \quad \gamma = \frac{C_{44} - C_{66}}{2C_{66}}. \tag{6.10}
$$

Comparing this definition for TIH with the original definition for TIV (Thomsen, 1986), one may notice an interchange of indices between 11 and 33, 44 and 66. This interchange is necessary in order to keep the quantities of Thomsen parameters of a TIH medium the same as its equivalent TIV medium. The interchange is the result of a 90 degrees rotation of the symmetry axis of an equivalent TIV medium (a Bond transformation, Winterstein, 1990) from vertical to horizontal. By keeping the Thomsen parameters of TIV and TIH with the same values and link the definition by the Bond transformation, the need to use a different set of effective Thomsen parameters for the TIH medium (Tsvankin, 1996) can be avoided. Any equations derived in terms of Thomsen parameters either for TIH or TIV will have the same meaning and quantities, hence avoiding confusion during applications.

A simplified δ is defined here, which is the first order approximation of the original δ (Thomsen, 1993, and Sayers, 1995). This approach is justified because linearised equations which are only accurate to the first order of the anisotropic parameters are considered.

Substituting equation (6.8) into (6.10) gives

$$\epsilon \approx 2\epsilon_d \left(1 - \frac{\beta_b^2}{\alpha_b^2}\right) U_{33}; \quad \delta \approx 2\epsilon_d \left(U_{33} - \frac{\beta_b^2}{\alpha_b^2} U_{11}\right); \quad \gamma \approx \frac{1}{2}\epsilon_d U_{11}, \tag{6.11}$$

which makes it possible to invert the physical fracture parameters (fracture density, aspect ratio and contents) from ϵ, δ, and γ. In particular, γ is completely determined by the fracture density, while ϵ and δ are determined by both the density and aspect ratio. For fluid-saturated fractures, ϵ will be completely determined by the fluid and the aspect ratio. This explains from another angle why P-wave anisotropy is very sensitive to fluid-saturated fractures, and shows that different behaviour of these parameters may be used to determined whether the fractures are dry or saturated.

6.4.3 Reduced equations

The reduced equations are now derived in terms of Thomsen parameters for the weakly fractured TIH medium. Since the vertical plane $(x_2 - x_3)$ parallel to the fracture strike is an isotropic plane, P- and SV-waves propagating in this plane is determined by the background velocities α_b and β_b, but the SH-wave (the slow wave) propagating in this plane is determined by the velocity $(1 - \gamma)\beta_b$. Thus only wave propagation in the $(x_1 - x_3)$ plane perpendicular to the fracture strike is considered. Therefore the velocities α and β, the elastic constants C_{kl}, and other relevant variables such as ρ', ζ_P and ζ_S, equations (D.11) and (D.29) need to be expressed in terms of the Thomsen parameters.

The velocities α and β in the $(x_1 - x_3)$ plane of the TIH medium can be written

as:

$$\begin{aligned} \alpha &= \alpha_b(1+\delta\sin^2 i\cos^2 i+\epsilon\cos^4 i-\epsilon), \\ \beta &= \beta_b\left(1+\frac{\alpha_0^2}{\beta_0^2}(\epsilon-\delta)\sin^2 j\cos^2 j-\gamma\right), \end{aligned} \tag{6.12}$$

which yield,

$$\begin{aligned} \frac{\Delta\alpha}{\alpha} &= \frac{\Delta\alpha_b}{\alpha_b}+(\delta_2-\delta_1)\sin^2 i\cos^2 i+(\epsilon_2-\epsilon_1)(\cos^4 i-1), \\ \frac{\Delta\beta}{\beta} &= \frac{\Delta\beta_b}{\beta_b}+\left(\frac{\alpha_b^2}{\beta_b^2}(\epsilon_2-\epsilon_1-\delta_2+\delta_1)\sin^2 j\cos^2 j-\gamma_2+\gamma_1\right), \end{aligned} \tag{6.13}$$

where ϵ_k, δ_k and γ_k $(k=1,2)$ are the corresponding Thomsen parameters for the upper $(k=1)$, and lower $(k=2)$ medium.

Following equations (6.8) and (6.10), the relevant TIH elastic constants and their changes across the interface can be written as:

$$\begin{aligned} C_{11} &= \rho(1-2\epsilon)\alpha_b^2; \quad C_{33}=\rho\alpha_b^2; \quad \frac{\Delta C_{33}}{C_{33}}=\frac{\Delta\rho}{\rho}+2\frac{\Delta\alpha_b}{\alpha_b}; \\ C_{55} &= C_{66}=\rho(1-2\gamma)\beta_b^2; \quad \frac{\Delta C_{55}}{C_{55}}=\frac{\Delta\rho}{\rho}+2\frac{\Delta\beta_b}{\beta_b}-2(\gamma_2-\gamma_1). \end{aligned} \tag{6.14}$$

Other relevant variables ρ', $\Delta\rho'$, $\Delta\zeta_P$ and $\Delta\zeta_S$ can be written as:

$$\begin{aligned} \rho' &= \rho\left[1+\frac{\alpha_b^2}{2\beta_b^2}(2\epsilon-\delta)-2\frac{\alpha_b^2}{\beta_b^2}(\epsilon-\delta)\sin^2 j\cos^2 j\right] \\ \frac{\Delta\rho'}{\rho'} &= \frac{\Delta\rho}{\rho}+\frac{\alpha_b^2}{2\beta_b^2}(2\epsilon_2-2\epsilon_1-\delta_2+\delta_1)-2\frac{\alpha_b^2}{\beta_b^2}(\epsilon_2-\epsilon_1-\delta_2+\delta_1)\sin^2 j\cos^2 j \end{aligned} \tag{6.15}$$

and

$$\begin{aligned} \Delta\zeta_P &= \frac{\alpha_b^2}{\alpha_b^2-\beta_b^2}[(\delta_2-\delta_1-2\epsilon_2+2\epsilon_1)-2(\delta_2-\delta_1-\epsilon_2+\epsilon_1)\sin^2 i]\cos^2 i; \\ \Delta\zeta_S &= \frac{\alpha_b^2}{\alpha_b^2-\beta_b^2}[(\delta_2-\delta_1-2\epsilon_2+2\epsilon_1)-2(\delta_2-\delta_1-\epsilon_2+\epsilon_1)\sin^2 j]\cos^2 j. \end{aligned} \tag{6.16}$$

Substituting equations (6.12) to (6.16) into equations (6.4) to (6.7) yields,

$$\begin{aligned} r_{qPqP} &= r_{PPb} + \frac{1}{2}\left[\delta_2 - \delta_1 - 2\epsilon_2 + 2\epsilon_1 + \frac{8\beta_b^2}{\alpha_b^2}(\gamma_2 - \gamma_1)\right]\sin^2 i \\ &- \frac{1}{2}(\epsilon_2 - \epsilon_1)\sin^2 i \tan^2 i; \end{aligned} \tag{6.17}$$

$$\begin{aligned} r_{qPqS} &= r_{PSb} + \frac{\sin i}{2\cos j}\left[\frac{4\beta_b}{\alpha_b}(\gamma_2 - \gamma_1)\cos i \cos j + (\delta_2 - \delta_1 - 2\epsilon_2 + 2\epsilon_1)\sin^2 i\right. \\ &- \left.\frac{4\beta_b^2}{\alpha_b^2}(\gamma_2 - \gamma_1)\sin^2 i + 2(\epsilon_2 - \epsilon_1 - \delta_2 + \delta_1)\sin^4 i\right] \\ &+ \frac{1}{2}\left(\frac{\sin i}{\cos j} - \frac{\sin j}{\cos i}\right)\Delta\zeta_P; \end{aligned} \tag{6.18}$$

$$\begin{aligned} r_{qSqP} &= r_{SPb} + \frac{\sin j}{2\cos i}\left[\frac{\alpha_b}{\beta_b}(\delta_2 - \delta_1 - 2\epsilon_2 + 2\epsilon_1)\cos i \cos j\right. \\ &+ \frac{4\beta_b}{\alpha_b}(\gamma_2 - \gamma_1)\cos i \cos j - 4(\gamma_2 - \gamma_1)\sin^2 j \\ &+ \left.\frac{2\alpha_b^2}{\beta_b^2}(\epsilon_2 - \epsilon_1 - \delta_2 + \delta_1)\sin^2 j \cos^2 j\right] + \frac{1}{2}\left(\frac{\sin j}{\cos i} - \frac{\sin i}{\cos j}\right)\Delta\zeta_S; \end{aligned} \tag{6.19}$$

$$\begin{aligned} r_{qSqS} &= r_{SSb} - \frac{1}{2}\frac{\alpha_b^2}{\beta_b^2}(\delta_2 - \delta_1 - \epsilon_2 + \epsilon_1)\sin^2 j \\ &+ \frac{1}{2}(\gamma_2 - \gamma_1)(1 - 7\sin^2 j + \sin^2 j \tan^2 j), \end{aligned} \tag{6.20}$$

where r_{PPb}, r_{PSb}, r_{SPb} and r_{SSb} are the isotropic reflectivities controlled by the background velocities α_b, and β_b and their associated changes $\Delta\alpha_b$ and $\Delta\beta_b$ across the interface, as defined in equations (6.23) to (6.26) which replace α_0 and β_0 with α_b and β_b.

6.5 Isotropy and TIV media

The isotropic reflectivities can often be used as a reference point for studying anisotropic behaviour. The reflection coefficients for a TIV medium in terms of Thomsen's parameters agrees with previous studies (Rüger, 1995).

6.5.1 Isotropic media

Denote the average density, P- and S-wave velocities of the upper and lower isotropic medium as ρ_0, α_0 and β_0, and their corresponding changes as $\Delta\rho_0$, $\Delta\alpha_0$ and $\Delta\beta_0$. The relevant isotropic elastic constants and their changes across the interface can be written as:

$$C_{33} = \rho_0\alpha_0^2; \quad \frac{\Delta C_{33}}{C_{33}} = \frac{\Delta Z_P}{Z_P} + \frac{\Delta\alpha_0}{\alpha_0}; \tag{6.21}$$

$$C_{55} = G = \rho_0\beta_0^2; \quad \frac{\Delta C_{55}}{C_{55}} = \frac{\Delta G}{G} = \frac{\Delta Z_S}{Z_S} + \frac{\Delta\beta_0}{\beta_0}, \tag{6.22}$$

where $Z_P = \rho_0\alpha_0$, $Z_S = \rho_0\beta_0$, and $G = \rho_0\beta_0^2$ are used as P-wave impedance, S-wave impedance and shear modulus.

Substituting equations (6.21) and (6.22) into equations (6.4) to (6.7), and using the relevant simplifications for isotropic media ($\rho' = \rho_0$, $\Delta\zeta_P = \Delta\zeta_S = 0$, $\alpha = \alpha_0$ and $\beta = \beta_0$), yields,

$$r_{PP0} = \frac{1}{2}\frac{\Delta Z_P}{Z_P} + \frac{1}{2}\left(\frac{\Delta\alpha_0}{\alpha_0} - \frac{4\beta_0^2}{\alpha_0^2}\frac{\Delta G}{G}\right)\sin^2 i + \frac{1}{2}\frac{\Delta\alpha_0}{\alpha_0}\sin^2 i\tan^2 i \tag{6.23}$$

$$r_{PS0} = \frac{\sin i}{\cos j}\left(-\frac{1}{2}\frac{\Delta\rho_0}{\rho_0} - \frac{\beta_0}{\alpha_0}\frac{\Delta G}{G}\cos i\cos j + \frac{\beta_0^2}{\alpha_0^2}\frac{\Delta G}{G}\sin^2 i\right) \tag{6.24}$$

$$r_{SP0} = \frac{\sin j}{\cos i}\left(-\frac{1}{2}\frac{\Delta\rho_0}{\rho_0} - \frac{\beta_0}{\alpha_0}\frac{\Delta G}{G}\cos i\cos j + \frac{\Delta G}{G}\sin^2 j\right) \tag{6.25}$$

$$r_{SS0} = -\frac{1}{2}\frac{\Delta Z_S}{Z_S} - \frac{1}{2}\left(\frac{\Delta\beta_0}{\beta_0} - 4\frac{\Delta G}{G}\right)\sin^2 j - \frac{1}{2}\frac{\Delta\beta_0}{\beta_0}\sin^2 j\tan^2 j. \tag{6.26}$$

Equations (6.23) to (6.26) agree fully with Aki and Richards (1980).

6.5.2 Weak TIV medium

TIV anisotropy often results from a sequence of thin layers (Bush and Crampin, 1991). The procedures to derive the reflection of coefficients for weak TIV media are similar to those for weak fractured TIH media apart from two major variations. The first variation is due to the symmetry axis. The TIV medium has a

vertical symmetry axis. Consequently, the corresponding stiffness tensor is often defined as,

$$\mathbf{C} = \begin{pmatrix} C_{11} & C_{11}-2C_{66} & C_{13} & & & \\ C_{11}-2C_{66} & C_{11} & C_{13} & & \mathbf{0} & \\ C_{13} & C_{13} & C_{33} & & & \\ & & & C_{44} & & \\ & \mathbf{0} & & & C_{44} & \\ & & & & & C_{66} \end{pmatrix}, \tag{6.27}$$

and the corresponding Thomsen parameters are defined as

$$\epsilon = \frac{C_{11}-C_{33}}{2C_{33}}; \quad \delta = \frac{2C_{44}+C_{13}-C_{33}}{C_{33}}; \quad \gamma = \frac{C_{66}-C_{44}}{2C_{44}}. \tag{6.28}$$

Comparing (6.28) with (6.10) shows the interchange of C_{11} and C_{33}, C_{44} and C_{66}, and these interchanges are intended to keep the quantities of Thomsen parameter the same for TIV and TIH.

The second variation in the derivation process is the choice of reference attributes. For a TIV medium, it is convenient to choose the vertical velocities (the velocity along the symmetry axis) for reference purposes, while for fracture-induced TIH medium it is convenient to choose the velocities of the un-fractured background medium. Assuming that the corresponding vertical velocities are α_0 (qP-wave) and β_0 (qS-wave), the velocities α and β can be expressed in terms of ϵ, δ, and γ as (Thomsen, 1986):

$$\alpha = \alpha_0(1+\delta\sin^2 i\cos^2 i+\epsilon\sin^4 i), \quad \text{and} \tag{6.29}$$

$$\beta = \beta_0\left(1+\frac{\alpha_0^2}{\beta_0^2}(\epsilon-\delta)\sin^2 j\cos^2 j\right). \tag{6.30}$$

With these differences in mind, and following the procedures for the TIH medium, the reflection coefficients and a weak TIV material can be derived as

$$r_{qPqP} = r_{PP0}+\frac{1}{2}(\delta_2-\delta_1)\sin^2 i+\frac{1}{2}(\epsilon_2-\epsilon_1)\sin^2 i\tan^2 i; \tag{6.31}$$

$$r_{qPqS} = r_{PS0} + \frac{\sin i}{2\cos j}\left[(\delta_2 - \delta_1)\sin^2 i + 2(\epsilon_2 - \epsilon_1 - \delta_2 + \delta_1)\sin^4 i\right] + \frac{1}{2}\left(\frac{\sin i}{\cos j} - \frac{\sin j}{\cos i}\right)\Delta\zeta_P \tag{6.32}$$

$$r_{qSqP} = r_{SP0} + \frac{\sin j}{2\cos i}\left[\frac{\alpha_0}{\beta_0}(\delta_2 - \delta_1)\cos i\cos j + 2\frac{\alpha_0^2}{\beta_0^2}(\epsilon_2 - \epsilon_1 - \delta_2 + \delta_1)\sin^2 j\cos^2 j\right] + \frac{1}{2}\left(\frac{\sin j}{\cos i} - \frac{\sin i}{\cos j}\right)\Delta\zeta_S; \tag{6.33}$$

$$r_{qSqS} = r_{SS0} - \frac{1}{2}\frac{\alpha_0^2}{\beta_0^2}(\delta_2 - \delta_1 - \epsilon_2 + \epsilon_1)\sin^2 j, \tag{6.34}$$

where the polarisation deviation is given by

$$\Delta\zeta_P = \frac{\alpha_0^2}{\alpha_0^2 - \beta_0^2}\left[(\delta_2 - \delta_1) - 2(\delta_2 - \delta_1 - \epsilon_2 + \epsilon_1)\sin^2 i\right]\cos^2 i, \tag{6.35}$$

$$\Delta\zeta_S = \frac{\alpha_0^2}{\alpha_0^2 - \beta_0^2}\left[(\delta_2 - \delta_1) - 2(\delta_2 - \delta_1 - \epsilon_2 + \epsilon_1)\sin^2 j\right]\cos^2 j, \tag{6.36}$$

where r_{PP0}, r_{PS0}, r_{SP0} and r_{SS0} are the isotropic reflectivities controlled by the vertical velocities α_0, and β_0 and their associated changes $\Delta\alpha_0$ and $\Delta\beta_0$ across the interface, as defined in equations (6.23) to (6.26).

Equation (6.31) of r_{qPqP} agrees fully with Rüger (1995). Similar to TIH medium, equations (6.31), (6.32), (6.33) and (6.34) show that the TIV anisotropy also has a first order effect on the AVO response for all four modes.

6.5.3 Accuracy of the equations

Equations (6.4), (6.5), (6.6) and (6.7) are sufficiently accurate for relatively strong anisotropy (up to 20% P- and 10% S-wave anisotropy) for the wave propagation in a symmetry plane of orthorhombic media, as shown in Figures 6.2 and 6.3. Figure 6.2 compares the reflection coefficients calculated by equations (6.4) to (6.7) with the numerical results for a TIV/TIV interface with anisotropic parameters and elastic constants shown in Table 6.1.

Medium	$\rho\,(g/cm^3)$	$\alpha_0\,(km/s)$	$\beta_0\,(km/s)$	δ	ϵ	γ
Upper	2.3	2.700	1.574	0.02	0.02	0.00
Lower	2.2	2.300	1.466	0.15	0.20	0.10

Table 6.1: Density ρ, P- and S-wave vertical velocities α_0 and β_0, and Thomsen parameters: δ, ϵ and γ.

For all four reflections, the approximate analytical results (solid lines) agree with the exact numerical results (dotted lines) very well (Figure 6.2). Figure 6.3 compares the reflection coefficients for a TIV/TIH interface, and the upper and lower media are the overburden and 10% fractured materials in Table 6.2. Again, for all four reflections, the overall agreement between the approximate analytical results (solid lines) and the exact numerical results (dotted lines) is acceptable (Figure 6.3), although the accuracy for r_{qPqP} is slightly lower (Figure 6.3a).

Materials	$\rho\,(g/cm^3)$	$\alpha_b\,(km/s)$	$\beta_b\,(km/s)$	ϵ_d	ϵ_{ar}	Content
Overburden	2.3	3.048	1.574	-	-	-
Fractured sand 10%	2.19	2.183	1.502	0.10	0.01	dry

Table 6.2: Elastic parameters of the overburden and the reservoir model. The overburden is assumed with TIV anisotropy ($\delta = 0.02$, $\epsilon = 0.02$ and $\gamma = 0$), and the listed background velocities are the vertical velocities. The columns show the density ρ, the background P- and S-wave velocities α_b and β_b, the fracture density ϵ_d, the aspect ratio ϵ_{ar}, and the fracture content.

The changes in accuracy from Figures 6.2a and 6.2d to Figures 6.3a and 6.3d are due to changes in impedance contrast. In Figure 6.2, the P- and S-wave impedance contrasts are 15% and 7%, while in Figure 6.3 the corresponding contrasts are changed to 28% and 5%. In general, equation (6.4) for qP-wave reflection coefficients is more robust than equation (6.7) for qS-wave reflection

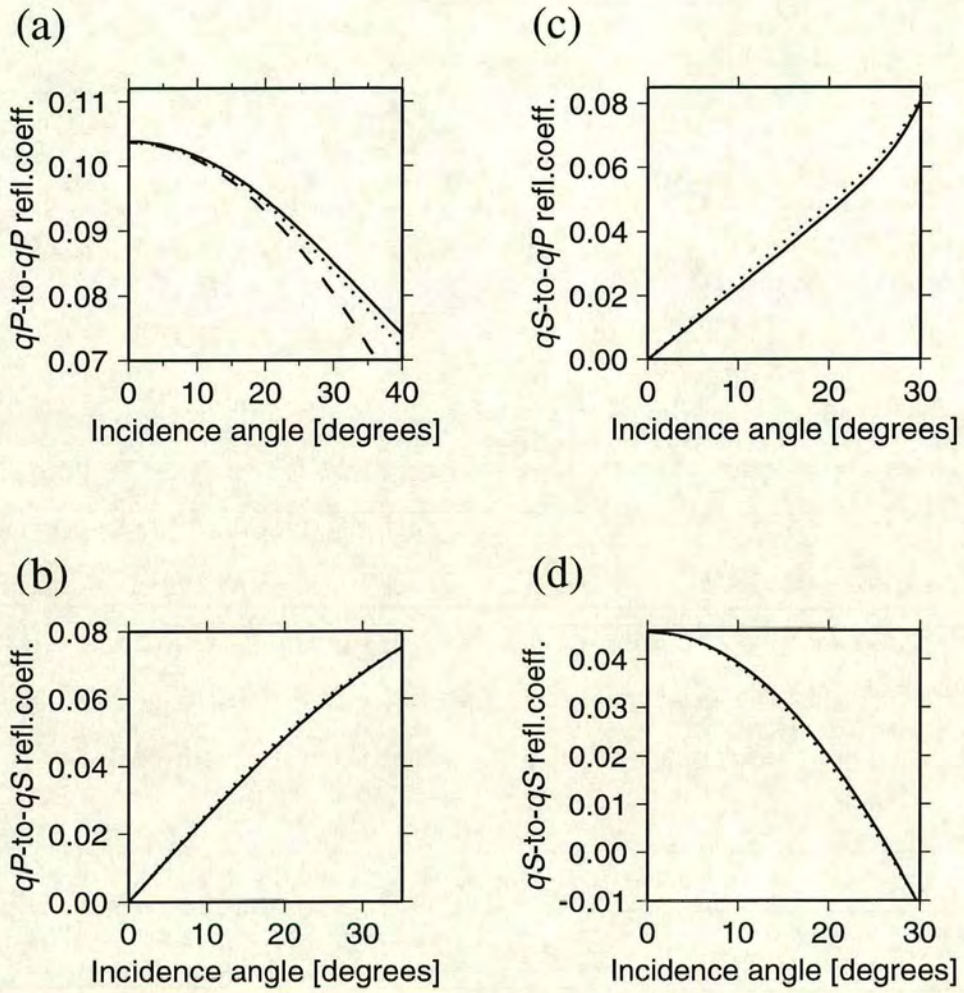

Figure 6.2: Comparison of reflection coefficients calculated using the linearised equations (6.4), (6.5), (6.6) and (6.7) (solid lines) with numerical results (dotted lines) for a TIV/TIV interface shown in Table 1: (a) r_{qPqP}, (b) r_{qPqS}, (c) r_{qSqP} and (d) r_{qSqS}. The dashed line in (a) is result of the calculation based on the equations given by Rüger (1995).

coefficients, in terms of percentage anisotropy and impedance contrast.

Equations (6.4) to (6.7) are expressed in terms of the stiffness tensor and are valid for wave propagation in the symmetry plane of orthorhombic anisotropy with a small impedance contrast.

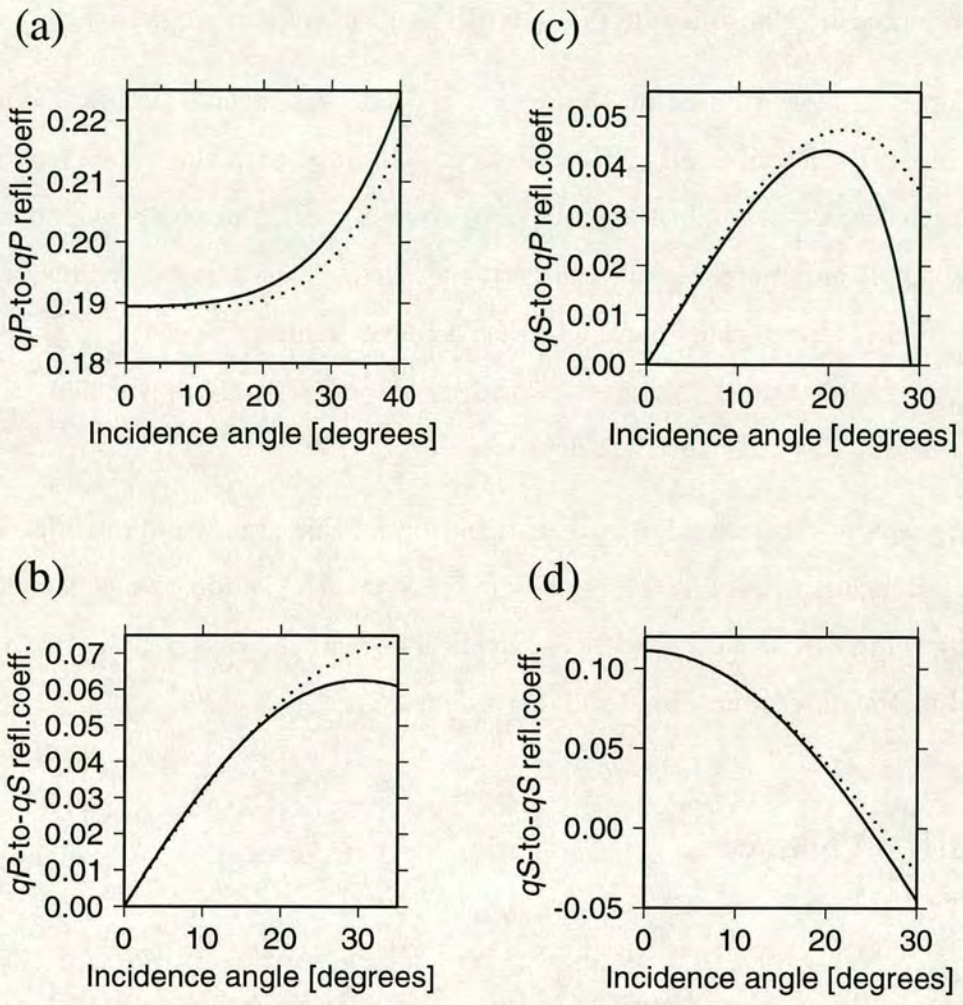

Figure 6.3: As Figure 6.2 but for a TIV/TIH interface. The upper medium is overburden materials with weakly TIV anisotropy and the lower medium is the material with 10% fracture intensity (equivalent 10% effective TIH anisotropy) in Table 6.2.

6.6 The separation approach

One possibility to interpret the difference of the AVO response in the two vertical symmetry planes is due to the orientation of fractures in the medium. As pointed out earlier, different stress regimes can also cause azimuthally varying medium parameters, but in this section I assume that the azimuthal changes are due to fractures. I show that the influence of these fractures or cracks on the reflection coefficient can be separated from the TIV background response if the cracks are

represented by Hudson-style random distributions of thin voids.

The expression is based on the reflection coefficient formulation for orthorhombic media as described in the last section, combined with the weak crack density perturbations to the elastic tensor and consequently the phase velocities. The anisotropic parameter γ can be directly measured in the vertical symmetry planes of a TIH medium. This parameter has a linear relationship with the crack density, and can thus characterise the material. Numerical results show that the perturbation is valid for crack densities up to 0.15.

The separation is valid for weak distributions of thin cracks and introduces a new crack-dependent term in the velocity expression. The validity range is defined by using comparisons with numerical calculations, and shows how a 3D survey could lead to the determination of the crack density.

6.6.1 Theory

The separation process is based upon the formula for the P-P reflection coefficient at the interface between two orthorhombic media (equation 6.4). The aim is to write the equation in the following form

$$r_{qPqP} = r^{TIV}_{qPqP} + r^{crack}_{qPqP}. \tag{6.37}$$

To separate this equation into TIV and crack-dependent parts the crack dependency of the elastic tensor elements is introduced and then the effects of this change in the elastic tensor on the velocity and the deviation term are investigated. The resulting expression is then linearised under the assumption that the anisotropy and the impedance contrast between the two media is weak.

The influence of the cracks on the elastic tensor can be described using a first order approach (Hudson, 1981), which separates the elastic tensor in a background

plus some crack-dependent perturbation

$$c_{ij} = c_{ij}^{background} + c_{ij}^{crack}. \tag{6.38}$$

Because the investigation concentrates on thin cracks for which the aspect ratio is less than 0.001, only the tensor element C_{55} is influenced. The additional contribution of the thin cracks can be expressed as

$$c_{55}^{crack} = -C_{55}^{background} U_{11} \epsilon_c, \tag{6.39}$$

where ϵ_c describes the crack density of the medium and

$$U_{11} = \frac{16}{3} \frac{\alpha_0^2}{3\alpha_0^2 - 2\beta_0^2}, \tag{6.40}$$

the diagonal matrix element introduced by Hudson (1981). This change of C_{55} has a non-negligible effect on the velocities.

In a weak anisotropic medium containing cracks the change in the polarisation deviation and the phase velocities of the P and S wave can be written similar to (Thomsen, 1986)

$$\begin{aligned} \zeta_P &= \zeta_P^{TIV} + \zeta_c, \\ \alpha &= \alpha_0(1 + y_p + y_c), \\ \beta &= \beta_0(1 + y_s + \xi_c), \end{aligned} \tag{6.41}$$

where ζ_c describes the crack contribution to the deviation, y_p and y_s denote the weak TIV anisotropy extension and y_c and ξ_c the crack-related parts. To find out the first order contribution of the cracks on the velocities I insert the changed tensor element

$$C_{55} = C_{55}^{background}(1 - U_{11}\epsilon_c), \tag{6.42}$$

into the equation for the phase velocity in a weak anisotropic medium (Backus, 1965)

$$\begin{aligned}\rho\alpha^2 &= \frac{3(C_{33}+C_{11})+2(C_{13}+2C_{55})}{8} \\ &+ \frac{C_{33}-C_{11}}{2}\cos(2\phi) \\ &+ \frac{C_{33}+C_{11}-2(C_{13}+2C_{55})}{8}\cos(4\phi). \end{aligned} \tag{6.43}$$

If only the C_{55} contributions are considered

$$\begin{aligned} y_c &= -\frac{1}{2}\frac{\beta_0^2}{\alpha_0^3}U_{11}\epsilon_c \sin^2(2i), \\ \xi_c &= -\frac{1}{2\beta_0}U_{11}\epsilon_c \cos^2(2i), \end{aligned} \tag{6.44}$$

where i is the incidence angle. The change of the elastic properties of the two media across the interface is assumed to be small. This weak impedance contrast allows the following perturbation approach for the crack related terms in equation (6.4)

$$\begin{aligned} \frac{\Delta C_{55}}{C_{55}} &= \frac{\Delta C_{55}^{TIV}}{C_{55}} + \Delta\eta_c, \\ \frac{\Delta\alpha}{\alpha} &= \frac{\Delta\alpha_0}{\alpha_0} + \Delta y_p + \Delta y_c, \\ \frac{\Delta\beta}{\beta} &= \frac{\Delta\beta_0}{\beta_0} + \Delta y_s + \Delta\xi_c, \\ \Delta\zeta_P &= \Delta\zeta_P^{TIV} + \Delta\zeta_c, \end{aligned} \tag{6.45}$$

where

$$\begin{aligned} \Delta\eta_c &= -(U_{11}^l\epsilon_c^l - U_{11}^u\epsilon_c^u), \\ \Delta\zeta_c &= 2\frac{\alpha_0^2}{\alpha_0^2-\beta_0^2}\Delta\eta_c\frac{\beta_0^2}{\alpha_0^2}\cos^2 i\cos(2i), \\ \Delta y_c &= \frac{1}{2}\frac{\beta_0^2}{\alpha_0^2}\Delta\eta_c \sin^2(2i). \end{aligned} \tag{6.46}$$

l and u denote the lower and upper layer. Inserting the results of equation (6.41), (6.44), (6.45) and (6.46) into equation (6.4) yields

$$r_{pp}^{crack} = -\frac{1}{2}\Delta y_c + \frac{1}{2}(\Delta y_c - 2\frac{\beta_0^2}{\alpha_0^2}\Delta\eta_c)\sin^2 i + \frac{1}{2}\Delta y_c \sin^2 i \tan^2 i + \frac{1}{2}(1 - \frac{\beta^2}{\alpha^2})\tan^2 i \Delta\zeta_c \quad (6.47)$$

This can be reduced to

$$r_{pp}^{crack} = \frac{\beta_1^2}{\alpha_1^2}(U_{11}^{(2)}\epsilon_c^{(2)} - U_{11}^{(1)}\epsilon_c^{(1)})\sin^2 i. \quad (6.48)$$

If the definition of the Thomsen parameter γ

$$\gamma = \frac{C_{44} - C_{66}}{2C_{44}}, \quad (6.49)$$

for a TIH medium is used as well as the fact that $C_{55} = C_{66}$, I can express the crack parameter $U_{11}\epsilon_c$ in terms of γ

$$\gamma = \frac{1}{2}U_{11}\epsilon_c. \quad (6.50)$$

Inserting equation (6.50) into equation (6.48) the final result is given by

$$r_{pp}^{crack} = 2\frac{\beta_1^2}{\alpha_1^2}(\gamma^{(2)} - \gamma^{(1)})\sin^2 i. \quad (6.51)$$

The importance of this equation is that the crack density has a first order influence on the reflection coefficient. Assuming an un-cracked overburden it may even be possible to invert the data for the anisotropic parameter γ, the parameter which describes the shear wave anisotropy. This can be done by measuring the difference in the *qP-qP* reflection coefficient parallel and perpendicular to the crack strike as suggested by Rüger (1995). The difference in these measurements is given by

$$r_{pp}^{sym} - r_{pp}^{iso} = 2\frac{\beta_1^2}{\alpha_1^2}\gamma^{(2)}\sin^2 i, \quad (6.52)$$

which allows a direct inversion for the anisotropic parameter γ.

6.6.2 Results

To establish the range of validity for equation (6.48) the reflection coefficient is calculated for three different models (Table 6.3), where the media always have a TIV background defined by the Thomsen parameters ϵ, δ and γ. Only the lower medium contains the cracks and they are introduced by altering the elastic tensor elements C_{55} and C_{66} according to the formula. C_{66} has no influence on the analytical expression but for the numerical calculation it has to be taken into account for completeness.

Layer	V_P	V_S	ρ	δ	ϵ	γ	ϵ_c
up 1	3.05	1.83	2.2	0.10	0.10	0.1	0.00
low 1	3.15	1.90	2.3	0.15	0.15	0.1	0.10
up 2	3.05	1.83	2.2	0.10	0.10	0.1	0.00
low 2	3.15	1.90	2.3	0.15	0.15	0.1	0.15
up 3	2.70	1.57	2.3	0.02	0.02	0.0	0.00
low 3	2.30	1.50	2.2	0.15	0.20	0.1	0.10

Table 6.3: Material properties for the modelling in the vertical symmetry plane. The velocities are given in km/s and the density in g/cm^3.

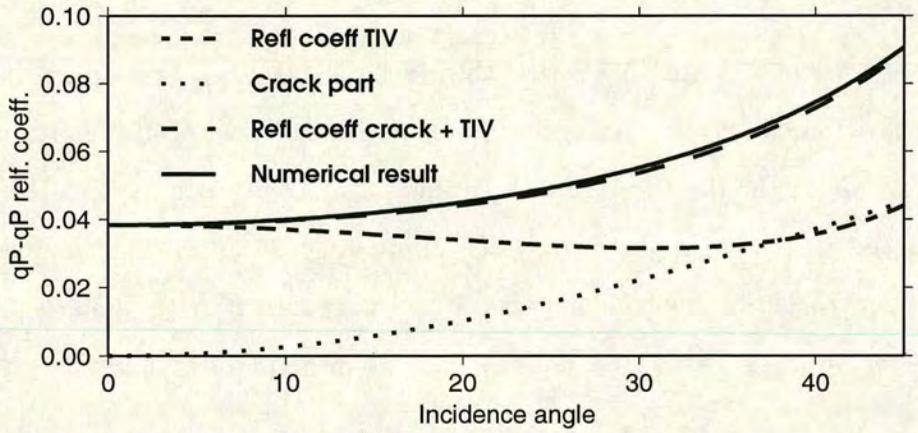

Figure 6.4: Reflection coefficient for the model up1/lower1 (Table 6.3). The numerical result is shown (solid line) together with the approximation and its two parts (TIV and crack).

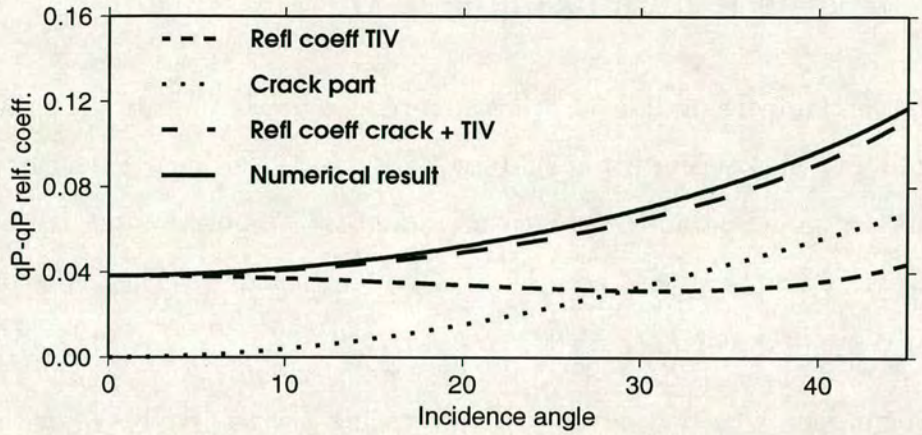

Figure 6.5: The same as Figure 6.4 but for the model up2/lower2.

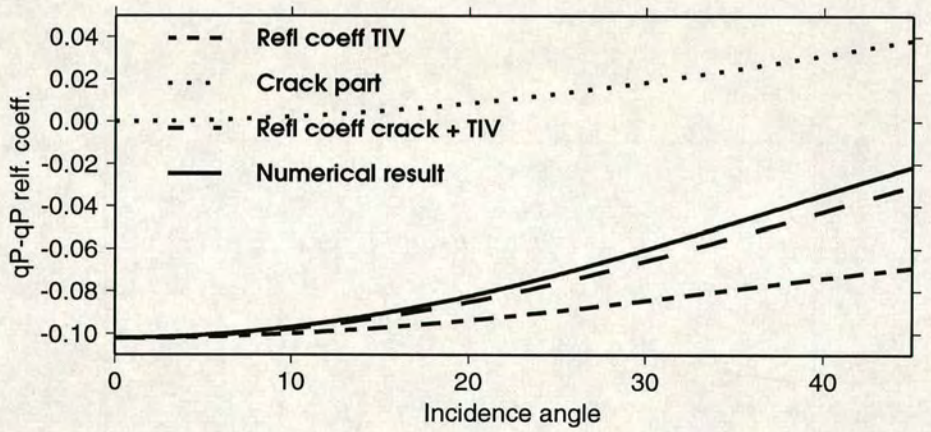

Figure 6.6: The same as Figure 6.4 but for the model up3/lower3.

Figure 6.4 demonstrates that even for high angles of incidence the difference between the separation formula and the numerical results is marginal. An increase in the crack density (Figure 6.5) shifts the highest point of agreement toward lower angles of incidence. The same effect has a change in the impedance contrast as can be seen in Figure 6.6, which reflects that the analytical formula is based on a small impedance contrast.

6.6.3 Synthetic data example of the separation

To verify the claim of equation 6.52 that an inversion for the anisotropic parameter γ is possible if the overburden is isotropic, a synthetic seismogram is calculated based on the model parameters given in Table 6.3. The overburden is isotropic but with the same velocities and density as material up 1. The orthorhombic material is given by low 1.

The calculation is carried out by the ray tracing package ANRAY for the two directions parallel and perpendicular to the fractures. The reflector depth is 500m and 30 geophones are positioned every 50m giving a total profile length of 1500m. Figure 6.7 shows the AVO variation for the complete length of both lines.

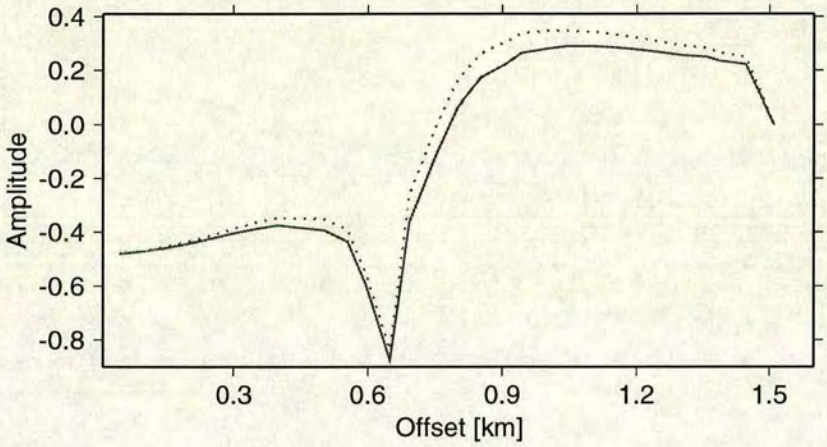

Figure 6.7: Amplitude variation with offset for an isotropic/orthorhombic model with the parameters given in Table 6.3. The solid line shows the direction parallel to the fractures, the dotted one perpendicular to the fractures.

For this synthetic example the velocities α_1 and β_1 as well as the depth of the reflector are assumed to be known. Using this information, the difference between the two directions (Figure 6.8) is inverted for incidence angles smaller than 30 degrees for the shear wave anisotropy of the target layer.

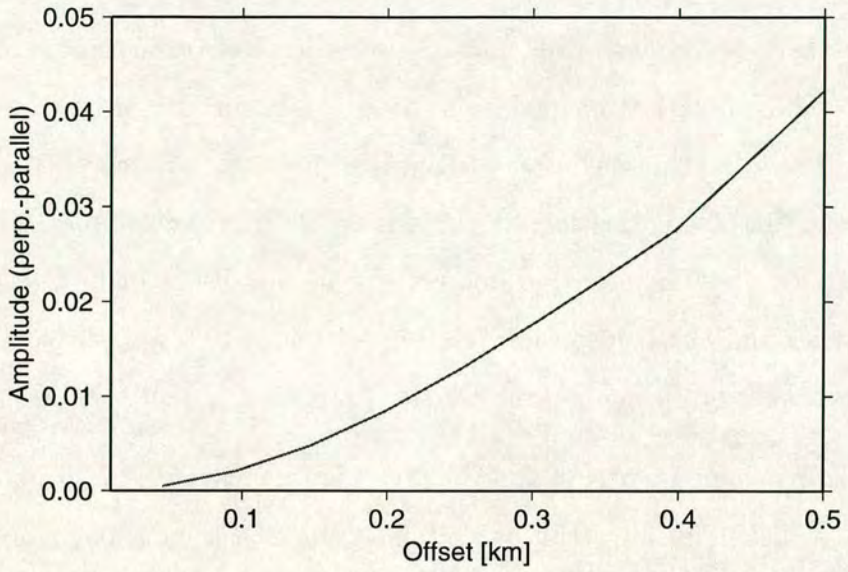

Figure 6.8: Difference of the amplitude variation with offset for the lines perpendicular and parallel to the fracture strike.

A value for γ is calculated for every incidence angle. The final averaged result reads $\gamma_{av} = 0.0938$. As it can be seen from Table 6.3 the input value for γ is 0.1, which shows a very good agreement.

6.7 Discussion and conclusions

Generalised and linearised equations for the tensor reflectivities of all anisotropic single and mixed modes in the vertical symmetry plane of media with monoclinic symmetry, probably the lowest symmetry which can be encountered in seismic wave propagation in rocks, have been developed. Furthermore reduced analytical equations for fracture-induced transversely isotropic media have been presented and in addition, a simple algebraic framework for the derivation of reflection coefficients was established. These expressions are valid for up to 20% P- and 10% S-wave anisotropy, and can be applied to interfaces with up to 20% P- and 10% S-wave impedance contrasts. They may be used as the basis for multicomponent AVO analysis and inversion in anisotropic media. More accurate expressions for

the polarisation deviations of qP and qS waves in anisotropic media have been developed. These polarisation deviations have significant first-order effects on the AVO signatures, and this is contrary to one's impression from travel time studies, where the effects of polarizations deviations on travel time are often negligible. A link between the Thomsen parameters (Thomsen, 1986) of measurable seismic quantities and the Hudson formulation (Hudson, 1981) of physical fracture parameters, equation (6.11) is established.

It was further demonstrated that it is possible to separate the formula for the reflection coefficient in an orthorhombic medium into a TIV and crack-related part. The crack dependent term can be used to invert for the anisotropic parameter γ if the upper medium contains no cracks. For weak crack densities (up to $\epsilon_c = 0.15$ which is the upper limit for realistic materials) the separation agrees with the numerical modelling results.

An analytical expression for the azimuthal behaviour of the P-S reflections could not be established. A numerical investigation (Li, 1998) shows that the azimuthal reflection response of the P-S wave for a shale/gas-sand interface for a range of aspect ratios and crack densities is still elliptical as it is known for the P-P reflection.

CHAPTER 7

Real data example

7.1 Introduction

In order to show the practical applicability of the techniques described in the previous chapters, especially the estimation of the fracture direction, an analysis of a real data set is required. For azimuthal analyses, the data should comprise more than one survey line which intersect in a common point. Saga Petroleum provided such a data set. It has been acquired at different times over a 15 year period as part of an exploration study in the North Sea. These marine seismic data are of high quality and should allow the detection of any anisotropy.

I apply three techniques to the data. They include the interval moveout, the azimuthal change of the NMO velocity, and analyses of the AVO gradient. A description of the data set is followed by the processing sequence and the results.

7.2 The data

The data I use comprise four lines of marine reflection data. Three lines are 2D surveys and one line is part of a much larger 3D survey. These lines intersect at the position where a well was drilled and density and velocity logs are recorded for depths up to 3200m. Figure 7.1 shows the relative position of the lines and

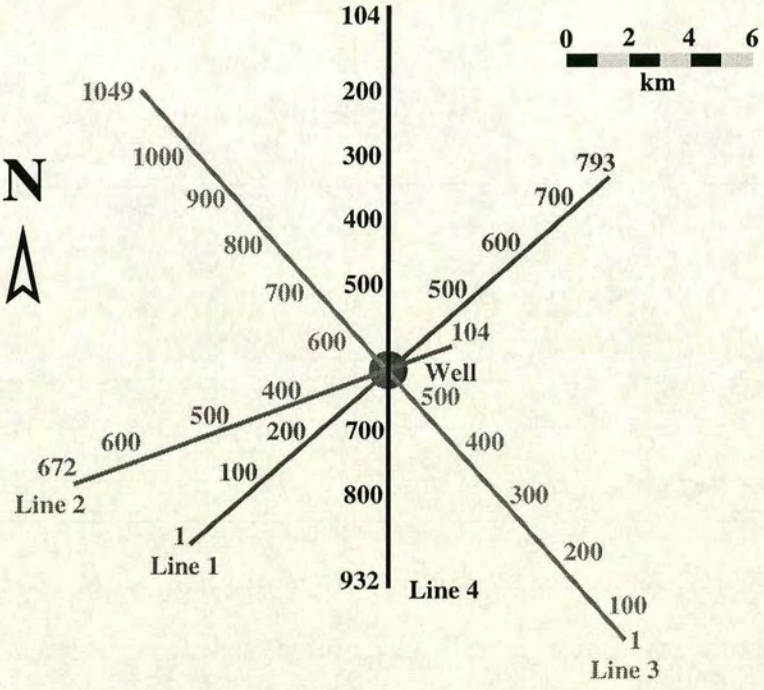

Figure 7.1: Orientation and position of the seismic lines and the well. The numbers along the lines indicate the shot points.

the well location. The numbers alongside each line indicate the shot numbers. All line and well labels are renamed for reasons of confidentiality.

Spreading the data acquisition over more than a decade results in different data quality and acquisition geometry which gives rise to the different spatial resolution. Table 7.1 gives details of the geometry (shots and channels) as well as the spatial resolution (CDP). The improvement in marine streamer technique enabled the recording at receiver intervals of 12.5m as shown in line 4. The high resolution is reflected in the small CDP interval (common depth points) with high fold. The length of the lines varies between 12 and 18km (see Figure 7.1).

This type of acquisition allows in principle the determination of most of the components of the elastic tensor at the well position if it is assumed that the ma-

terial is TI. The vertical velocity is given by the log itself, while the NMO velocity can be determined for every reflector during processing. They are connected to the anisotropy parameter δ. The parameter ϵ can be found from the vertical and horizontal velocity. In this case no shear log is available and also because it is marine data, no shear waves are recorded. The lack of shear information does not allow the determination of C_{44} or C_{66}. For the modelling in the following sections I have to assume a fixed ratio between P and S wave velocity. The main interest in this chapter is to apply the the fracture strike estimation technique to one single layer, not the inversion of the elastic tensor with depth. This problem might be interesting for future studies.

7.3 Processing

The raw data are provided in SEG-Y format. In order to apply the estimation techniques, a basic processing sequence is applied to the data. For the fracture strike estimation it is essential to define the target and to find the shot and CDP gathers for each line near the well location. Because no navigation data are available and the map is not precise enough, a comparison of the stacked sections for each line in the region of the well with a synthetic reflection seismogram is required in order to estimate the FFID and CDP for the well position for each line. This is important, as only for these shots and CDP can any changes in the parameters be attributed to azimuthal changes in the rocks. The following processing steps are applied equally to each line.

7.3.1 Geometry

The raw SEG-Y data, acquired in shot-receiver gathers , contains no geometry information in its trace headers. These information are crucial for any later

	Line 1	Line 2	Line 3	Line 4
Azimuth:				
from North [degrees]	49	250	319	179
Shots:				
Total	793	568	1049	828
Interval [m]	25	25	25	25
Channels per shot:				
Number	60	132	60	240
Interval [m]	50	25	50	12.5
CDP:				
Range	1-852	1-1268	1-1107	1-3560
Maximal fold	60	66	60	30
Interval [m]	25	12.5	25	6.25
Numbers with max fold	60-793	131-1138	60-1049	233-3328
Well position	410	200	550	2250
Recording:				
Sampling interval [ms]	4	2	4	2
Record length [s]	6	7	6	6.144
Velocity analysis:				
Minimum [m/s]	1000	1000	1000	1000
Maximum [m/s]	3500	3500	3500	3500
Sampling interval [m/s]	50	50	50	50

Table 7.1: Shot, receiver and CDP (Common Depth Point) information for the four survey lines shown in Figure 7.1.

processing as they provide the connection between all shots and receivers.

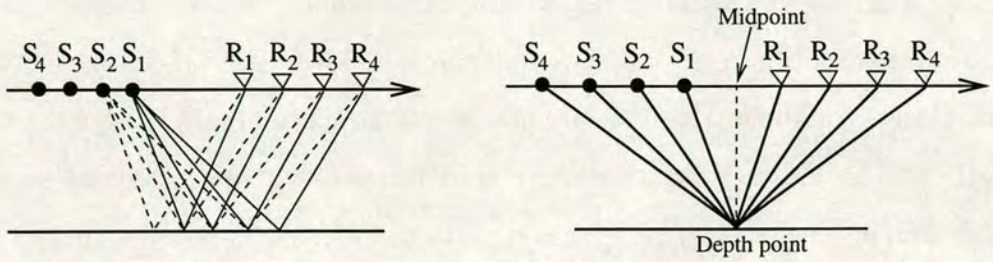

Shot-receiver coordinates

Midpoint-offset coordinates
(CDP gather)

Figure 7.2: On the left, the shot-receiver coordinates are displayed. This is the way seismic data is recorded. S denotes the shot, R the receiver positions. For two different shots (1 and 2) the seismic ray paths are indicated by the solid and the dashed lines. On the right the midpoint-offset domain is displayed. The projection of the midpoint of the gathers is equal to the CDP for a horizontally layered Earth. The subscripts in the right graph indicate corresponding shot and receiver numbers (after Yilmaz, 1987).

For most processing purposes it is important to be able to sort the data into different domains. Such sorting can only be achieved if the proper geometrical information is combined with the data. Figure 7.2 shows the two different data domains.

The lack of any navigation information means that only the observer logs and the survey map (Figure 7.1) could be used to establish the geometry. The map is provided as a hardcopy which is not precise enough and the logs contain the geometry for the line, but all coordinates are relative. Therefore an additional correlation between the lines is needed. I use the horizon calibration to gain this information.

7.3.2 Example gather and muting

Figure 7.3 shows a typical shot gather for line 1. It is characterised by high amplitudes of the first arrivals. These high amplitudes require the application

of a mute. Data are often muted prior to other processing as it reveals lower reflections, especially the ones from the target zone. Figure 7.4 shows the same shot gather as Figure 7.3 after adding the top mute. The reflections at two way travel times of about 3 seconds are now much more prominent than in the original gather. The mute parameters are picked for one or two representative gathers and then applied to all shots for one particular survey line. Even though all the lines were shot in the same area, different acquisition time and equipment require the application of a different mute for each line.

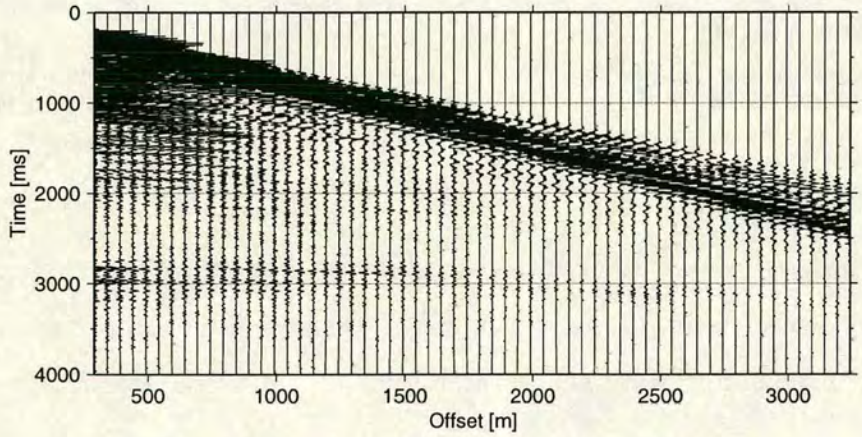

Figure 7.3: Shot gather for line 1, shot no. 410.

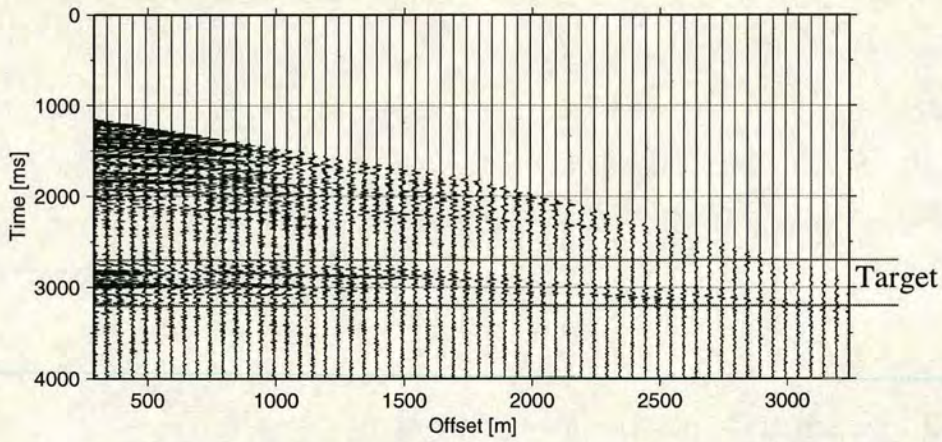

Figure 7.4: Shot gather for line 1, shot no. 410 after the application of a top mute. The two horizontal lines at 2700ms and 3200ms indicate the target area. This area is examined in more detail in the AVO analysis section.

7.3.3 Velocity analysis

A velocity analysis is performed for some selected CDP gathers and the velocity function is then spatially interpolated across the whole line (Yilmaz, 1987). Semblance analysis is often used which measures the signal coherency along the hyperbolas defined by the velocity, offset and travel time. The advantage is that areas of low amplitude coherent signals are magnified and those of high coherency limited to a certain maximum.

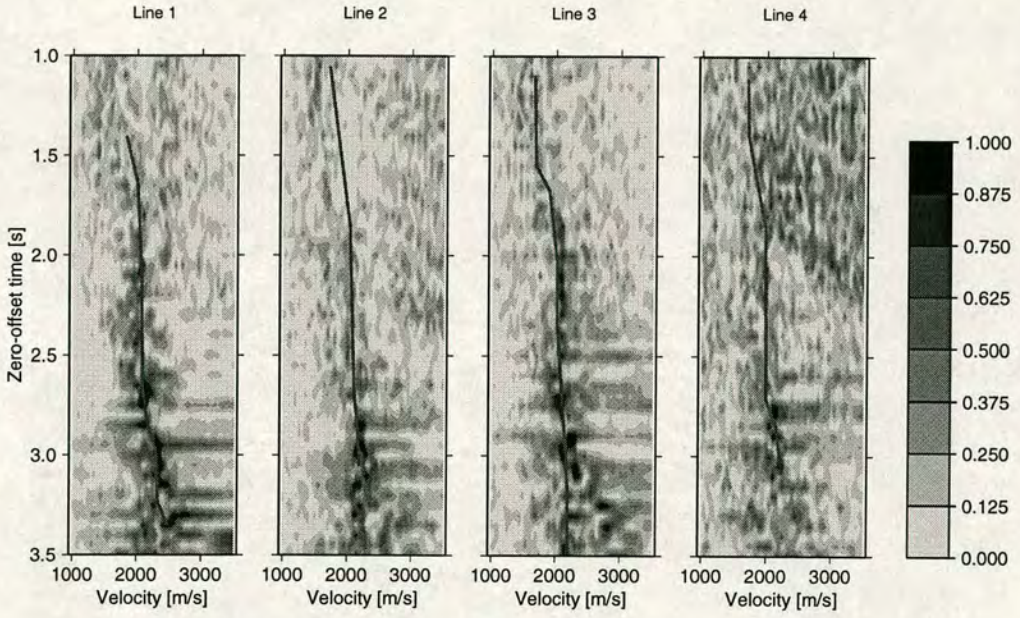

Figure 7.5: Semblance analysis for the CDP gathers at the well location for all lines. Dark areas indicate a high coherency. The lines on top of the semblance plot show the velocity picks. These values were used for the NMO correction as well as the inversion.

Figure 7.5 shows the results of a semblance analysis for the four lines at the well position. Dark areas indicate good agreement between the hyperbola and the data. The fact that all four lines show the same characteristics confirms the choice of these specific CDPs as the ones for the intersection point.

7.3.4 Normal moveout correction (NMO) and stack

The normal moveout correction is designed to remove the offset effects from seismic data. The results of the velocity analysis provide the depth dependent velocity function which is used to flatten an event for each offset. After NMO correction, the traces are stacked which improves the signal to noise ratio. Figures 7.6, 7.7, 7.8 and 7.9 show the stacked sections for all four lines. They are used to determine the target horizons and the CDP for the well location which is indicated by the arrow.

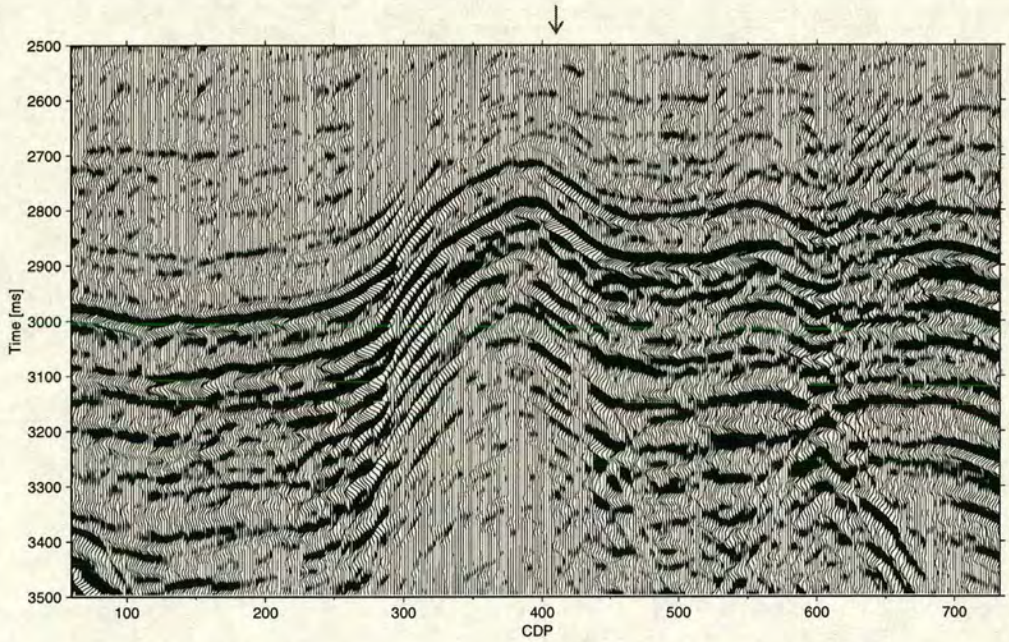

Figure 7.6: Stacked section for line 1 for CDPs with maximum fold.

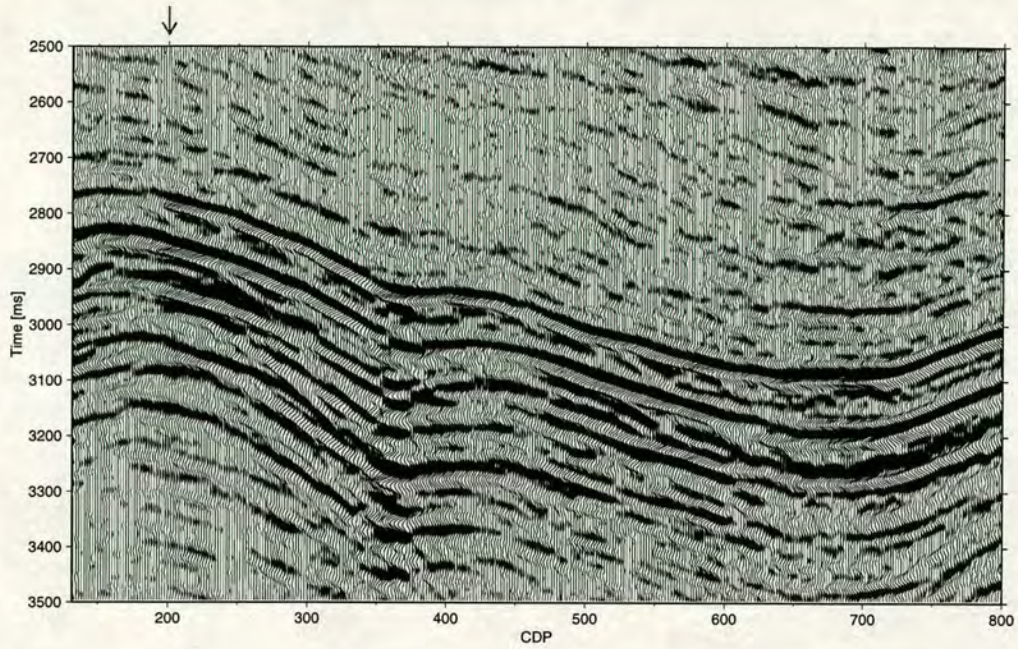

Figure 7.7: Stacked section for line 2 for CDPs with maximum fold.

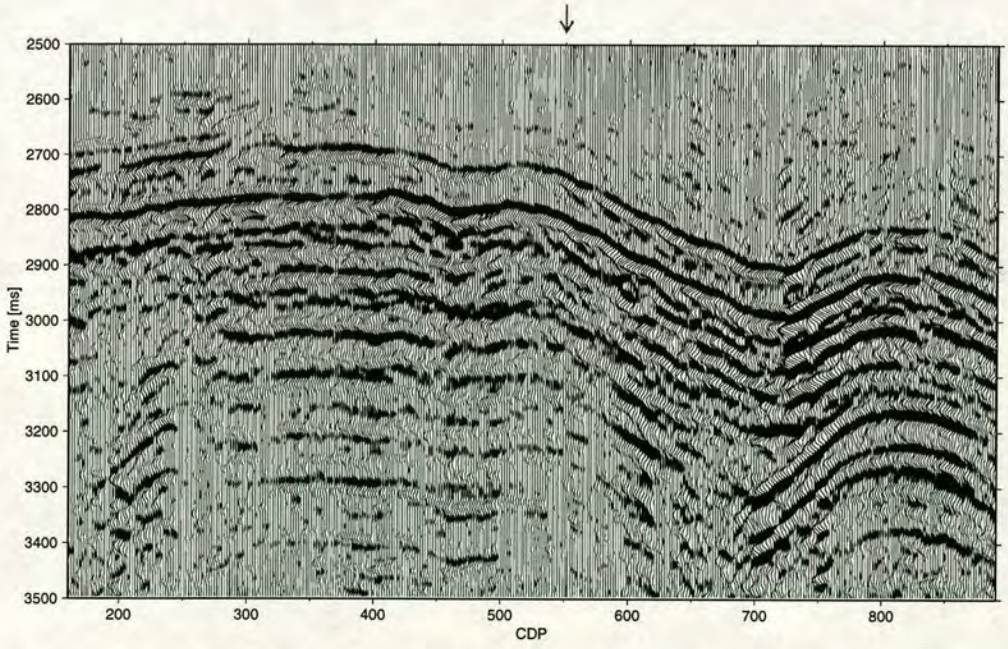

Figure 7.8: Stacked section for line 3 for CDPs with maximum fold.

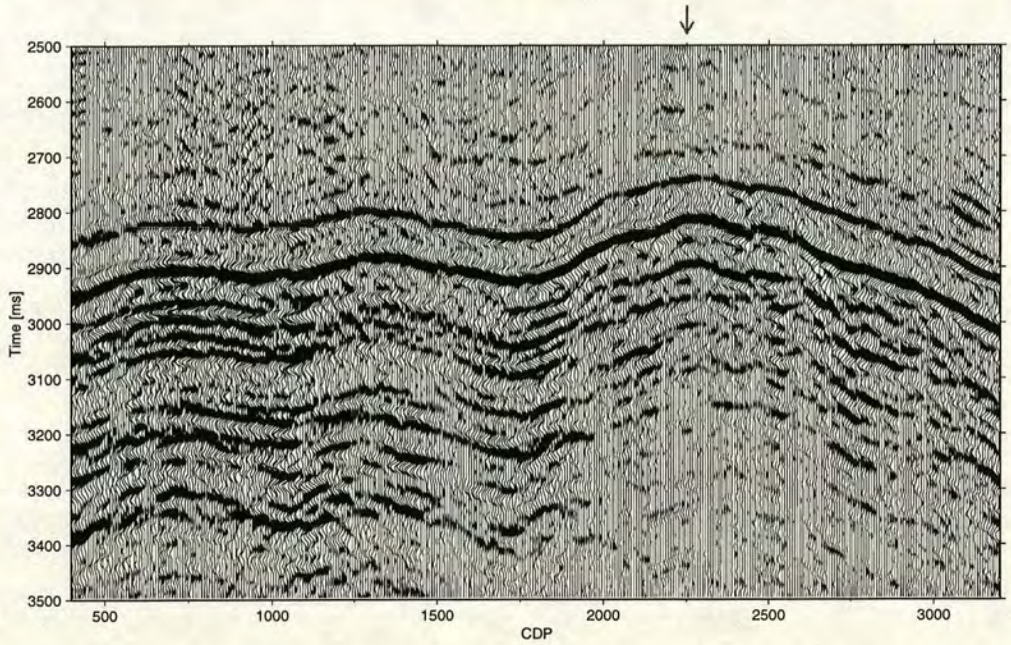

Figure 7.9: Stacked section for line 4 for CDPs with maximum fold.

7.3.5 Well tie

The final horizon calibration and quality control of the choice for the CDP at the well location is done by a comparison between a synthetic seismogram and the stacked section. The synthetic seismogram is calculated on the basis of the log information for the well. Both density and velocity logs are available. Figure 7.10 shows both data for the whole depth range. Note that the logging does not start at the sea bottom but at a depth of 781m. The assumption of a constant velocity and density between the sea bottom and the beginning of the logging can lead to small static shifts.

The model derived from the logs contains only twelve major layers (Figure 7.10, right). The materials are isotropic and a constant V_P/V_S-wave ratio of 1.8 is assumed. The interfaces are placed at depth positions where a visible change in either the velocity or the density is detectable (Figure 7.10, right). Multiple suppression is applied during the calculation of the synthetic seismogram. The

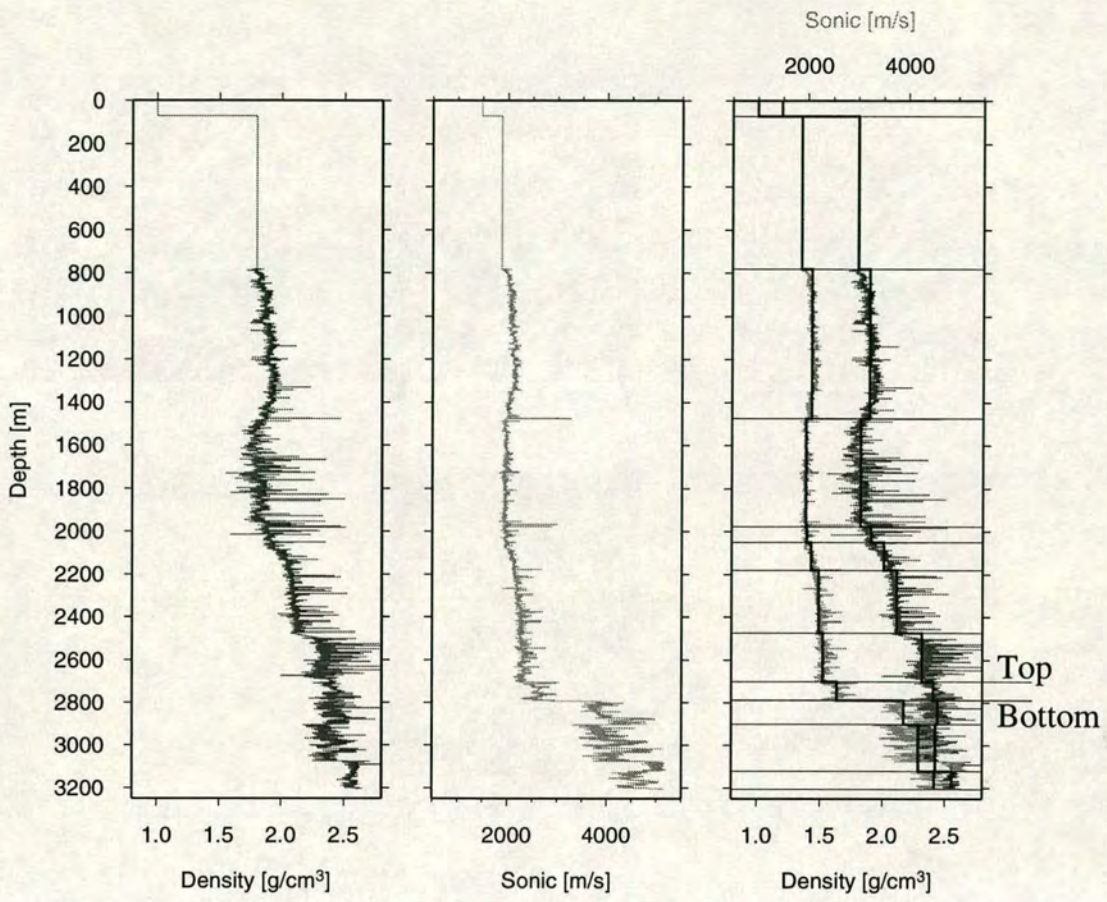

Figure 7.10: Density (left) and velocity (middle) log for the well at the intersection point of the four lines. The right graph shows both logs again. The horizontal lines indicate the interfaces of the model used to calculate the synthetic seismograms and the thick lines on top of the log data show the model parameters derived from the log. The top and bottom of the target are indicated.

area of interest is the thin layer just above the sharp velocity and density increase at a depth of about 2800m.

Figure 7.11 shows shot gathers for all lines for locations near the well. The reflection from the bottom of the target is indicated. It is clear that all lines match well apart from line 2 which shows a mismatch of about 20ms. This can be due to different recording equipment and conditions. Line 2 is the oldest of the four lines. Figure 7.11 (top right) shows line 2 with reversed polarity which could be due to errors during the pre-processing of the data. However, the mistie

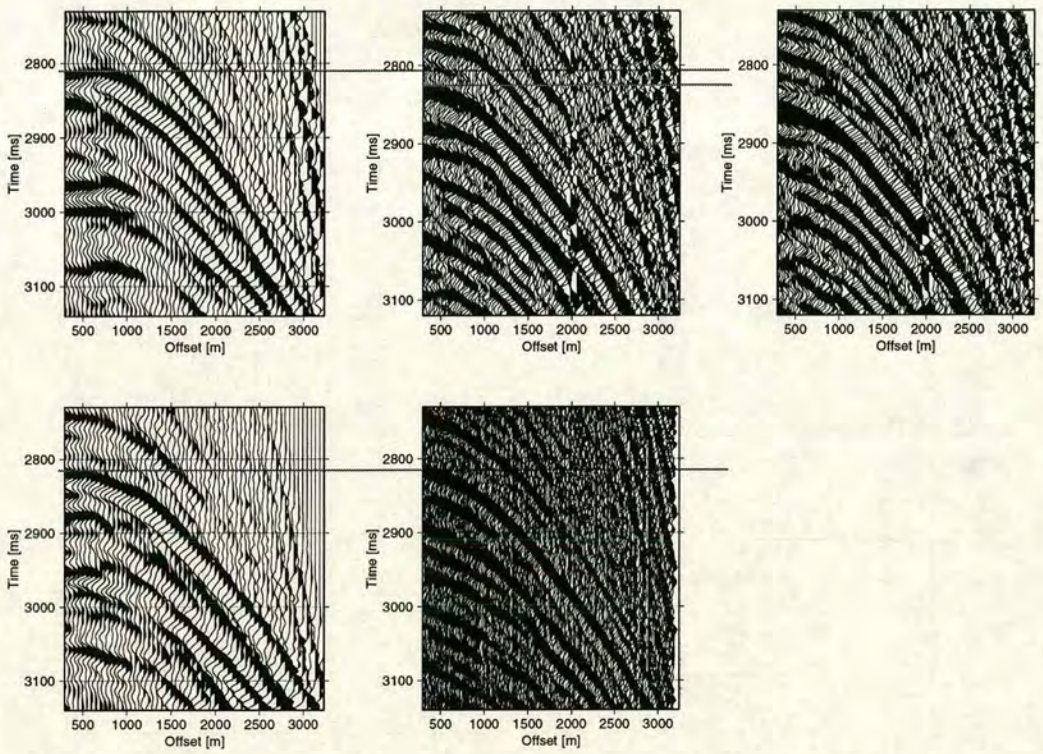

Figure 7.11: Shot gathers for locations near the well for each line. Top left: line 1; Top middle: line 2; Top right: line 2 with reversed polarity, Bottom left: line 3; Bottom right: line 4. The horizontal lines indicate the bottom of the target. Only line 2 (middle) shows a mismatch of about 20ms. The polarity change can not reduce the mistie.

is not smaller than before.

Figure 7.12 shows the zero offset synthetic seismogram together with representative CDP gathers for line 2. The real data is shifted by the 20ms which the shot gathers suggest. The synthetic trace is repeated ten times for clarity. The most important feature is the good agreement of the two sections after the shift for the reflection from the top and the bottom of the target zone as well as the last prominent reflection in the data above the target zone at around 2100ms.

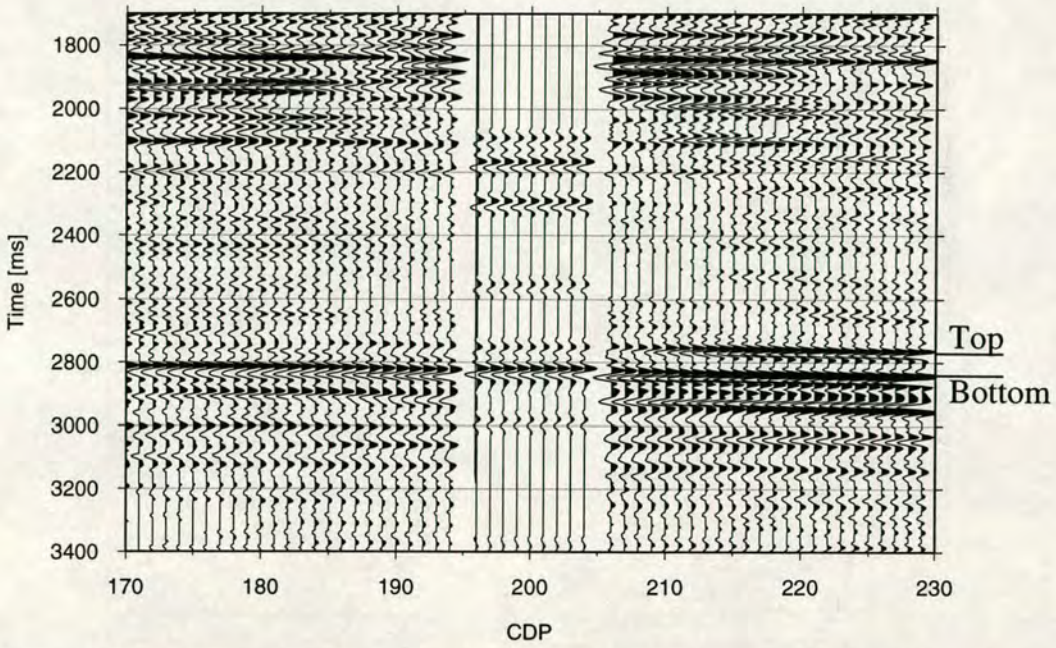

Figure 7.12: Comparison between the synthetic seismogram calculated from the well logs and selected CDP gathers for line 2. The top and the bottom of the target are indicated. The CDP gathers are time shifted by 20ms.

7.4 Geological setting and structural variation

Apart from the log data no further geological information is available, which makes it difficult to describe the geology for the area of study in detail. The data were collected in the Norwegian sector of the Fife field in the Central North Sea. In the UK sector of the Fife field the primary reservoir is sandstone but additionally a fractured chalk sequence is used for its potential as hydrocarbon reservoir. The chalk sequence is known to be fractured (MacBeth et al., 1997). The information provided with the log data shows that the overburden is formed of a uniform sequence of calystone similar to the other study of the area (Mackertich, 1996). It is therefore reasonable to assume that a similar sequence can be found in the area of study. This is one of the reasons why Saga Petroleum provided the data set for fracture analyses.

Structural variations in the target zone can be best identified in the CDP gathers for the well position. Note that the big influence as it can be seen in Figures 7.6,

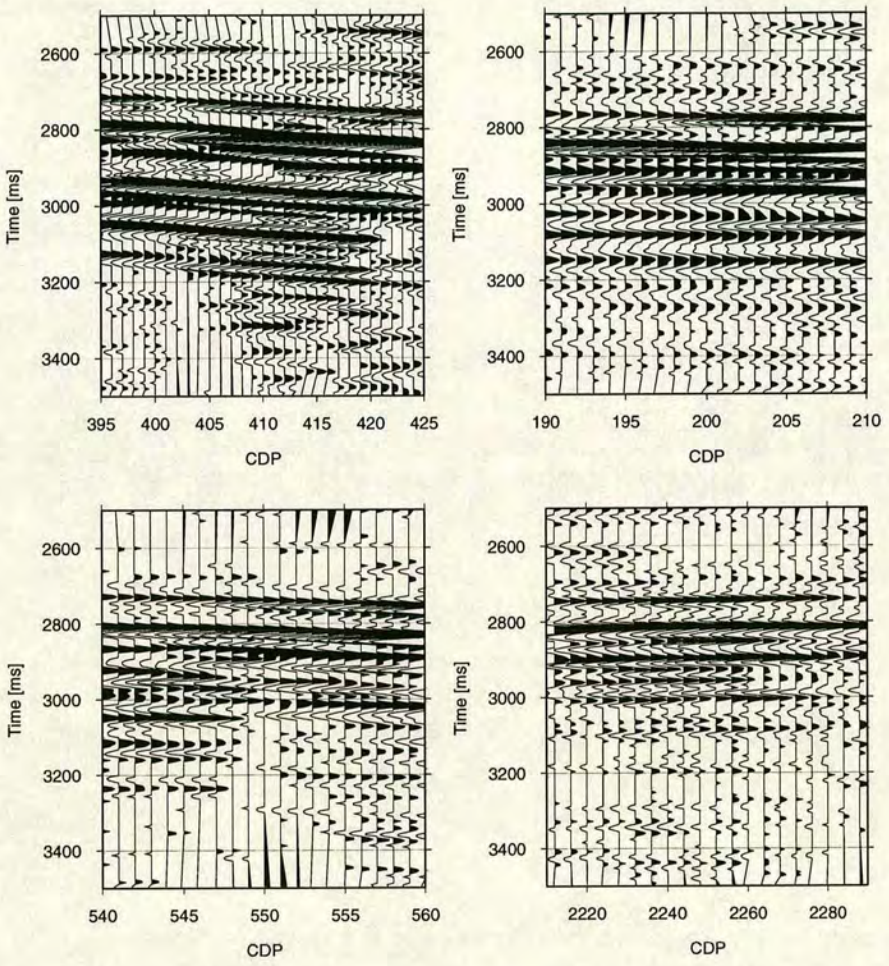

Figure 7.13: Stacked sections for CDP gathers around the well for each line. Top left: line 1; Top right: line 2; Bottom left: line 3; Bottom right: line 4.

7.7, 7.8 and 7.9 is only apparent because each Figure shows the complete line and therefore any structural variation is amplified.

A more precise way is to look at a stacked section for CDP gathers just around the well (Figure 7.13) and to quantify the influence in terms of milliseconds per CDP.

The maximum can be seen in line 1 where a difference of about 20ms is observable. However, synthetic calculations for reflections from a depth of 2600m and for the same offset range as in Figure 7.13 show that a dip of 3 degrees already exceeds the 20ms limit. Therefore the influence of the structure can be ignored.

7.5 Azimuthal moveout and velocity analysis

To estimate directional changes in physical parameters, investigations of the azimuthal behaviour are required. The analyses can focus on kinematic attributes such as the interval travel time or the NMO velocity or dynamic ones such as the AVO gradient which are discussed in section 7.6. This section concentrates on the kinematic parameters.

7.5.1 Moveout for shot gathers

As shown in Chapter 5, the azimuthal variation of the interval travel time allows the estimation of the fracture strike.

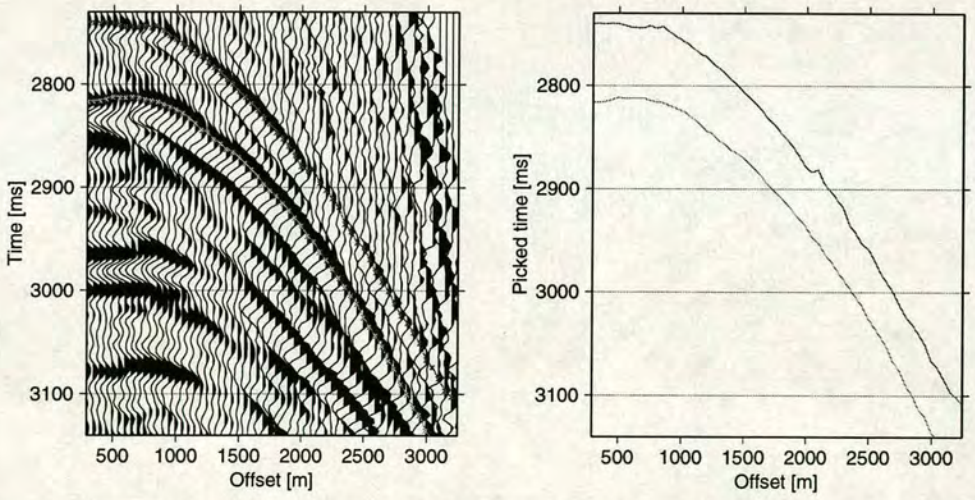

Figure 7.14: Left: Shot gather at the well location for line 1, together with the time picks which are used for the inversion. Right: Picked time versus offset diagram for the top and the bottom of the target zone.

As shown in Chapter 3, in order to calculate the fracture strike, the travel time difference between the top and the bottom of the target is required. Once the top and the bottom horizons for the four lines are established, the travel times for the reflections from the top and the bottom of the target zone are picked manually.

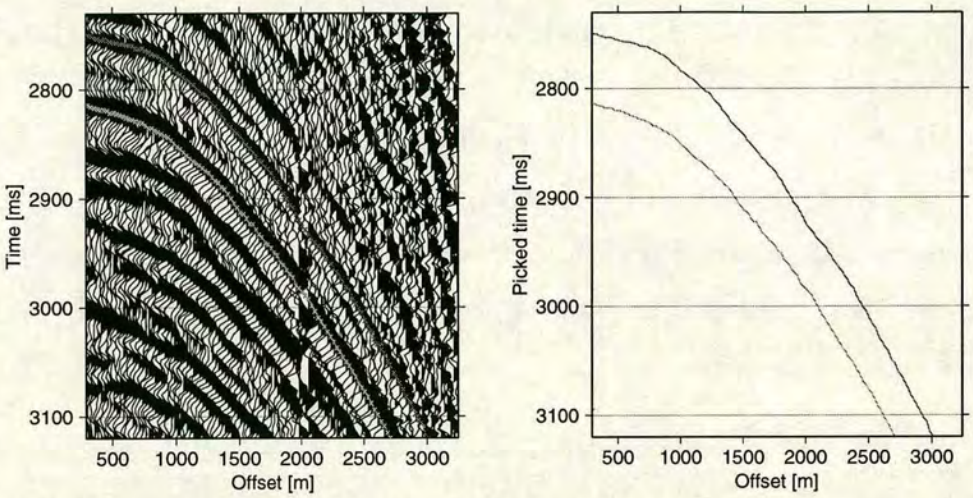

Figure 7.15: Left: Shot gather at the well location for line 2, together with the time picks which are used for the inversion. Right: Picked time versus offset diagram for the top and the bottom of the target zone.

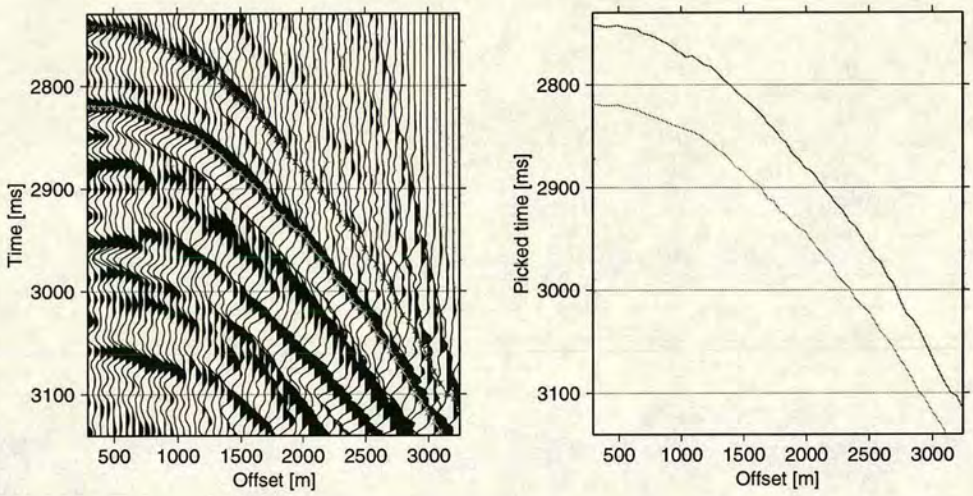

Figure 7.16: Left: Shot gather at the well location for line 3, together with the time picks which are used for the inversion. Right: Picked time versus offset diagram for the top and the bottom of the target zone.

The good quality of the data narrows the error margin for these picks substantially. Only in the far offset the picking accuracy is reduced. These events are muted and not included in the following fracture strike estimation process. Figures 7.14, 7.15, 7.16 and 7.17 show the shot gathers for each line at the well position together with the travel time picks.

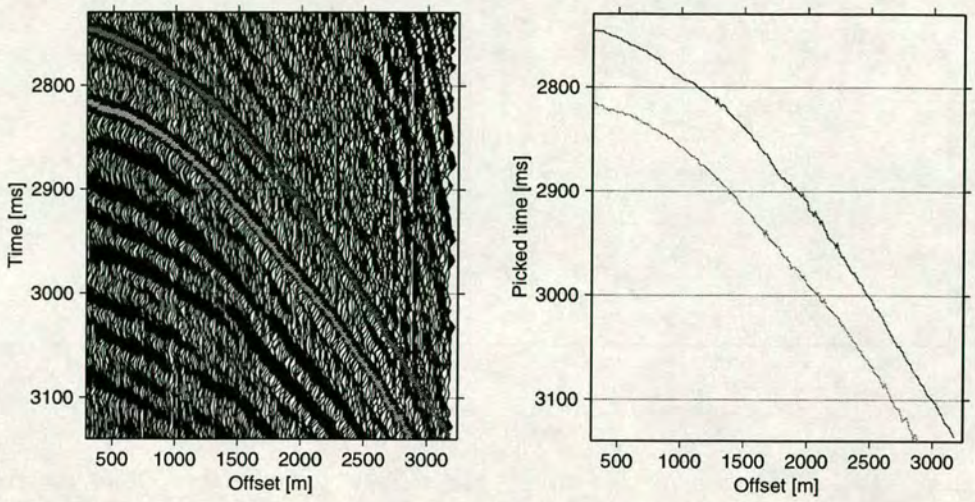

Figure 7.17: Left: Shot gather at the well location for line 4, together with the time picks which are used for the inversion. Right: Picked time versus offset diagram for the top and the bottom of the target zone.

After the pick, the interval travel time is calculated as the difference between the bottom and the top. Figure 7.18 gives the difference for all the four survey lines for the shots at the well position.

A smoothing is necessary for the inversion procedure where one specific value for the difference is required for each line. The smoothing is achieved by a least-squares fit of a high order polynomial to the original data. The result is given on the right side of Figure 7.18.

Equal interval travel times for each line are then used as input parameters for the genetic algorithm. To ensure no dependence on the choice of pick I used several different times. The development of the best fitting parameters for these picks are shown in Figure 7.19.

The fracture strike direction is given by about North 12 degrees East with a TIH anisotropy of about 5%.

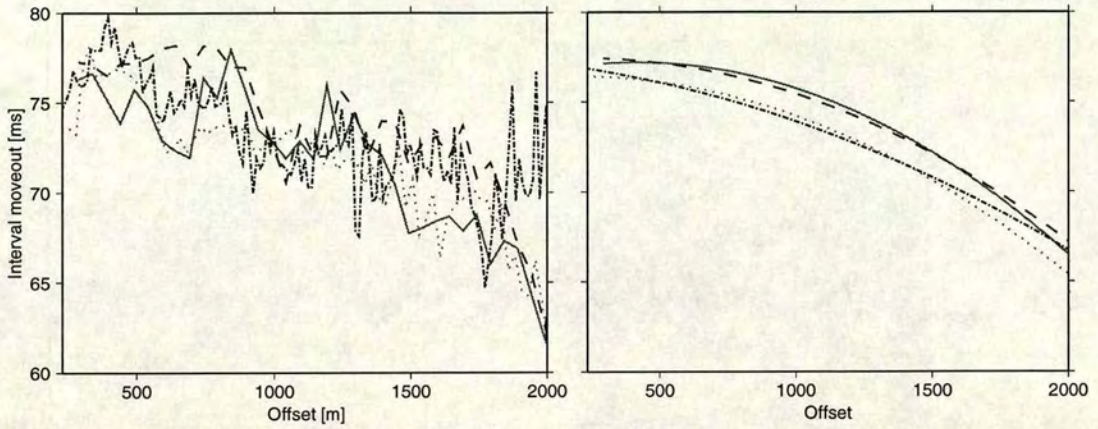

Figure 7.18: Difference in the travel time for the four different lines for the shot gathers at the well location. On the left the original picks and on the right the smoothed results. Line 1: solid, Line 2: dotted, Line 3; dashed, Line 4: dash-dotted.

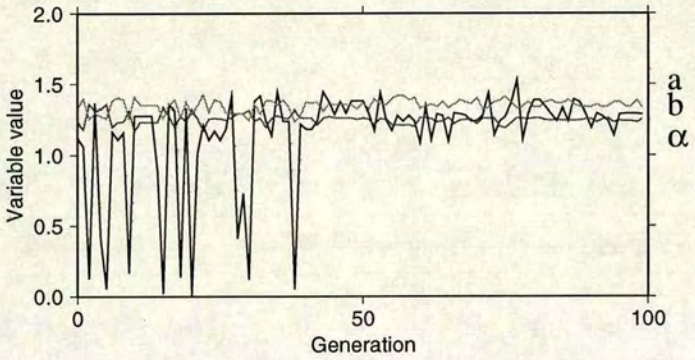

Figure 7.19: Development of the best fitting parameters for the ellipse.

7.5.2 Moveout for CDP gathers

In this section the estimation of the strike direction from the interval travel time is repeated for CDP gathers. The negligible amount of dip present in the data at the well location should lead to very similar results as in the shot gather analysis. Figures 7.20, 7.21, 7.22 and 7.23 show the CDP gathers for each line at the well position together with the travel time picks.

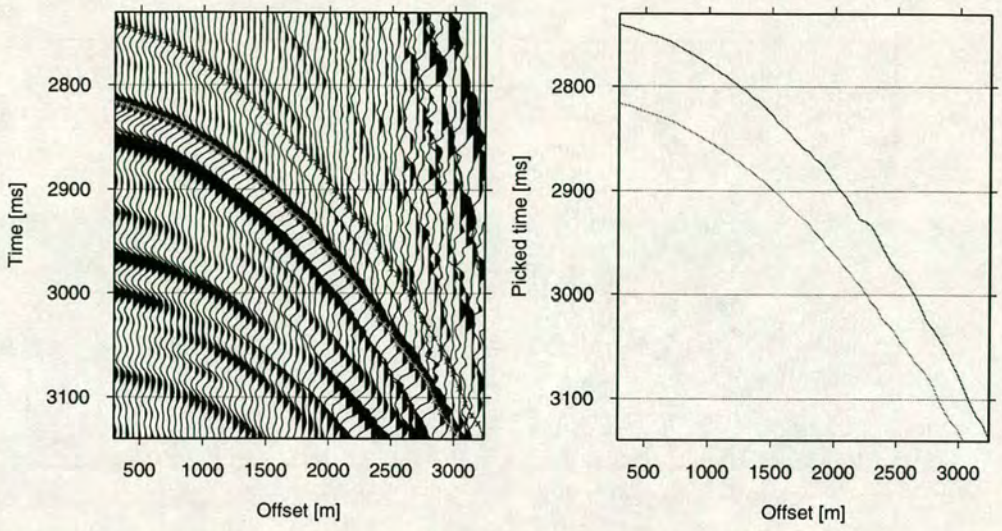

Figure 7.20: Left: CDP gather at the well location for line 1, together with the time picks which are used for the inversion. Right: Picked time versus offset diagram for the top and the bottom of the target zone.

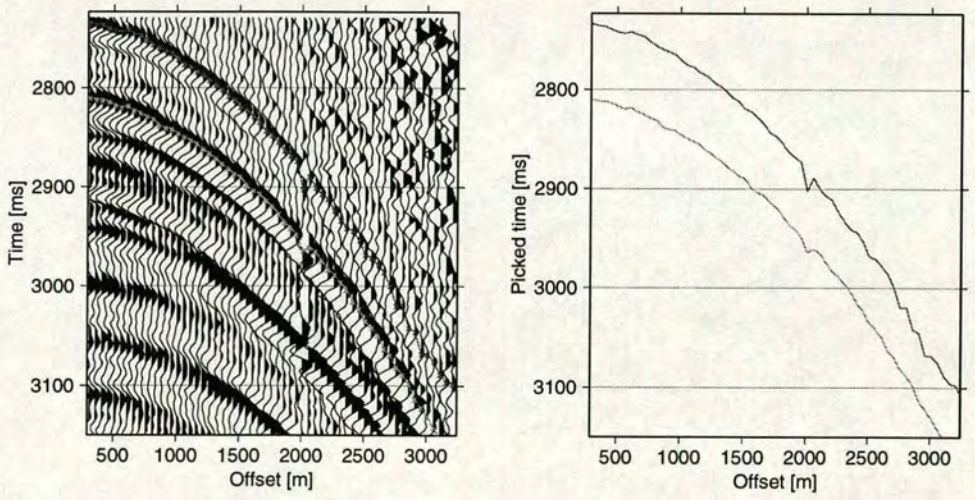

Figure 7.21: Left: CDP gather at the well location for line 2, together with the time picks which are used for the inversion. Right: Picked time versus offset diagram for the top and the bottom of the target zone. The data is shifted by -20ms to equal the vertical travel times for the other lines. This static shift may be due to different recording conditions and equipment. Line 2 is the oldest of the four lines.

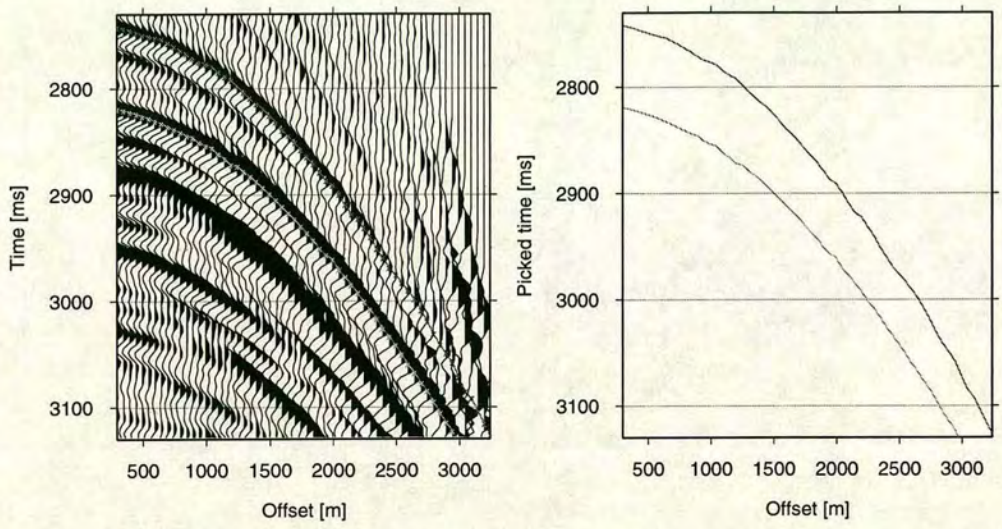

Figure 7.22: Left: CDP gather at the well location for line 3, together with the time picks which are used for the inversion. Right: Picked time versus offset diagram for the top and the bottom of the target zone.

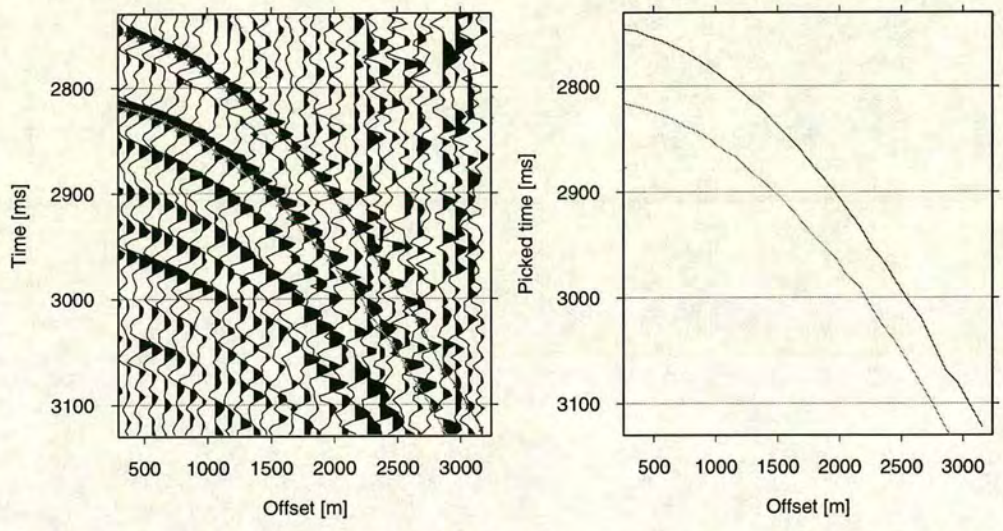

Figure 7.23: Left: CDP gather at the well location for line 4, together with the time picks which are used for the inversion. Right: Picked time versus offset diagram for the top and the bottom of the target zone.

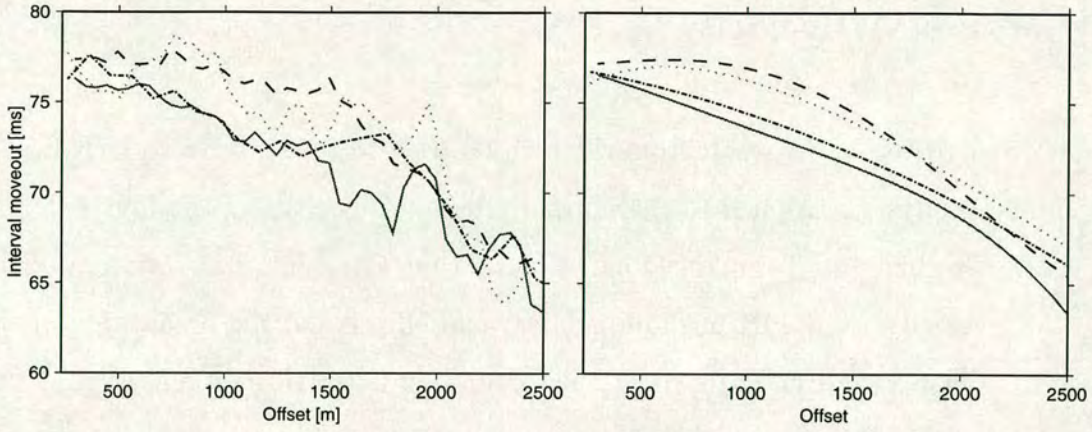

Figure 7.24: Difference in the travel time for the four different lines for the CDPs at the well location. On the left the original picks and on the right the smoothed results. Because of the unreliable time pick in the far offset region, offsets greater than 2000m are not considered in the inversion process.

Figure 7.24 shows the resulting interval travel times and Figure 7.25 gives the result of the GA inversion..

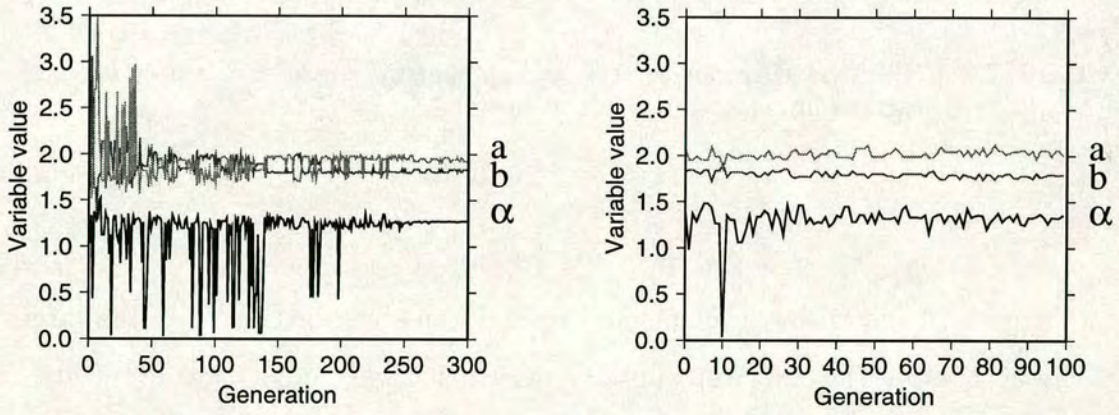

Figure 7.25: Development of the best fitting parameters for the ellipse for two different set of input parameters.

The fracture strike direction is given by about North 10 degrees East with an TIH anisotropy of about 5%. This result is very similar to the shot gather. It confirms that the dip has a negligible influence on the parameter estimation for the well location.

7.5.3 NMO velocity

In order to verify the result from the investigation for the interval travel time, a similar analysis is applied to the normal moveout velocities of the four different lines. Grechka and Tsvankin (1996) showed that the azimuthal variation of the NMO velocity for a TIH medium is always an ellipse and the orientation of the axis indicates the fracture strike. This prediction is tested here for the moveout velocities which are picked for the top and the bottom reflection from the target for the four survey lines (Table 7.2).

	Line 1	Line 2	Line 3	Line 4
V_{NMO} top [m/s]	2068	2061	2058	2065
V_{NMO} bottom [m/s]	2144	2193	2177	2110

Table 7.2: NMO velocities for the top and the bottom of the target area which are used as input for the GA inversion.

Figure 7.26 shows the development of the parameters for the top of the target. It indicates that the anisotropy in the overburden is very small because the length of the half axes of the ellipse a and b are almost equal. This behaviour is reflected in the development of the rotation angle. Because the solution is almost a circle the GA can not find a good solution for the angle.

In contrast, Figure 7.27, which shows the development of the parameters for the bottom of the target verifies the existence of anisotropy. The two half axes are not the same any more. The percentage of anisotropy derived from the inversion is about 3% and the rotation angle is given by North 10° East.

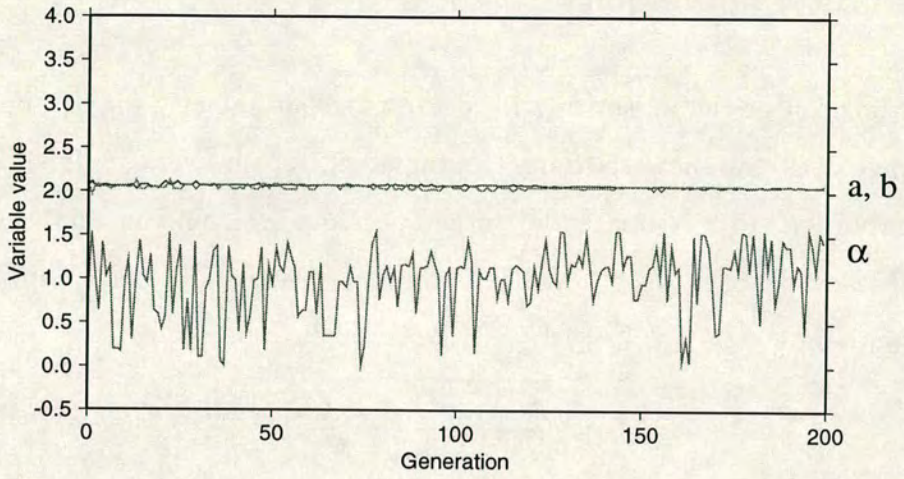

Figure 7.26: Development of the parameters for the best fitting ellipse for the NMO velocity for the top of the target.

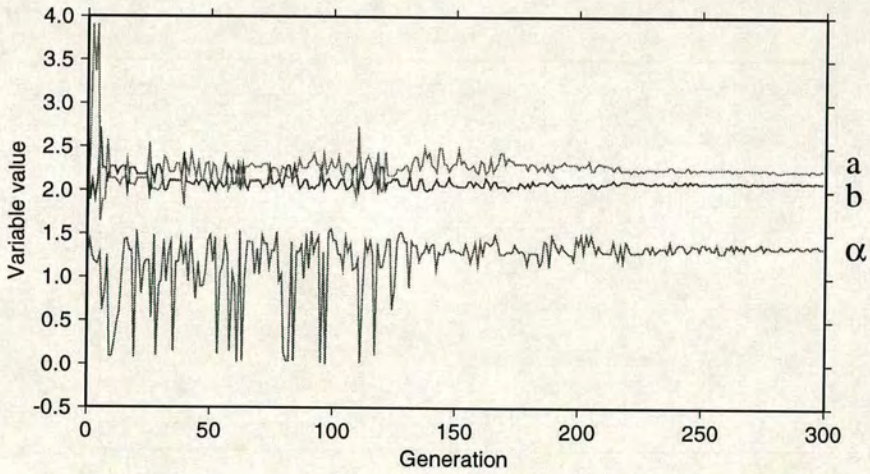

Figure 7.27: Development of the parameters for the best fitting ellipse for the NMO velocity for the bottom of the target. Each generation contains 4000 individuals to increase the spread in the parameter space.

7.5.4 Interval velocity

The estimation of the anisotropy from the moveout velocity for the bottom of the target does not show the target parameters but an average which includes the overburden. To estimate the target parameters itself, an analysis of the interval velocities has to be done. The interval velocities are calculated by the Dix equation

$$v_{int} = \sqrt{\frac{t_{bottom} v_{bottom}^2 - t_{top} v_{top}^2}{t_{bottom} - t_{top}}}. \tag{7.1}$$

The interval velocities are then used as input for the GA. The development of the three parameters is shown in Figure 7.28.

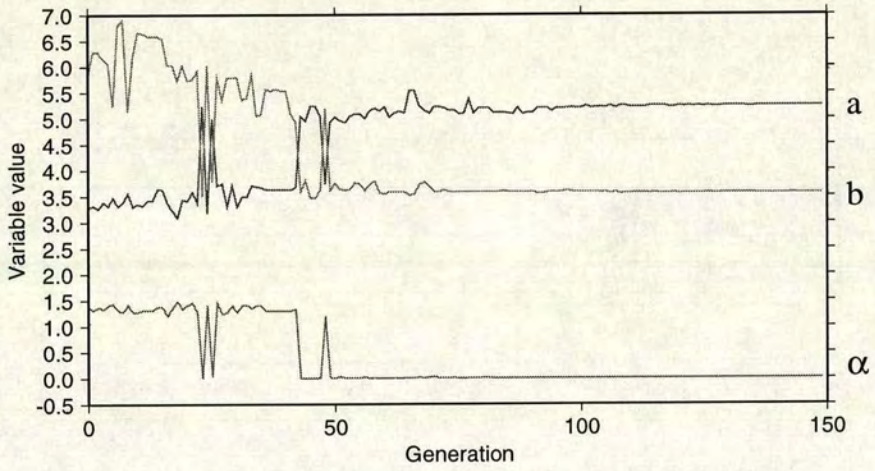

Figure 7.28: Development of the parameters for the best fitting ellipse for the interval velocity.

The unusual high anisotropy (33%) and the fracture strike of $\alpha = 0$ are due to two factors. First, the estimation of the interval velocity with the Dix equation produces errors especially for thin layers. Secondly Al-Dajani and Alkhalifah (1998) have shown that a reliable estimation is based upon the target thickness, the absolute travel time, the error which is allowed for the velocity estimation

and the expected velocity anisotropy. It can be expressed in the following form

$$\frac{\Delta t}{t} \geq \frac{\text{velocity error \%}}{\text{velocity anisotropy \%}}. \tag{7.2}$$

This means that for a velocity error of 4% and a 40% velocity anisotropy for a target at the time depth of 2810ms, the thickness in time should be at least 281ms. But because the target zone in the data set is only 85ms it is clear that the percentage of anisotropy and the strike direction can not be resolved confidently from the interval velocities.

7.5.5 Influence of the dip

Because the results of the shot gather and CMP gather analyses are very similar, the influence of the dip has to be very small. To confirm this result, the influence of the dip can be estimated by applying the GA to the residual moveout. As shown in Chapter 6, the most general ellipse is defined by 5 parameters. With the strike direction given by the interval moveout and the NMO analysis only four unknown parameters remain which can be resolved by the input from four lines. Table 7.3 gives the parameter range. The bit length is 15 which allows 32769 different values for each parameter.

Parameter	Range
Long axis a	$0km < a < 4km$
Short axis b	$0km < b < 4km$
Rotation angle α	North 10° East
Midpoint x_0	$-2km < x_0 < 2km$
Midpoint y_0	$-2km < y_0 < 2km$

Table 7.3: Value range for the parameters of the ellipse.

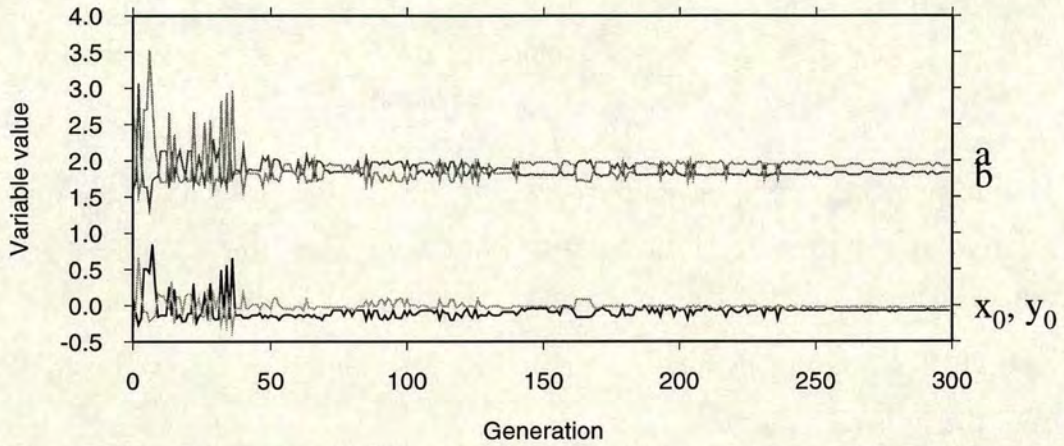

Figure 7.29: Development of the parameters for the best fitting ellipse for 300 generations.

To estimate the fracture strike direction the positions of equal interval travel time are calculated for each line. This forms the input data for the genetic algorithm. The whole inversion is repeated for several different time picks to ensure that the inversion result is not biased by one specific pick. Figure 7.29 shows the development of the parameters for the best fitting ellipse. The travel time for this example is picked at 71ms.

Figure 7.30 shows again the smoothed interval travel times but now the different lines are plotted according to their geographical orientation. The different colours indicate different travel times. The four bigger dots mark the position where the interval travel time is 71ms for each of the lines. The ellipse is calculated for the parameters of the best fit for the 300th generation. An average over several inversions leads to the following results:

- The fracture strike direction is about North 10° East.
- The dip has almost no influence on the estimation.
- The TIH anisotropy calculated from the different length of the axis of the ellipse gives about 5% from the interval travel time and 3% from the NMO velocity analysis for the bottom of the target.

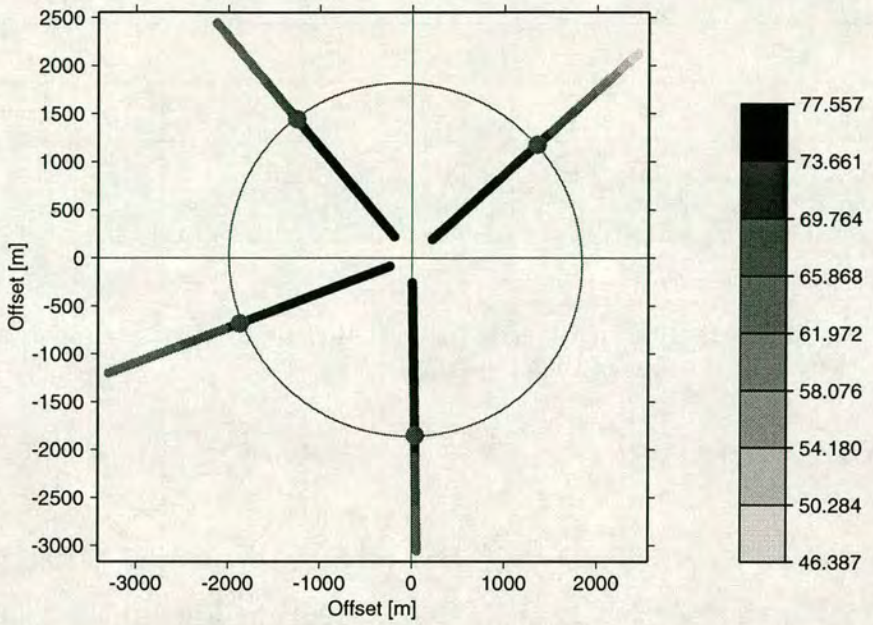

Figure 7.30: The smoothed interval shot gather travel times together with the best fitting ellipse calculated from the inversion results. The big dots mark the four points of equal interval travel time which were used as input for the inversion.

7.5.6 Error analysis for the GA inversion

To estimate an error for the GA itself is difficult because the algorithm is constructed to produce always the best possible fit for a given resolution and input data. The fit is no indicator of any error as it changes with changing input data. In order to asses what errors are introduced in the inversion by the data, I use the NMO velocities for the top of the target layer because the result is a circle and both axis have the same length. I perturb the input data randomly by a maximum of $\pm 5\%$ which is a good average of the picking error. The resulting new data set is then inverted and the difference between the length of the axis of the ellipse is used as an indicator how errors in the picking propagate to the inversion result. The final error is given by an average over 10 different perturbation results. It shows that the error in the inversion is about the same as the error in the picking.

	Run no.										
	1	2	3	4	5	6	7	8	9	10	Average
a	2.08	2.13	2.12	2.08	1.99	2.11	2.07	2.10	2.06	2.11	2.085
b	2.03	2.03	1.99	1.98	1.99	1.99	1.98	1.99	1.98	1.99	1.995

Table 7.4: Inversion results for different perturbated input data. a and b are the length of the axis of the ellipse.

7.6 AVO analysis

The AVO analysis is an additional tool to confirm the fracture strike. As it is shown by Rüger (1996) and Li and Mavko (1996) the azimuthal variation of the amplitude as well as the AVO gradient follow a $\cos(2\phi)$ variation. Because a cosine is completely described by three parameters it should be possible to estimate the strike direction from the four data lines.

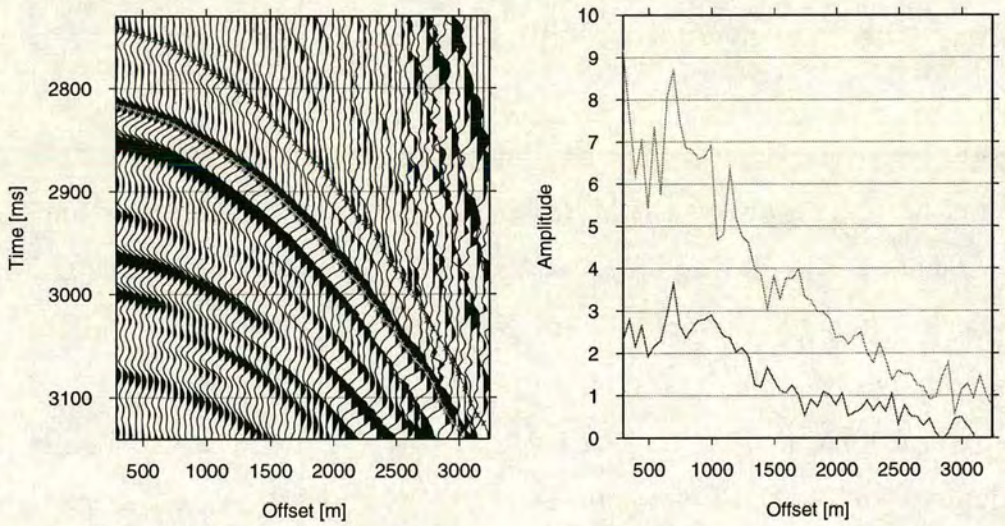

Figure 7.31: Left: CDP gather at the well location for line 1, together with the time picks at which the amplitude is used for the AVO analysis. Right: Amplitude versus offset diagram for the picked times for the top and the bottom of the target zone.

I use information from reflections from the top and the bottom of the target

zone. The first step is to pick the amplitude for each line for the CDP gather at the well. The Figures 7.31, 7.32, 7.33 and 7.34, show these CDP gathers together with the travel time picks. The diagrams on the right side always show the amplitude variation for the picked times for both reflections.

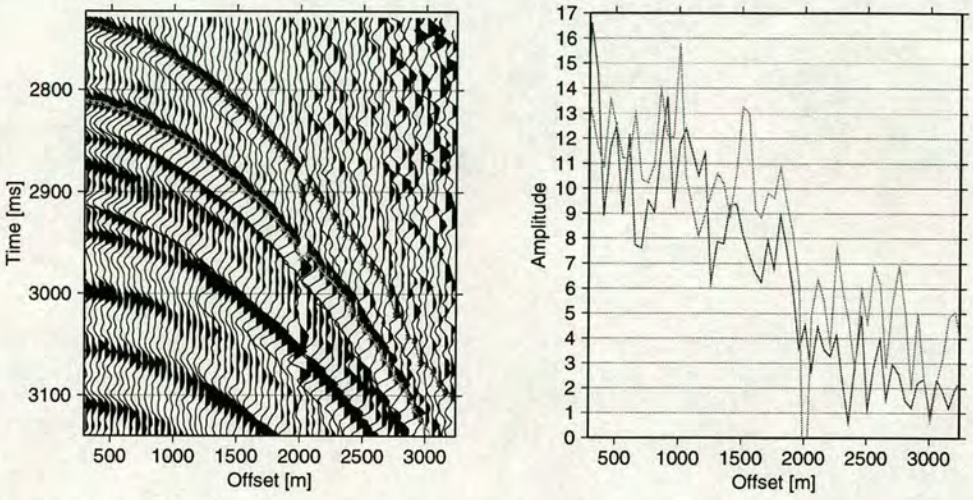

Figure 7.32: Left: CDP gather at the well location for line 2, together with the time picks at which the amplitude is used for the AVO analysis. Right: Amplitude versus offset diagram for the picked times for the top and the bottom of the target zone.

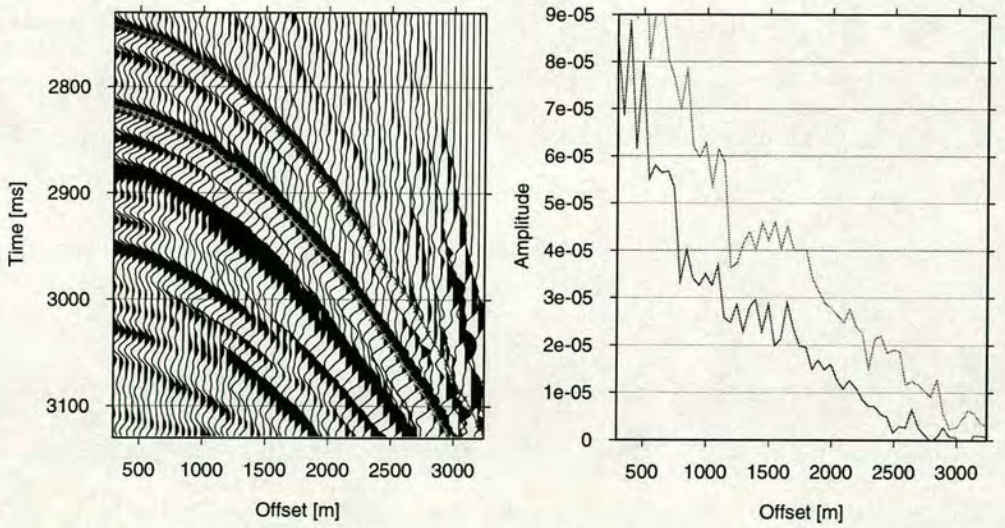

Figure 7.33: Left: CDP gather at the well location for line 3, together with the time picks at which the amplitude is used for the AVO analysis. Right: Amplitude versus offset diagram for the picked times for the top and the bottom of the target zone.

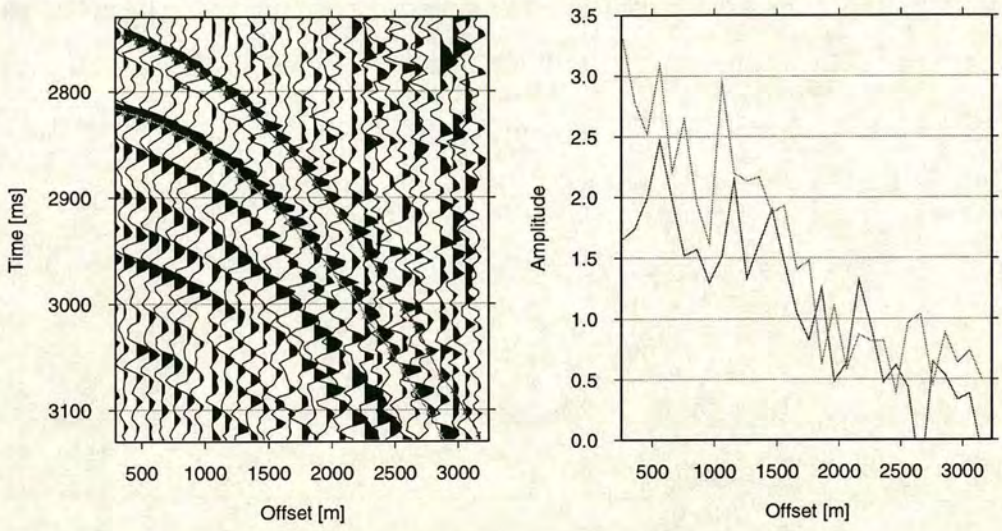

Figure 7.34: Left: CDP gather at the well location for line 4, together with the time picks at which the amplitude is used for the AVO analysis. Right: Amplitude versus offset diagram for the picked times for the top and the bottom of the target zone.

The AVO response is given by

$$Amplitude = A_0 + G \cdot \sin(i)^2, \tag{7.3}$$

where A_0 is the zero-incidence amplitude, G the gradient and i the incidence angle at the reflection point. The gradient is therefore given by the slope of the best fitting line in a coordinate system where the units on the x-axis are $\sin^2$ and on the y-axis the amplitude. To calculate this angle i, I use ray tracing in the same model (Figure 7.10) which is used to calculate the well tie (Figure 7.12). The model is the same for all lines.

For the calculation of the AVO gradient, the zero-incident amplitudes for all lines are normalised to the same number. Theoretically, zero incidence amplitudes at the well position must be the same for all lines. The differences in the measured data are due to different recording procedures. Figure 7.35 shows the results for all lines for the reflection from the top of the target zone. All lines (Figure 7.35a, 7.35b, 7.35c and 7.35d) show an acceptable distribution of the data points. The

strike direction is now determined by the best fitting cosine function with the periodicity two.

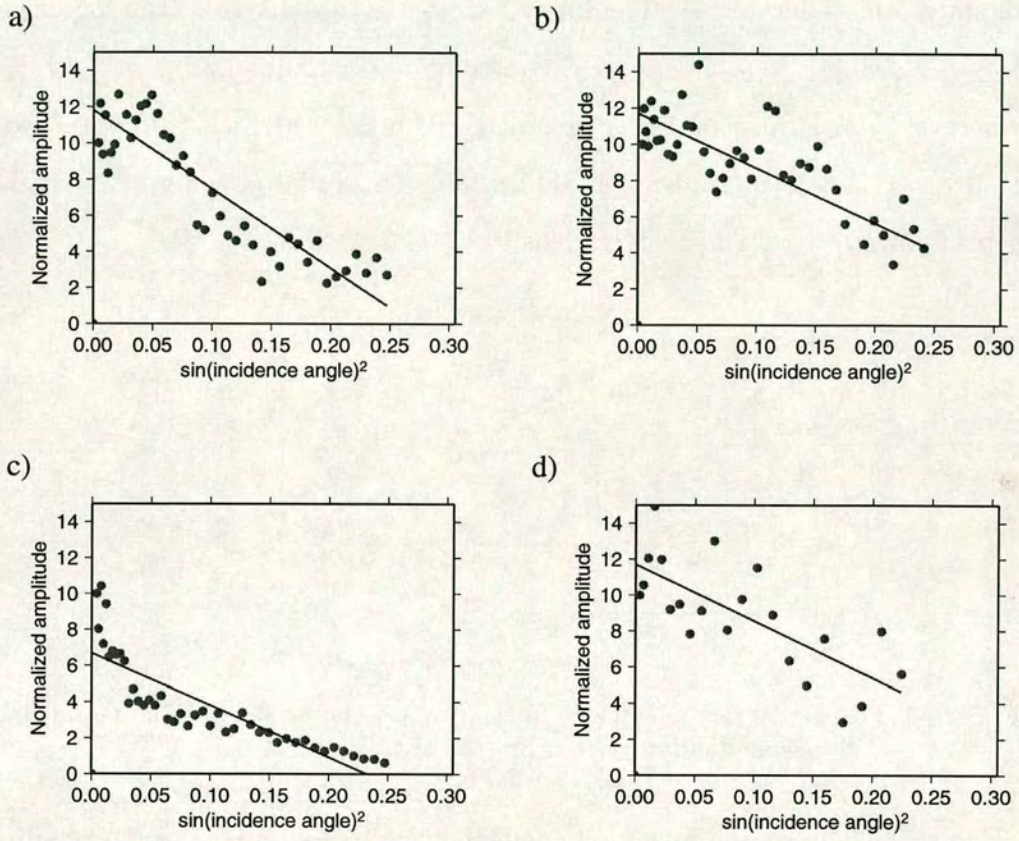

Figure 7.35: All diagrams show the normalised amplitude versus the squared sin of the incidence angle at the reflector together with the best fitting line: a) Line 1, b) Line 2, c) Line 3 and d) Line 4.

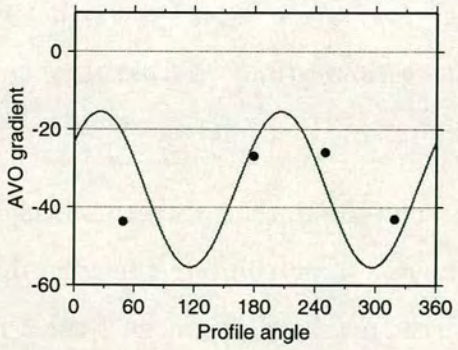

Figure 7.36: Best fitting cosine for the AVO gradients for all lines.

In order to decide whether the minimum or the maximum in the cosine function gives the strike direction, I analyse the reflection response both parallel and perpendicular to the fractures using the equation for the P-P reflection coefficient (equation 6.4 Chapter 6). The input parameters are given by the log data (top: $V_P = 2.304m/s, \rho = 2.314g/cm^3$, bottom: $V_P = 2.587m/s, \rho = 2.407g/cm^3$), where a V_P/V_S ratio of 1.8 is assumed. The cracked rock contains fluid-filled Hudson style cracks (Hudson, 1981) up to second order (Crampin, 1993) with an aspect ratio of 0.01 and a crack density of 0.06.

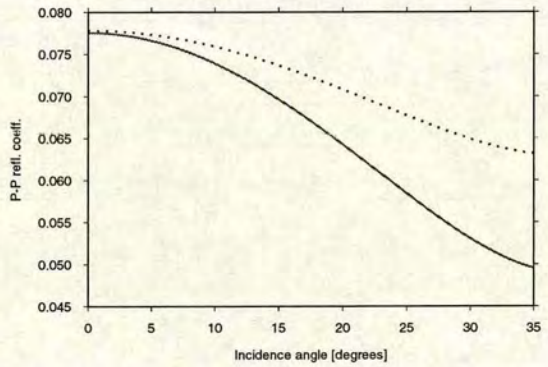

Figure 7.37: Reflection coefficient for the top of the target parallel (solid line) and perpendicular (dotted line) to the fractures.

Figure 7.37 shows the reflection coefficient for the low-high impedance interface on the top of the target. It is obvious that the gradient parallel to the cracks (solid line) is more negative than perpendicular to the fractures. The minimum in the cosine function must therefore give the fracture strike.

The strike direction (Figure 7.36) is given by North 80 degrees West which is very different from the direction estimated from the kinematic measurements which is calculated to be about North 10 degrees East.

The failure of the estimation of the fracture direction from the AVO response for the top of the target may be due to overburden effects in the different directions. In order to compensate for the overburden effects, I use a normalisation scheme based on the the amplitude of the reflection event from the top of the target zone.

As demonstrated by Sayers and Rickett (1997) and Li (1998), the azimuthal AVO response from the bottom of a fracture layer is often more significant than the response from the top. Thus the reflection event from the top of the fractured layer may be used as a calibration horizon. To reveal the AVO response from the bottom of the fractured layer and to compensate for the overburden effects, scaling factors can be calculated from the top event based upon normalisation. These scaling factors can then be applied to the reflection amplitudes of the bottom event. This procedure was first used by MacBeth et al. (1997).

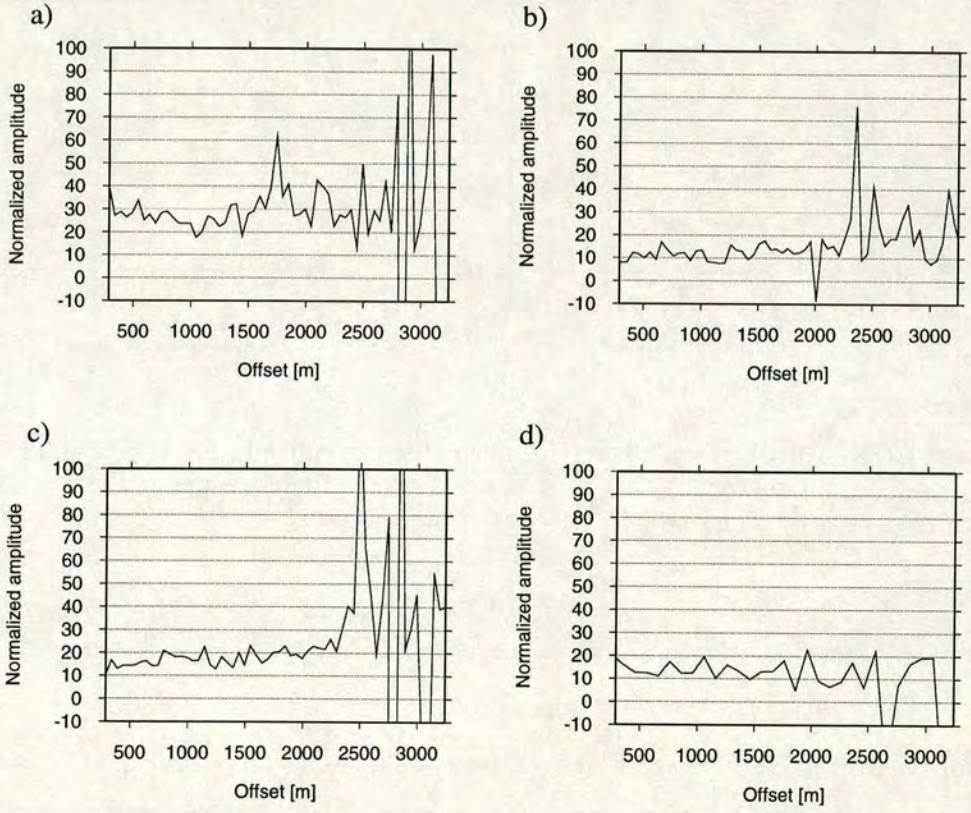

Figure 7.38: All diagrams show the normalised amplitude for the bottom of the target versus the offset. a) Line 1, b) Line 2, c) Line 3 and d) Line 4.

After calibrating the top reflection event, the resulting amplitude from the bottom should then be governed only by the target itself. Figure 7.38 shows the normalised amplitudes for all lines. They are normalised to an amplitude of 10 for the top reflection.

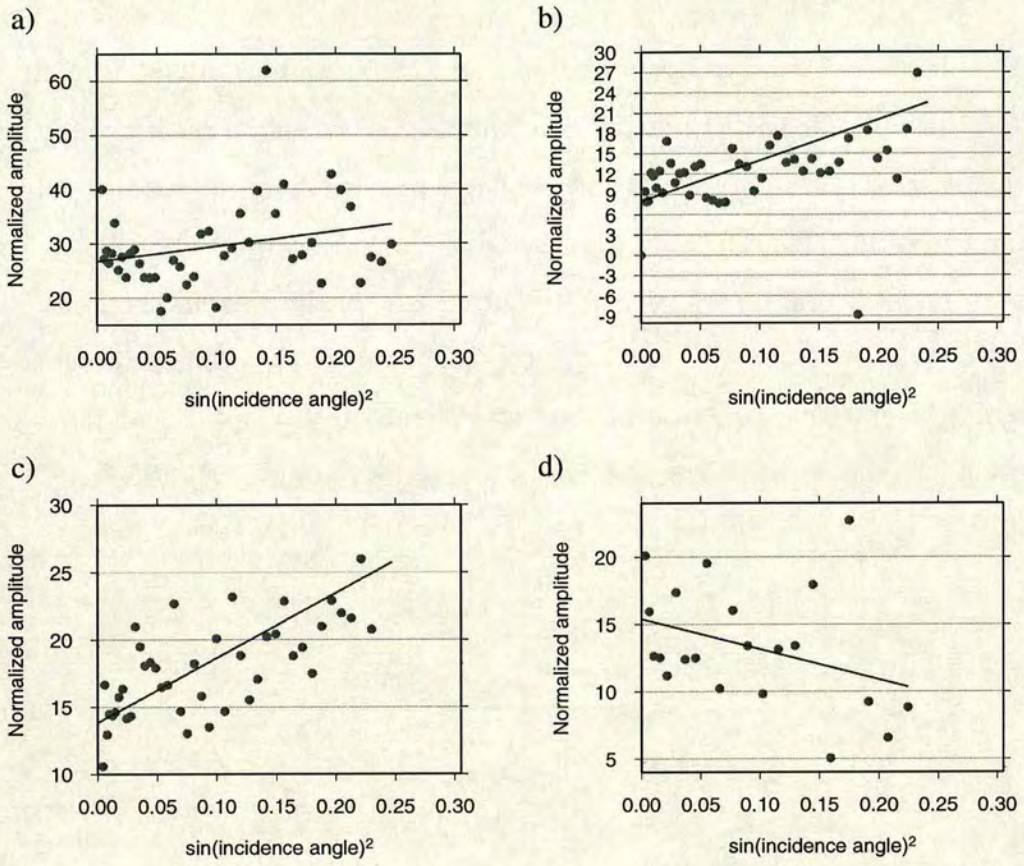

Figure 7.39: All diagrams show the normalised amplitude for the bottom of the target versus the squared sin of the incidence angle at the reflector. a) Line 1, b) Line 2, c) Line 3 and d) Line 4.

The calculation of the AVO gradient is conducted for the same model as for the top reflection with the only addition that the target itself is now part of the model. Figure 7.39 shows, similar to Figure 7.35, the squared sine of the incidence angle versus amplitude diagrams for all data lines. Again, the AVO gradient as one of parameters of the best fitting line, is used as input for the calculation of the fracture strike.

In contrast to the reflection from the top of the target, the distribution of the data points allows me to include all AVO gradients for the fracture strike estimation. Only line 4 (Figure 7.39d) is not as good defined as the others. Figure 7.40 shows the results of the best fitting $\cos 2\phi$ analysis for the AVO gradient.

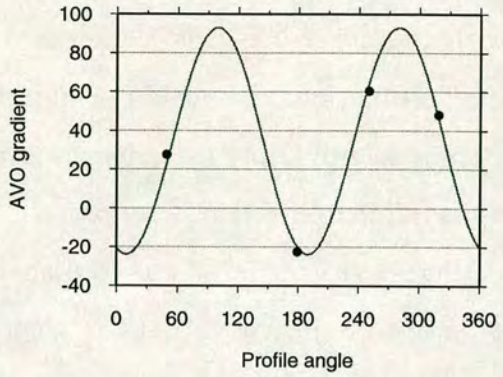

Figure 7.40: Best fitting cosine for the gradient for the reflection from the bottom of the target.

The fracture strike is given at about North 10 degrees East, which is in very good agreement with the results from the kinematic section.

7.7 Conclusions

In this chapter I analysed a four-line marine data set in order to apply some of the techniques I developed in the previous chapters of this thesis. The main area of interest is the estimation of the fracture strike direction for the target zone. The seismic lines intersect at the point where a well is drilled and log information for the density and velocity are available. However, the data contained no geometry information in the trace headers and in order to apply any technique it is essential to estimate the CDP gather at the well position accurately. Only for these CDP gathers can the differences between the lines be connected to azimuthal changes in the parameters. After the normal processing steps of geometry setup, velocity analysis, NMO correction and stack, I compared the stacked sections for each line with a synthetic seismogram which was calculated based on the log data. The result not only gives an accurate estimate for the CDP number for each line at the well position but also helps to identify the top and the bottom of the target horizon in the stacked section.

Three techniques are used to estimate the fracture strike. First the residual moveout is combined with the analysis of the azimuthal changes in the NMO velocity to gain an initial estimation. Because the number of data lines was limited to four it was not possible to apply the estimation technique for dipping TIH layers as it requires a minimum of five observations. The analyses of the stacked sections for each line in the region of the well showed no evidence of a structural variation greater than 3 degrees dip. I was then able to estimate the fracture strike by fitting an ellipse to the residual moveouts for the different lines.

This procedure was carried out for both shot gathers and CMP gathers. The shot gather approach is chosen because the theoretical developments, which are presented in the previous chapters, are all based on shot gathers. The CMP gather analysis was used to verify the shot gather analysis. For small dips the results of the two configurations should be the same. The GA inversion for both gathers gave very similar results.

To confirm the result, I estimated the fracture strike by fitting an ellipse to the NMO velocities and then fixed the direction to analyse the effects of the dip using the interval moveout. The results for this analysis are an anisotropic behaviour of about 5% and a strike direction of about North 10 degrees East. The analysis shows no evidence of the influence of dip.

The results of the NMO analysis have to be viewed with some caution. The inversion for the velocities from the top of the target zone showed no sign of anisotropy, while the bottom indicated about 3%. But this is an average for the whole depth range. To analyse specifically the target I used the interval velocity. But errors in the estimation of the interval velocity and the small thickness of the target do not allow a confident estimation.

I could also show that the errors in the inversion using the GA are of the same order as the picking error for the velocities.

Secondly, I analysed the AVO gradient for both the reflection from the top and the reflection from the bottom of the target zone. The normalised amplitudes for the bottom of the target lead to the same fracture strike as the kinematic analysis while the AVO analysis for the top of the target showed no agreement at all. This can be due to overburden effects which are eliminated by the normalisation.

Overall, the application of the different techniques to the real data showed that it is possible to estimate the fracture strike. However, the reliability of the results depends very much on the thickness of the target zone and even more on the number of observations that are available. If more observations than inversion parameters are available, the GA is much better constrained and therefore the confidence in the results is higher.

CHAPTER 8

Summary

The primary purpose of this thesis has been to investigate the anisotropic parameter estimation in the presence of dipping interfaces. This has been achieved by deriving approximate analytical equations for the problems. Synthetic analyses lead to the anisotropic parameter range where these equations are valid. This allowed the derivation of estimation methods for anisotropic parameters in the presence of dip. The methods were tested successfully for a marine reflection survey where the fracture strike was estimated independently with two different methods. Below I summarise the main conclusions.

8.1 Effects of anisotropy and dip

For a single dipping TIV layer, I derived a travel time equation and showed that it can be decomposed into four terms: an isotropic horizontal, an isotropic dip residual, an anisotropic horizontal residual and an anisotropic dip residual. I have demonstrated that each consecutive term is at least one order of magnitude lower than the previous one. The validity range of this equation was investigated in terms of the P-wave anisotropy (ϵ), the ellipticity ($\epsilon - \delta$), dip and orientation of the symmetry axis of the elastic tensor. It was shown that it is applicable up to $\epsilon = 0.2$ ($\epsilon - \delta \approx 0.19$) and 20 degrees dip. A separation procedure for the effects

of anisotropy and dip, based on the travel time is valid for dip angles up to 20 degrees and Thomsen parameters of $\epsilon = 0.15$ to $\epsilon = 0.2$. It is shown that the deviation of the group from the phase direction has only a second order influence in the position of the minimum point upon which the separation scheme is based. If the orientation of the symmetry axis is changed the range for the anisotropic parameters becomes smaller. Cases can even occur where the anisotropic effects are compensated by a special orientation of the symmetry axis, where anisotropy can no longer be detected and the separation process is thus not applicable.

8.2 Estimation technique and real data results

Traditional estimation methods such as the one for the fracture strike detection are not able to predict correct results if the target layer is dipping. It was therefore necessary to investigate the influence of the dip from a theoretical point of view and to derive an estimation method from the synthetic data results. For the two layer case, a sophisticated inversion scheme using a genetic algorithm proved to be necessary to resolve the problem of the fracture strike direction. The study of the behaviour of the residual travel time for a dipping target zone revealed that the contour lines of equal travel time can still be approximated by an ellipse if the TIH anisotropy of the target layer is smaller than 20%. This observation leads to the inversion idea. For any given number of survey lines, equal residual travel times are assumed to lie on or close to an ellipse. The problem of determining this ellipse is solved by the application of a non-linear inversion scheme, a genetic algorithm. This scheme is able to estimate all the parameters of the ellipse simultaneously and therefore represents a method for the determination of the fracture strike direction for a dipping target zone.

The method was used successfully for the real data where the NMO ellipse and the residual travel time were fitted. It is shown that the error in the estimation

of the direction is about the same as the error which is assumed for th pick of the velocity. The fracture strike was estimated to be North 10 degrees East which was confirmed by analyses of the AVO gradient but only after a normalisation for the reflection from the bottom of the target zone.

The results for the inversion of the interval travel time shows that the method is not applicable to deep thin targets. The anisotropy estimation shows at least 33% TIH anisotropy in the target zone and a direction far different from the other inversions. The low confidence interval is due to the limited number of observations that are used for the inversion procedure.

8.3 AVO studies

I analysed the AVO response for the interface of two orthorhombic media. Generalised and linearised equations for the tensor reflectivities of all anisotropic single and mixed modes have been developed. Furthermore, reduced analytical equations for TIH media were presented and, in addition, a simple algebraic framework for the derivation of reflection coefficients was established. Comparisons with numerical calculations show that these expressions are valid for up to 20% P- and 10% S-wave anisotropy, and can be applied to interfaces with up to 20% P- and 10% S-wave impedance contrasts. More accurate expressions for the polarizations deviations of qP and qS waves in anisotropic media were developed. These polarisation deviations have significant first order effects on the AVO signatures, and this is contrary to one's impression from travel time studies, where the effects polarisation deviations on travel time are often negligible.

It was further demonstrated that it is possible to separate the reflectivity of an orthorhombic-orthorhombic interface into a TIV background and a crack parameter related part. The crack dependent term can be used to invert for the

anisotropic parameter γ if the upper medium contains no cracks. For weak crack densities (up to $\epsilon_c = 0.15$ which is the upper limit for realistic materials) the separation agrees with the numerical modelling results.

8.4 Suggestions for future work

This thesis identified some areas for further research. I think the most likely to achieve positive results is the application of the hierarchical travel time equation and the separation algorithm to a real data set where the target zone is highly anisotropic and the structural variation is greater than a minimum of 10 degrees dip. However, the successful application of this technique depends on high quality data. This type of recordings are achievable using the latest acquisition techniques such as seabed recordings. The synthetic applications suggest that it should be possible to enhance the stacked section and to estimate anisotropic parameters in due course.

The theoretical work in this thesis is based upon shot gathers. This is due to the fact that it turned out to be very difficult and time consuming to calculate CMP gathers with ANRAY. An interesting field could be the investigation of the observed phenomena in CMP gathers as they are commonly used in exploration processing. It may also be that some of the difficulties I encountered are due to the fact that I used the shot gather formulation.

Time lapse investigations try to monitor the changes of the behaviour of a reservoir over a certain period of time. Two of the key parameters in fractured reservoir characterisation are the crack geometry and their filling. An extension of the separation technique for the crack-related reflectivity from a TIV background for an orthorhombic medium for other than thin cracks could fill the gap between recordings and theoretical investigations. Changes in the AVO response could

then be linked directly to the crack parameters.

It is important that 3D data are properly sampled (Ziolkowski, 1997), in order to realize the full potential of the azimuthal parameter estimation techniques and to achieve reliable results of high resolution. Four line configurations as shown in Chapter 7 satisfy the theoretical criteria for obtaining a solution but with a higher sampling the reliability of the results could be increased substantially.

8.5 Software used for this thesis

The layout of the thesis is achieved by using LaTeX, the references and citations are produced by BibTeX. Most diagrams are produced with the Generic Mapping Tool (GMT) written by Wessel and Smith (1995). Other diagrams are drawn with the Unix tool Xfig. ANRAY is used for the ray tracing and ANISEIS for the zero-offset well tie seismograms. ProMax version 6.0 is used for all the data processing. All other calculations are done by C and FORTRAN programs which are written by myself.

References

Aki, K., and Richards, P., 1980, Quantitative seismology: Theory and methods: Freeman.

Al-Dajani, A., and Alkhalifah, T., 1998, Reflection moveout inversion in azimuthally anisotropic media - accuracy and limitations: 60th EAEG Conference, Expanded Abstracts, pages 5–22.

Alford, R. M., 1986, Shear data in the presence of azimuthal anisotropy: Dilley, Texas: 56th Annual Internat. Mtg., Soc. Expl. Geophys., Expanded Abstracts, **86**, Session: S9.6.

Alkhalifah, T., and Tsvankin, I., 1995, Velocity analysis for transversely isotropic media: Geophysics, **60**, no. 5, 1550–1566.

Alkhalifah, T., 1995, Anisotropy processing in vertically inhomogeneous media: 65th Annual Internat. Mtg., Soc. Expl. Geophys., Expanded Abstracts, **95**, 348–351.

Anderson, J. E. A., and Tsvankin, I., 1994, Dip-moveout processing by Fourier transform in anisotropic media: 64th Annual Internat. Mtg., Soc. Expl. Geophys., Expanded Abstracts, pages 1213–1216.

Backus, G., 1965, Possible forms of seismic anisotropy of the uppermost mantle under oceans: Journ. Geophys. Res., pages 3429–3439.

Banik, N., 1984, Velocity anisotropy of shales and depth estimation in the North Sea basin: Geophysics, pages 1411–1419.

Berryman, J. G., 1979, Long-wave elastic anisotropy in transversely isotropic media: Geophysics, **44**, 896–917.

Brown, R., Lawton, D., and Cheadle, S., 1991, Scaled physical modeling of anisotropic wave propagation - multioffset profiles over an orthorhombic medium: Geophys. J. Int., **107**, 693–702.

Bush, I., and Crampin, S., 1991, Paris basin VSPs: case history establishing combinations of fine-layer (or lithologic) anisotropy and crack anisotropy from modelling shear wavefields near point singularities: Geophys. J. Int., **107**, 433–447.

Červeny, V., Molotkov, I., and Pšenčík, I., 1977, Ray method in seismology: Univ. Karlova, Praha.

Červeny, V., 1987, Ray methods for three-dimensional seismic modelling: Lecture Notes for the Petroleum Industry Course at the Norwegian Institute of Technology.

Clærbout, J., 1994, Imaging the Earth's interior: Stanford University.

Crampin, S., 1981, A review of wave motion in anisotropic and cracked elastic media: Wave motion, **3**, 343–391.

Crampin, S., 1993, A review of the effects of crack geometry on wave propagation through aligned cracks: Canadian Journal of Exploration Geophysics, **29**.

Daley, P. F., and Hron, F., 1977, Reflection and transmission coefficients for transversely isotropic media: Bull. Seis. Soc .Am., **67**, 661–675.

Dellinger, J., and Muir, F., 1988, Imaging reflections in elliptically anisotropic media (short note): Geophysics, **53**, no. 12, 1616–1618.

Feynman, R. P., Leighton, R., and Sands, M., 1963, The Feynman Lectures on Physics. Vol. II. Mainly Electromagnetism and Matter: California Institute of Technology.

Fryer, G., and Frazer, N., 1987, Seismic waves in stratified anisotropic media II. Elastodynamic eigensolutions for some anisotropic systems: Geophys. J. R. astr. Soc., **91**, 73–101.

Fuchs, K., and Müller, G., 1971, Computation of synthetic seismograms with the reflectivity method and comparison with observations: Geophys. J. R. astr. Soc., **23**, 417–433.

Gajewski, D., and Pšenčík, I., 1987, Computation of high frequency seismic wave fields in 3D laterally inhomogeneous anisotropic media: Geophys. J. R. astr. Soc., **91**, 383–411.

Gajewski, D., and Pšenčík, I., 1995, Program package ANRAY95, version 3.01: The manual pages.

Garotta, R., 1989, Detection of azimuthal anisotropy: 59th Annual Internat. Mtg., Soc. Expl. Geophys., Expanded Abstracts.

Goldberg, D., 1989, Genetic algorithms in search, optimization & machine learning: Addison -Wesley Publishing Company, Inc.

Grechka, V., and Tsvankin, I., 1996, 3-D description of normal moveout in anisotropic media: 66th Annual Internat. Mtg., Soc. Expl. Geophys., Expanded Abstracts.

Hale, D., 1984, Dip-moveout by Fourier transform: Geophysics, **49**, no. 6, 741–757.

Helbig, K., 1983, Elliptical anisotropy - its significance and meaning: Geophysics, **48**, no. 7, 825–832.

Helbig, K., 1994, Foundations of anisotropy for exploration seismics: Handbook of Geophysical Exploration, **22**.

Hood, J., and Schoenberg, M., 1989, Estimation of vertical fracturing from measured elastic moduli: Journ. Geophys. Res., **94**, 15611–15618.

Hubral, P., 1980, Wave front curvatures in 3-D laterally inhomogenous media with curved interfaces: Geophysics, **45**, no. 905-913.

Hudson, J., 1981, Wave speed and attenuation of elastic waves in material containing cracks: Geophys. J. R. astr. Soc., **64**, 113–150.

Kühnel, T., and Li, X.-Y., 1996, Anisotropy versus dip - a separation approach: 66th Annual Internat. Mtg., Soc. Expl. Geophys., Expanded Abstracts.

Kühnel, T., and Li, X.-Y., 1997, Separation of anisotropy and structure during processing: 59th EAEG Conference, Expanded Abstracts.

Levin, F., 1978, The reflection, refraction, and diffraction of waves in media with an elliptical velocity dependence: Geophysics, pages 528–537.

Levin, F. K., 1990, Reflection from a dipping plane - Transversely isotropic solid: Geophysics, **55**, no. 7, 851–855.

Lewis, C., Davis, T., and Vuillermoz, C., 1991, Three-dimensional multicomponent imaging of reservoir heterogeneity Soli Field, Wyoming: Geophysics, **56**, 2048–2056.

Li, T., and Mavko, G., 1996, Fracture signatures on P-wave AVOZ: 66th Annual Internat. Mtg., Soc. Expl. Geophys., Expanded Abstracts, pages 1818–1821.

Li, X.-Y., and Crampin, S., 1993a, Approximations to shear-wave velocity and moveout equations in anisotropic media: Geophysics, **41**, 833–858.

——— 1993b, Linear-transform techniques for processing shear-wave anisotropy in four-component seismic data: Geophysics, **58**, 240–256.

——— 1993c, Variation of reflection and transmission coefficients with crack strike and crack density in anisotropic media: Geophys. Prosp., **41**, 859–882.

Li, X.-Y., Kühnel, T., and MacBeth, C., 1996a, Converted wave AVO in fractured media and its implications: Submitted to Geophysical Prospecting.

——— 1996b, Mixed mode AVO response in fractured media: 66th Annual Internat. Mtg., Soc. Expl. Geophys., Expanded Abstracts.

Li, X.-Y., 1997, Viability of azimuthal variation in P-wave moveout for fracture detection: 67th Annual Internat. Mtg., Soc. Expl. Geophys., Expanded Abstracts.

Li, X.-Y., 1998, Processing PP and PS waves in multicomponent sea-floor data for azimuthal anisotropy: theory and overview: Revue de l' Institut Français du Pétrole, pages 607–620.

Liu, E., MacBeth, C., Pointer, T., Hudson, J., and Crampin, S., 1996, The effective elastic complience of fractured rock: 66th Annual Internat. Mtg., Soc. Expl. Geophys., Expanded Abstracts.

MacBeth, C., Li, X.-Y., Ohlsen, F., Jakubowicz, H., and Kirk, W., 1997, Fracture-related amplitude variations with offset and azimuth in marine seismic data: 67th Annual Internat. Mtg., Soc. Expl. Geophys., Expanded Abstracts, **62**, no. 2, 195–198.

Mackertich, D., 1996, The Fife Field, UK Central North Sea: Pet. Geoscience, **2**, 373–380.

Miller, D., and Spencer, C., 1994, An exact inversion for anisotropic moduli from phase slowness data: Journ. Geophys. Res., **99**, 21651–21657.

Mueller, M., 1991, Prediction of lateral variability in fracture intensity using multicomponent shear-wave surface seismic as a precursor to horizontal drilling in the Austin Chalk: Geophys. J. Int., **107**, 409–417.

Pšenčík, I., 1979, Ray amplitudes of compressional, shear and converted body waves in three dimensional laterally inhomogenous media with curved interfaces: Journ. Geophys. Res., **45**, 381–390.

Resnick, J., Ng, P., and Larner, K., 1987, Amplitude versus offset analysis in the presence of dip: 57th Annual Internat. Mtg., Soc. Expl. Geophys., Expanded Abstracts.

Rommel, B., 1993, Approximate stacking velocities in a weakly transversely isotropic layer: Canadian Journal of Exploration Geophysics, **29**.

Rüger, A., 1995, P-wave reflection coefficients for transversely isotropic media with vertical and horizontal axis of symmetry: 65th Annual Internat. Mtg., Soc. Expl. Geophys., Expanded Abstracts, **95**, 278–281.

Rüger, A., 1996, Variation of P-wave reflectivity with offset and azimuth in anisotropic media: 66th Annual Internat. Mtg., Soc. Expl. Geophys., Expanded Abstracts, **95**, 1810–1813.

Savić, M., 1995, Ultrasonic scattering from hydraulic fracture: theory, computation and experiment: Ph.D. thesis.

Sayers, C., and Rickett, J., 1997, Azimuthal variation in AVO response for fractured gas sands: Geophysical Prospecting, **45**, 165–182.

Sayers, C., 1995, Simplified anisotropy parameters for transversely isotropic sedimentary rocks: Geophysics, **60**, 1933–1935.

Sayers, C., 1997, Determination of anisotropic velocity models from walkaway VSP data acquired in the presence of dip: Geophysics, **62**, 723–729.

Schoenberg, M., and Douma, J., 1988, Elastic-wave propagation in media with parallel fractures and aligned cracks: Geophysics, **36**, 571–590.

Schoenberg, M., and Protazio, K., 1992, 'Zoeppritz' rationalized and gerneralized to anisotropy: Journal of seismic exploration, **1**, 125–144.

Sena, A., 1991, Seismic traveltime equations for azimuthally anisotropic and isotropic media: Estimation of interval elastic properties: Geophysics, **56**, 2090–2101.

Shuck, E. L., Benson, R. D., and Davis, T. L., 1993, Analysis of shear wave polarizations from a nine- component 3-D dataset, Cedar Hill, New Mexico: 63rd Annual Internat. Mtg., Soc. Expl. Geophys., Expanded Abstracts, **93**, 271–274.

Taylor, D. B., 1991, Aniseis ii manual: Available to licencees of ANISEIS from Applied Geophysical Software Inc., Houston.

Thomsen, L., 1986, Weak elastic anisotropy: Geophysics, **51**, no. 10, 1954–1966.

Thomsen, L., 1988, Reflection seismology over azimuthally anisotropic media Geophysics, **53**, 304–313.

Thomsen, L., 1993, Weak anisotropic reflections, *in* Castagna, J. P., and Backus, M. M., Eds., Offset-dependent reflectivity - Theory and practice of AVO analysis: Soc. Expl. Geophys., 103–111.

Thomsen, L., 1995, Elastic anisotropy due to aligned cracks in porous rock: Geophysics, **43**, 805–829.

Tsvankin, I., and Thomsen, L., 1994, Nonhyperbolic reflection moveout in anisotropic media: Geophysics, **59**, 1290–1304.

Tsvankin, I., 1994, Analytic description of dip moveout in anisotropic media: 64th Annual Internat. Mtg., Soc. Expl. Geophys., Expanded Abstracts, **94**, 1209–1212.

Tsvankin, I., 1995a, Inversion of moveout velocities for horizontal transverse isotropy: 65th Annual Internat. Mtg., Soc. Expl. Geophys., Expanded Abstracts, **94**, 735–738.

——— 1995b, Normal moveout from dipping reflectors in anisotropic media: Geophysics, **60**, 268–284.

Tsvankin, I., 1996, Effective parameters and P-wave velocity for azimuthal anisotropic media: 66th Annual Internat. Mtg., Soc. Expl. Geophys., Expanded Abstracts, pages 1850–1853.

Uren, N. F., Gardner, G. H. F., and McDonald, J. A., 1990a, The migrator's equation for anisotropic media: Geophysics, **55**, 1429–1434.

——— 1990b, Normal moveout in anisotropic media (short note): Geophysics, **55**, 1634–1636.

Wessel, P., and Smith, W., 1995, New version of Generic Mapping Tool released: EOS trans. AGU, **76**, 329.

Winterstein, D. F., 1990, Velocity anisotropy terminology for geophysicists: Geophysics, **55**, 1070–1088.

Yilmaz, Ö., 1987, Seismic data processing: Society of Exploration Geophysicists: Investigations in geophysics 2.

Ziolkowski, A., 1997, Shot-by-shot removal of sea surface multiples: 59th EAEG Conference, Expanded Abstracts, page A011.

Appendix A

Travel time related derivations

A.1 Decomposition of the travel time equation

In the following the ray angle is expressed in terms of the given parameters dip angle (ϕ), receiver offset (Rec_x) and depth of the reflector at the source point (D_z). See Figure 4.1 for the definition of the symbols. I start with the triangle $SRRec_x$ (source, reflection point, receiver). The length of the first side of the triangle (this is equal to the first segment of the ray d_1, Figure 4.1) can be expressed as

$$d_1 = \frac{D_z \cos(\phi)}{\cos(\psi)}. \tag{A.1}$$

The second part is given by

$$d_2 = \frac{\cos(\phi)(D_z - Rec_x \tan(\phi))}{\cos(\psi)}. \tag{A.2}$$

Using the cosine rule

$$Rec_x^2 = d_1^2 + d_2^2 - 2d_1 d_2 \cos(2\psi), \tag{A.3}$$

insert equation (A.1) and (A.2) and solve for $\cos(2\psi)$, yields

$$\begin{aligned} \cos(2\psi) &= \frac{1}{2} \frac{2D_z^2 \cos(\phi)^2 - 2D_z \cos(\phi) Rec_x \sin(\phi)}{\cos(\phi) D_z (D_z \cos(\phi) - Rec_x \sin(\phi))} \\ &+ \frac{1}{2} \frac{Rec_x^2 - Rec_x^2 \cos(\phi)^2 - Rec_x^2 \cos(\psi)^2}{\cos(\phi) D_z (D_z \cos(\phi) - Rec_x \sin(\phi))}. \end{aligned} \tag{A.4}$$

This can be rewritten and solved in terms of $\cos^2(\psi)$

$$\cos^2(\psi) = \frac{-2D_z^2\cos(\phi)^2 + 2D_z\cos(\phi)Rec_x\sin(\phi) - Rec_x^2 + Rec_x^2\cos(\phi)^2}{4\cos(\phi)D_z(-D_z\cos(\phi) + Rec_x\sin(\phi)) - Rec_x^2} + \frac{2\cos(\phi)D_z(-D_z\cos(\phi) + Rec_x\sin(\phi))}{4\cos(\phi)D_z(-D_z\cos(\phi) + Rec_x\sin(\phi)) - Rec_x^2}. \quad \text{(A.5)}$$

A.1.1 P-P reflection

Now the group angle can be replace in the residual anisotropic term of equation 4.13 by inserting equation A.5 and expanding the resulting term into a Taylor series for small offsets Rec_x. Let Q be the part of the residual anisotropic term of equation 4.13 which contains anisotropic parameters

$$\begin{aligned} Q &= 2\delta\sin^2(\psi)\cos^2(\psi) + 2\epsilon\sin^4(\psi) \\ &\approx \frac{1}{2}\delta\frac{Rec_x^2}{D_z^2} + \frac{1}{2}\frac{\delta\sin(\phi)}{\cos(\phi)}\frac{Rec_x^3}{D_z^3} + \frac{1}{8}\frac{3\delta - 5\delta\cos(\phi)^2 + \epsilon\cos(\phi)^2}{D_z^4\cos(\phi)^2}Rec_x^4 + O(Rec_x^5). \end{aligned} \quad \text{(A.6)}$$

Finally, rearranging the equation into dip dependent (Υ) and independent (ζ) parts gives

$$\begin{aligned} Q &= \zeta + \Upsilon \\ \zeta &= \delta\frac{Rec_x^2}{2D_z^2} + (\epsilon - 2\delta)\frac{Rec_x^4}{8D_z^4}, \quad \text{(A.7)} \\ \Upsilon &= \delta\frac{\sin(\phi)Rec_x^3}{2\cos(\phi)D_z^3} + \delta\frac{3Rec_x^4}{8D_{D_z}^4}\tan(\phi)^2. \quad \text{(A.8)} \end{aligned}$$

A.1.2 qSV-qSV reflection

If the symmetry axis is perpendicular to the reflector the image point construction is valid for S-waves as well. Therefore, to find the travel time equation I only have to replace the velocity with the weak anisotropic expression for the qSV-wave (equation 2.29). Then I can use the same scheme as above to separate

between dip dependent and independent parts. Because of the velocity change, the definition of Q changes

$$\begin{aligned} Q &= 2\frac{V_{P0}^2}{V_{SV0}^2}\sin^(\psi)\cos^2(\psi)(\epsilon-\delta) \\ &\approx \frac{1}{2}\frac{V_{P0}^2}{V_{SV0}^2}\frac{Rec_x^2}{D_z^2}(\epsilon-\delta)+\frac{1}{2}\frac{V_{P0}^2}{V_{SV0}^2}\frac{Rec_x^3}{D_z^3}\frac{\sin(\phi)}{\cos(\phi)}(\epsilon-\delta) \\ &- \frac{1}{8}\frac{V_{P0}^2}{V_{SV0}^2}\frac{Rec_x^4}{D_z^4}\frac{(-3\epsilon+3\delta-5\delta\cos(\phi)^2+5\epsilon\cos(\phi)^2)}{\cos^2(\phi)}+O(r^5), \end{aligned} \tag{A.9}$$

and finally

$$\zeta = (\delta-\epsilon)\frac{V_{P0}^2}{2V_{SV0}^2}\frac{Rec_x^2}{D_z^2}(\frac{13}{8}\frac{Rec_x^2}{D_z^2}-1), \tag{A.10}$$

$$\Upsilon = (\epsilon-\delta)\frac{V_{P0}^2}{2V_{SV0}^2}\frac{Rec_x^3}{D_z^3}\tan\phi(1-\frac{3}{8}\frac{Rec_x}{D_z}\tan(\phi)). \tag{A.11}$$

A.1.3 SH-SH reflection

Using equation 2.30, the weak anisotropy expression for V_{SH} and a Taylor expansion gives

$$\begin{aligned} Q &= 2\gamma\sin^2(\psi) \\ &\approx \frac{1}{2}\frac{Rec_x^2}{D_z^2}\gamma+\frac{1}{2}\frac{Rec_x^3}{D_z^3}\frac{\sin(\phi)}{\cos(\phi)}\gamma-\frac{1}{8}\frac{Rec_x^4}{D_z^4}\frac{(-3+4\cos^2(\phi))}{\cos^2(\phi)}\gamma+O(Rec_x^5). \end{aligned} \tag{A.12}$$

Which leads to the final result

$$\zeta = \gamma\frac{Rec_x^2}{2D_z^2}(1+2\frac{Rec_x^2}{D_z^2}). \tag{A.13}$$

$$\Upsilon = \gamma\frac{Rec_x^3}{2D_z^3}\tan\phi(1+\frac{3Rec_x}{D_z}\tan\phi). \tag{A.14}$$

A.2 Ray parameter perturbation

If the symmetry axis is perpendicular to the surface, the reflecting angle θ_2 is not equal to the incidence angle θ_1 and the image point construction is not longer valid. Here I prove that for gentle dips and weak anisotropy the image point construction may still be a good approximation because the perturbation of the ray parameter caused by the change in the orientation of the symmetry axis is small in terms of the parameters ϵ and δ. In the following I will show that

$$\frac{\sin\theta_1}{V_{P1}} = \frac{\sin\theta_1}{V_{P2}}(1+\nu), \tag{A.15}$$

is a good approximation, where V_{P1} and V_{P2} are the phase velocities connected to the phase angles θ_1 and θ_2. ν represents a small perturbation term. Let

$$\Delta\theta = \theta_2 - \theta_1 \tag{A.16}$$

$$\Delta V = V_P(\theta_1+\Delta\theta) - V_P(\theta_1) \tag{A.17}$$

If I use the weak anisotropy expression for the P-wave phase velocity [equation (2.28)], I can write ΔV, which is a second order term, for small $\Delta\theta$ as

$$\Delta V = \frac{\partial V}{\partial\theta}\Delta\theta = V'\Delta\theta = V_{P0}(\delta\sin(2\theta)\cos(2\theta) + 4\epsilon\sin^3(\theta)\cos(\theta))\Delta\theta. \tag{A.18}$$

For small ΔV and $\Delta\theta$ the horizontal slowness at the reflection point is given by

$$\frac{\sin(\theta_1)}{V_P(\theta_1+\phi)} = \frac{\sin(\theta_2)}{V_P(\theta_2-\phi)} \tag{A.19}$$

$$= \frac{\sin(\theta_1+\Delta\theta)}{V_P(\theta_1-\phi+\Delta\theta)} \tag{A.20}$$

$$\approx \frac{\sin(\theta_1)+\cos(\theta_1)\Delta\theta}{V_P(\theta_1-\phi)+\Delta V} \tag{A.21}$$

$$= \frac{\sin(\theta_1)+\cos(\theta_1)\Delta\theta}{V_P(\theta_1-\phi)(1+\frac{\Delta V}{V_P(\theta_1-\phi)})}. \tag{A.22}$$

This leads after a Taylor expansion of equation A.22 for small ΔV to the following expression for the horizontal slowness

$$\frac{\sin(\theta_1)}{V_P(\theta_1+\phi)} = \left(\frac{\sin(\theta_1)}{V_P(\theta_1-\phi)} + \frac{\cos(\theta_1)\Delta\theta}{V_P(\theta_1-\phi)}\right)(1-\frac{\Delta V}{V_P(\theta_1-\phi)}) \quad \text{(A.23)}$$

$$\approx \frac{\sin(\theta_1)}{V_P(\theta_1-\phi)}(1+\cot(\theta_1)\Delta\theta)\,. \quad \text{(A.24)}$$

Figures A.1 and A.2 show the variation of $\Delta\theta$ for two materials ($\epsilon = 0.15$ and $\epsilon = 0.25$) for a range of dip angles. For $\epsilon = 0.15$ and 30 degrees incidence angle $\Delta\theta$ is less than 1 degree for 10 degrees of dip.

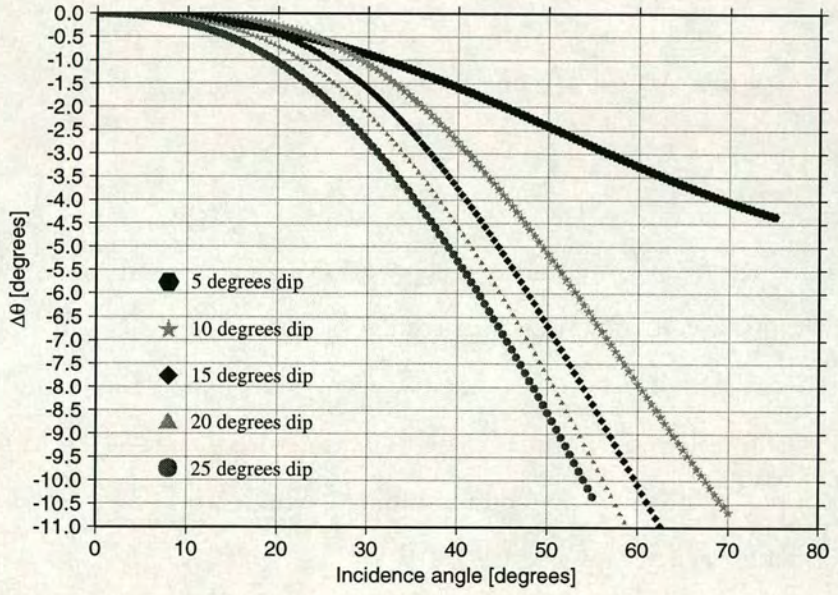

Figure A.1: The deviation of the reflection angle from the angle of incidence for a symmetry axis perpendicular to the surface for $\epsilon = 0.15$.

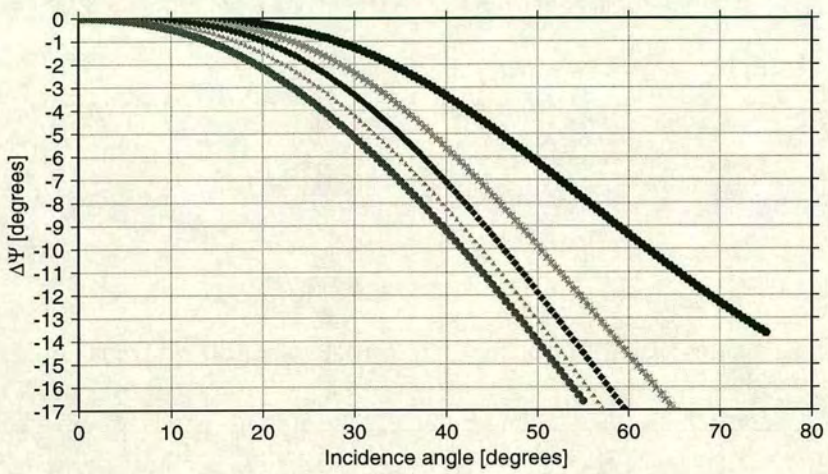

Figure A.2: The same as Figure A.1 but for $\epsilon = 0.25$.

A.3 3-D data analysis

In this section the travel time and the separation equation will be derived for a three dimensional layout of source and receiver. The reflector is a plane defined by a dip and a strike angle and one point in space. I start with the formula for the coordinates of the reflection point for the 3D case, where the source ($\vec{S}$) and the receiver ($\vec{Rec}$) position, the dip (ϕ) and strike (φ) angle and one point belonging to the reflector ($\vec{D}$) are given (Figure A.3).

Assume

$$\vec{S} = S_x\vec{i} + S_y\vec{j} + S_z\vec{k}, \tag{A.25}$$

$$\vec{Rec} = Rec_x\vec{i} + Rec_y\vec{j} + Rec_z\vec{k}, \tag{A.26}$$

$$\vec{D} = D_x\vec{i} + D_y\vec{j} + D_z\vec{k}, \tag{A.27}$$

$$\vec{R} = R_x\vec{i} + R_y\vec{j} + R_z\vec{k}, \tag{A.28}$$

$$\vec{I} = I_x\vec{i} + I_y\vec{j} + I_z\vec{k}, \tag{A.29}$$

where $\vec{i}$, $\vec{j}$ and $\vec{k}$ are the Cartesian unit vectors.

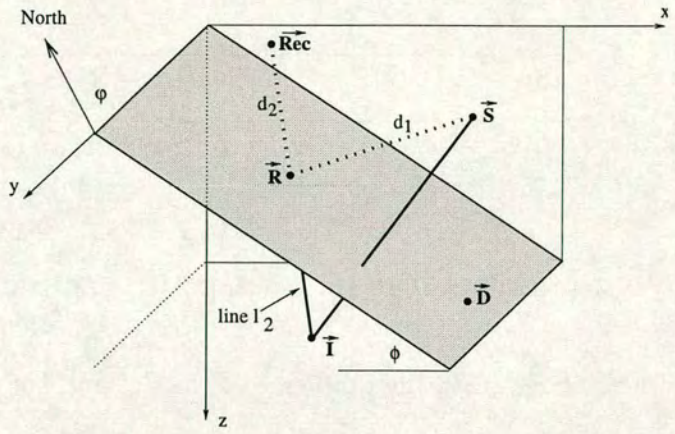

Figure A.3: 3-D ray path and image point.

To find the reflection point $\vec{R}$, a line $l_2(j) = \vec{Rec} + j(\vec{Rec} - \vec{I})$ connecting the image point and the receiver, intersects with the reflector for a special value j'. The explicit formula for $\vec{R}$ is given below.

$$\vec{R} = \vec{Rec} + j'(\vec{Rec} - \vec{I}), \tag{A.30}$$

with

$$j' = \frac{-\sin\varphi\sin\phi(D_x - Rec_x) - \cos\varphi\sin\phi(Rec_y - D_y) + \cos\phi(Rec_z - D_z)}{-\sin\varphi\sin\phi(Rec_x - I_x) + \cos\varphi\sin\phi(Rec_y - I_y) - \cos\phi(Rec_z - I_z)}, \tag{A.31}$$

$$R_x = Rec_x + j'(Rec_x - I_x),\ R_y = Rec_y + j'(Rec_y - I_y),\ R_z = Rec_z + j'(Rec_z - I_z), \tag{A.32}$$

and

$$I_x = S_x - B(\sin\varphi\sin\phi),\ I_y = S_y + B(\cos\varphi\sin\phi),\ I_z = S_z - B\cos\phi, \tag{A.33}$$

where

$$B = 2(-\sin\varphi\sin\phi(D_x - S_x) - \cos\varphi\sin\phi(S_y - D_y) + \cos\phi(S_z - D_z)). \tag{A.34}$$

The length of the ray path L can now be found,

$$L = d_1 + d_2, \tag{A.35}$$

with

$$d_1 = \sqrt{(S_x - R_x)^2 + (S_y - R_y)^2 + (S_z - R_z)^2} \quad (A.36)$$

$$d_2 = \sqrt{(Rec_x - R_x)^2 + (Rec_y - R_y)^2 + (Rec_z - R_z)^2}. \quad (A.37)$$

A.3.1 Moveout extension for a dipping reflector

The principle of how to separate the influence of the dip and the anisotropy is the same as it was applied for the 2D case. Starting with the formula for the non-dipping reflector and isolating this term in the general formula, so that $l^2(\phi = 0)$ and $\Delta l^2(\phi, \varphi)$ remains. The source is located at the origin of the coordinate system, the receiver on the surface ($Rec_z = 0$) and the vector of the known point belonging to the reflector equals $\vec{D} = (0, 0, D_z)$. For the non-dipping case I find

$$t^2 V_G^2 = Rec_x^2 + Rec_y^2 + 4D_z^2. \quad (A.38)$$

The squared general formula looks the same as in the 2D case except that a y term is added.

$$t^2 V_G^2 = (Rec_x - I_x)^2 + (Rec_y - I_y)^2 + I_z^2, \quad (A.39)$$

with

$$I_x = 2D_z \cos\phi \sin\phi \sin\varphi, \quad (A.40)$$

$$I_y = -2D_z \cos\phi \sin\phi \cos\varphi, \quad (A.41)$$

$$I_z = 2D_z \cos^2\phi. \quad (A.42)$$

Inserting A.40, A.41, A.42 into A.39 and adding and subtracting $4D_z^2$ as it is done in the 2D case, leads to

$$t^2 V_G^2 = \underbrace{Rec_x^2 + Rec_y^2 + 4D_z^2}_{l^2(\phi=0)}$$

$$+ \underbrace{4D_z^2 \sin^2\phi\cos^2\phi\sin^2\varphi + D_z^2\sin^2\phi\cos^2\phi\cos^2\varphi + D_z^2\cos^4\phi - D_z^2}_{=-D_z^2\sin^2\phi}$$
$$- 4Rec_x D_z \cos\phi\sin\phi\sin\varphi + 4Rec_y D_z\cos\phi\sin\phi\cos\varphi. \quad \text{(A.43)}$$

The expression for $\Delta l^2(\phi,\varphi)$ can be simplified and the final result is

$$t^2V_G^2 = l^2(\phi=0) - \underbrace{4D_z\sin\phi\left[D_z\sin\phi + \cos\phi(x\sin\varphi - y\cos\varphi)\right]}_{\Delta l^2(\phi,\varphi)}. \quad \text{(A.44)}$$

Equation (A.44) shows that even in the 3-D case it is possible to separate the travel time equation for a plane reflector with an arbitrary dip and strike angle into a dip dependent and a dip independent part as long as the symmetry axis of the elastic tensor is perpendicular to the interface. This suggests that I can use the same separation procedure as in 2-D.

A.3.2 Separation process

For the separation process, if travel time data are given, I have to find the dip and the strike angle of the reflector from the minimum position of the travel time curve. As in the 2D case, I assume the source to be located at the origin of the coordinate system and the point belonging to the reflector at the same x,y position ($\vec{D} = (0,0,D_z)$). The apex of the travel time curve is measured at the position I_x, I_y.

φ is the strike and ϕ the dip angle. Dividing A.40 by A.41 yields

$$-\frac{I_x}{I_y} = \frac{\sin\varphi}{\cos\varphi} = \tan\varphi, \quad \text{(A.45)}$$

or

$$\varphi = \arctan(-\frac{I_x}{I_y}). \quad \text{(A.46)}$$

To find an expression for ϕ, A.40 and A.41 are squared and then added. Keep in mind, that $\sin\phi\cos\phi = \frac{1}{2}\sin(2\phi)$ and I use $C = -\frac{I_x}{D_z}$ and $E = \frac{I_y}{D_z}$. This leads to

$$C^2 + E^2 = \sin^2(2\phi)\sin^2\phi + \sin^2(2\phi)\cos^2\phi \quad (A.47)$$

$$C^2 + E^2 = \sin^2(2\phi). \quad (A.48)$$

The desired solution is therefore

$$\phi = \frac{1}{2}\arcsin(\sqrt{C^2 + E^2}). \quad (A.49)$$

In real data processing the strike may be directly determined from the 3-D travel time contour map as shown in Figure 4.15.

A.4 Interval moveout

Consider two line-azimuths at ϕ_1 and ϕ_2 to the fracture strike in the target. Denoting the interval moveout for the two line-azimuths as Δt_{i1} and Δt_{i2}. For azimuth ϕ_1, Δt_{i1} can be written as, according equation (3.5),

$$\Delta t_{i1}(\phi_1, x) = t_{bottom} - t_{top} = \frac{2\sqrt{x_2^2 + \Delta z^2}}{v_{p2}(\theta_2, \phi_1)} + \frac{2\sqrt{x_1^2 + z_1^2}}{v_{p1}(\theta_1)} - t_{top}, \quad (A.50)$$

and similarly, for azimuthal ϕ_2,

$$\Delta t_{i2}(\phi_2, x) = t'_{bottom} - t'_{top} = \frac{2\sqrt{x_2'^2 + \Delta z^2}}{v_{p2}(\theta'_2, \phi_2)} + \frac{2\sqrt{x_1'^2 + z_1^2}}{v_{p1}(\theta'_1)} - t'_{top}, \quad (A.51)$$

where x'_1, x'_2, θ'_1 and θ'_2 are the corresponding values of x_1, x_2, θ_1 and θ_2, for azimuth ϕ_2. The differences in these variables are caused by the azimuthal velocity variation. For an azimuthal isotropic overburden, $t_{top} = t'_{top}$, and it follows that,

$$\Delta t_{ai} = \Delta t_{i2} - \Delta t_{i1} = \Delta t_{ai1} + \Delta t_{ai2}; \quad (A.52)$$

$$\Delta t_{ai1} = \frac{2\sqrt{x_1'^2 + z_1^2}}{v_{p1}(\theta_1')} - \frac{2\sqrt{x_1^2 + z_1^2}}{v_{p1}(\theta_1)}, \tag{A.53}$$

$$\Delta t_{ai2} = \frac{2\sqrt{x_2'^2 + \Delta z^2}}{v_{p2}(\theta_2', \phi_2)} - \frac{2\sqrt{x_2^2 + \Delta z^2}}{v_{p2}(\theta_2, \phi_1)}. \tag{A.54}$$

Let

$$x_1' = x_1(1+\nu_1), \quad x_2' = x_2(1+\nu_2), \quad \theta_1' = \theta_1 + \Delta\theta_1, \quad \theta_2' = \theta_2 + \Delta\theta_2, \tag{A.55}$$

where ν_1, ν_2, $\Delta\theta_1$ and $\Delta\theta_2$ are small quantities and in the same order as the anisotropy parameters ϵ and δ. For weak anisotropy, higher orders of these terms can also neglected in searching for linearized solutions. For the model in Figure 3.8, noting

$$x_1 + x_2 = x/2, \quad x_1' + x_2' = x/2,$$

and

$$x_1 = z_1 \tan\theta_1, \; x_1' = z_1 \tan\theta_1'; \quad x_2 = \Delta z \tan\theta_2, \; x_2' = \Delta z \tan\theta_2'$$

yields the following linearized relations,

$$\nu_1 = -\frac{x_2}{x_1}\nu_2, \quad \Delta\theta_1 = -\frac{x2\sin 2\theta_1}{x_1 \sin 2\theta_2}\Delta\theta_2. \tag{A.56}$$

and

$$\nu_1 = \frac{\Delta\theta_1}{\sin\theta_1\cos\theta_1}, \quad \nu_2 = \frac{\Delta\theta_2}{\sin\theta_2\cos\theta_2}. \tag{A.57}$$

From the velocity equation (3.7) in the main text, it can been shown that for small $\Delta\theta_1$ and $\Delta\theta_2$, to the first order of the anisotropy parameters,

$$v_{p1}(\theta_1') = v_{p1}(\theta_1), \tag{A.58}$$

and

$$v_{p2}(\theta_2', \phi_2) = v_{p2}(\theta_2, \phi_2) = v_{p02}[1 + (\delta - 2\epsilon)\sin^2\phi_2 \sin^2\theta_2 + (\epsilon - \delta)\sin^4\phi_2 \sin^4\theta_2]. \tag{A.59}$$

Also applying the Snell's law for the two azimuths gives,

$$\frac{\sin\theta_1}{v_{p1}(\theta_1)} = \frac{\sin\theta_2}{v_{p2}(\theta_2,\phi_2)}; \quad \frac{\sin\theta_1'}{v_{p1}(\theta_1')} = \frac{\sin\theta_2'}{v_{p2}(\theta_2',\phi_2')}. \tag{A.60}$$

Note that strictly speaking, the Snell's law should be applied to the phase velocities and the phase angles. Although the differences between the ray and phase properties are first order anisotropy terms, their contributions to the azimuthal velocity difference are of second order or higher, hence are ignored here.

Substituting equations (A.56), (A.57),(A.58) and (A.59) into (A.60) gives,

$$\nu_1 = \frac{x_2(\sin^2\phi_2 - \sin^2\phi_1)\sin^2\theta_2\left[2\epsilon - \delta - (\epsilon-\delta)(\sin^2\phi_2 + \sin^2\phi_1)\sin^2\theta_2\right]}{x_1\cos^2\theta_2 + x_2\cos^2\theta_1}, \tag{A.61}$$

and

$$\nu_2 = -\frac{x_1(\sin^2\phi_2 - \sin^2\phi_1)\sin^2\theta_2\left[2\epsilon - \delta - (\epsilon-\delta)(\sin^2\phi_2 + \sin^2\phi_1)\sin^2\theta_2\right]}{x_1\cos^2\theta_2 + x_2\cos^2\theta_1}. \tag{A.62}$$

Substituting equations (A.56), (A.57), (A.58), (A.59), (A.61) and (A.62) into equations (A.53) and (A.54), and keeping only the linear terms of the anisotropic parameters gives,

$$\begin{aligned}\Delta t_{ai1} &= \frac{2\sqrt{x_1^2+z_1^2}}{v_{p1(\theta_1)}}\frac{x_2\sin^2\theta_1}{x_1\cos^2\theta_2 + x_2\cos^2\theta_1}\times \\ &\times \ (\sin^2\phi_2 - \sin^2\phi_1)\sin^2\theta_2\left[2\epsilon - \delta - (\epsilon-\delta)(\sin^2\phi_2 + \sin^2\phi_1)\sin^2\theta_2\right],\end{aligned} \tag{A.63}$$

and

$$\begin{aligned}\Delta t_{ai2} &= \frac{2\sqrt{x_2^2+\Delta z^2}}{v_{p02}}\left(1 - \frac{x_1\sin^2\theta_2}{x_1\cos^2\theta_2 + x_2\cos^2\theta_1}\right)\times \\ &\times \ (\sin^2\phi_2 - \sin^2\phi_1)\sin^2\theta_2\left[2\epsilon - \delta - (\epsilon-\delta)(\sin^2\phi_2 + \sin^2\phi_1)\sin^2\theta_2\right].\end{aligned} \tag{A.64}$$

From the Snell's law, equation (A.63) can be rewritten as,

$$\begin{aligned}\Delta t_{ai1} &= \frac{2\sqrt{x_2^2+\Delta z^2}}{v_{p02}} \frac{x_1 \sin^2\theta_2}{x_1\cos^2\theta_2 + x_2\cos^2\theta_1} \times \\ &\times \left(\sin^2\phi_2 - \sin^2\phi_1\right)\sin^2\theta_2 \left[2\epsilon - \delta - (\epsilon-\delta)(\sin^2\phi_2 + \sin^2\phi_1)\sin^2\theta_2\right].\end{aligned} \tag{A.65}$$

Finally, substituting equations (A.64) and (A.65) into equation (A.52) gives,

$$\begin{aligned}\Delta t_{ai} &= \frac{2\sqrt{x_2^2+\Delta z^2}}{v_{p02}} \times \\ &\times \left(\sin^2\phi_2 - \sin^2\phi_1\right)\sin^2\theta_2 \left[2\epsilon - \delta - (\epsilon-\delta)(\sin^2\phi_2 + \sin^2\phi_1)\sin^2\theta_2\right].\end{aligned} \tag{A.66}$$

Noting $x_2 = x/2 - x_1$ and equation (3.9) in the main text gives rise to equation (3.8).

Appendix B

The minimum travel time for two isotropic layers

In this appendix I will derive a formula for the minimum of the travel time for two dipping isotropic layers. The known parameters are $z_1, \Delta z, v_1, v_2$ and θ. All the variables which are used in the following derivation are defined in Figure 5.3. I try to find expressions for the different segments of the ray L_i, its depth z_{L_i} and its offset x_i. First I define some trigonometric relations.

$$\alpha = \phi - \theta, \tag{B.1}$$

$$\cos\alpha = \frac{z_1}{L_1}, \tag{B.2}$$

$$\cos(90-\alpha) = \frac{x_1}{L_1}, \tag{B.3}$$

$$\cos\phi = \frac{z_{L_1}}{L_1}. \tag{B.4}$$

For the first segment this leads to

$$L_1 = \frac{z_1}{\cos(\phi-\theta)}, \tag{B.5}$$

$$x_1 = \frac{z_1}{\cos(\phi-\theta)}\cos(90-\phi), \tag{B.6}$$

$$z_{L_1} = \frac{z_1}{\cos(\phi-\theta)}\cos\phi. \tag{B.7}$$

The length of L_2 and L_3 are equal. Therefore only one of them has to be consid-

ered. To find the angle β Snell's law is applied at the interface.

$$\frac{\sin\alpha}{v_1} = \frac{\sin\beta}{v_2}. \tag{B.8}$$

$$\cos\beta = \sqrt{1-\frac{v_2^2}{v_1^2}sin^2(\phi-\theta)}, \tag{B.9}$$

$$\cos\beta = \frac{\Delta z}{L_2}, \tag{B.10}$$

$$\cos(\theta+\beta) = \frac{z_{L_2}}{L_2}, \tag{B.11}$$

$$\sin(\theta+\beta) = \frac{x_2}{L_2}. \tag{B.12}$$

Which leads for the second segment to

$$L_2 = L_3 = \frac{\Delta z}{\sqrt{1-\frac{v_2^2}{v_1^2}\sin^2(\phi-\theta)}}, \tag{B.13}$$

$$x_2 = \frac{\Delta z}{\sqrt{1-\frac{v_2^2}{v_1^2}\sin^2(\phi-\theta)}}\sin(\theta+\beta), \tag{B.14}$$

$$z_{L_2} = \frac{\Delta z}{\sqrt{1-\frac{v_2^2}{v_1^2}\sin^2(\phi-\theta)}}\cos(\theta+\beta). \tag{B.15}$$

$$\tag{B.16}$$

The length of the third segment is equal to the second but only in the horizontal case are the depth and the offsets equal as well. For a dipping layer it reads

$$\cos(\beta-\theta) = \frac{z_{L_3}}{L_3}, \tag{B.17}$$

$$\sin(\beta-\theta) = \frac{x_3}{L_3}. \tag{B.18}$$

$$\tag{B.19}$$

Which means for the third segment

$$x_3 = \frac{\Delta z}{\sqrt{1-\frac{v_2^2}{v_1^2}\sin^2(\phi-\theta)}}\cos(\beta-\theta), \tag{B.20}$$

$$z_{L_3} = \frac{\Delta z}{\sqrt{1-\frac{v_2^2}{v_1^2}\sin^2(\phi-\theta)}}\sin(\beta-\theta). \tag{B.21}$$

To derive the expression for the fourth segment I need to know the depth at A (z_A). But this is given by

$$\begin{aligned} z_A &= z_{L_1} + z_{L_2} - z_{L_3} && \text{(B.22)} \\ &= L_1 \cos\phi + L_2 \cos(\theta+\beta) + L_3 \cos(\beta-\theta) && \text{(B.23)} \\ &= L_1 \cos\phi - 2L_2 \frac{v_2}{v_1} \sin\theta \sin(\phi-\theta) && \text{(B.24)} \\ &= \frac{z_1}{\cos(\phi-\theta)} \cos\phi - \frac{2\Delta z}{\sqrt{1-\frac{v_2^2}{v_1^2}\sin^2(\phi-\theta)}} \frac{v_2}{v_1} \sin\theta \sin(\phi-\theta). && \text{(B.25)} \end{aligned}$$

Together with

$$\begin{aligned} \cos(\alpha-\theta) &= \frac{z_A}{L_4}, && \text{(B.26)} \\ \sin(\alpha-\theta) &= \frac{x_4}{L_4}, && \text{(B.27)} \end{aligned}$$

I find

$$L_4 = \frac{\frac{z_1}{\cos(\phi-\theta)} \cos\phi - \frac{2\Delta z}{\sqrt{1-\frac{v_2^2}{v_1^2}\sin^2(\phi-\theta)}} \frac{v_2}{v_1} \sin\theta \sin(\phi-\theta)}{\cos(\phi-2\theta)} \qquad \text{(B.28)}$$

$$\begin{aligned} x_4 = \Bigg(& \frac{z_1}{\cos(\phi-\theta)} \cos\phi \\ & - \frac{2\Delta z}{\sqrt{1-\frac{v_2^2}{v_1^2}\sin^2(\phi-\theta)}} \frac{v_2}{v_1} \sin\theta \sin(\phi-\theta) \Bigg) \sin(\phi-2\theta). \end{aligned} \qquad \text{(B.29)}$$

The travel time as a function of the take off angle ϕ is therefore given by

$$\begin{aligned} t(\phi) &= \frac{L_1}{v_1} + \frac{L_2+L_3}{v_2} + \frac{L_4}{v_1} && \text{(B.30)} \\ &= \frac{z_1}{\cos(\phi-\theta)v_1} + 2\frac{\Delta z}{v_2\sqrt{1-\frac{v_2^2}{v_1^2}\sin^2(\phi-\theta)}} \\ &\quad + \frac{\frac{z_1}{\cos(\phi-\theta)} \cos\phi - \frac{2\Delta z}{\sqrt{1-\frac{v_2^2}{v_1^2}\sin^2(\phi-\theta)}} \frac{v_2}{v_1} \sin\theta \sin(\phi-\theta)}{\cos(\phi-2\theta)v_1}. && \text{(B.31)} \end{aligned}$$

To find the minimum for $0 < \phi < 90$ I have to solve

$$\frac{\partial t(\phi)}{\partial \phi} = 0. \tag{B.32}$$

It can be shown that this problem has the unique solution

$$\phi_{min} = 2\theta. \tag{B.33}$$

Appendix C

The LSQ solution for a cosine

In this appendix I will derive a formula for the least squares solution for a cosine function with arbitrary frequency. I will show that the problem is uniquely solvable if at least three data points are given

The function to minimize is given by

$$\epsilon(\phi, A, y_0) = \sum_{i=1}^{i=N} (y_i - (A\cos(x_i + \phi) + y_0))^2. \tag{C.1}$$

First the derivatives with respect to the unknown parameters have to be calculated. The next step is to separate in each term the variables dependent on the unknown parameters from the observed data. The resulting three equations have to be zero to satisfy the criteria to be an extrema. I will show that this system of equations is solvable.

$$\begin{aligned}
\frac{\partial \epsilon}{\partial A} &= \sum_{i=1}^{i=N} (2(y_i - y_0 - A(\cos x_i \cos\phi - \sin x_i \sin\phi))(\sin x_i \sin\phi - \cos x_i \cos\phi)) \\
&= 2\sin\phi \underbrace{\sum_{i=1}^{i=N} (y_i \sin x_i)}_{f} - 2\cos\phi \underbrace{\sum_{i=1}^{i=N} (y_i \cos x_i)}_{e} - 4A\cos\phi\sin\phi \underbrace{\sum_{i=1}^{i=N} (\cos x_i \sin x_i)}_{h} \\
&+ 2A\cos^2\phi \underbrace{\sum_{i=1}^{i=N} (\cos^2 x_i)}_{g} - 2y_0 \sin\phi \underbrace{\sum_{i=1}^{i=N} (\sin x_i)}_{c} + 2y_0 \cos\phi \underbrace{\sum_{i=1}^{i=N} (\cos x_i)}_{b}
\end{aligned}$$

$$+ \quad A\sin^2\phi \underbrace{\sum_{i=1}^{i=N}(\sin^2 x_i)}_{k}, \tag{C.2}$$

$$\begin{aligned}\frac{\partial\epsilon}{\partial y_0} &= \sum_{i=1}^{i=N}(-2y_i + 2A\cos x_i\cos\phi - 2A\sin x_i\sin\phi + y_0)\\ &= -2\underbrace{\sum_{i=1}^{i=N}(y_i)}_{a} + 2A\cos\phi\underbrace{\sum_{i=1}^{i=N}(\cos x_i)}_{b} - 2A\sin\phi\underbrace{\sum_{i=1}^{i=N}(\sin x_i)}_{c} + 2y_0\underbrace{\sum_{i=1}^{i=N}(1)}_{i},\end{aligned} \tag{C.3}$$

$$\begin{aligned}\frac{\partial\epsilon}{\partial\phi} &= \sum_{i=1}^{i=N}(-2(y_i - y_0 - A(\cos x_i\cos\phi - \sin x_i\sin\phi))\\ &\quad \cdot A(-cosx_i\sin\phi - \sin x_i\cos\phi))\\ &= 2A\sin\phi\underbrace{\sum_{i=1}^{i=N}(y_i\cos x_i)}_{e} + 2A\cos\phi\underbrace{\sum_{i=1}^{i=N}(y_i\sin x_i)}_{f} 2Ay_0\sin\phi\underbrace{\sum_{i=1}^{i=N}(\cos x_i)}_{b}\\ &\quad - 2Ay_0\cos\phi\underbrace{\sum_{i=1}^{i=N}(\sin x_i)}_{c} - 2A^2\sin\phi\cos\phi\underbrace{\sum_{i=1}^{i=N}(\cos^2 x_i)}_{g}\\ &\quad - 2A^2\cos^2\phi\underbrace{\sum_{i=1}^{i=N}(\cos x_i\sin x_i)}_{h} + 2A^2\sin^2\phi\underbrace{\sum_{i=1}^{i=N}(\cos x_i\sin x_i)}_{h}\\ &\quad + 2A^2\sin\phi\cos\phi\underbrace{\sum_{i=1}^{i=N}(\sin^2 x_i)}_{k}.\end{aligned} \tag{C.4}$$

It follows that the equation system I have to solve can be written as

$$\begin{aligned}0 &= f\sin\phi - e\cos\phi - 2hA\cos\phi\sin\phi + gA\cos^2\phi - cy_0\sin\phi + by_0\cos\phi\\ &\quad + kA\sin^2\phi\end{aligned} \tag{C.5}$$

$$0 = -a + bA\cos\phi - cA\sin\phi + iy_0 \tag{C.6}$$

$$\begin{aligned}0 &= e\sin\phi + f\cos\phi - by_0\sin\phi - cy_0\cos\phi - gA\sin\phi\cos\phi - hA\cos^2\phi\\ &\quad + hA\sin^2\phi + kA\sin\phi\cos\phi.\end{aligned} \tag{C.7}$$

The solution involves the solving equation C.6 in terms of y_0,

$$y_0 = -\frac{a}{i} + \frac{b}{i} A\cos\phi - \frac{c}{i} A\sin\phi + i, \tag{C.8}$$

inserting it into equation C.5 and solving the resulting equation in terms of A

$$A = \frac{e\cos\phi - f\cos\phi + \frac{ca}{i}\sin\phi - \frac{ba}{i}\cos\phi}{(k - \frac{c^2}{i})\sin^2\phi + 2(\frac{bc}{i} - h)\cos\phi\sin\phi + (g - \frac{b^2}{i})\cos^2\phi}. \tag{C.9}$$

Now insert equation C.9 into equation C.8 and both the results from new equation C.8 and C.9 into equation C.7. This equation now only contains ϕ as parameter and can be solved. The result is

$$\phi = -\arctan\left(\frac{-b^2 f - ehi + ebc + bah + gfi - gca}{-ec^2 + eki - bak + bcf - hfi + hca}\right) \tag{C.10}$$

To find the solution for another frequency than 1, x_i has to be replaced by $n \cdot x_i$ where n is the number of cycles in the interval $0 < x < 2\pi$. This will change nothing in the solution, just the values of the sums will change.

Appendix D

Orthorhombic AVO

In this appendix, the derivation of how to set up the impedance matrices, derive its changes and the effect of the deviation of the polarisation direction are explained and it is shown how the general form of the reflection coefficient is obtained.

D.1 The impedance matrices

Using the definition in Figure 6.1, vectors used in equation 6.2 and 6.3 can be written as:

$$\begin{pmatrix} e_{P_1} \\ e_{P_3} \end{pmatrix} = \begin{pmatrix} \sin i^* \\ \cos i^* \end{pmatrix}$$
$$\begin{pmatrix} e_{S_1} \\ e_{S_3} \end{pmatrix} = \begin{pmatrix} \cos j^* \\ -\sin j^* \end{pmatrix} \tag{D.1}$$

$$\begin{pmatrix} s_1 \\ s_{3_P} \end{pmatrix} = \begin{pmatrix} \sin i/\alpha \\ \cos i/\alpha \end{pmatrix}$$
$$\begin{pmatrix} s_1 \\ s_{3_S} \end{pmatrix} = \begin{pmatrix} \sin j/\beta \\ \cos j/\beta \end{pmatrix}. \tag{D.2}$$

Following the convention of Aki and Richards (1980), i and j are used as the average propagation angles of the upper and lower media for qP and qS; i^* and

j^* as the corresponding average polarisation angles. α and β are the average qP - and qS -phase velocities of the upper and lower media associated with direction i and j, and $C_{kl}\,(k,l=1,2,...,6)$ as the average elastic constants of the upper and lower media. Substituting equations (D.1) and (D.2) into (6.2) and (6.3) gives,

$$\mathbf{X} = \begin{pmatrix} \sin i^* & \cos j^* \\ 2\rho'\beta \sin j \sin i^* - \frac{C_{33}}{\alpha}\cos(i^* - i) & 2\rho'\beta \cos j \sin j^* + \frac{C_{13}}{\beta}\sin(j^* - j) \end{pmatrix}, \tag{D.3}$$

$$\mathbf{Y} = \begin{pmatrix} -\frac{C_{55}}{\alpha}\sin(i^* + i) & -\frac{C_{55}}{\beta}\cos(j^* + j) \\ \cos i^* & -\sin j^* \end{pmatrix}. \tag{D.4}$$

Similar to Thomsen (1993), the definition of polarisation deviations is given by

$$\begin{aligned} \sin i^* &= (1 + \zeta_P)\sin i \\ \sin j^* &= (1 + \zeta_S)\sin j. \end{aligned} \tag{D.5}$$

where the variables ζ_P and ζ_S define the deviations between the polarisation direction (i^* and j^*) and the propagation direction (i and j) of qP-wave and the qS-wave. These quantities are small for weak anisotropy and therefore the impedance matrices can be expressed as

$$\begin{aligned} \mathbf{X} &= \mathbf{X}^{(0)} + \mathbf{X}^{(1)} \\ \mathbf{Y} &= \mathbf{Y}^{(0)} + \mathbf{Y}^{(1)} \end{aligned} \tag{D.6}$$

where $\mathbf{X}^{(0)}$ and $\mathbf{Y}^{(0)}$ are the impedance matrices for $i^* = i$ and $j^* = j$, the wave propagating in an isotropic plane where no polarisation deviation occurs.

$$\begin{aligned} \mathbf{X}^{(0)} &= \begin{pmatrix} \sin i & \cos j \\ 2\rho'\alpha \sin^2 j - \frac{C_{33}}{\alpha} & \rho'\beta \sin 2j \end{pmatrix} \\ |\mathbf{X}^{(0)}| &= \frac{C_{33}}{\alpha}\cos j, \end{aligned} \tag{D.7}$$

$$\mathbf{Y}^{(0)} = \begin{pmatrix} -\frac{C_{55}}{\alpha}\sin 2i & -\frac{C_{55}}{\beta}\cos 2j) \\ \cos i & -\sin j \end{pmatrix}$$

$$|\mathbf{Y}^{(0)}| = \frac{C_{55}}{\beta}\cos i, \tag{D.8}$$

and $\mathbf{X}^{(1)}$ and $\mathbf{Y}^{(1)}$ are the small perturbations in the impedance matrices related the polarisation deviations ζ_P and ζ_S,

$$\mathbf{X}^{(1)} = \begin{pmatrix} \zeta_P \sin i & -\zeta_S \cos j \tan^2 j \\ 2\zeta_P \rho' \alpha \sin^2 j & \zeta_S(2\rho'\beta\cos^2 j + \frac{C_{13}}{\beta})\tan j \end{pmatrix} \tag{D.9}$$

$$\mathbf{Y}^{(1)} = \begin{pmatrix} -\zeta_P \frac{C_{55}}{\alpha}\cos 2i \tan i & 2\zeta_S \frac{C_{55}}{\beta}\sin^2 j \\ -\zeta_P \cos i \tan^2 i & -\zeta_S \sin j \end{pmatrix}. \tag{D.10}$$

The variable ρ' is defined as

$$\rho' = \frac{1}{2\beta^2}(C_{33} - C_{13}), \tag{D.11}$$

which can be interpreted as a generalised density. Equation (D.6) shows that impedance matrices $\mathbf{X}$ and $\mathbf{Y}$ can be separated into an initial term plus a small perturbation due to the polarisation deviation.

D.1.1 Changes in the impedance matrices $\Delta\mathbf{X}$ and $\Delta\mathbf{Y}$

In order to calculate the reflection coefficient, the changes of the impedance matrices $\Delta\mathbf{X}$ and $\Delta\mathbf{Y}$ have to be derived. This is done by differentiating $\mathbf{X}$ and $\mathbf{Y}$ with respect to each of the relevant variables in equation (D.6). A differentiation operator ∂ is defined

$$\begin{aligned} \partial = {} & \Delta\rho'\frac{\partial}{\partial\rho'} + \Delta C_{33}\frac{\partial}{\partial C_{33}} + \Delta C_{55}\frac{\partial}{\partial C_{55}} + \Delta C_{13}\frac{\partial}{\partial C_{13}} + \Delta\alpha\frac{\partial}{\partial\alpha} + \Delta\beta\frac{\partial}{\partial\beta} \\ + {} & \Delta i\frac{\partial}{\partial i} + \Delta j\frac{\partial}{\partial j} + \Delta\zeta_P\frac{\partial}{\partial\zeta_P} + \Delta\zeta_S\frac{\partial}{\partial\zeta_S} \end{aligned} \tag{D.12}$$

which leads to

$$\begin{aligned}\Delta\mathbf{X} &= \Delta\mathbf{X}^{(0)} + \Delta\mathbf{X}^{(1)} = \partial(\mathbf{X}^{(0)}) + \partial(\mathbf{X}^{(1)}) \\ \Delta\mathbf{Y} &= \Delta\mathbf{Y}^{(0)} + \Delta\mathbf{Y}^{(1)} = \partial(\mathbf{Y}^{(0)}) + \partial(\mathbf{Y}^{(1)}).\end{aligned} \tag{D.13}$$

Differentiating $\mathbf{X}^{(0)}$ and $\mathbf{Y}^{(0)}$ in equations (D.7) and (D.8), and noting $\Delta i = \frac{\Delta\alpha}{\alpha}\tan i$ and $\Delta j = \frac{\Delta\beta}{\beta}\tan j$, gives

$$\Delta\mathbf{X}^{(0)} = \begin{pmatrix} \cos i\tan i\Delta\alpha/\alpha & -\sin j\tan j\Delta\beta/\beta \\ 2\alpha\sin^2 j\Delta\rho' + 2\rho'\sin^2 j\Delta\alpha & \beta\sin 2j\Delta\rho' + \rho'\sin 2j\Delta\beta \\ +4\rho'\alpha\sin^2 j\frac{\Delta\beta}{\beta} + \frac{C_{33}}{\alpha}\left(\frac{\Delta\alpha}{\alpha} - \frac{\Delta C_{33}}{C_{33}}\right) & +2\rho'\beta\cos 2j\tan j\frac{\Delta\beta}{\beta} \end{pmatrix}, \tag{D.14}$$

$$\Delta\mathbf{Y}^{(0)} = \begin{pmatrix} \frac{C_{55}}{\alpha}\left[2\tan i\frac{\Delta\alpha}{\alpha}\right. & \frac{C_{55}}{\beta}\left[4\sin^2 j\frac{\Delta\beta}{\beta}\right. \\ \left. -\sin 2i\left(\frac{\Delta\alpha}{\alpha} + \frac{\Delta C_{55}}{C_{55}}\right)\right] & \left. -\cos 2j\left(\frac{\Delta\beta}{\beta} + \frac{\Delta C_{55}}{C_{55}}\right)\right] \\ -\sin i\tan i\Delta\alpha/\alpha & -\cos j\tan j\Delta\beta/\beta \end{pmatrix}. \tag{D.15}$$

Similarly, differentiating $\mathbf{X}^{(1)}$ and $\mathbf{Y}^{(1)}$ in equations (D.9) and (D.10) leads to

$$\Delta\mathbf{X}^{(1)} = \begin{pmatrix} \Delta\zeta_P\sin i & -\Delta\zeta_S\cos j\tan^2 j \\ 2\Delta\zeta_P\rho'\alpha\sin^2 j & \Delta\zeta_S(2\rho'\beta\cos^2 j + \frac{C_{13}}{\beta})\tan j \end{pmatrix}; \tag{D.16}$$

$$\Delta\mathbf{Y}^{(1)} = \begin{pmatrix} -\Delta\zeta_P\frac{C_{55}}{\alpha}\cos 2i\tan i & 2\Delta\zeta_S\frac{C_{55}}{\beta}\sin^2 j \\ -\Delta\zeta_P\cos i\tan^2 i & -\Delta\zeta_S\sin j \end{pmatrix}. \tag{D.17}$$

All the Δ quantities are assumes to be small and therefore any other than linear term are ignored.

D.2 Polarisation deviations ζ_P and ζ_S

The polarisation deviations, as defined in equation (D.5), are determined by the polarisation vectors which are in turn determined by the eigenvectors of the

Kelvin-Christoffel equation. For wave propagation in the $x_1 - x_3$ symmetry plane of the orthorhombic medium, a simple analytical solution of the polarisation vectors can be obtained (Fryer and Frazer, 1987),

$$\begin{pmatrix} e_{P_1} \\ e_{P_3} \end{pmatrix} = \begin{pmatrix} \sin i^* \\ \cos i^* \end{pmatrix} = \frac{1}{N_P} \begin{pmatrix} (C_{55} + C_{13}) \dfrac{\sin i \cos i}{\alpha^2} \\ \rho - \left(C_{11} \dfrac{\sin^2 i}{\alpha^2} + C_{55} \dfrac{\cos^2 i}{\alpha^2} \right) \end{pmatrix}, \tag{D.18}$$

$$\begin{pmatrix} e_{S_1} \\ e_{S_3} \end{pmatrix} = \begin{pmatrix} \cos j^* \\ -\sin j^* \end{pmatrix} = \frac{1}{N_S} \begin{pmatrix} (C_{55} + C_{13}) \dfrac{\sin j \cos j}{\beta^2} \\ \rho - \left(C_{11} \dfrac{\sin^2 j}{\beta^2} + C_{55} \dfrac{\cos^2 j}{\beta^2} \right) \end{pmatrix}, \tag{D.19}$$

where

$$N_P = \sqrt{\left[(C_{55} + C_{13}) \frac{\sin i \cos i}{\alpha^2} \right]^2 + \left[\rho - \left(C_{11} \frac{\sin^2 i}{\alpha^2} + C_{55} \frac{\cos^2 i}{\alpha^2} \right) \right]^2}, \tag{D.20}$$

$$N_S = \sqrt{\left[(C_{55} + C_{13}) \frac{\sin j \cos j}{\beta^2} \right]^2 + \left[\rho - \left(C_{11} \frac{\sin^2 j}{\beta^2} + C_{55} \frac{\cos^2 j}{\beta^2} \right) \right]^2}, \tag{D.21}$$

are the normalisation factors for obtaining unit polarisation vectors.

To derive equation (D.29) for polarisation deviations ζ_P and ζ_S, the inverse of the normalisation factors ($1/N_P$ and $1/N_S$) has to be linearised in terms of the small anisotropic quantities δ', ϵ'_P and ϵ'_S which are defined as follows:

$$\begin{aligned} \delta' &= \frac{(C_{55} + C_{13})^2 - (C_{11} - C_{55})^2}{2C_{11}(C_{11} - C_{55})} \\ &\approx \frac{2C_{55} + C_{13} - C_{11}}{C_{11}} \\ \epsilon'_P &= \frac{\rho\alpha^2}{C_{11}} - 1 \\ \epsilon'_S &= \frac{\rho\beta^2}{C_{55}} - 1. \end{aligned} \tag{D.22}$$

$1/N_P$ and $1/N_S$ can be re-written as,

$$\frac{1}{N_P} = \frac{\alpha^2}{C_{11}} \left[\frac{(C_{55} + C_{13})^2}{C_{11}^2} \sin^2 i \cos^2 i + \left(\epsilon'_P + \frac{C_{11} - C_{55}}{C_{11}} \cos^2 i \right)^2 \right]^{-\frac{1}{2}}$$

$$\approx \frac{1}{N_{P0}} \frac{\alpha^2}{C_{11}\cos i}\left(1 - \epsilon'_P \frac{C_{11}-C_{55}}{C_{11}N_{P0}^2}\right), \tag{D.23}$$

$$\begin{aligned}\frac{1}{N_S} &= \frac{\beta^2}{C_{55}}\left[\frac{(C_{55}+C_{13})^2}{C_{55}^2}\sin^2 j\cos^2 j + \left(\epsilon'_S - \frac{C_{11}-C_{55}}{C_{55}}\sin^2 j\right)^2\right]^{-\frac{1}{2}} \\ &\approx \frac{1}{N_{S0}}\frac{\beta^2}{C_{55}\sin j}\left(1 + \epsilon'_S \frac{C_{11}-C_{55}}{C_{55}N_{S0}^2}\right),\end{aligned} \tag{D.24}$$

$$\begin{aligned}N_{P0}^2 &= \frac{1}{C_{11}^2}\left[(C_{55}+C_{13})^2\sin^2 i + (C_{11}-C_{55})^2\cos^2 i\right], \\ N_{S0}^2 &= \frac{1}{C_{55}^2}\left[(C_{55}+C_{13})^2\cos^2 j + (C_{11}-C_{55})^2\sin^2\right].\end{aligned}$$

Further, $1/N_{P0}$ and $1/N_{S0}$ can be linearised as,

$$\begin{aligned}\frac{1}{N_{P0}} &= \frac{C_{11}}{C_{11}-C_{55}}\left(1 + \delta'\frac{2C_{11}\sin^2 i}{C_{11}-C_{55}}\right)^{-\frac{1}{2}} \\ &\approx \frac{C_{11}}{C_{11}-C_{55}}\left(1 - \delta'\frac{C_{11}}{C_{11}-C_{55}}\sin^2 i\right),\end{aligned} \tag{D.25}$$

$$\begin{aligned}\frac{1}{N_{S0}} &= \frac{C_{55}}{C_{11}-C_{55}}\left(1 + \delta'\frac{2C_{11}\cos^2 j}{C_{11}-C_{55}}\right)^{-\frac{1}{2}} \\ &\approx \frac{C_{55}}{C_{11}-C_{55}}\left(1 - \delta'\frac{C_{11}}{C_{11}-C_{55}}\cos^2 j\right).\end{aligned} \tag{D.26}$$

Substituting these two equations into equations (D.23) and (D.24) gives the linearised version of the inverse of these normalisation factors as,

$$\frac{1}{N_P} = \frac{\alpha^2}{(C_{11}-C_{55})\cos i}\left(1 - \delta'\frac{C_{11}}{C_{11}-C_{55}}\sin^2 i - \epsilon'_P\frac{C_{11}}{C_{11}-C_{55}}\right), \tag{D.27}$$

$$\frac{1}{N_S} = \frac{\beta^2}{(C_{11}-C_{55})\sin j}\left(1 - \delta'\frac{C_{11}}{C_{11}-C_{55}}\cos^2 j + \epsilon'_S\frac{C_{55}}{C_{11}-C_{55}}\right). \tag{D.28}$$

Finally, substituting (D.27) and (D.28) into e_{P_1} and e_{S_1} in equations (D.18) and (D.19), together with the definition of polarisation deviation in equation (D.5), and making some manipulations yields the polarisation deviations.

$$\zeta_P = \frac{C_{11}}{C_{11}-C_{55}}(\delta'\cos^2 i - \epsilon'_P)$$

$$\zeta_S = -\frac{C_{11}}{C_{11}-C_{55}}\left(\delta' \cos^2 j + \frac{C_{55}\cos^2 j}{C_{11}\sin^2 j}\epsilon'_S\right); \tag{D.29}$$

D.3 Reflection coefficients

To find the reflection coefficients, equations (D.6) and (D.13) are substituted into equation (6.1) where $\mathbf{X}^{(1)}$ and $\mathbf{Y}^{(1)}$ are assumed to be small.

$$\mathbf{R} = \frac{1}{2}\left(\mathbf{X}^{(0)-1}\Delta\mathbf{X}^{(0)} - \mathbf{Y}^{(0)-1}\Delta\mathbf{Y}^{(0)}\right) + \frac{1}{2}\left(\mathbf{X}^{(0)-1}\Delta\mathbf{X}^{(1)} - \mathbf{Y}^{(0)-1}\Delta\mathbf{Y}^{(1)}\right). \tag{D.30}$$

Two 2×2 matrices are introduced

$$\begin{aligned} \mathbf{I}_A &= \begin{pmatrix} 0 & -1 \\ 1 & 0 \end{pmatrix} \\ \mathbf{I}_B &= \begin{pmatrix} 0 & 1 \\ -1 & 0 \end{pmatrix} \end{aligned} \tag{D.31}$$

in order to write the inverse of matrices $\mathbf{X}^{(0)}$ and $\mathbf{Y}^{(0)}$ as,

$$\begin{aligned} \mathbf{X}^{(0)-1} &= \frac{1}{|\mathbf{X}^{(0)}|}\mathbf{I}_A\mathbf{X}^{(0)T}\mathbf{I}_B \\ \mathbf{Y}^{(0)-1} &= \frac{1}{|\mathbf{Y}^{(0)}|}\mathbf{I}_A\mathbf{Y}^{(0)T}\mathbf{I}_B, \end{aligned} \tag{D.32}$$

where superscript T denotes matrix transpose operation. Substituting (D.32) into (D.30) gives,

$$\begin{aligned} \mathbf{R} &= \frac{1}{2}\left(\frac{\mathbf{I}_A\mathbf{X}^{(0)T}\mathbf{I}_B}{|\mathbf{X}^{(0)}|}\Delta\mathbf{X}^{(0)} - \frac{\mathbf{I}_A\mathbf{Y}^{(0)T}\mathbf{I}_B}{|\mathbf{Y}^{(0)}|}\Delta\mathbf{Y}^{(0)}\right) \\ &+ \frac{1}{2}\left(\frac{\mathbf{I}_A\mathbf{X}^{(0)T}\mathbf{I}_B}{|\mathbf{X}^{(0)}|}\Delta\mathbf{X}^{(1)} - \frac{\mathbf{I}_A\mathbf{Y}^{(0)T}\mathbf{I}_B}{|\mathbf{Y}^{(0)}|}\Delta\mathbf{Y}^{(1)}\right) \end{aligned} \tag{D.33}$$

Substituting equations (D.7), (D.8),(D.14), (D.15), (D.16), and (D.17) into (D.33) and manipulating them accordingly leads to the formulation of the linearised reflection coefficients for orthorhombic media

$$r_{qPqP} = \frac{1}{2}\left(\frac{\Delta C_{33}}{C_{33}} - \frac{\Delta\alpha}{\alpha}\right) + \frac{1}{2}\left[\frac{\Delta\alpha}{\alpha} - \frac{2\rho'\beta^2}{C_{33}}\left(\frac{\Delta\rho'}{\rho'} + 2\frac{\Delta\beta}{\beta}\right) - \frac{2\beta^2}{\alpha^2}\frac{\Delta C_{55}}{C_{55}}\right]\sin^2 i$$
$$+ \frac{1}{2}\frac{\Delta\alpha}{\alpha}\sin^2 i\tan^2 i + \frac{1}{2}\left(1 - \frac{\beta^2}{\alpha^2}\right)\tan^2 i\,\Delta\zeta_P, \tag{D.34}$$

$$r_{qPqS} = \frac{\sin i}{\cos j}\left[-\frac{1}{2}\left(\frac{\Delta C_{33}}{C_{33}} - 2\frac{\Delta\alpha}{\alpha}\right) - \frac{\beta}{\alpha}\frac{\Delta C_{55}}{C_{55}}\cos i\cos j\right.$$
$$\left. + \frac{\rho'\beta^2}{C_{33}}\left(\frac{\Delta\rho'}{\rho'} + 2\frac{\Delta\beta}{\beta}\right)\sin^2 i + \frac{1}{2}\left(1 - \frac{\sin 2j}{\sin 2i}\right)\Delta\zeta_P\right], \tag{D.35}$$

$$r_{qSqP} = \frac{\sin j}{\cos i}\left[-\frac{1}{2}\left(\frac{\Delta C_{55}}{C_{55}} - 2\frac{\Delta\beta}{\beta}\right) - \frac{\rho'\alpha\beta}{C_{33}}\left(\frac{\Delta\rho'}{\rho'} + 2\frac{\Delta\beta}{\beta}\right)\cos i\cos j\right.$$
$$\left. + \frac{\Delta C_{55}}{C_{55}}\sin^2 j + \frac{1}{2}\left(1 - \frac{\sin 2i}{\sin 2j}\right)\Delta\zeta_S\right], \tag{D.36}$$

$$r_{qSqS} = -\frac{1}{2}\left(\frac{\Delta C_{55}}{C_{55}} - \frac{\Delta\beta}{\beta}\right) - \frac{1}{2}\left[\frac{\Delta\beta}{\beta} - \frac{2\rho'\alpha^2}{C_{33}}\left(\frac{\Delta\rho'}{\rho'} + 2\frac{\Delta\beta}{\beta}\right) - 2\frac{\Delta C_{55}}{C_{55}}\right]\sin^2 j$$
$$- \frac{1}{2}\frac{\Delta\beta}{\beta}\sin^2 j\tan^2 j + \frac{1}{2}\left(\frac{\alpha^2}{\beta^2} - 1\right)\tan^2 j\,\Delta\zeta_S. \tag{D.37}$$

Appendix E

List of publications

[1] Kühnel, T. and Li, X.-Y. 1996, Can we separate the effects of anisotropy and structure from P-wave seismic data? Proceedings of the 7th International Workshop on Seismic Anisotropy, 10-15 February, 1996, Miami, in press

[2] Li, X.-Y., Kühnel, T. and MacBeth, C., 1996. Converted wave AVO and its implication. 58th EAEG Meeting, Amsterdam, Expanded Abstracts, M046.

[3] Kühnel, T., and Li, X-Y., 1996. Can we separate the effects of anisotropy and structure from P-wave travel-time data?, 58th EAGE Meeting, Amsterdam, Expanded Abstracts, C017.

[4] Li, X.-Y., Kühnel, T. and MacBeth, C., 1996. Mixed mode AVO response in fractured media. 66th SEG meeting, Expanded Abstracts, 1822-1825.

[5] Kühnel, T., and Li, X-Y, 1996. Anisotropy versus dip - a separation approach. 66th SEG Meeting, Expanded Abstracts, 1866-1869.

[6] Kühnel, T. and Li, X.-Y., 1997. Separation of anisotropy and structure during processing. 59th EAGE Meeting, Geneva, Expanded Abstracts, P052.

[7] Kühnel, T., Li, X.-Y. and MacBeth, C., 1997. Crack-related variations in the reflection coefficient. 67th SEG meeting, Dallas, Expanded Abstracts, 1993-1996.

[8] Li, X.-Y., Kühnel, T. and MacBeth, C., 1997. Converted wave AVO in fractured media and implications. Geophysical Prospecting, submitted.